



AKADEMIA GÓRNICZO-HUTNICZA IM. STANISŁAWA STASZICA W KRAKOWIE

**DZIEDZINA Nauki ścisłe i przyrodnicze**

DYSCYPLINA Nauki Fizyczne

DYSCYPLINA DODATKOWA Nauki Biologiczne

## **ROZPRAWA DOKTORSKA**

*Memrystywnne układy neuromimetyczne i rezerwurowe*

Autor: mgr inż. Dawid Franciszek Przyczyna

Pierwszy promotor rozprawy: prof. dr hab. Konrad Szaciłowski

Drugi promotor rozprawy: prof. dr hab. Grzegorz Hess

Promotor pomocniczy: dr inż. Kacper Pilarczyk

Praca wykonana: Akademia Górniczo Hutnicza im. Stanisława Staszica

Wydział Fizyki i Informatyki Stosowanej

Akademickie Centrum Materiałów i Nanotechnologii



## PODZIĘKOWANIA

*Chciałbym złożyć serdeczne podziękowania mojemu pierwszemu promotorowi prof. dr hab. Konradowi Szaciłowskiemu za wsparcie, zrozumienie oraz ogrom możliwości. Jestem wdzięczny za dyskusje poszerzające wyobraźnię, za wyprawy od protestującego Hong Kongu, poprzez świętą górę Kogaionon aż po Operę Krakowską, oraz za praktyczną pomoc w laboratoryjnych sytuacjach, które wydawały się bez wyjścia.*

*Dziękuję mojemu drugiemu promotorowi prof. dr hab. Grzegorzowi Hessowi za wsparcie i pomoc udzieloną w trakcie trwania studiów doktoranckich.*

*Dziękuję mojemu promotorowi pomocniczemu dr inż. Kacprowi Pilarczykowi za współpracę – zarówno na scenie, jak i w laboratorium – liczne dyskusje, rekursje, rozważania, dociekania, spekulacje, dywagacje i dygresje oraz nieocenioną pomoc w badaniach.*

*Dziękuję moim współlokatorom biurowym dr Michałowi Szuwarzyńskiemu, dr Adze Podborskiej oraz dr Magdzie Bisztyga-Szklarz za wsparcie i wspaniałe towarzystwo.*

*Dziękuję wszystkim kolegom i koleżankom za wspólnie spędzony czas na przerwach kawowo-lunchowych oraz w laboratoriach.*

*Dziękuję załodze ACMiN za ciepłą atmosferę, otwartość i wsparcie.*

*Dziękuję współautorom publikacji za ich wkład w wykonanie badań i wspólną interpretację wyników.*

*Dziękuję przyjaciółom i rodzinie za wsparcie.*

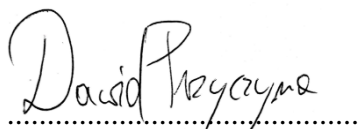
*Dziękuję za obecność i wsparcie Karolinie Szafrąńskiej.*



## *OŚWIADCZENIE AUTOA ROZPRAWY*

Oświadczam, świadom odpowiedzialności karnej za poświadczenie nieprawdy, że niniejszą rozprawę doktorską wykonałem osobiście i samodzielnie oraz że nie korzystałem z innych źródeł niż wymienione w pracy.

19 września 2022 r.



mgr inż. Dawid Przyczyna

## *OŚWIADCZENIA PROMOTORÓW*

Niniejsza rozprawa jest gotowa do oceny przez recenzentów.

19 września 2022 r.

.....  
prof. dr hab. Konrad Szaciłowski

.....  
prof. dr hab. Grzegorz Hess





NARODOWE CENTRUM NAUKI

Dawid Przczyzna uzyskał środki finansowe z Narodowego Centrum Nauki w ramach projektu PRELUDIUM16 nr 2018/31/N/ST5/03112



**Fundusze Europejskie**  
Wiedza Edukacja Rozwój

**Unia Europejska**  
Europejski Fundusz Społeczny



Niniejsza rozprawa doktorska została wykonana w ramach Programu Operacyjnego Wiedza Edukacja Rozwój, nr projektu POWR.03.02.00-00-I004/16, współfinansowanego ze środków Unii Europejskiej.



**AKADEMICKIE CENTRUM  
MATERIAŁÓW  
i NANOTECHNOLOGII AGH**

Praca wsparta infrastrukturą badawczą Akademickiego Centrum Materiałów i Nanotechnologii.





## Spis treści

<i>Streszczenie</i> .....	11
<i>Abstract</i> .....	15
<i>Spis rysunków</i> .....	19
<i>Wprowadzenie, kontekst oraz układ pracy</i> .....	23
<i>Bibliografia</i> .....	31
<i>Streszczenia artykułów wchodzących w skład rozprawy</i> .....	35
D1. Ewelina Właźlak, Dawid Przyczyna, Rafael Gutierrez, Gianarelio Cuniberti, Konrad Szaciłowski „Towards synthetic neural networks: can artificial electrochemical neurons be coupled with artificial memristive synapses?”, <i>Jpn. J. Appl. Phys.</i> 2020, 59, SI0801. ....	37
D2. Dawid Przyczyna, Maria Lis, Kacper Pilarczyk, Konrad Szaciłowski „Hardware realization of the pattern recognition with an artificial neuromorphic device exhibiting a short-term memory”, <i>Molecules</i> 2019, 24, 2738.....	45
D3. Dawid Przyczyna, Maciej Suhecki, Andrew Adamatzky, Konrad Szaciłowski „Towards Embedded Computation with Building Materials”, <i>Materials</i> 2021, 14, 1724.....	51
D4. Dawid Przyczyna, Sebastien Pecqueur, Dominique Vuillaume, Konrad Szaciłowski „Reservoir computing for sensing: an experimental approach”, <i>Int. J. Unconv. Comput.</i> , 2019, 14, 267.....	57
D5. Dawid Przyczyna, Maria Szaciłowska, Marek Przybylski, Marcin Strzelecki, Konrad Szaciłowski „Recognition of Musical Dissonance and Consonance in a Simple Neuromorphic Computing System”, <i>Int. J. Unconv. Comput.</i> 2022, 17, 81.....	63
D6. Dawid Przyczyna, Grzegorz Hess, Konrad Szaciłowski „KNOWM Memristors in a Bridge Synapse delay-based Reservoir Computing system for detection of epileptic seizures”, <i>Int. J. Parallel Dist. Syst.</i> 2022, 10.1080/17445760.2022.2088751. ....	71
<i>Dorobek naukowy</i> .....	79
<i>Załączniki</i> .....	81



## Streszczenie

Opracowywanie materiałów półprzewodnikowych i badanie mechanizmów ich działania pozwoliło na stworzenie i rozwój technologii komputerowych stanowiących fundament cywilizacji informacji, z którą mamy do czynienia w dzisiejszych czasach. Analiza i przetwarzanie danych w domenach usług internetowych, finansów, autonomicznych pojazdów czy inteligentnej infrastruktury bazującej na urządzeniach Internetu Rzeczy jest wykonywane z wykorzystaniem narzędzi *uczenia maszynowego* (obok klasycznych metod statystycznych). Jedną z intensywnie rozwijanych gałęzi uczenia maszynowego są *sztuczne sieci neuronowe*. W swojej funkcjonalności i/lub strukturze wzorują się one na biologicznych układach nerwowych. Wynika to z ogromnych zdolności mózgu do uczenia się, rozpoznawania wzorców oraz ich klasyfikacji. Jego zdolności bazują głównie na wysoce równoległym i iteracyjnie zoptymalizowanym przetwarzaniu danych w oparciu o wielką liczbę połączonych ze sobą neuronów.

W ramach prób poprawy wydajności urządzeń komputerowych, prowadzone są intensywne badania z zastosowaniem *inżynierii neuromorficznej*. Ta interdyscyplinarna dziedzina, w której głównym wzorcem układów obliczeniowych są biologiczne struktury nerwowe, czerpie inspiracje z matematyki, elektroniki, inżynierii materiałowej, biologii i informatyki. Wykorzystanie nowoczesnych technologii materiałowych umożliwia symulowanie neuronalnych oraz synaptycznych funkcji o różnych stopniach złożoności, co w efekcie zapewnia zwiększoną równoległość działania w obszarach takich jak rozpoznawanie wzorców i analiza grafów. Obecnie zagadnienia związane z inżynierią neuromorficzną znajdują się w domenie niekonwencjonalnego przetwarzania informacji, lecz ten fakt powoli się zmienia. Wiele jednostek naukowych prowadzi intensywne badania czerpiące inspiracje z biologicznych struktur nerwowych w celu osiągnięcia wydajniejszych układów obliczeniowych, potencjalnie o uniwersalnym charakterze.

Jedną z innowacyjnych technologii z domeny inżynierii neuromorficznej są urządzenia *memrystywne*. Wykorzystanie urządzeń memrystywnych pozwala delegować niektóre etapy obliczeniowe sztucznych sieci neuronowych tak, aby były wykonane *in materia*, bazując wprost na właściwościach danego urządzenia. Takie podejście wydaje się omijać problem „wąskiego gardła von Neumanna”. W klasycznych systemach obliczeniowych informacje są przechowywane w pamięci, a wszystkie obliczenia wykonywane są w mikroprocesorze. Architektura von Neumanna zakłada stały przepływ danych pomiędzy tymi komponentami komputera, co w efekcie spowalnia obliczenia i zużywa energię. Systemy dynamiczne (zarówno półprzewodnikowe, jak i układy „mokre” (ang. *wetware*)) umożliwiają przeprowadzanie obliczeń również w układach posiadających funkcje pamięci.

W klasycznej konfiguracji urządzeń memrystywnych, materiał pojemnościowy (np. dielektryk lub półprzewodnik) umieszczany jest pomiędzy elektrodami o przewodnictwie metalicznym w układzie warstwowym. Urządzenia memrystywne cechują się nieliniową charakterystyką prądowo-napięciową, która przyjmuje formę pętli histerezy. Dla klasycznych urządzeń memrystywnych można zaobserwować dwa stany oporności (niskiej oraz wysokiej). Poprzez zastosowanie impulsów elektrycznych lub przebiegów zmiennonapięciowych o odpowiedniej amplitudzie potencjału elektrycznego, materiały można przełączać do odpowiednich stanów przewodnictwa w zależności od typu memrystora i jego stanu początkowego. Zmienność działania w zależności od częstotliwości impulsów/skanów wzbudzających jest kolejną cechą urządzeń memrystywnych. Ze względu na retencję stanów obserwowaną dla elementów

memrystywnych po wyłączeniu źródła zasilania, efekt przełączania rezystywnego może zostać wykorzystany jako element konstrukcyjny nowej pamięci nieulotnej.

Jednym z problemów sztucznych sieci neuronowych jest ich kosztowny proces uczenia, szczególnie w przypadku rekurencyjnych bądź głębokich sieci neuronowych. Optymalizacji podlegają wszystkie wagi połączeń pomiędzy poszczególnymi neuronami, jak również sam poziom aktywacji danego neuronu. Gdy sieć zawiera rekurencyjne połączenia bądź wiele warstw, każda iteracja aktualizacji wag wydłuża trenowanie całej sieci. Aby rozwiązać ten problem, Jaeger oraz Maas niezależnie zaproponowali odpowiednio *Echo State Network* oraz *Liquid State Machine*. W ich podejściu, trenowaniu podlega jedynie fragment sieci próbujący stan warstwy przetwarzającej informacje. W swoich pracach wskazali na kluczowe znaczenie wielowymiarowej, bogatej oraz dynamicznej przestrzeni stanów warstwy przetwarzającej informacji. Z czasem, oba z tych podejść efektywnego trenowania sieci neuronowych zostały ujęte we wspólne ramy koncepcyjne, które określono jako *obliczanie rezerwuarowe*.

Aby poprawnie działać, te niekonwencjonalne systemy obliczeniowe muszą posiadać kilka cech, a mianowicie muszą wykazywać bogatą dynamikę wewnętrzną, pamięć „ulotną” oraz właściwość *echa stanów*. Obwody obliczania rezerwuarowego są oparte na: (i) elemencie nieliniowym (np. memrystorze), który zapewnia również funkcje pamięci, (ii) warstwie wejściowej, która dostarcza informacje/sygnał do przetwarzania, (iii) warstwie odczytu i opcjonalnie (iv) opóźnionej pętli sprzężenia zwrotnego, która uzupełnia i rozwija wewnętrzną dynamikę systemu. Do odczytu stanu warstwy rezerwuaru nie jest potrzebna wyrafinowana sztuczna sieć neuronowa, lecz wystarczą proste modele, takie jak regresja liniowa czy drzewo binarne (zakładając że układ rezerwuarowy dokonuje odpowiedniej transformacji sygnału).

*Single Node Echo-State Machine* (SNESM) to nowatorskie systemy obliczania rezerwuarowego, które wykorzystują tylko jeden węzeł obliczeniowy działający w pętli opóźnionego sprzężenia zwrotnego. Zasadniczo zarówno sygnał, jak i stan węzła obliczeniowego zmieniają się za każdym razem, gdy sygnał przechodzi przez urządzenie w każdym kolejnym cyklu. Ewolucja sygnału w pętli może potencjalnie poprawić możliwości grupowania i klasyfikacji systemu obliczania rezerwuarowego. System SNESM daje dodatkową korzyść w postaci rozszerzenia zestawu danych wejściowych. Każda kolejna epoka sygnału jest nieco inną wersją sygnału bazowego ze względu na nieliniową transformację i tłumienie

w układzie SNESM. Echo sygnału pierwotnego może być łatwiejsze do sklasyfikowania ze względu na zmiany w jego złożoności i korelacji pomiędzy opisującymi je parametrami.

W ramach pracy doktorskiej „Memrystywne układy neuromimetyczne i rezerwuarowe” wykonane zostały badania nad wykorzystaniem kilku substratów obliczeniowych w domenie niekonwencjonalnego przetwarzania informacji. Wykonane prace uporządkowano tak, aby wprowadzać kolejne elementy i koncepcje zarówno konstrukcji układu, jak i sposobów przetwarzania informacji i jej analizy, które finalnie są zsyntezowane w pojedynczych badaniach.

W pierwszej kolejności przedstawiono artykuł przeglądowy w którym zawarty jest opis memfraktorów (model uwzględniający urządzenia memrystywne), prostych algorytmów sztucznych sieci neuronowych oraz układów obliczania rezerwuarowego. Zawarto również matematyczny opis układów rezerwuarowych z pętlą sprzężenia zwrotnego.

Następnie przedstawiono badania nad fotoelektrochemicznym sztucznym neuronem, które wskazują na możliwość wykorzystania prostego układu neuromorficznego do zadania klasyfikacji pisma odręcznego. Pomiary zrealizowano na bazie polimorficznego siarczku kadmu, przedstawiono również jego charakterystykę spektroskopową. Wyniki wskazują na poprawę w separowalności danych wejściowych przetworzonych przez układ neuromorficzny względem surowych danych. Praca wprowadza koncepcje konstrukcji układu przetwarzającego informacje przy wykorzystaniu pojedynczego węzła obliczeniowego. Wprowadzono również elementy analizy danych.

Paradygmat obliczeniowy rezerwurowego obliczania wprowadzony jest wprost w badaniach bazujących na układzie zawierającym cement domieszkowany nanomateriałami półprzewodnikowymi oraz drobinami metalicznymi. Właściwości elektryczne wybranych próbek zostały zbadane za pomocą woltamperometrii cyklicznej oraz spektroskopii impedancyjnej. Prezentowany układ został wykorzystany do klasyfikacji sygnałów elektrycznych o prostych kształtach – sinusoidalny, trójkątny oraz prostokątny. Dodatkowo, jeden z parametrów złożoności analizowanych sygnałów umożliwia rozróżnienie pomiędzy domieszkowaniem próbki. Badania podtrzymują i uzupełniają doniesienia literaturowe o możliwości realizacji obliczania rezerwurowego na najprostszych substratach obliczeniowych przeznaczonych do zadań klasyfikacyjnych.

Możliwość wykorzystania pojedynczego węzła obliczeniowego w rezerwurowym układzie z pętlą sprzężenia zwrotnego (SNESM) przedstawiono na bazie polimerowego tranzystora polowego. Prezentowany układ SNESM jest bardzo bliski koncepcyjnie do algorytmu *State Weaving Environment Echo Tracker*, w którym układ rezerwurowy jest w bezpośrednim kontakcie z analizowanym środowiskiem. Badany układ wykorzystano do poprawy działania tranzystora polimerowego w roli prostego sensora jonów. Dokonano tego poprzez zmianę reprezentacji danych, możliwą dzięki transformacji (zależnej od stężenia analizowanych jonów  $K^+$ ) sygnału w układzie SNESM.

Badania nad wykorzystaniem rezerwurowego układu SNESM do analizy i grupowania interwałów muzycznych zrealizowano na bazie symulacji *synapsy mostkowej*. Synapsa mostkowa składa się z czterech memrystorów oraz wzmacniacza operacyjnego. W ramach badań przedstawiono generacje wyższych harmonicznych w kilku układach memrystywnych. Przedstawiono porównanie efektów transformacji sygnałów sinusoidalnych reprezentujących interwały muzyczne w skali naturalnej z krzywą konsonansów/dysonansów sensorycznych oraz wyznaczonych na podstawie algorytmu Setharesa. Reprezentacja danych w przestrzeni odległości składowych harmonicznych umożliwia częściowe grupowanie interwałów muzycznych względem ich stopnia konsonansu/dysonansu.

Finalnie, prezentowane są badania nad fizyczną implementacją synapsy mostkowej na bazie pół-komercyjnych memrystorów KNOWM w układzie rezerwurowym SNESM w celu rozpoznania ataku epilepsji. W badaniach tych do trenowania modelu wykorzystano prosty algorytm uczenia maszynowego – drzewo binarne. Analizowany, pobrany online standardowy zestaw danych został zebrany z wykorzystaniem trójosiowego akcelerometru noszonego na rękę dla prostej diagnostyki ataku epilepsji bez konieczności stosowania systemu EEG. W ramach *cech* wykorzystywanych do szkolenia modelu zastosowano szereg parametrów określających złożoność analizowanych sygnałów. Obliczenia parametrów złożoności wykonano również dla nieprzetworzonych danych aby porównać wpływ układu SNESM na

dany sygnał oraz jakość jego klasyfikacji. Do oceny dokładności klasyfikacji wykorzystano F1-score – zbalansowany parametr statystyczny lepiej oddający zdolność do klasyfikacji układu niż prosta *precyzja*. Przedstawiono wyniki poprawy dokładności klasyfikacji sygnałów symulujących atak epilepsji dla restrykcyjnych warunków (niewielkie zestawy danych) gdzie istotna jest szybkość i prostota – co tym samym wpływa na niski koszt – trenowania i testowania finalnego modelu klasyfikacyjnego. Źródłem poprawy klasyfikacji mogą być zmiany w dystrybucjach analizowanych parametrów oraz zmiany w korelacji pomiędzy nimi. Dodatkowo korzystny wpływ ma zdolność do ekspansji zestawu danych przez układ SNESM.

## *Abstract*

The development of semiconductor materials and the study of their mechanisms of operation have allowed the creation and development of powerful computer technologies that are the foundation of the information civilization we see today. Analysis and processing of data in the domains of Internet services, finance, autonomous vehicles or intelligent infrastructure based on Internet of Things devices are performed using *machine learning* tools (in addition to classical statistical methods). One of the intensively developed branches of machine learning is artificial neural networks. In their functionality and/or structure they are modeled on biological nervous systems. This is due to the brain's tremendous ability to learn, recognize patterns and classify them. Its abilities are based mainly on highly parallel and iteratively optimized data processing based on a large number of interconnected neurons.

In an attempt to improve the performance of computing devices, intensive research is being conducted using *neuromorphic engineering*. This interdisciplinary field draws inspiration from biology, mathematics, electronic engineering, materials engineering, and computer science where biological neural structures are the main template for computing systems. The use of modern materials technology enables the simulation of neuronal and synaptic functions of varying degrees of complexity, resulting in increased parallelism in areas such as pattern recognition and graph analysis. At the moment, neuromorphic engineering is still in the domain of unconventional computing, but this too is slowly changing. Many research institutes are conducting intensive research drawing inspiration from biological neural structures to achieve more efficient computational systems, potentially of universal applicability.

One of the innovative technologies from the neuromorphic engineering domain are memristive devices. The use of memristive devices makes it possible to delegate some of the computational steps of artificial neural networks so that they are performed *in materia*, based directly on the properties of the device in question. This approach seems to circumvent the von-Neumann bottleneck problem. In classical computing systems, information is stored in memory and all calculations are performed in the microprocessor. The von-Neuman architecture assumes a constant flow of data between these computer components, which in effect slows down computation and consumes energy. Dynamic systems (both semiconductor and wetware) also allow computations to be performed in systems that have memory functions.

In the classical configuration of memristive devices, a capacitive material (e.g., a dielectric or semiconductor) is placed between electrodes with metallic conductivity in a layered arrangement. Memristive devices are characterized by nonlinear current-voltage characteristics, which take the form of a pinched hysteresis loop. For classical memristive devices, two states of resistance (low and high) can be observed. By applying electrical pulses (or alternating-voltage waveforms) with the appropriate amplitude of the electrical potential, materials can be switched to the appropriate conductivity states depending on the type of memristor and its initial state. The variability of operation depending on the frequency of the excitation pulses/scans is another feature of memristive devices. Because of the retention of states observed for memristive elements when the power source is turned off, the effect of resistive switching can be used as a building block for new non-volatile memory.

One of the problems of artificial neural networks is their expensive learning process, especially in the case of recurrent or deep neural networks. All the connection weights between individual

neurons, as well as the activation level of a given neuron itself, are subject to optimization. When the network contains recursive connections or multiple layers, each iteration of weight updates prolongs the training of the entire network. To solve this problem, Jaeger and Maas independently proposed the Echo State Network and Liquid State Machine, respectively. In their approach, only the portion of the network sampling the state of the information processing layer is trained. In their work, they pointed out the crucial importance of a multidimensional, rich and dynamic state space of the information processing layer to simplify the training stage of the reading layer as much as possible. Over time, both of these approaches for efficiently training neural networks were subsumed into a common conceptual framework, which was referred to as *reservoir computing*.

To work properly, these unconventional computing systems must have several features, namely, they must exhibit rich internal dynamics, "fleeting" memory, and echo-state property. Reservoir computing circuits are based on: (i) a nonlinear element (e.g., a memristor) that also provides memory functions, (ii) an input layer that provides information/signal for processing, (iii) a readout layer, and optionally (iv) a delayed feedback loop that complements and develops the internal dynamics of the system. A sophisticated artificial neural network is not needed to read the state of the reservoir layer, but simple models such as linear regression or a binary tree will suffice (assuming the reservoir system performs the appropriate signal transformation).

Single Node Echo-State Machine (SNESM) are novel reservoir computing systems that use only one computing node operating in a delayed feedback loop. Essentially, both the signal and the state of the computing node change each time the signal passes through the machine in each successive cycle. The evolution of the signal in the loop can potentially improve the clustering and classification capabilities of a reservoir computing system. The SNESM system has the added benefit of expanding the data set. Each successive epoch of the signal is a slightly different version of the primary signal due to nonlinear transformation and attenuation in the SNESM system. The echo of the primary signal may be easier to classify due to changes in its complexity and the correlation between the parameters describing it.

The dissertation, "Memristive Neuromimetic and Reservoir Computing Systems" includes research on the use of several computational substrates in the domain of unconventional information processing. The work performed was organized to introduce successive elements and concepts of both system design and methods of information processing and analysis, which are finally synthesized in single studies. A review article is presented first, which includes a description of memfractors (a general model that describes memristive devices), simple artificial neural network models, and reservoir computing systems. A mathematical description of delay-based reservoir computing systems is also included. Following, research on photoelectrochemical artificial neuron indicates the possibility of using a simple neuromorphic system for the task of handwriting classification. Measurements were realized based on polymorphic cadmium sulfide, for which spectroscopic characteristics are also presented. The results show an improvement in the separability index of the input data processed by the neuromorphic system relative to the raw data. The paper introduces concepts for the design of an information processing system using a single computational node. Elements of data analysis are also introduced. The computational paradigm of reservoir computing is introduced directly in a study based on a system containing cement doped with semiconductor nanomaterials and metallic particles. The electrical properties of selected samples have been studied by cyclic voltammetry and impedance spectroscopy. The presented system was used to classify electrical



signals of simple shapes – sinusoidal, triangular, and rectangular. In addition, one of the complexity parameters of the analyzed signals allows for distinguish between doping of the sample. The research sustains and complements literature reports on the possibility of implementing reservoir computing on the simplest possible computational substrates for classification tasks. The possibility of using a single computational node in a SNESM system is presented based on a polymer field-effect transistor. The presented SNESM circuit is very close conceptually to the State Weaving Environment Echo Tracker algorithm, in which the reservoir circuit is in direct contact with the analyzed environment. The studied circuit was used to improve the performance of a polymer transistor in the role of an ion sensor. This was done by changing the data representation, made possible by signal transformation (dependent on the concentration of  $K^+$  ions) in the SNESM system. Research on the use of the SNESM reservoir system for analyzing and clustering musical intervals was realized with simulations of a bridge synapse. The bridge synapse consists of four memristors and an operational amplifier. The study presents the generation of higher harmonics in several memristive systems. A comparison of the effects of transforming sinusoidal signals representing musical intervals (from natural scale) with the consonance/sensory dissonance curve and curves determined by the Sethares algorithm is presented. Representation of the data in the space of harmonic component distances allows for partial clustering of musical intervals with respect to their degree of consonance/dissonance. Finally, research is presented on the physical implementation of a bridge synapse (based on semi-commercial KNOWM memristors) in a SNESM reservoir system for epilepsy attack recognition where a simple machine learning algorithm (binary tree) was used to train the model. The analyzed standard data set (downloaded online) was collected using a wearable triaxial accelerometer for simple diagnosis without the need for an EEG system. Complexity parameters of the analyzed signals were used as *features* to train the model. Computations of the complexity parameters were also performed for raw data to compare the effect of the SNESM system on a given signal and its classification quality. The F1-score – a balanced statistical parameter that better reflects the classification ability of the given system than simple *precision* – was used to evaluate the classification accuracy. Results are presented for improving the classification accuracy of signals simulating an epilepsy attack for restrictive conditions (small data sets) where speed and simplicity - thus affecting low cost - of training and testing the final classification model are important. Changes in the distributions of the analyzed parameters and changes in the correlation between them could be the sources of improvement in classification scores. In addition, the ability of the SNESM system to expand the data set has a beneficial effect on resulting classification accuracy.



## Spis rysunków

<b>Rysunek 1.</b> Schemat klasycznej architektury obliczeniowej von Neumanna (a) oraz niekonwencjonalny system obliczeniowy in materia (b). „Wąskie gardło von Neumana” oznaczono czerwonymi strzałkami. Niebieskie strzałki oznaczają transfer informacji między substratem obliczeniowym a interfejsem/systemem odczytu. <sup>26</sup> .....	25
<b>Rysunek 2.</b> Przecinające się pętle histerezy zarejestrowane dla warstw jodobizmutanu metyloamonowego z różnymi proporcjami jodku metyloamonowego (MAI) i jodku bizmutu (a) oraz STDP dla materiału 3:1 (b). <sup>35</sup> .....	26
<b>Rysunek 3.</b> Schemat klasycznej struktury jednokierunkowej sieci neuronowej (a), typowego układu RC (b) z losowo, rekurencyjnie i rzadko połączonymi węzłami sieci oraz układ RC z opóźnioną pętlą sprzężenia zwrotnego o topologii kołowej (układ SNESM) (c). Niebieskie węzły reprezentują różne wejścia oddziałujące na rezerwuar. Czerwone węzły reprezentują różne funkcje odczytu, w zależności od tego, które parametry rezerwuaru planujemy sondować. $\theta$ — oznacza czas między wirtualnymi neuronami (pełny czas linii opóźniającej), $\tau$ — czas potrzebny na efektywną ewolucję systemu, NL — węzeł nieliniowy. <sup>26</sup> .....	28
<b>Rysunek 4.</b> Uproszczona ilustracja koncepcji układu SNESM (sygnał wyjściowy generowany jest przy każdym „obiegu” sygnału w pętli sprzężenia zwrotnego) (a). Przykład klasyfikacji sygnałów na podstawie ich amplitudy oraz efekt metaplastyczności obserwowany przy 1.6Vpp (b). Zarejestrowane sygnały z eksperymentów z zamkniętą pętlą dla 1,7 Vpp (c) oraz 1.9Vpp (d) amplitudy początkowej. <sup>44</sup> .....	29
<b>Rysunek 5.</b> Zestawienie pasywnych elementów elektrycznych: R oznacza rezystor, C – kondensator, L – cewkę, a M – memrystor, $\alpha$ i $\beta$ na osiach wyrażają rząd operatora różniczkowego. Czerwona kropka wskazuje położenie memfraktora $\frac{1}{4}$ rzędu ( $\alpha = 0,25$ ), natomiast gruba niebieska linia w poprzek żółtego obszaru wskazuje najprostsze elementy memfrakcyjne, które nie mogą akumulować energii, ale nadal zapewniają funkcje pamięciowe istotne dla przetwarzania sygnałów i informacji (a). Pętle histerezy otrzymane dla modelu memrystora sterowanego ładunkiem dla różnych wartości parametrów $\alpha$ i stałej wartości $\beta = 1$ (b). Przypadek $\alpha = 0,25$ (czerwona krzywa) jest zbliżony do doświadczalnie zmierzonych pętli histerezy w memrystorach na bazie halogenków ołowiu (c). .....	40
<b>Rysunek 6.</b> Schematyczna struktura jednoelementowej sieci perceptronowej (a) i jednoelementowej sieci neuronowej typu spiking (spiking neural network) (b). .....	41
<b>Rysunek 7.</b> Proponowany mechanizm obserwowanego efektu pamięci dla badanych próbek CdS. CB – pasmo przewodnictwa, VB – pasmo walencyjne (a). Szpilki fotoprądowe rejestrowane po impulsowym wzbudzeniu świetlnym dla różnych interwałów pomiędzy impulsami (b). Analiza wzmocnienia fotoprądu przedstawiona względem odstępu czasu pomiędzy impulsami (c). .....	47
<b>Rysunek 8.</b> Obraz odręcznego znaku o rozmiarach 28 na 28 pikseli z zaznaczonym wierszem (a) przetłumaczonym na sekwencję bitów i odpowiadających im impulsów świetlnych (b). Znormalizowana odpowiedź fotoprądowa układu dla danego wejścia binarnego. Linie oznaczają trzy wartości progowe (c). Rekonstrukcja obrazu na podstawie znormalizowanych wartości fotoprądu. ...	48
<b>Rysunek 9.</b> Schemat przedstawiający procedurę określania wydajności układu klasyfikującego (a). Porównanie parametru całkowitej separowalności względem różnych wartości progowych. Wyniki dla czterech rzutów 3d poszczególnych ćwiartek ( $\kappa_1, \kappa_2, \kappa_3, \kappa_4$ ). .....	49
<b>Rysunek 10.</b> Pomiary voltamperometryczne dla niedomieszkowanego betonu (a), betonu domieszkowanego 10% masowo półprzewodnikiem SbSI (b) oraz betonu domieszkowanego 10% masowo mieszkanką 1:1 opiłkami metalicznymi oraz ziarnami półprzewodnika SbSI (c). .....	53
<b>Rysunek 11.</b> Widma impedancyjne próbek betonu niedomieszkowanego oraz domieszkowanego metalem i półprzewodnikiem: wykres Nyquista (a) kąty przesunięcia fazowego (wraz z uproszczonym obwodem zastępczym) (b) i zależność impedancji od częstotliwości (c). .....	54
<b>Rysunek 12.</b> Schemat podwójnego systemu obliczania rezerwuarowego opartego na betonie używanego do klasyfikacji prostych sygnałów. ....	55

<b>Rysunek 13.</b> Wykres współrzędnych równoległych dla wybranych parametrów złożoności analizowanych sygnałów: wykładnik wahań (detrended fluctuation exponent) ( $\alpha$ ), entropia próbki ( $S_s$ ), wymiar fraktalny Petrosiana (DP) i entropia permutacyjna ( $S_p$ ). .....	56
<b>Rysunek 14.</b> Ogólny zarys systemu detekcji SWEET. Rezerwuar wrażliwy na środowisko jest wykorzystywany do uzyskiwania informacji o nim. Może się to odbywać na drodze bezpośredniej, co daje nieprzetworzoną informację o środowisku, $\xi(q,t)$ , lub na drodze pośredniej, poprzez badanie odpowiedzi rezerwuaru $\Phi(q,t)$ po użyciu sygnału wzbudzającego $u(t)$ . Opóźnione sprzężenie zwrotne jest dodawane w celu zwiększenia złożoności przestrzeni konfiguracji i uzyskania lepszych właściwości obliczeniowych rezerwuaru (a). Symboliczna reprezentacja złożonego problemu wykrywania. Czujnik ma za zadanie wykryć stan układu (żółty lub zielony) na podstawie pomiaru obserwabli $\alpha$ i $\beta$ . Po lewej stronie przypadek niskiej separacji danych w przestrzeni fazowej, w którym problem detekcji jest trudny i podatny na błędy. Zastosowanie czujnika opartego na obliczeniach rezerwuarowych z odpowiednim sygnałem wzbudzającym (drive) powoduje separację analizowanych danych, dzięki czemu może dać znacznie bardziej wiarygodne informacje. W tym scenariuszu do wnioskowania o stanie środowiska można wykorzystać stosunkowo prostą warstwę odczytową. Większość obliczeń jest wykonywana przez urządzenie, a nie przez warstwę odczytu. ....	59
<b>Rysunek 15.</b> Schemat oraz zdjęcie wykonane przy pomocy mikroskopii optycznej organicznego tranzystora elektrochemicznego PEDOT:PSS. ....	60
<b>Rysunek 16.</b> Schemat układu systemu rezerwuarowego z pętlą sprzężenia zwrotnego na bazie organicznego tranzystora elektrochemicznego. Wejście potencjostatu steruje źródłem zadanego potencjału, wyjście jest analogowym monitorem prądu. ....	60
<b>Rysunek 17.</b> Przykładowa odpowiedź badanego układu obliczania rezerwuarowego z pętlą sprzężenia zwrotnego przy wysokim stężeniu jonów $K^+$ (a). Transformaty Fouriera dla wszystkich paczek sygnału zarejestrowane przy określonym stężeniu. (b). Amplitudy pierwszej składowej (20 Hz) w funkcji czasu dla różnych stężeń jonów potasu (c). Krzywa kalibracyjna na podstawie wartości stałych czasowych zaniku krzywych eksponencjalnych w funkcji stężenia jonów potasu (d) .....	61
<b>Rysunek 18.</b> Percepcja dysonansu przez osoby z (49 osób) i bez (100 osób) wykształcenia muzycznego, na podstawie danych z ref. (Lopresto 2015) (a). Dysonans muzyczny obliczony dla tonu podstawowego $A_2 = 110$ Hz i zmiennej liczby składowych harmonicznnych: przykładowe widmo Fouriera tonu $A_2$ (b) oraz obliczone na podstawie modelu Setharesa krzywe dysonansu sensorycznego dla zmiennej liczby składowych harmonicznnych (c).....	65
<b>Rysunek 19.</b> Rozpatrywane obwody memrystywne zaimplementowane na platformie MULTISIM. Obwody bazujące na pojedynczym memrystorze (a), synapsie mostkowej bez (b) oraz ze wzmacniaczem różnicowym (c). ....	66
<b>Rysunek 20.</b> Przykład sygnałów wejściowych (a) i wyjściowych (b) zarejestrowanych w pętli sprzężenia zwrotnego układu SNESM: sygnał wejściowy – kwinta ( $A_1-E_1$ , niebieski) i echo wyjściowe (czerwony). Zielona strzałka wskazuje czas trwania każdej epoki. Przykładowe transformaty Fouriera dla ewolucji sygnału odpowiadającego septymie wielkiej $C_2-B_2$ (c). Schemat układu Single Node Echo-State Machine zaimplementowany na platformie MULTISIM (d).....	67
<b>Rysunek 21.</b> Liczba składowych częstotliwościowych dla różnych interwałów muzycznych dla kolejnych transformat Fouriera sygnału krążącego w pętli sprzężenia zwrotnego (a) oraz odwrotność liczby szczytów w funkcji stosunku częstotliwości dla różnych interwałów. Obszar zacieniony na szaro przedstawia symulowaną krzywą "konsonansu sensorycznego" (lustrzane odbicie krzywej dysonansu z Rys. 18c dla 5 harmonicznnych). Punkty reprezentują dane eksperymentalne. ....	67
<b>Rysunek 22.</b> Ilustracja metody analizy sygnału na podstawie odległości między składowymi częstotliwościowymi obecnymi w widmach Fouriera.....	68
<b>Rysunek 23.</b> Geometryczne przedstawienie różnych interwałów na podstawie odległości między kolejnymi składowymi widm Fouriera. Wszystkie interwały (a), sekundy i tercje (b), prymy, oktawy, kwinty i kwarty (c) oraz trytony, seksty i septymy (d).....	69

<b>Rysunek 24.</b> Schematy badanych układów. Synapsa mostkowa bez (a), ze wzmacniaczem różnicowym (b) oraz włączona do układu SNESM (c).....	74
<b>Rysunek 25.</b> Przykładowy wynik woltamperometrii sinusoidalnej o dużej amplitudzie o prędkości skanu 10 Hz (a) oraz obliczone na jego podstawie widmo Fouriera (z prostokątną funkcją apodyzującą) (b). Całkowite zniekształcenie harmoniczne określone na podstawie transformaty Fouriera dla częstotliwości od 1 do 100 Hz (c). Przedstawiono wyniki dla pojedynczego memrystora (I), synapsy mostkowej bez wzmacniacza różnicowego (II) oraz ze wzmacniaczem różnicowym (III). Przykładowy szum mierzony dla pojedynczego memrystora KNOWM przedstawiony w domenie częstotliwości, dla potencjałów od 0V do 1V. Czarna linia wskazuje szum termiczny przy 0 V (d). Przykład dopasowania linii do kilku filtrowanych widm szumu (e). Zebrane wartości nachylenia widm szumu przy różnych potencjałach prądu stałego. Strzałki służą do wskazania kierunku przeprowadzania eksperymentu. Przykładowe wyniki dla pojedynczego memrystora KNOWM (f). .	74
<b>Rysunek 26.</b> Zbiór wartości stałej czasowej zaniku wykładniczego dla trzech prostych kształtów sygnału tłumionych w układzie SNESM bazującym na synapsie mostkowej (a). Przykłady czterech klas sygnału z analizowanego zbioru danych (po standaryzacji) (b). Ewolucja sygnału w układzie SNESM (c). Najpierw sygnał sterujący przechodzi przez system, a następnie, po transformacji przez synapsę mostkową, jest opóźniany i zwracany ponownie na wejście układu Strzałki wskazują kierunek przepływu danych.....	76
<b>Rysunek 27.</b> Wynik oceny dokładności klasyfikacji (na podstawie parametru F-score) dla kolejnych epok sygnału (a) oraz dla kilku epok na raz (b). Liczba „0” symbolizuje nieprzetworzone dane wejściowe służące jako odniesienie. ....	77
<b>Rysunek 28.</b> Porównanie histogramów dla parametrów złożoności sygnału nieprzetworzonego („Pure”, zabarwiony na czerwono) i sygnału przetworzonego w układzie obliczania rezerwurowego („RC”, zabarwiony na niebiesko) dla pacjenta nr. 1 (epoka nr 5 dla RC).....	77



## *Wprowadzenie, kontekst oraz układ pracy*

Opracowywanie materiałów półprzewodnikowych i badanie mechanizmów ich działania pozwoliło na stworzenie i rozwój potężnych technologii komputerowych stanowiących fundament cywilizacji informacji, którą obserwujemy w dzisiejszych czasach.<sup>1</sup> Obecnie można zauważyć drastyczny rozwój technologiczny i prawdziwą „eksplozję” danych tworzonych i gromadzonych poprzez różne działania. Naukowcy zaczynają zwracać uwagę na efekt, który można obserwować na świecie – tzw. informacyjną czarną dziurę. Koncepcja ta opiera się na fakcie, że generowana jest tak duża ilość informacji, że ich pełne przetworzenie przestaje być możliwe.<sup>2-4</sup> Z tego powodu ważne informacje mogą zostać utracone w „czarnej dziurze”, przytłoczone powszechnie generowanym szumem danych. Nie powinno to dziwić w czasach, gdy wśród artykułów gospodarstwa domowego znajdować może się szereg inteligentnych urządzeń m.in. telefon, lodówka, żarówka, telewizor, pralka, odkurzacz, zasłony, ogrzewanie czy nawet asystent (np. Apple Siri, Google Assistant, Samsung Bixby). Te złożone systemy gromadzenia i przetwarzania informacji określane są mianem „Internetu rzeczy”.<sup>5-7</sup> Dodatkowo, w każdej sekundzie w cyberprzestrzeni generowana jest ogromna porcja danych. Powszechnie korzysta się z mediów społecznościowych, komunikatorów, sklepów internetowych, usług streamingowych itp. Dane zbierane na każdej z tych platform są analizowane i profilowane, aby móc dostarczać użytkownikom bardziej spersonalizowane reklamy i generować większy zysk usługodawcy. Ponadto, Internet dostarcza użytkownikom informacje publikowane przez znajomych lub grupy, do których należy lub subskrybuje na tematy, które przyciągają uwagę ze względu na preferencje estetyczne, intelektualne lub polityczne.<sup>8</sup> Zbieranie i analiza tych danych przekłada się na realne efekty w świecie w postaci zysków/strat pieniężnych,<sup>9,10</sup> wyborów użytkowników jako konsumentów i wreszcie jako wyborców (przypadek Cambridge Analytica dotyczący wyborów prezydenckich w USA i Brexitu).<sup>11</sup>

Analiza i przetwarzanie danych wymienionych powyżej (obok klasycznych metod statystycznych) jest wykonywana z wykorzystaniem narzędzi *uczenia maszynowego*. Jedną z intensywnie rozwijanych gałęzi uczenia maszynowego są *sztuczne sieci neuronowe*.<sup>12</sup> W swojej funkcjonalności i/lub strukturze wzorują się one na biologicznych układach nerwowych. Wynika to z ogromnych zdolności mózgu do uczenia się, rozpoznawania wzorców oraz ich klasyfikacji. Te zdolności bazują głównie na wysoce równoległym i iteracyjnie zoptymalizowanym przetwarzaniu danych w oparciu o wielką liczbę połączonych ze sobą neuronów. Szacuje się, że w ludzkim organizmie znajduje się około 10–20 mld neuronów zlokalizowanych w korze mózgowej oraz około 55–70 mld neuronów w mózdzku, przy czym każdy z nich zdolny jest do tworzenia aż do  $10^4$  połączeń z innymi komórkami.<sup>13</sup> Szacuje się, że mózg wykazuje gęstość mocy rzędu  $10\text{mW}/\text{cm}^2$ , pracując w trybie niskoczęstotliwościowym (o średniej częstotliwości aktywności neuronów równej 10Hz) w porównaniu do wysokoczęstotliwościowych procesorów krzemowych (działających z gigahercową częstotliwością) o wysokiej gęstości mocy rzędu  $100\text{W}/\text{cm}^2$ .<sup>14</sup> Z tego też powodu, wzorowanie się na mózgu przy konstrukcji nowoczesnych substratów komputerowych wydaje się być naturalnym krokiem w rozwoju technologii informatycznych.

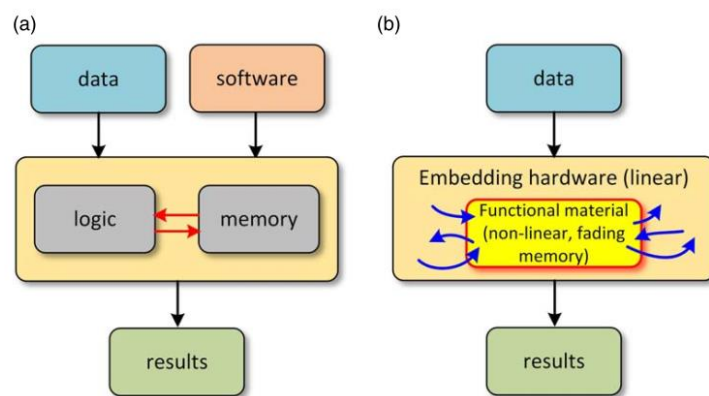
*„Można sobie wyobrazić, że natura generuje obliczalną funkcję zmiennej rzeczywistej bezpośrednio i niekoniecznie przez przybliżenie, jak w tradycyjnym podejściu.”* William Thompson (Lord Kelvin)<sup>15</sup>

Pomimo futurystycznie brzmiącej nazwy, pierwsze algorytmy sztucznych sieci neuronowych powstały już w 1957 roku.<sup>16</sup> Perceptron, jako najprostsza spośród sztucznych sieci neuronowych, należąca do grupy algorytmów uczenia nadzorowanego, jest zdolny jedynie do binarnej klasyfikacji liniowo-separowalnych danych. Niecałe dwadzieścia lat temu zadania obliczeniowe wykonywane przy wykorzystaniu sztucznych sieci neuronowych były postrzegane jako niekonwencjonalne, lecz obecnie tego typu algorytmy są powszechnie wykorzystywane w bardzo wielu branżach (*vide supra*). Ta obserwacja pasuje do stwierdzenia Toffoli'ego:

*„Schemat obliczeniowy, który dziś jest postrzegany jako niekonwencjonalny, może być taki, ponieważ jego czas jeszcze nie nadszedł – lub już przeminął.”<sup>17</sup>*

W ramach prób poprawy wydajności urządzeń komputerowych, prowadzone są intensywne badania z zastosowaniem *inżynierii neuromorficznej*.<sup>18,19</sup> Ta interdyscyplinarna dziedzina, wzorująca się na biologicznych strukturach nerwowych, czerpie dodatkowo inspiracje z matematyki, inżynierii elektronicznej, inżynierii materiałowej i informatyki. Wykorzystanie nowoczesnych technologii materiałowych umożliwia symulacje neuronalnych oraz synaptycznych funkcji o różnych stopniach złożoności, co w efekcie zapewnia zwiększoną równoległość działania w obszarach takich jak rozpoznawanie wzorców i analiza grafów. Inżynieria neuromorficzna rozwija materiały oraz algorytmy obliczeniowe o właściwościach adaptacyjnych względem szumu i defektów lokalnego środowiska, jak również umożliwiających procesy kontroli oraz uczenia się w czasie rzeczywistym.<sup>20</sup> Obecnie zagadnienia związane z inżynierią neuromorficzną znajdują się w dziedzinie niekonwencjonalnego przetwarzania informacji, lecz ten fakt powoli się zmienia. Wiele jednostek naukowych prowadzi intensywne badania czerpiące inspiracje z biologicznych struktur nerwowych w celu osiągnięcia wydajniejszych układów obliczeniowych, potencjalnie o uniwersalnym charakterze. O popularności tego kierunku badań może świadczyć duża liczba publikacji ukazujących się w prestiżowych czasopismach naukowych oraz liczne spotkania konferencyjne nawiązujące do tej tematyki.<sup>18,21–25</sup> Jak można zauważyć, obliczanie neuromorficzne wydaje się kierować w stronę „konwencjonalnego” obliczania, lub przynajmniej w stronę modułów obliczeniowych specjalnego przeznaczenia. Przykładem może być projekt SyNAPSE (ang. *Systems of Neuromorphic Adaptive Plastic Scalable Electronics* – Systemy neuromorficznej adaptacyjnej, plastycznej i skalowalnej elektroniki), zrealizowany w 2014 roku przez IBM Research i HP Labs (wraz ze wsparciem finansowym DARPA, amerykańskiej agencji rządowej departamentu obrony (łącznie US \$76.5mln)), w ramach którego zaprezentowano chip składający się z 5,4 miliarda tranzystorów wraz z 4096 neurosynaptycznymi rdzeniami integrującymi 1 milion sztucznych neuronów i 256 milionów konfigurowalnych sztucznych synaps.<sup>14</sup> Układ z powodzeniem wykonywał klasyfikację obrazu, równocześnie prezentując bardzo dobrą wydajność energetyczną.



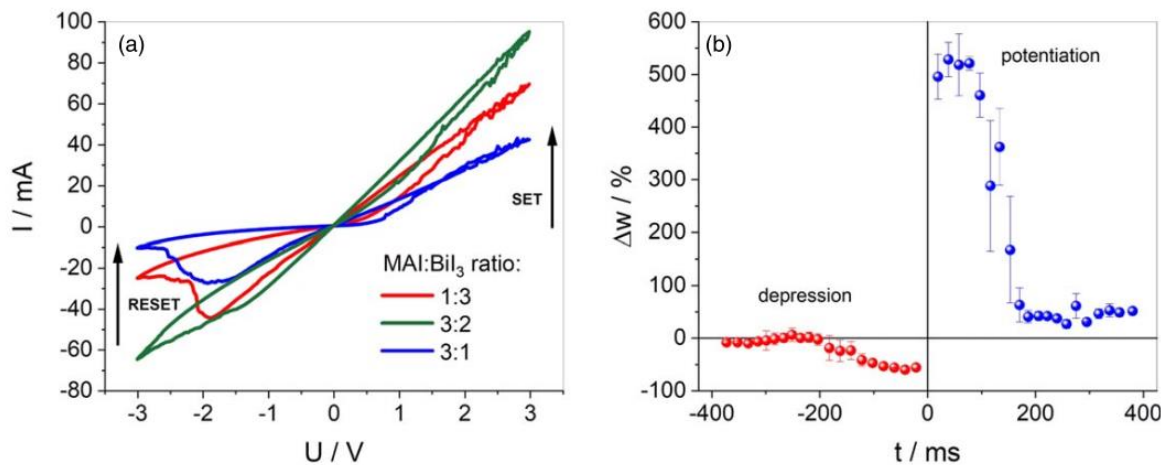


**Rysunek 1.** Schemat klasycznej architektury obliczeniowej von Neumanna (a) oraz niekonwencjonalny system obliczeniowy in materia (b). „Wąskie gardło von Neumana” oznaczono czerwonymi strzałkami. Niebieskie strzałki oznaczają transfer informacji między substratem obliczeniowym a interfejsem/systemem odczytu.<sup>26</sup>

Jedną z innowacyjnych technologii materiałowych z domeny inżynierii neuromorficznej są urządzenia memrystywne.<sup>27,28</sup> Wykorzystanie urządzeń memrystywnych pozwala delegować niektóre etapy obliczeniowe sztucznych sieci neuronowych tak, aby były wykonane *in materia*, bazując wprost na właściwościach danego urządzenia (Rys 1).<sup>29</sup> Takie podejście wydaje się omijać problem „wąskiego gardła von Neumanna”.<sup>26,30</sup> W klasycznych systemach obliczeniowych informacje są przechowywane w pamięci, a wszystkie obliczenia wykonywane są w mikroprocesorze. Architektura von Neumana zakłada stały przepływ danych pomiędzy tymi komponentami komputera, co w efekcie spowalnia obliczenia i zużywa energię. Systemy dynamiczne (zarówno półprzewodnikowe, jak i układy „mokre” (ang. *wetware*)) umożliwiają przeprowadzanie obliczeń również w układach posiadających funkcje pamięci.<sup>31</sup> Obliczenia przeprowadzane bezpośrednio w pamięci mogą bazować na przechowywaniu ładunku elektrycznego jak również na zmianach rezystancji danego układu. Powszechnie dostępne urządzenia do przechowywania danych bazujące na przechowaniu ładunku elektrycznego to: dynamiczna pamięć o dostępie swobodnym (DRAM), statyczna pamięć o dostępie swobodnym (SRAM) oraz pamięć flash. Do pamięci bazującej na zmianach w rezystancji danego układu (obok klasycznych układów memrystywnych) należą dodatkowo układy magnetorezystywnej pamięci o dostępie swobodnym (MRAM) oraz układy zmiennofazowe. W każdej z wymienionych klas układów przechowujących dane możliwe jest przeprowadzanie działań arytmetycznych bez konieczności komunikacji z procesorem.<sup>30</sup> Wykonywanie mnożenia macierzy w pamięci może być zastosowane m.in. do kompresji obrazu, analizy głównych składowych, optymalizacji kombinatorycznych jak również do optymalizacji działania konwolucyjnych, rekurencyjnych czy głębokich sieci neuronowych.

W klasycznej konfiguracji urządzeń memrystywnych, materiał pojemnościowy (np. dielektryk lub półprzewodnik) umieszczany jest pomiędzy elektrodami o przewodnictwie metalicznym w układzie warstwowym.<sup>32-34</sup> Urządzenia memrystywne cechują się nieliniową charakterystyką prądowo-napięciową, która przyjmuje formę pętli histerezy. Dla klasycznych urządzeń memrystywnych można zaobserwować dwa stany oporności, zwane odpowiednio HRS (ang. High Resistive State – stan wysokiej rezystancji) i LRS (ang. Low Resistive State – stan niskiej rezystancji). Poprzez zastosowanie impulsów elektrycznych lub przebiegów zmiennonapięciowych o odpowiedniej amplitudzie potencjału elektrycznego, materiały można przełączać do stanów LRS lub HRS w zależności od typu memrystora i jego stanu

początkowego. Zmienność działania w zależności od częstotliwości impulsów/skanów wzbudzających jest kolejną cechą urządzeń memrystywnych. Ze względu na retencję stanów LRS/HRS obserwowaną dla elementów memrystywnych po wyłączeniu źródła zasilania, efekt przełączania rezystywnego może zostać wykorzystany jako element konstrukcyjny nowej pamięci nieulotnej. Jest to nowy gatunek elementów przechowujących informacje, zwany RRAM (rezystywna pamięć o dostępie swobodnym), który konkuruwałby z obecnie dostępną pamięcią flash i niektórymi innymi stale rozwijanymi technologiami (m.in. MRAM). Niemniej jednak, wciąż poszukuje się nowych materiałów, aby sprostać wysokim wymaganiom dotyczącym efektywności energetycznej przełączania, jego statystycznej powtarzalności i szybkości działania.<sup>30</sup>



**Rysunek 2.** Przecinające się pętle histerezy zarejestrowane dla warstw jodobizmutanu metyloamonowego z różnymi proporcjami jodku metyloamonowego (MAI) i jodku bizmutu (a) oraz STDP dla materiału 3:1 (b).<sup>35</sup>

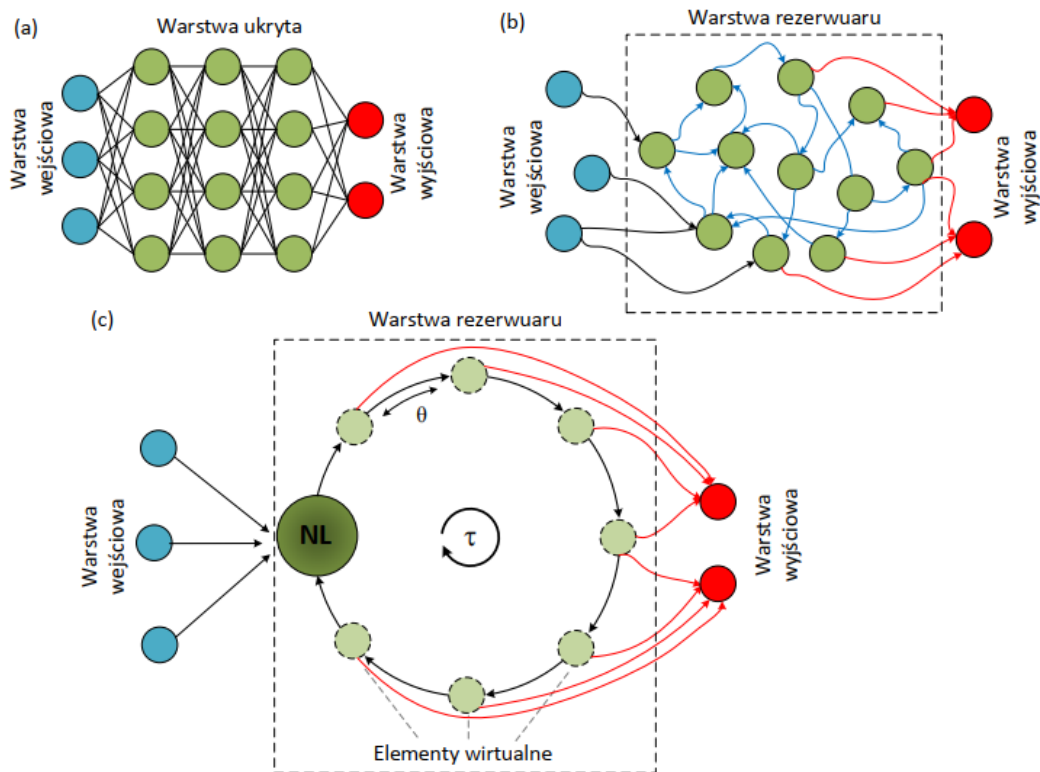
Co więcej, na bazie analogowego charakteru działania, urządzenia memrystywne zdolne są do symulacji reguł uczenia opisanych w teorii Hebb'a o plastyczności synaptycznej.<sup>27,32,36</sup> Według niej, wzmacniane są połączenia pomiędzy neuronami, przez które potencjał czynnościowy neuronu przemieszcza się zgodnie z kierunkiem przepływu informacji, zaś osłabiane są te, w których przemieszcza się przeciwnie. Jest to głównym założeniem modelu plastyczności synaptycznej zależnej od kolejności impulsów występujących w pre- oraz postsynaptycznym neuronie (ang. STDP – *s-pike-timing dependent plasticity*). Wzmacnianie/osłabianie połączeń pomiędzy neuronami w modelu STDP podsumowuje powiedzenie „*Cells that fire together wire together and those who fire out of sync, lose their link*”. Przykład STDP zrealizowany w układzie sztucznym zamieszczono na Rys. 2b, gdzie można zaobserwować dwa obszary odpowiadające wzmacnianiu („*potentiation*”) oraz osłabianiu („*depression*”) wag połączeń synaptycznych ( $\Delta w / \%$  na osi OY Rys 2b) w zależności od kolejności impulsów. Wagi połączeń synaptycznych są zdefiniowane jako stosunek różnicy amplitudy sygnału postsynaptycznego i presynaptycznego do amplitudy sygnału presynaptycznego<sup>35</sup>:

$$\Delta w = \frac{I_{post} - I_{pre}}{I_{pre}} \cdot 100\% \quad (1).$$

gdzie  $I_{post}$  i  $I_{pre}$  oznacza prąd zarejestrowany dla odpowiednio elektrody postsynaptycznej i presynaptycznej. W przedstawianym układzie, obszar gdzie następuje wzmocnienie wag

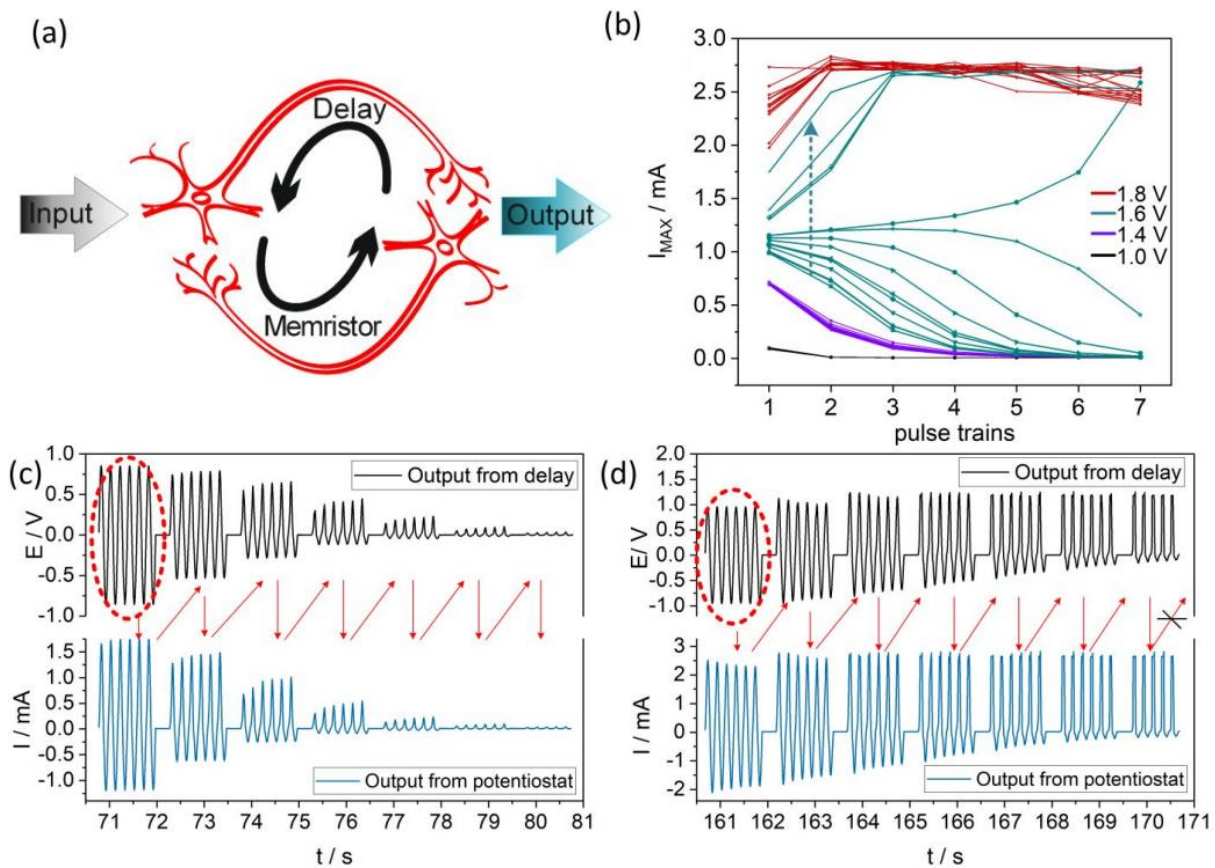
synaptycznych występuje dla przypadku, gdy impulsy docierają do elektrody traktowanej jako postsynaptyczna po tym jak dotarły do elektrody presynaptycznej. Gdy czas impulsów przedstawiony na wykresie przyjmuje wartości ujemne – impuls dociera w pierwszej kolejności do elektrody postsynaptycznej – można zaobserwować osłabianie wag synaptycznych. Kolejną z reguł uczenia, którą można zaimplementować na bazie memrystorów to plastyczność zależna od częstotliwości impulsów (ang. SRDP – *spike-rate dependent plasticity*). Urządzenia memrystywne umożliwiają symulację efektów, które w innym wypadku wymagałyby bardziej złożonych układów zastępczych, tym samym oszczędzają energię oraz czas potrzebny na wykonanie danego działania obliczeniowego.<sup>27</sup>

Jednym z problemów sztucznych sieci neuronowych jest ich kosztowny proces uczenia, szczególnie w przypadku rekurencyjnych bądź głębokich sieci neuronowych. Optymalizacji podlegają wszystkie wagi połączeń pomiędzy poszczególnymi neuronami, jak również sam poziom aktywacji danego neuronu. Gdy sieć zawiera rekurencyjne połączenia bądź wiele warstw, każda iteracja aktualizacji wag wydłuża trenowanie całej sieci. Aby rozwiązać ten problem, Jaeger oraz Maas niezależnie zaproponowali odpowiednio *Echo State Network*<sup>37</sup> oraz *Liquid State Machine*.<sup>38</sup> W ich podejściu, trenowaniu podlega jedynie fragment sieci próbujący stan warstwy przetwarzającej informacje. W swoich pracach wskazali na kluczowe znaczenie wielowymiarowej, bogatej oraz dynamicznej przestrzeni stanów warstwy przetwarzającej informacje, aby możliwie uprościć etap trenowania warstwy odczytującej. Z czasem oba z tych podejść efektywnego trenowania sieci neuronowych zostały ujęte we wspólne ramy koncepcyjne, które określono jako *obliczanie rezerwuarowe*, zaś warstwę przetwarzającą informację nazwano *rezerwuarem*.<sup>39-42</sup> Rezerwuar w paradygmacie obliczania rezerwuarowego oznacza substrat obliczeniowy zdolny do generacji wielowymiarowej przestrzeni konfiguracyjnej stanów, gdzie obliczanie reprezentowane jest jako trajektoria pomiędzy kolejnymi stanami układu w tej przestrzeni. Jako że warstwa rezerwuarowa nie podlega trenowaniu, jej struktura jest z góry zadana bądź wygenerowana losowo. Z tego powodu paradygmat obliczania rezerwuarowego jest z powodzeniem implementowany na bazie fizycznych substratów obliczeniowych, gdzie po pierwotnej konstrukcji sieci, jej zmiany mogą być bardzo trudne (np. w przypadku klasycznych komponentów elektronicznych). Nie jest to jednak ścisła reguła, gdyż dynamicznie zmieniające się układy mogą również pełnić rolę substratu obliczeniowego zapewniającego rezerwuar stanów. Obliczanie rezerwuarowe jest paradygmatem inkluzywnym, stąd też, jako dowód na słuszność tej tezy, zostało ono zrealizowane w tak prostych układach jak wiaderko z wodą, gdzie wzbudzenia tafli wody oraz wykonywanie zdjęć jej zmian zostało wykorzystane do zadania klasyfikacji mowy.<sup>43</sup> Wrażliwość układu na zaburzenia oraz jego właściwości samoorganizacji okazały się istotne w efektywnym przetwarzaniu wstępnym danych wejściowych.



**Rysunek 3.** Schemat klasycznej struktury jednokierunkowej sieci neuronowej (a), typowego układu RC (b) z losowo, rekurencyjnie i rzadko połączonymi węzłami sieci oraz układ RC z opóźnioną pętlą sprzężenia zwrotnego o topologii kołowej (układ SNESM) (c). Niebieskie węzły reprezentują różne wejścia oddziałujące na rezerwuar. Czerwone węzły reprezentują różne funkcje odczytu, w zależności od tego, które parametry rezerwuaru planujemy sondować.  $\theta$  — oznacza czas między wirtualnymi neuronami (pełny czas linii opóźniającej),  $\tau$  — czas potrzebny na efektywną ewolucję systemu, NL — węzeł nieliniowy.<sup>26</sup>

Aby poprawnie działać, te niekonwencjonalne systemy obliczeniowe muszą posiadać kilka cech, a mianowicie muszą wykazywać bogatą dynamikę wewnętrzną, pamięć „ulotną” oraz właściwość *echa stanów*. Obwody obliczania rezerwuarowe go są oparte na: (i) elemencie nieliniowym (np. memrystorze), który zapewnia również funkcje pamięci, (ii) warstwie wejściowej, która dostarcza informacje/sygnal do przetwarzania, (iii) warstwie odczytu i opcjonalnie (iv) opóźnionej pętli sprzężenia zwrotnego, która uzupełnia i rozwija wewnętrzną dynamikę systemu. Jak wcześniej wspomniano, warstwa odczytu jest jedyną częścią systemu, którą można i należy „trenować”, której zadaniem jest próbkowanie i reprezentacja wewnętrznego stanu rezerwuaru. Innymi słowy, wymagane jest jedynie dopasowanie prostego modelu na podstawie określonych cech sygnału transformowanego przez rezerwuar. W takim przypadku do odczytu nie jest potrzebna wyrafinowana sztuczna sieć neuronowa, lecz wystarczą proste modele, takie jak regresja liniowa czy drzewo binarne.



**Rysunek 4.** Uproszczona ilustracja koncepcji układu SNESM (sygnał wyjściowy generowany jest przy każdym „obiegu” sygnału w pętli sprzężenia zwrotnego) (a). Przykład klasyfikacji sygnałów na podstawie ich amplitudy oraz efekt metaplastyczności obserwowany przy 1.6Vpp (b). Zarejestrowane sygnały z eksperymentów z zamkniętą pętlą dla 1,7 Vpp (c) oraz 1.9Vpp (d) amplitudy początkowej.<sup>44</sup>

Single Node Echo-State Machine (SNESM) to nowatorskie systemy obliczania rezerwurowego, które wykorzystują tylko jeden węzeł obliczeniowy działający w pętli opóźnionego sprzężenia zwrotnego (Rys. 4).<sup>44-47</sup> Zasadniczo zarówno sygnał, jak i stan węzła obliczeniowego zmieniają się za każdym razem, gdy sygnał przechodzi przez urządzenie w każdym kolejnym cyklu. Ewolucja sygnału w pętli może potencjalnie poprawić możliwości grupowania i klasyfikacji systemu obliczania rezerwurowego. System SNESM daje dodatkową korzyść w postaci rozszerzenia zestawu danych. Każda kolejna epoka sygnału jest nieco inną wersją sygnału bazowego ze względu na nieliniową transformację i tłumienie w układzie SNESM. Echo sygnału pierwotnego może być łatwiejsze do sklasyfikowania ze względu na zmiany w jego złożoności i korelacji pomiędzy opisującymi je parametrami. Właźlak i in. pokazali implementację systemu SNESM opartego na pojedynczym fizycznym memrystorze na bazie cienkowarstwowego PbI<sub>2</sub>. Prezentowany system SNESM (Rys. 4) wykonuje następujące przetwarzanie sygnału: symetryczny sygnał przechodzący przez węzeł obliczeniowy zmienia się z powodu asymetrycznej charakterystyki prądowo/napięciowej wykorzystanego memrystora. Sygnał jest następnie opóźniany i kilkakrotnie zawracany do tego samego memrystora. Rysunki 4c-d przedstawiają dwa możliwe scenariusze, które można zaobserwować podczas eksperymentu. W pierwszym przypadku sygnał krąży w utworzonej pętli kilka razy i ulega wygaszeniu. W drugim scenariuszu amplituda sygnału wzrasta w każdej pętli aż do momentu wysycenia. Te funkcje prezentowanego układu SNESM można

wykorzystać do wykonania zadania klasyfikacyjnego – klasyfikacji sygnałów sinusoidalnych na podstawie ich amplitudy (Fig 4b). Co więcej, w badanym układzie w przypadku wielokrotnego powtarzania pomiaru dla granicznych wartości amplitudy można zaobserwować efekt metaplastyczności (Rys 4b) – zdolności do modulacji pierwotnej plastyczności układu, zgodnie z definicją W.C. Abrahama oraz M.F. Beara.<sup>48</sup> Metaplastyczność można określić jako "plastyczność plastyczności", gdzie plastyczność synaptyczna ulega zmianom poprzez dodatkową aktywność neuronalną. Z biologicznego punktu widzenia metaplastyczność umożliwia zmiany plastyczności synaptycznej w określonym zakresie dynamicznym.<sup>49</sup> W rozważanym układzie efekt metaplastyczności można zaobserwować dla wartości potencjału ok.  $1.6V_{pp}$ , gdzie filtrowanie sygnału przez układ stopniowo się zmienia w trakcie wielokrotnego podawania tego samego sygnału do układu.

W pracy doktorskiej „Memrystywny układy neuromimetyczne i rezerwuarowe” zawarte są badania nad wykorzystaniem kilku substratów obliczeniowych w domenie niekonwencjonalnego przetwarzania informacji. Wykonane prace uporządkowano tak, aby wprowadzać kolejne elementy i koncepcje konstrukcji układu oraz sposobów przetwarzania informacji i jej analizy.

W pierwszej kolejności przedstawiono artykuł przeglądowy, w którym zawarty jest opis memfraktorów (model uwzględniający urządzenia memrystywny), prostych algorytmów sztucznych sieci neuronowych oraz układów obliczania rezerwuarowego. Zawarto tam również matematyczny opis układów rezerwuarowych z pętlą sprzężenia zwrotnego. W kolejnej pracy zawarte są badania nad fotoelektrochemicznym sztucznym neuronem, które wskazują na możliwość wykorzystania prostego układu neuromorficznego do zadania klasyfikacji pisma odręcznego. Praca wprowadza koncepcje konstrukcji układu przetwarzającego informacje przy wykorzystaniu pojedynczego węzła obliczeniowego. Wprowadzono również elementy analizy danych. Paradygmat obliczania rezerwuarowego wprowadzony jest wprost w badaniach bazujących na układzie zawierającym cement domieszkowany nanomateriałami półprzewodnikowymi oraz drobinami metalicznymi. Badania podtrzymują i uzupełniają doniesienia literaturowe o możliwości realizacji obliczania rezerwuarowego na możliwie jak najprostszym substratach obliczeniowych przeznaczonych do zadań klasyfikacyjnych. Możliwość wykorzystania pojedynczego węzła obliczeniowego w rezerwuarowym układzie z pętlą sprzężenia zwrotnego (SNESM) przedstawiono na bazie polimerowego tranzystora polowego. Układ SNESM wykorzystano do poprawy działania tranzystora polimerowego w roli prostego sensora jonów. Badania nad wykorzystaniem rezerwuarowego układu SNESM do analizy i grupowania interwałów muzycznych zrealizowano na bazie symulacji synapsy mostkowej. Finalnie prezentowane są badania nad fizyczną implementacją synapsy mostkowej na bazie memrystorów KNOWM w heterotypycznym układzie rezerwuarowym SNESM w celu rozpoznania ataku epilepsji, w którym do trenowania modelu wykorzystano drzewo binarne, prosty algorytm uczenia maszynowego. Przedstawiono wyniki poprawy dokładności klasyfikacji sygnałów symulujących atak epilepsji dla restrykcyjnych warunków, gdzie istotna jest szybkość i prostota – co tym samym wpływa na niski koszt – trenowania i testowania finalnego modelu klasyfikacyjnego.

## Bibliografia

1. Łukasiak, L. & Jakubowski, A. History of semiconductors. *J. Telecommun. Inf. Technol.* 3–9 (2010).
2. Zgurovsky, M. Z. & Zaychenko, Y. P. *Big Data: Conceptual Analysis and Applications*. (Springer, 2020).
3. Schuster, A. J. *Understanding information*. (Springer, 2017).
4. Sangaiah, A. K., Thangavelu, A. & Sundaram, V. M. Cognitive computing for big data systems over IoT. *Gewerbestrasse* **11**, 6330 (2018).
5. Arora, G. *et al.* Artificial intelligence in surveillance, diagnosis, drug discovery and vaccine development against COVID-19. *Pathogens* **10**, 1048 (2021).
6. Yassine, A., Singh, S., Hossain, M. S. & Muhammad, G. IoT big data analytics for smart homes with fog and cloud computing. *Futur. Gener. Comput. Syst.* **91**, 563–573 (2019).
7. Reis, R. Strategies for reducing power consumption and increasing reliability in IoT. in *IFIP International Internet of Things Conference* 76–88 (Springer, 2018).
8. Zafarani, R., Abbasi, M. A. & Liu, H. *Social media mining: an introduction*. (Cambridge University Press, 2014).
9. Lee, T. K., Cho, J. H., Kwon, D. S. & Sohn, S. Y. Global stock market investment strategies based on financial network indicators using machine learning techniques. *Expert Syst. Appl.* **117**, 228–242 (2019).
10. Tkáč, M. & Verner, R. Artificial neural networks in business: Two decades of research. *Appl. Soft Comput.* **38**, 788–804 (2016).
11. Rathi, R. Effect of Cambridge Analytica’s Facebook ads on the 2016 US Presidential Election. *Towar. Data Sci.* (2019).
12. Da Silva, I. N., Spatti, D. H., Flauzino, R. A., Liboni, L. H. B. & dos Reis Alves, S. F. Artificial neural networks. *Cham Springer Int. Publ.* 39 (2017).
13. von Bartheld, C. S., Bahney, J. & Herculano-Houzel, S. The search for true numbers of neurons and glial cells in the human brain: A review of 150 years of cell counting. *J. Comp. Neurol.* **524**, 3865–3895 (2016).
14. Akopyan, F. *et al.* Truenorth: Design and tool flow of a 65 mw 1 million neuron programmable neurosynaptic chip. *IEEE Trans. Comput. Des. Integr. circuits Syst.* **34**, 1537–1557 (2015).
15. Pour-El, M. B. Abstract computability and its relation to the general purpose analog computer (some connections between logic, differential equations and analog computers). *Trans. Am. Math. Soc.* **199**, 1–28 (1974).
16. Kanal, L. N. Perceptron. (2003).
17. Toffoli, T. Programmable matter methods. *Futur. Gener. Comput. Syst.* **16**, 187–201 (1999).
18. Schuman, C. D., Kulkarni, S. R., Parsa, M., Mitchell, J. P. & Kay, B. Opportunities for

- neuromorphic computing algorithms and applications. *Nat. Comput. Sci.* **2**, 10–19 (2022).
19. Burr, G. W. *et al.* Neuromorphic computing using non-volatile memory. *Adv. Phys. X* **2**, 89–124 (2017).
  20. Kaspar, C., Ravoo, B. J., van der Wiel, W. G., Wegner, S. V & Pernice, W. H. P. The rise of intelligent matter. *Nature* **594**, 345–355 (2021).
  21. Marković, D., Mizrahi, A., Querlioz, D. & Grollier, J. Physics for neuromorphic computing. *Nat. Rev. Phys.* **2**, 499–510 (2020).
  22. Shastri, B. J. *et al.* Photonics for artificial intelligence and neuromorphic computing. *Nat. Photonics* **15**, 102–114 (2021).
  23. Roy, K., Jaiswal, A. & Panda, P. Towards spike-based machine intelligence with neuromorphic computing. *Nature* **575**, 607–617 (2019).
  24. Upadhyay, N. K. *et al.* Emerging memory devices for neuromorphic computing. *Adv. Mater. Technol.* **4**, 1800589 (2019).
  25. van De Burgt, Y., Melianas, A., Keene, S. T., Malliaras, G. & Salleo, A. Organic electronics for neuromorphic computing. *Nat. Electron.* **1**, 386–397 (2018).
  26. Właźlak, E., Przyczyna, D., Gutierrez, R., Cuniberti, G. & Szaciłowski, K. Towards synthetic neural networks: can artificial electrochemical neurons be coupled with artificial memristive synapses? *Jpn. J. Appl. Phys.* **59**, SI0801 (2020).
  27. Jeong, D. S., Kim, K. M., Kim, S., Choi, B. J. & Hwang, C. S. Memristors for energy-efficient new computing paradigms. *Adv. Electron. Mater.* **2**, 1600090 (2016).
  28. Mehonic, A. *et al.* Memristors—From in-memory computing, deep learning acceleration, and spiking neural networks to the future of neuromorphic and bio-inspired computing. *Adv. Intell. Syst.* **2**, 2000085 (2020).
  29. Graves, C. E. *et al.* In-Memory Computing with Memristor Content Addressable Memories for Pattern Matching. *Adv. Mater.* **32**, 2003437 (2020).
  30. Sebastian, A., Le Gallo, M., Khaddam-Aljameh, R. & Eleftheriou, E. Memory devices and applications for in-memory computing. *Nat. Nanotechnol.* **15**, 529–544 (2020).
  31. Przyczyna, D. *et al.* In-materio neuromimetic devices: dynamics, information processing and pattern recognition. *Jpn. J. Appl. Phys.* **59**, (2020).
  32. Sun, K., Chen, J. & Yan, X. The future of memristors: materials engineering and neural networks. *Adv. Funct. Mater.* **31**, 2006773 (2021).
  33. Li, Y., Wang, Z., Midya, R., Xia, Q. & Yang, J. J. Review of memristor devices in neuromorphic computing: materials sciences and device challenges. *J. Phys. D. Appl. Phys.* **51**, 503002 (2018).
  34. Pilarczyk, K. *et al.* Molecules, semiconductors, light and information: Towards future sensing and computing paradigms. *Coord. Chem. Rev.* **365**, 23–40 (2018).
  35. Mazur, T., Zawal, P. & Szaciłowski, K. Synaptic plasticity, metaplasticity and memory effects in hybrid organic–inorganic bismuth-based materials. *Nanoscale* **11**, 1080–1090 (2019).



36. Liao, K. *et al.* Memristor Based on Inorganic and Organic Two-Dimensional Materials: Mechanisms, Performance, and Synaptic Applications. *ACS Appl. Mater. Interfaces* **13**, 32606–32623 (2021).
37. Jaeger, H. The “echo state” approach to analysing and training recurrent neural networks—with an erratum note. *Bonn, Ger. Ger. Natl. Res. Cent. Inf. Technol. GMD Tech. Rep.* **148**, 13 (2001).
38. Maass, W., Natschläger, T. & Markram, H. Real-time computing without stable states: A new framework for neural computation based on perturbations. *Neural Comput.* **14**, 2531–2560 (2002).
39. Lukoševičius, M. & Jaeger, H. Reservoir computing approaches to recurrent neural network training. *Comput. Sci. Rev.* **3**, 127–149 (2009).
40. Tanaka, G. *et al.* Recent advances in physical reservoir computing: A review. *Neural Networks* **115**, 100–123 (2019).
41. Konkoli, Z., Nichele, S., Dale, M. & Stepney, S. Reservoir computing with computational matter. in *Computational Matter* 269–293 (Springer, 2018).
42. Ghosh, S., Nakajima, K., Krisnanda, T., Fujii, K. & Liew, T. C. H. Quantum neuromorphic computing with reservoir computing networks. *Adv. Quantum Technol.* **4**, 2100053 (2021).
43. Fernando, C. & Sojakka, S. Pattern recognition in a bucket. in *European conference on artificial life* 588–597 (Springer, 2003).
44. Wlaźlak, E., Marzec, M., Zawal, P. & Szaciłowski, K. Memristor in a Reservoir System—Experimental Evidence for High-Level Computing and Neuromorphic Behavior of PbI<sub>2</sub>. *ACS Appl. Mater. Interfaces* **11**, 17009–17018 (2019).
45. Wlaźlak, E., Zawal, P. & Szaciłowski, K. Neuromorphic Applications of a Multivalued [SnI<sub>4</sub> {(C<sub>6</sub>H<sub>5</sub>)<sub>2</sub>SO} <sub>2</sub>] Memristor Incorporated in the Echo State Machine. *ACS Appl. Electron. Mater.* (2020).
46. Przyczyna, D., Hess, G. & Szaciłowski, K. KNOWM memristors in a bridge synapse delay-based reservoir computing system for detection of epileptic seizures. *Int. J. Parallel, Emergent Distrib. Syst.* 1–16 (2022).
47. Przyczyna, D., SZACIŁOWSKA, M., Przybylski, M., Strzelecki, M. & SZACIŁOWSKI, K. Recognition of Musical Dissonance and Consonance in a Simple Neuromorphic Computing System. *Int. J. Unconv. Comput.* **17**, (2022).
48. Abraham, W. C. & Bear, M. F. Metaplasticity: the plasticity of synaptic plasticity. *Trends Neurosci.* **19**, 126–130 (1996).
49. Zhu, X., Du, C., Jeong, Y. & Lu, W. D. Emulation of synaptic metaplasticity in memristors. *Nanoscale* **9**, 45–51 (2017).



*Streszczenia artykułów wchodzących w skład rozprawy*



*DI. Ewelina Właźlak, Dawid Przyczyna, Rafael Gutierrez, Gianarelio Cuniberti, Konrad Szaciłowski „Towards synthetic neural networks: can artificial electrochemical neurons be coupled with artificial memristive synapses?”, Jpn. J. Appl. Phys. 2020, 59, SI0801.*



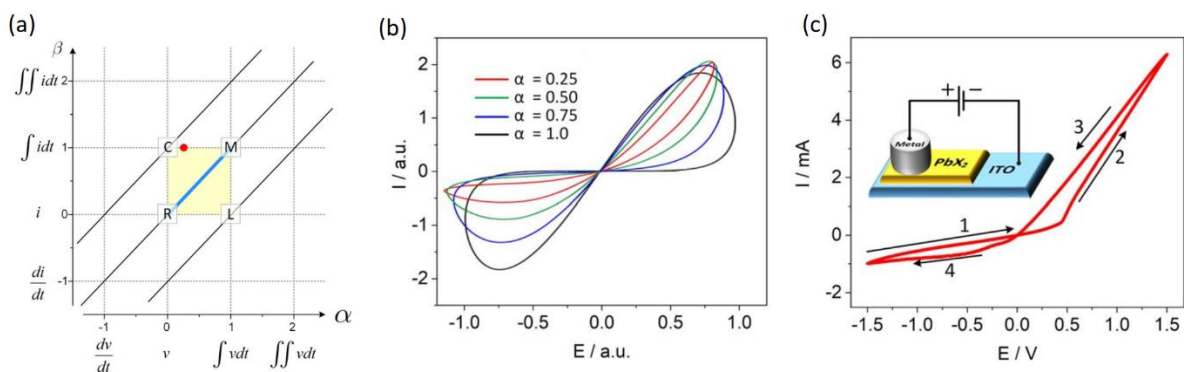
W przedstawianym artykule przeglądowym omówiono zagadnienia związane z elementami memrystywnymi i neuromorficznymi, przedstawiono model memfraktorów oraz podstawowe zasady działania prostych sztucznych neuronów, jak również pełnych systemów obliczania rezerwurowego. Jako przykład w omawianym artykule wybrano autonomiczny układ kontroli robota opartego o prosty kontroler neuromorficzny. W ramach tego streszczenia przedstawiono jedynie zagadnienia związane tematycznie z pozostałymi pracami zawartymi w tej rozprawie.

Pomimo bezprecedensowych osiągnięć technologii komputerowych opartych o krzemowe materiały półprzewodnikowe, klasyczne paradygmaty obliczeniowe obejmują niewielki podzbiór wszystkich możliwych scenariuszy obliczeniowych. Istnieje bardzo szeroka klasa substratów i środowisk obliczeniowych, których bogata dynamika może być wykorzystana jako medium obliczeniowe. Zaobserwowano, że możliwe jest korzystanie wprost z właściwości określonych materiałów do symulowania etapów bądź całych procesów pierwotnie obserwowanych w biologicznych strukturach neuronalnych, co otwiera nowe możliwości rozwoju technik obliczeniowych.

Memrystor to – obok rezystora, kondensatora oraz cewki – czwarty fundamentalny element pasywny obwodu elektrycznego, który był postulowany przez Leona Chua już w 1971 roku. Przez długi czas był uważany jedynie za ciekawostkę naukową, lecz w 2008 r. po raz pierwszy zaprezentowano fizyczną implementację urządzenia memrystywnego. R. S. Williams i współpracownicy z laboratoriów HP opracowali urządzenie oparte na cienkiej warstwie  $\text{TiO}_2$  umieszczonej pomiędzy elektrodami platynowymi, które wykazało oczekiwaną przecinającą się pętlę histerezy przewidzianą w pracy L. Chua. Element memrystywny jest pasywnym, nieliniowym elementem obwodu, którego właściwości (rezystancja, pojemność lub indukcyjność) zależą od jego historii, a w szczególności od całkowitego ładunku elektrycznego, który przez niego przepłynął.

Wciąż prowadzone są prace nad uogólnianiem teorii elementów memrystywnych, które mają na celu ściślejsze powiązanie z rzeczywistymi układami eksperymentalnymi. Podejście to, zaprezentowane przez M. Abdelouahaba, R. Lozi i L. Chua, bazuje na operatorach różniczkowych niecałkowitego rzędu, tzn. zamiast stosowania równań różniczkowych zwyczajnych pierwszego rzędu wykorzystuje koncepcję pochodnych i całek ułamkowego rzędu w celu uzyskania elastyczności w opisie efektów pamięci (Rys. 5b). Podejście to zakłada mieszany charakter danego elementu memrystywnego z pozostałymi elementami pasywnymi obwodów elektrycznych (Rys. 5a). Ten model obejmuje różnorodność w obserwowanych doniesieniach literaturowych na temat memrystorów, meminduktorów oraz memkondensatorów (z ang. *Memristor*, *meminductor*, *memcapacitor*). W takim ujęciu elementy memrystywne „niecałkowitego rzędu” zwane są *memfraktorami*.

Liczne materiały półprzewodnikowe, m.in. jodek ołowiu, jodobizmutany metyloamoniowe oraz kompleks cyny z ligandem mieszanym  $[\text{SnI}_4\{(\text{C}_6\text{H}_5)_2\text{SO}\}_2]$  wykazują wysoce asymetryczne pętli histerezy w układach ITO/półprzewodnik/Cu (Przykład na Rys. 5c). Otrzymane krzywe są bardzo podobne do otrzymanych modeli pętli histerezy memfraktorów.



**Rysunek 5.** Zestawienie pasywnych elementów elektrycznych:  $R$  oznacza rezystor,  $C$  – kondensator,  $L$  – cewkę, a  $M$  – memrystor,  $\alpha$  i  $\beta$  na osiach wyrażają rząd operatora różniczkowego. Czerwona kropka wskazuje położenie memfraktora  $1/4$  rzędu ( $\alpha = 0,25$ ), natomiast gruba niebieska linia w poprzek żółtego obszaru wskazuje najprostsze elementy memfrakcyjne, które nie mogą akumulować energii, ale nadal zapewniają funkcje pamięciowe istotne dla przetwarzania sygnałów i informacji (a). Pętle histerezy otrzymane dla modelu memrystora sterowanego ładunkiem dla różnych wartości parametrów  $\alpha$  i stałej wartości  $\beta = 1$  (b). Przypadek  $\alpha = 0,25$  (czerwona krzywa) jest zbliżony do doświadczalnie zmierzonych pętli histerezy w memrystorach na bazie halogenków ołowiu (c).

Właściwości memrystyczne prezentowane przez różne urządzenia półprzewodnikowe mogą być konsekwencją kilku dynamicznych procesów fizycznych i chemicznych, między innymi: tworzenia się włókien/aglomeratów przewodzących, przejść fazowych, migracji jonów, wakancji i/lub domieszek, lub modulacji wysokości bariery Schottky'ego złącza pomiędzy materiałem memrystycznym oraz elektrodą metaliczną.

Memrystory i inne urządzenia memrystyczne (lub memfrakcyjne) posiadają cechy pamięci (krótko- i długotrwałej), plastyczność podobną do tej obserwowanej w biologicznych synapsach oraz prezentują nieliniową charakterystykę elektryczną. Cechy te idealnie nadają się do różnych protokołów przetwarzania informacji, w tym do sztucznych sieci neuronowych (np. mnożenie macierzy wag połączeń), systemów obliczania rezerwuarowego, generowania liczb losowych oraz kryptografii, w tym do fizycznych funkcji nieklonowalnych. Ze względu na silnie nieliniową charakterystykę i możliwość generowania wyższych częstotliwości harmonicznych nadają się one również do modulacji sygnałów elektrycznych.

Mózg ludzki jest zdecydowanie najbardziej złożonym systemem przetwarzania informacji znanym ludzkości. Jego bezprecedensowa złożoność jest wynikiem działania ok.  $10^{11}$  neuronów połączonych w niezwykle skomplikowaną dynamiczną sieć z ok.  $10^{14}$  synapsami. Każdy neuron zbiera informacje z licznych synaps i w zależności od własnych cech oraz danych wejściowych (częstotliwość, amplituda i sekwencja czasowa sygnałów wejściowych) generuje impuls wyjściowy. O ile wyzwalamie potencjału czynnościowego i propagacja sygnału wzdłuż aksonu jest zjawiskiem elektrycznym, o tyle przekazywanie i przetwarzanie informacji na poziomie synaps opiera się na różnych chemicznych nośnikach informacji: neuroprzebieżnikach. Dalsze komplikacje wynikają z faktu, że istnieje wiele rodzajów neuronów o różnych właściwościach, a także wiele rodzajów synaps i neuroprzebieżników.

Inżynieria Neuromorficzna to niezwykle istotna i intensywnie rozwijana domena niekonwencjonalnego przetwarzania informacji badająca urządzenia i systemy których



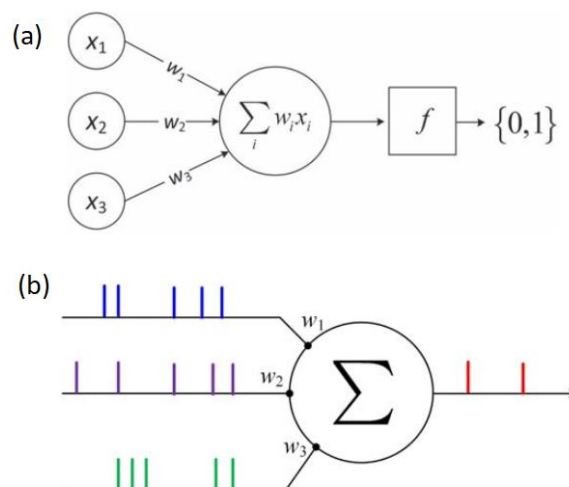
struktura i/lub działanie jest wzorowane na układach nerwowych. Rozwiązania neuromorficzne wdrażane przez inżynierów oprogramowania zaczęły rewolucjonizować świat. Sieci neuronowe, uczenie maszynowe i sztuczna inteligencja (AI) znajdują się w centrum zainteresowania przemysłu motoryzacyjnego i lotniczego, a także firm specjalizujących się w usługach związanych z Internetem. Systemy te są jednak oparte na klasycznej elektronice cyfrowej, funkcje obliczeń neuromorficznych są realizowane programowo i nie są w stanie naśladować pełnego potencjału systemów neuronowych ani pod względem struktury, ani złożoności i wydajności energetycznej. Na rozwijanie dedykowanych, neuromorficznych rozwiązań sprzętowych zdecydowały się największe firmy technologiczne, między innymi: Hewlett-Packard (USA), IBM (USA), Intel Corporation (USA) oraz Samsung Group (Korea Południowa) Praca będąca elementem tej rozprawy „Hardware realization of the pattern recognition with an artificial neuromorphic device exhibiting a short-term memory” jest krokiem w kierunku molekularnych i analogowych układów neuromorficznych.

Rozwój modelowania procesów neuronowych obejmuje trzy etapy, w których złożoność i dokładność modelowania wzrasta. Najprostszymi sieciami są jednokierunkowe sieci neuronowe – systemy naśladujące neuronowe przetwarzanie informacji oparte na podstawowej zasadzie uczenia się: modulacji wag synaptycznych między węzłami sieci. Pierwszym, najmniej zaawansowanym modelem jest perceptron – sieć neuronowa pierwszej generacji (Rys. 6a). Zawiera on jedną warstwę wejściową i jeden (lub więcej) węzeł przetwarzający. Każdy węzeł oblicza ważoną sumę wejść (2) i wykorzystuje prostą progową funkcję aktywacji (3) do wygenerowania wyjścia, które ma charakter binarny:

$$s = \sum_i w_i x_i \quad (2).$$

$$f(s) = \begin{cases} 1, & \text{jeśli } s > T \\ 0, & \text{jeśli } s \leq T \end{cases} \quad (3).$$

Uczenie perceptronu polega na aktualizowaniu wszystkich wag ( $w_i$ ) po wprowadzeniu na wejście znanych danych ( $x_i$ ) w celu zminimalizowania błędów klasyfikacji.



**Rysunek 6.** Schematyczna struktura jednoelementowej sieci perceptronowej (a) i jednoelementowej sieci neuronowej typu spiking (spiking neural network) (b).

Sieci neuronowe drugiej generacji wzorują się na schemacie perceptronu, lecz nowa sieć (i) może zawierać więcej warstw oraz (ii) wykorzystuje funkcję logistyczną (4) jako funkcję aktywacji zamiast prostej funkcji progowej:

$$f(s) = \frac{1}{1 + e^{-s}} \quad (4).$$

gdzie  $s$  określa nachylenie krzywej. W efekcie generowane jest continuum stanów wyjściowych, które może być dalej przetwarzane przy użyciu metod logiki rozmytej. W różnych warstwach sieci mogą być stosowane różne funkcje aktywacji (m.in. funkcja Heaviside'a, funkcje logistyczne, tangens hiperboliczny i inne);. Trzeci, najbardziej zaawansowany model neuronowego przetwarzania informacji opiera się na modelach neuronów generujących szpilki potencjału czynnościowego (Rys. 6b). Podczas gdy poprzednie modele operują informacją zakodowaną w amplitudzie sygnałów wejściowych, model trzeciej generacji jest wrażliwy na czas trwania i sekwencję czasową impulsów (rola wag synaptycznych jest podobna do tych z poprzednich dwóch generacji).

Istnieje wiele modeli matematycznych zachowania się sztucznych neuronów, począwszy od modelu Hodgkina-Huxleya, Izhikevicha, Thorpe'a czy *Leaky-integrate and fire*, aż po modele adaptacyjne czy stochastyczne. Wspólną cechą wszystkich tych modeli jest ich wewnętrzna dynamika, prowadząca do generowania „szpilek” sygnału (impulsów) na wyjściu przy odpowiednich warunkach wejściowych. Modele te umożliwiają również symulowanie różnych sposobów kodowania sygnałów na bazie ich częstotliwości lub ich określonej sekwencji. W pierwszym podejściu istotna informacja zakodowana jest w liczbie impulsów w określonym oknie czasowym. W drugim natomiast głównym nośnikiem informacji jest dokładny odstęp czasowy między kolejnymi impulsami. Są to dwa główne składniki naturalnych mechanizmów uczenia się w paradygmacie Hebba. Sieci te reagują na sekwencję czasową zdarzeń, stąd też mogą reprezentować wyższą formę pamięci wewnętrznej. Wysoki poziom wydajności układów neuromorficznych można również osiągnąć, gdy węzły sieci mają wewnętrzną dynamikę, np. gdy funkcja aktywacji węzłów zmienia się w czasie – podobnie jak np. w przypadku metaplastyczności układu *Single Node Echo-State Machine* opisywanym we wstępie (Rys. 4 b).

Krokiem w kierunku integracji większych systemów, bądź systemów ewoluujących w czasie może być wykorzystanie koncepcji obliczania rezerwarowego. We wstępie do rozprawy „Memrystyczne układy neuromimetyczne i rezerwarowe” przedstawiono główne założenia tego paradygmatu, jak również obecnie rozwijanych koncepcji (układ *Single Node Echo-State Machine*). W niniejszym streszczeniu przedstawiono matematyczny opis obliczania rezerwarowego autorstwa Zorana Konkoli.

Dynamikę stanu wewnętrznego rezerwaru można opisać za pomocą prostych formuł matematycznych. W uproszczeniu, rezerwar ewoluuje i jest aktualizowany w dyskretnych krokach czasowych  $t$ . Zależy to od dwóch czynników – jego stanu początkowego  $x_{t-1}$  i sygnału wejściowego  $u_t$ , na podstawie którego można uzyskać bieżący stan rezerwaru  $x_t$ , co daje:

$$x_t = F(x_{t-1}, u_t) \quad (5).$$

gdzie  $F$  jest funkcją zawierającą opis stanu rezerwaru i jego reaktywność na sygnały wejściowe. Warstwa odczytu może składać się z dowolnej funkcji  $\psi$ , w zależności od tego, który parametr rezerwaru sondujemy, aby uzyskać informację wyjściową  $y_t$ :

$$y_t = \psi(x_t) \quad (6).$$

Funkcja odczytu  $y_t$  sonduje tylko aktualny stan rezerwuaru  $x_t$  (lub jego fragmenty, Rys. 3b) i – jak opisano wcześniej – jest to jedyna część całego systemu obliczeniowego, którą trzeba wytrenować.

Właściwość *echa stanu* – jak sama nazwa wskazuje – polega na wpływie sygnału wejściowego na dynamikę rezerwuaru, który jest następnie reprezentowany w jego przyszłych stanach niczym zanikające echo. Innymi słowy, bieżący stan przestrzeni konfiguracyjnej rezerwuaru zależy od poprzednich stymulacji sygnałami wejściowymi. Z matematycznego punktu widzenia, układ posiada właściwość echa stanu jeśli istnieje funkcja  $\varepsilon$ , taka że:

$$x_t = \varepsilon(u_t, u_{t-1}, u_{t-2}, \dots, u_{-\infty}) \quad (7).$$

która nie zależy od stanu początkowego rezerwuaru, lecz jedynie od historii sygnałów wejściowych. Sondowanie echa stanów w skończonym czasie na podstawie równania (5) można opisać rekurencyjnym wzorem określającym stan rezerwuaru:

$$x_t = H^h(u_t, u_{t-1}, u_{t-2}, \dots, u_{t-h+1}, x_{t-h}) \quad (8).$$

Gdzie  $h$  należy do liczb naturalnych i określa „głębokość” próbkowania echa stanu. Poniżej zamieszczono dwa przykłady: dla  $h = 2$  i  $h = 3$ :

$$H^{(2)} = F(F(x_{t-2}, u_{t-1}), u_t) \quad (9).$$

$$H^{(3)} = F(F(F(x_{t-3}, u_{t-2}), u_{t-1}), u_t) \quad (10).$$

Dla układów prezentujących właściwość echa stanów można przyjąć:

$$\varepsilon = \lim_{h \rightarrow \infty} H^{(h)} \quad (11).$$

Z uwagi na właściwość zanikającej pamięci, wpływ echa poprzednich sygnałów wejściowych można uprościć i ograniczyć do skończonych wartości czasu. W takim wypadku właściwość echa stanu przyjmuje formę:

$$x_t = \tilde{\varepsilon}^{(h)}(u_t, u_{t-1}, u_{t-2}, \dots, u_{t-h+1}) \quad (12).$$

Dokładniejszy opis przedstawionych koncepcji zawarty jest w źródłowej pracy opisującej algorytm SWEET (*State-Weaving Environment Echo Tracker*) Zorana Konkoli, którym inspirowano się w pracy eksperymentalnej „Reservoir Computing for sensing: an experimental approach”. Co więcej, układy Single-Node Echo State Machine również można opisywać za pomocą algorytmów SWEET – w tym ujęciu środowiskiem z jakim rezerwuar ma kontakt może być np. wzbudzający sygnał elektryczny (jak w przypadku prac „Towards embedded computation with building materials”, „Recognition of Musical Dissonance and Consonance in a Simple Neuromorphic Computing System” oraz „KNOWM memristors in a bridge synapse delay-based reservoir computing system for detection of epileptic seizures”).

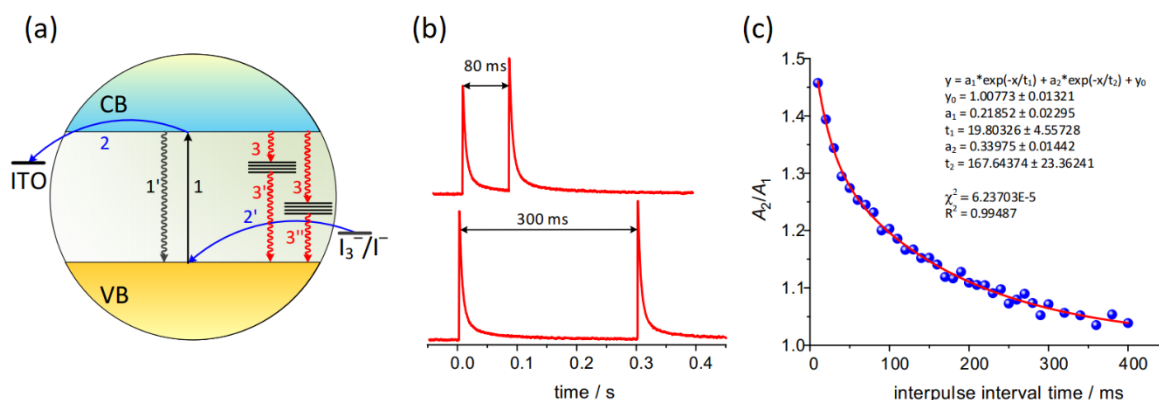


*D2. Dawid Przyczyna, Maria Lis, Kacper Pilarczyk, Konrad Szaciłowski „Hardware realization of the pattern recognition with an artificial neuromorphic device exhibiting a short-term memory”, *Molecules* 2019, 24, 2738.*



Efekt pamięci krótkotrwałej – istotny z punktu widzenia neuromorficznego przetwarzania informacji – można uzyskać w układach fotoelektrochemicznych bazujących na półprzewodnikach szerokopasmowych. Podstawą tych prac jest odkryty kilka lat temu sztuczny neuron fotoelektrochemiczny – układ wykazujący cechy plastyczności biorące początek w procesach pułpkowania ładunku w nanostrukturach półprzewodnikowych. W pracy źródłowej bazowano na siarczku kadmu wraz z nanorurkami węglowymi oraz zaproponowano elektroniczny układ zastępczy symulujący działanie układu.

Pod wpływem impulsów monochromatycznego światła o długości fali 465nm (zakres widzialny) oraz o interwałach czasowych pomiędzy impulsami rzędu 50ms, fotoelektrody z polikrystalicznego siarczku kadmu wykazują efekty pamięci krótkotrwałej. Zjawisko to można opisać na bazie biologicznego modelu torowania (facylitacji), zjawiska z zakresu plastyczności krótkotrwałej. Po przekroczeniu odpowiedniego progu energetycznego (ładunek elektryczny dla neuronów, światło o określonej długości fali dla rozważanych materiałów syntetycznych) oraz po wzbudzeniu układu w odpowiednich interwałach czasowych, układ „pamięta” poprzednie wzbudzenia. W przypadku układów sztucznych fizyczna interpretacja tego zjawiska opiera się na konkurencji pomiędzy procesami międzyfazowego przeniesienia a procesami pułpkowania i rekombinacji nośników ładunku (Rys. 7a). Padające światło wzbudza elektrony z pasma walencyjnego do pasma przewodnictwa. Wzbudzone elektrony dążą do rekombinacji z powstałymi dziurami, lecz są powstrzymywane do momentu wysycenia stanów pułpkowych pochodzących z pasma energetycznego defektów obecnych w danym materiale. W przypadku niewystarczającego zdefektowania materiału możliwa jest modyfikacja układu poprzez wprowadzenie nanostruktur węglowych, takich jak fullereny, nanopłatki grafenu czy też nanorurki, które w efekcie wprowadzają dodatkowe poziomy energetyczne pełniące rolę pułapek elektronowych. W rezultacie obserwuje się wzrost amplitudy fotoprądu wraz z każdym kolejnym wzbudzeniem.



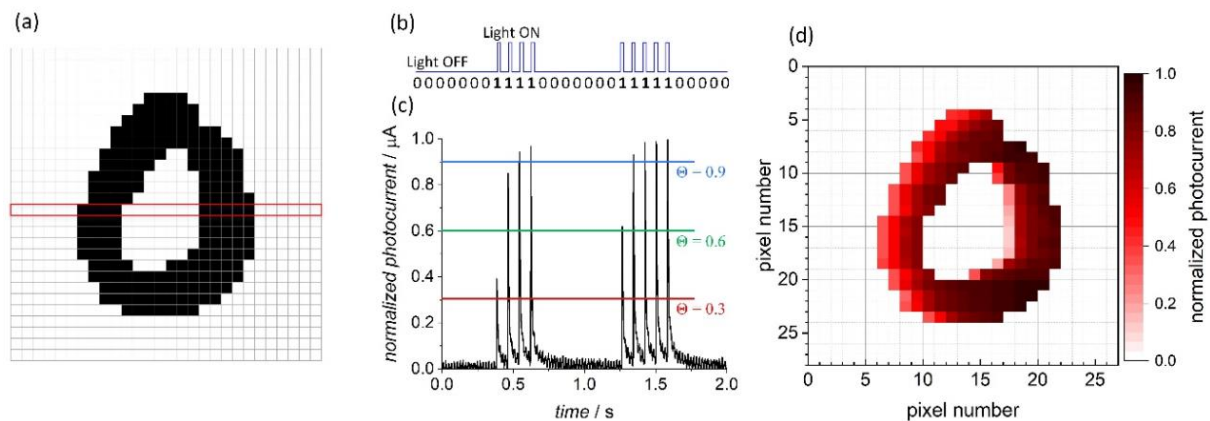
**Rysunek 7.** Proponowany mechanizm obserwowanego efektu pamięci dla badanych próbek CdS. CB – pasmo przewodnictwa, VB – pasmo walencyjne (a). Szpilki fotoprądowe rejestrowane po impulsowym wzbudzeniu świetlnym dla różnych interwałów pomiędzy impulsami (b). Analiza wzmocnienia fotoprądu przedstawiona względem odstępu czasu pomiędzy impulsami (c).

Pułpkowane elektrony rekombinują ze stałymi czasowymi wyznaczonymi na podstawie podwójnie eksponencjalnej krzywej zaniku dopasowanej do danych pomiarowych ( $\tau_1=19.8 \pm 4.5$  ms oraz  $\tau_2=167.6 \pm$  ms, Rys 7c). Podwójnie eksponencjalna krzywa zaniku oraz otrzymane

stałe czasowe można porównać do szybko-zanikającej facylitacji F1 oraz wolno-zanikającej facylitacji F2 obserwowanych w neuronach biologicznych.

Dyfraktometria proszkowa promieniami rentgenowskimi wskazuje na obecność dwóch faz w badanym materiale – tetragonalny hawleit oraz heksagonalny grenokit w stosunku 1:1. Obok występowania defektów w próbce, polimorfizm badanego CdS może być źródłem występowania podwójnie eksponencjalnego efektu pamięci z uwagi na prawdopodobne różnice w występowaniu energetycznych stanów pułapkowe w obu odmianach polimorficznych, a także na granicach pomiędzy ziarnami o różnej strukturze. Spektroskopia dyspersji energii promieni X potwierdza czystość próbki, zaś zdjęcia pochodzące ze skaningowego mikroskopu elektronowego dają informację o średnim rozmiarze nanometrycznych ziaren rzędu  $71 \pm 3$  nm (dla największej liczby ziaren o rozmiarze  $53 \pm 1$  nm). Analiza Tauca widm absorpcyjnych materiału pozwoliła na wyznaczenie optycznej przerwy energetycznej (dla przejścia prostego) o wartości  $E_g = 2.33\text{eV}$ .

Na bazie występujących efektów pamięci krótkotrwałej przeprowadzono testy nad wykorzystaniem badanego układu do poprawy klasyfikacji pisma odręcznego. Do testów wykorzystano standardowy zestaw danych MINST z pismem odręcznym. Poszczególne obrazki poddano binaryzacji (czarny pixel = 1, biały pixel = 0), następnie otrzymane wartości wykorzystano do uruchomienia źródła światła generującego krótkie ( $300\mu\text{s}$ ) impulsy monochromatycznego światła ( $465\text{nm}$ ).



**Rysunek 8.** Obraz odręcznego znaku o rozmiarach 28 na 28 pikseli z zaznaczonym wierszem (a) przetłumaczonym na sekwencję bitów i odpowiadających im impulsów świetlnych (b). Znormalizowana odpowiedź fotoprądu układu dla danego wejścia binarnego. Linie oznaczają trzy wartości progowe (c). Rekonstrukcja obrazu na podstawie znormalizowanych wartości fotoprądu.

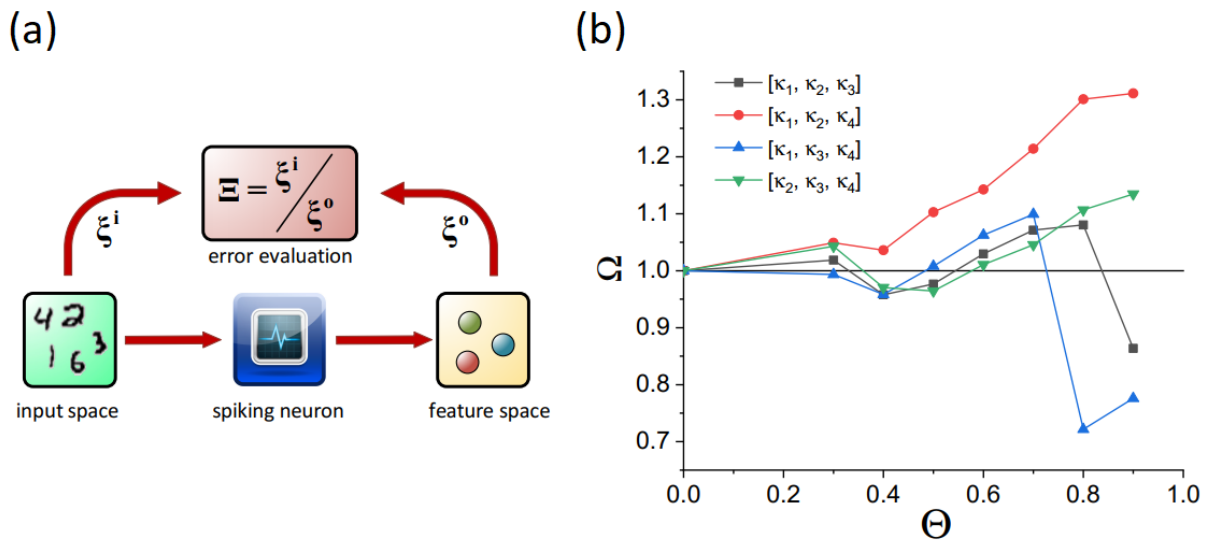
Ogólnie z uwagi na występujący efekt pamięci w badanym układzie fotoelektrochemicznym, po rekonstrukcji obrazów można zaobserwować gradientowy wzrost wartości natężenia fotoprądu (Rys. 8d). Umożliwia to filtrowanie danego obrazu po ustawieniu różnych wartości progowych, poniżej których rejestrowane fotoprądy były ignorowane, w efekcie stopniowo zmniejszając liczbę występujących pixeli. Aby sprawdzić wpływ układu neuromorficznego na potencjalną poprawę w separowalności danych mających umożliwić ich łatwiejszą klasyfikację, zaproponowano następującą analizę: (i) obrazy podzielono na cztery równe części,

(ii) policzono pixele w każdej z części, (iii)\* zrzutowano liczbę pixeli dla każdej z ćwiartek do



przestrzeni 3d – liczba pixeli w danej ćwiartce posłużyła jako współrzędna osi xyz układu kartezjańskiego (sporządzono wykresy dla różnych kombinacji trzech spośród czterech ćwiartek), (iv) dopasowano elipsoidy do zbiorów pixeli, (v) porównano przekrywanie się elipsoidy danego obrazu z elipsoidami pozostałych obrazków, (vi) porównano różnice w przekrywaniu się elipsoid danych przetworzonych względem danych nieprzetworzonych.

\*Etap (iii) w powyżej opisanym toku działań może nie wydawać się oczywisty – dzielenie obrazów na ćwiartki sprawia, że każdy obraz posiada cztery współrzędne (których wartości określone są przez liczbę czarnych pikseli), innymi słowy, można go przedstawić w przestrzeni czterowymiarowej. Aby umożliwić wizualizację danych, postanowiono zrzutować reprezentację 4d do 3d, wybierając trzy spośród czterech ćwiartek i powtarzając procedurę cztery razy, otrzymując w efekcie cztery różne scenariusze klasyfikacji. To podejście umożliwia analizę kluczowych obszarów potrzebnych do poprawnej separacji danych, tym samym pozwalając na potencjalną redukcję danych wymaganych do trenowania modelu uczenia maszynowego.



**Rysunek 9.** Schemat przedstawiający procedurę określania wydajności układu klasyfikującego (a). Porównanie parametru całkowitej separowalności względem różnych wartości progowych. Wyniki dla czterech rzutów 3d poszczególnych ćwiartek ( $\kappa_1$ ,  $\kappa_2$ ,  $\kappa_3$ ,  $\kappa_4$ ).

Aby porównać ilościowo nachodzenie na siebie elipsoid poszczególnych obrazów zdefiniowano indeks separowalności. Najpierw określono objętości  $V(m(\kappa_i, \kappa_j, \kappa_k))$  elipsoidy  $m$ , otrzymanej z projekcji  $\kappa_i, \kappa_j, \kappa_k$ . Następnie określono stosunek części niewspólnej objętości elipsoid  $m$  oraz  $n$  względem objętości elipsoidy  $m$ . W efekcie otrzymujemy:

$$\xi_{m/n} = \frac{V(m(\kappa_i, \kappa_j, \kappa_k)) / (n(\kappa_i, \kappa_j, \kappa_k))}{V(m(\kappa_i, \kappa_j, \kappa_k))} \quad (13).$$

Dany indeks separowalności otrzymano dla każdej możliwej pary elipsoid w danym zestawie danych oraz dla każdej z czterech analizowanych kombinacji ćwiartek. Aby przedstawić kolektywne zmiany separowalności danych nieprzetworzonych względem danych przetworzonych zdefiniowano integralny indeks separowalności:

$$\Omega(\kappa_i, \kappa_j, \kappa_k, \Theta) = \frac{\sum_m \sum_n \xi_{m/n}^{output}}{\sum_m \sum_n \xi_{m/n}^{input}} \quad (14).$$

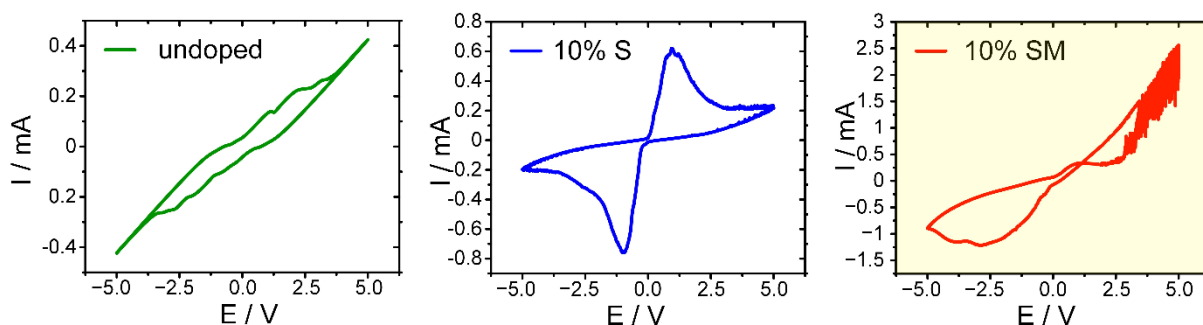
gdzie  $\Theta$  oznacza daną wartość progową,  $\xi_{m/n}^{output}$  oznacza indeks separowalności dla danych przetworzonych przez układ neuromorficzny, zaś  $\xi_{m/n}^{input}$  oznacza indeks separowalności dla nieprzetworzonych danych wejściowych. Integralny indeks separowalności przedstawiony na Rys. 9b wskazuje na poprawę w separowalności danych przetworzonych względem surowych danych wejściowych. Dla wartości progowych  $\Theta = 0.6$  oraz  $\Theta = 0.7$  otrzymano poprawę całkowitego indeksu separowalności dla wszystkich scenariuszy klasyfikacji.

*D3. Dawid Przyczyna, Maciej Suchecki, Andrew Adamatzky, Konrad Szaciłowski „Towards Embedded Computation with Building Materials”, Materials 2021, 14, 1724.*



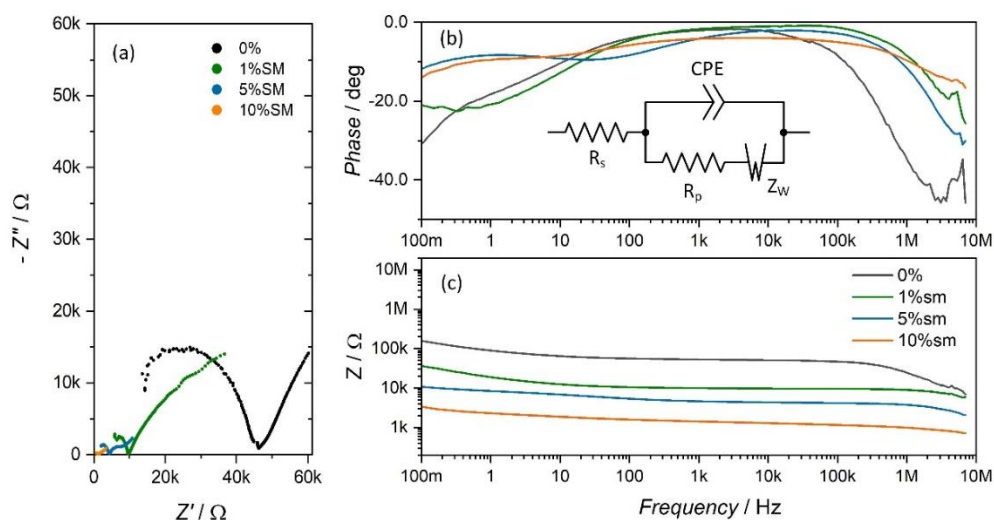
Połączenie idei obliczeń *in materio* oraz inteligentnych domów prowadzi do koncepcji betonu obliczeniowego – inteligentnego materiału łączącego cechy konstrukcji i przetwarzania informacji. Ta koncepcja została pierwotnie przedstawiona w rozdziale „On buildings that compute: a proposal”, gdzie inteligentne bloki betonowe i panele z inteligentnymi farbami reagującymi na bodźce stanowią rdzeń proponowanej architektury. Dzięki wykorzystaniu niekonwencjonalnych metod uczenia maszynowego – takich jak obliczanie rezerwarowe – możliwe staje się stworzenie inteligentnej infrastruktury opartej na elementach budowlanych zdolnych do wbudowanego i rozproszonego przetwarzania informacji. Zgodnie z paradygmatem obliczania rezerwarowego, do przetwarzania informacji można wykorzystać każdy fizyczny układ o wystarczająco złożonej strukturze, wewnętrznej dynamice i/lub reakcji na bodźce zewnętrzne. Beton nadaje się do nano- lub mikromodyfikacji pełniąc rolę spoiwa wybranych domieszek i dodatków. Szczególnie pożądane jest domieszkowanie wprowadzające właściwości memrystywne do materiałów na bazie betonu.

Niniejsza praca ma na celu wykazanie, że beton – wszechobecny materiał budowlany – może również służyć jako medium obliczeniowe. Ze względu na ograniczone właściwości memrystywne oraz mobilność nośników ładunku, zadania obliczeniowe w domieszkowanym betonie przeprowadzono w podejściu heterotycznym — obliczeniom *in materia* musi towarzyszyć dodatkowa analiza sygnału przy użyciu klasycznych metod w celu odczytu i analizy stanu rezerwaru. Niemniej jednak domieszkowany beton okazuje się użytecznym medium obliczeniowym zdolnym do prostej klasyfikacji sygnałów.



**Rysunek 10.** Pomiar voltamperometryczny dla niedomieszkowanego betonu (a), betonu domieszkowanego 10% masowo półprzewodnikiem SbSI (b) oraz betonu domieszkowanego 10% masowo mieszaną 1:1 opilkami metalicznymi oraz ziarnami półprzewodnika SbSI (c).

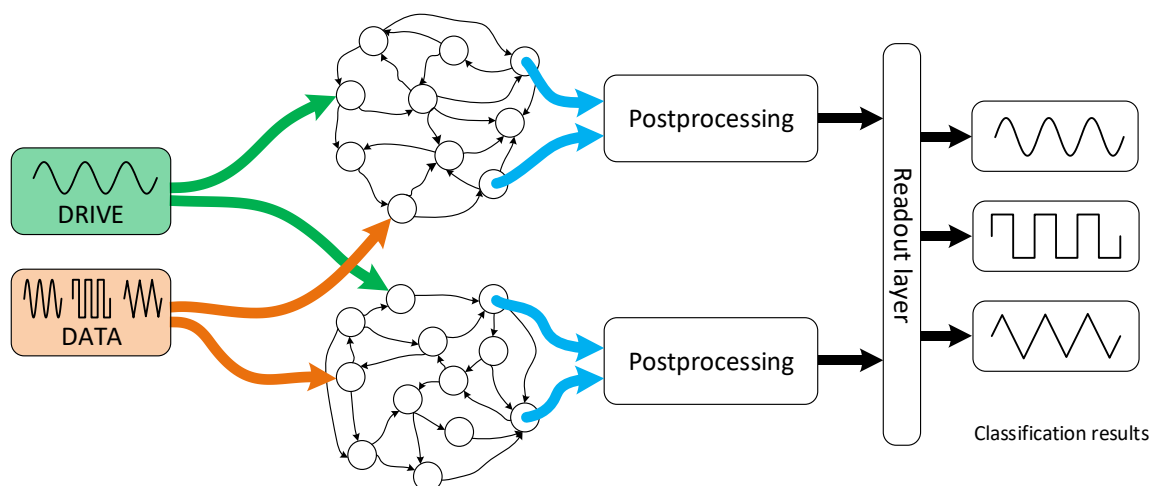
W pierwszym kroku próbki o różnym stężeniu domieszek scharakteryzowano metodą voltamperometrii cyklicznej (Rys. 10). Beton niedomieszkowany, jak również beton z niską zawartością jakiegokolwiek domieszki, wykazuje dominującą pętlę histerezy pojemnościowej nałożoną na prąd omowy. Złożony charakter krzywych prądowo/napięciowych można interpretować pod kątem mieszanego ferroelektryczno-antyferroelektrycznego charakteru badanych próbek, czego źródłem jest obecność ziaren SbSI. Ze względu na złożoną strukturę chemiczną i fazową próbek jest to w pełni uzasadnione. Nieliniowa odpowiedź układu na bazie domieszkowanego betonu może wynikać z dostępności wielu różnych ścieżek przewodzących dla nośników ładunku, jak również z nakładania się efektów pojemnościowych z przewodnictwem jonowym betonu.



**Rysunek 11.** Widma impedancyjne próbek betonu niedomieszkowanego oraz domieszkowanego metalem i półprzewodnikiem: wykres Nyquista (a) kąty przesunięcia fazowego (wraz z uproszczonym obwodem zastępczym) (b) i zależność impedancji od częstotliwości (c).

Właściwości elektryczne wybranych próbek zostały dodatkowo zbadane za pomocą spektroskopii impedancyjnej. Zaobserwowano spadek impedancji (zarówno składowej rzeczywistej, ja i urojonej) wraz ze wzrostem stężenia domieszki (Rys. 11a). Ponadto beton niedomieszkowany wykazuje stosunkowo duży kąt przesunięcia fazowego przy niskich częstotliwościach (Rys. 11b), co może być związane z powolnymi procesami dyfuzyjnymi (modelowanymi impedancją Warburga) w osnowie ceramicznej. Zwiększenie koncentracji domieszek zmniejsza ten udział, ponieważ zaczynają dominować inne mechanizmy transportu nośników ładunku (Rys. 11c). Liniowa składowa Warburga przy niskich częstotliwościach jest widoczna tylko w przypadku próbki niedomieszkowanej (fragment danych za przegięciem krzywych na Rys. 11a). Zwiększone domieszkowanie jest skorelowane ze spadkiem wartości impedancji oraz ze znaczną krzywizną wykresów Nyquista przy wysokich częstotliwościach.

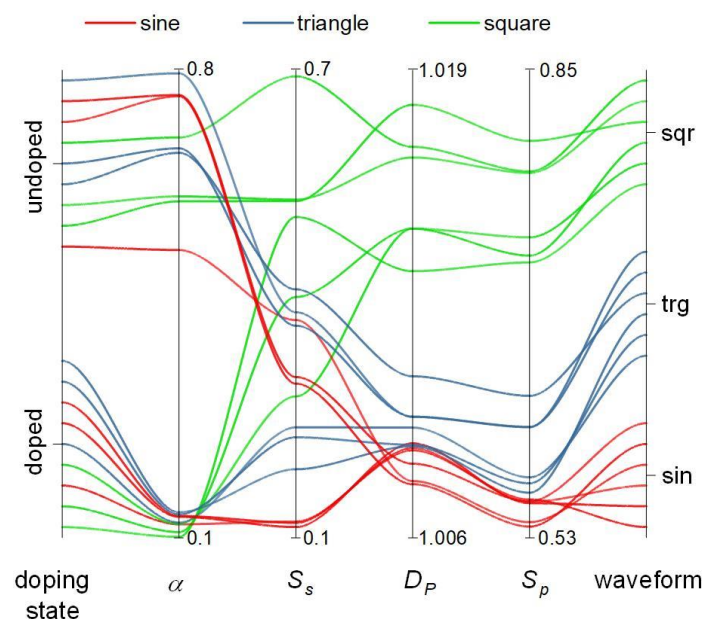
Aby dokonać klasyfikacji sygnałów wykorzystano dodatkowy sinusoidalny sygnał pobudzający o stałej częstotliwości (300Hz). Następnie wykonano mieszanie sygnałów – pobudzający z klasyfikowanym – w próbce niedomieszkowanej oraz domieszkowanej (Rys. 12). Zarówno sygnał pobudzający jak i próbka niedomieszkowana służyły jako odniesienie. Sygnał pobudzający pełni dodatkową rolę – wprowadza dodatkową dynamikę do wewnętrznego ruchu nośników ładunku. Po zmieszaniu sygnałów analizowano trendy zmian w parametrach złożoności otrzymanego sygnału w próbce domieszkowanej względem niedomieszkowanej. Sygnały klasyfikowane o trzech kształtach (sinusoidalnym, trójkątnym oraz prostokątnym) dostrojono do częstotliwości 290Hz, 280Hz i 275Hz każdy.



**Rysunek 12.** Schemat podwójnego systemu obliczania rezerwuarowego opartego na betonie używanego do klasyfikacji prostych sygnałów.

Stacjonarny charakter otrzymanych danych potwierdzono na bazie standardowego testu statystycznego – rozszerzonego testu Dickeya-Fullera. Następnie wykonano kolejne testy statystyczne aby określić odpowiednie opóźnienie czasowe oraz wymiar zagnieżdżenia potrzebne do dobrej wizualizacji danych (konstrukcja map opóźnionych koordynatów) oraz elementów dalszej analizy. W tym celu posłużono się odpowiednio metodami autokorelacji i opóźnionej wzajemnej informacji oraz algorytmów fałszywych sąsiadów i uśrednionych fałszywych sąsiadów. W kolejnym kroku obliczono szereg parametrów złożoności sygnału, m.in. parametry jego entropii oraz wymiary fraktalne. Analizując otrzymane parametry zaproponowano kilka scenariuszy klasyfikacji. Skonstruowano proste drzewko decyzyjne umożliwiające klasyfikację sygnałów, w zależności od trendów zmian trzech różnych parametrów złożoności (entropii permutacyjnej, wymiaru fraktalnego Katza i Petrosiana). Zmiany w trendach pojedynczego parametru złożoności – fraktalnego wymiaru korelacji – również umożliwiają klasyfikację analizowanych sygnałów. Finalnie, określono pojedynczy parametr – entropia permutacji – umożliwiający liniowe odseparowanie klasyfikowanych sygnałów (Rys. 13).

Dodatkowo, w przypadku analizy wahań z wyodrębnionym trendem możliwe staje się określenie, która z próbek była domieszkowana (w przypadku odwrotnego scenariusza klasyfikacji, gdzie rozpatrywany byłby stan domieszkowania próbek, Rys. 12). Przyszłe badania mogłyby połączyć klasyczne pomiary elektryczne z funkcjami przetwarzania sygnału w betonie, aby uzyskać bardziej wydajne techniki jego monitorowania.



**Rysunek 13.** Wykres współrzędnych równoległych dla wybranych parametrów złożoności analizowanych sygnałów: wykładnik wahań (detrended fluctuation exponent) ( $\alpha$ ), entropia próbki ( $S_s$ ), wymiar fraktalny Petrosiana ( $D_P$ ) i entropia permutacyjna ( $S_p$ ).

Należy zaznaczyć, że wydajność urządzeń obliczeniowych opartych na betonie jest ograniczona. Przedstawione wyniki można traktować jako dowód na słuszność tezy o możliwości przetwarzania informacji i przeprowadzania zadań klasyfikacyjnych na bazie odpowiednio domieszkowanych materiałów budowlanych pełniących rolę substratu obliczeniowego w heterotycznym układzie rezerwuarowego obliczania.



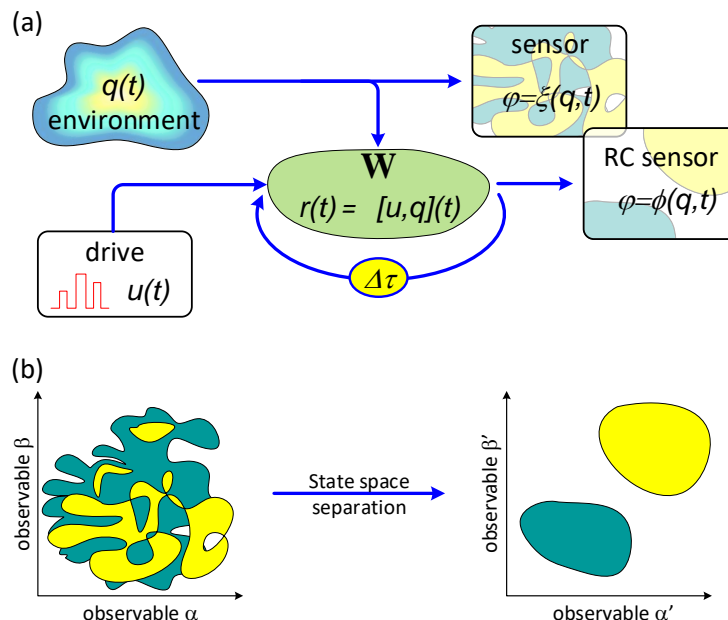
*D4. Dawid Przychyna, Sebastien Pecqueur, Dominique Vuillaume, Konrad Szaciłowski  
„Reservoir computing for sensing: an experimental approach”, Int. J. Unconv. Comput.,  
2019, 14, 267.*



W dzisiejszym świecie efektywne pozyskiwanie i przetwarzanie informacji ma kluczowe znaczenie. Z tego powodu prowadzone są liczne badania nad nowymi układami specjalnego przeznaczenia (sensory, elementy wykonawcze, klasyfikatory sygnału/dźwięku/obrazu), a także nad nowymi, niekonwencjonalnymi koncepcjami działania systemu obliczeniowego i analizy danych.

Paradygmat *obliczania rezerwuarowego* proponuje nowe podejście do rozwiązywania problemów obliczeniowych poprzez wykorzystanie odpowiednich substratów (materiałów bądź procesów) zapewniających *rezerwuar stanów*. Rezerwuar stanów można określić jako odpowiednią (np. do danego zadania) ilość możliwych konfiguracji (w postaci np. wewnętrznej dynamiki materiału) w jakich wykorzystywany rezerwuar może się znaleźć. Transformacja sygnału w układzie obliczania rezerwuarowego może również umożliwić uzyskanie dodatkowych informacji, analizując nowe reprezentacje danego sygnału. Konwencjonalne czujniki muszą spełniać określone kryteria jakościowe, m.in.: próg detekcji, selektywność, czułość oraz szybkość reakcji na dany bodziec. W ramach poprawy działania danego układu detekcyjnego można zastosować algorytmy uczenia maszynowego (w tym obliczanie rezerwuarowe), aby usprawnić klasyfikację jego odpowiedzi bez konieczności angażowania inżynierii materiałowej.

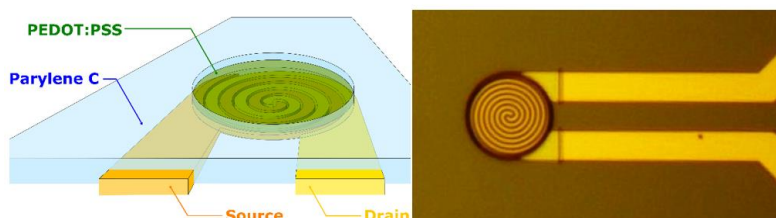
Podejście do zagadnienia detekcji chemicznej na bazie układów obliczania rezerwuarowego zostało zaproponowane przez Zorana Konkoli (Rys. 14). W algorytmie SWEET (*State Weaving Environment Echo Tracker*) wykorzystuje się rezerwuar sprzężony z badanym środowiskiem – subtelne zmiany w wewnętrznej dynamice rezerwuaru będą wynikać ze zmian w danym środowisku (np. stężeniu określonego analitu).



**Rysunek 14.** Ogólny zarys systemu detekcji SWEET. Rezerwuar wrażliwy na środowisko jest wykorzystywany do uzyskiwania informacji o nim. Może się to odbywać na drodze bezpośredniej, co daje nieprzetworzoną informację o środowisku,  $\xi(q, t)$ , lub na drodze pośredniej, poprzez badanie odpowiedzi rezerwuaru  $\Phi(q, t)$  po użyciu sygnału wzbudzającego  $u(t)$ . Opóźnione sprzężenie zwrotne jest dodawane w celu zwiększenia złożoności przestrzeni konfiguracji i uzyskania lepszych właściwości obliczeniowych rezerwuaru (a). Symboliczna reprezentacja złożonego problemu wykrywania. Czujnik ma za zadanie wykryć stan układu

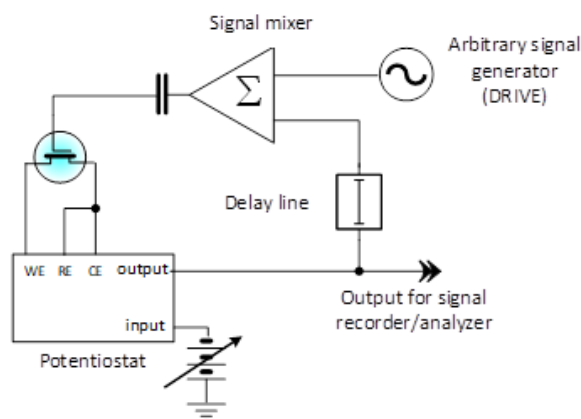
(żółty lub zielony) na podstawie pomiaru obserwabli  $\alpha$  i  $\beta$ . Po lewej stronie przypadek niskiej separacji danych w przestrzeni fazowej, w którym problem detekcji jest trudny i podatny na błędy. Zastosowanie czujnika opartego na obliczeniach rezerwuarowych z odpowiednim sygnałem wzbudzającym (drive) powoduje separację analizowanych danych, dzięki czemu może dać znacznie bardziej wiarygodne informacje. W tym scenariuszu do wnioskowania o stanie środowiska można wykorzystać stosunkowo prostą warstwę odczytową. Większość obliczeń jest wykonywana przez urządzenie, a nie przez warstwę odczytu.

W układzie SWEET dodanie do rezerwuaru pętli opóźnionego sprzężenia zwrotnego zwiększa potencjał detekcyjny układu dzięki stopniowemu narastaniu nawet najmniejszych zmian jego stanu, podobnie jak w układach o charakterze chaotycznym. Oznacza to, że interakcja rezerwuaru z otoczeniem może być bardzo mała, bez pogorszenia jakości detekcji. Realizację eksperymentalną układu SWEET opracowano na bazie organicznego tranzystora elektrochemicznego (OECT) gdzie kanał urządzenia został wykonany z cienkiej warstwy polimeru przewodzącego PEDOT:PSS. (Rys. 15). W pracy zastosowano OECT jako pojedynczy węzeł dynamiczny działający w pętli sprzężenia zwrotnego w celu detekcji jonów potasu  $K^+$ .



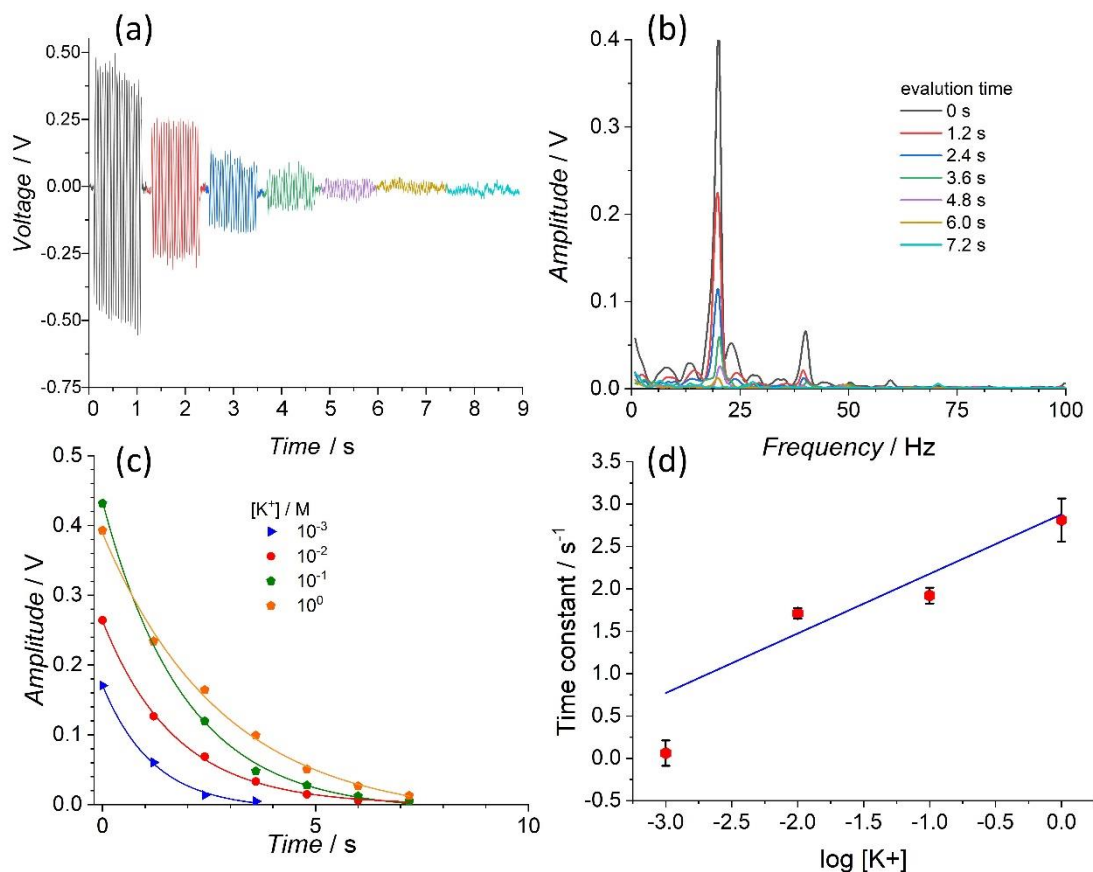
**Rysunek 15.** Schemat oraz zdjęcie wykonane przy pomocy mikroskopii optycznej organicznego tranzystora elektrochemicznego PEDOT:PSS.

Przepływ prądu „źródło-dren” (S-D) mierzono za pomocą potencjostatu analogowego w układzie dwuelektrodowym (przeciw-elektroda zwarta z elektrodą referencyjną Rys. 16). Umieszczony w elektrolicie drut platynowy pełnił funkcję bramki tranzystora. Bramka tranzystora była podłączona do pętli sprzężenia zwrotnego wraz z generatorem sygnału.



**Rysunek 16.** Schemat układu systemu rezerwuarowego z pętlą sprzężenia zwrotnego na bazie organicznego tranzystora elektrochemicznego. Wejście potencjostatu steruje źródłem zadanego potencjału, wyjście jest analogowym monitorem prądu.

Przepływ prądu w obwodzie S-D był wymuszany potencjałem stałym o wartości 100 mV wykorzystując potencjostat analogowy. Po wstrzyknięciu elektrolitu (zawierającego jony  $K^+$ ) bezpośrednio do warstwy PEDOT:PSS, układ wzбудzano sygnałem sinusoidalnym o częstotliwości 20 Hz. Uzyskany sygnał był następnie opóźniany i zawracany do układu poprzez pętlę sprzężenia zwrotnego aż do momentu całkowitego wytlumienia. Wraz ze wzrostem stężenia jonów zaobserwowano wzrost prądów rejestrowanych w obwodzie S-D, co ostatecznie wpływało na liczbę powtórzonych epok sygnału (Rys. 17a).



**Rysunek 17.** Przykładowa odpowiedź badanego układu obliczania rezerwurowego z pętlą sprzężenia zwrotnego przy wysokim stężeniu jonów  $K^+$  (a). Transformaty Fouriera dla wszystkich paczek sygnału zarejestrowane przy określonym stężeniu. (b). Amplitudy pierwszej składowej (20 Hz) w funkcji czasu dla różnych stężeń jonów potasu (c). Krzywa kalibracyjna na podstawie wartości stałych czasowych zaniku krzywych eksponencjalnych w funkcji stężenia jonów potasu (d)

Analizę sygnału przeprowadzono z zastosowaniem transformaty Fouriera (Rys. 17b). Najpierw przedstawiono amplitudy pików częstotliwości podstawowej w funkcji czasu, następnie dopasowano krzywe eksponencjalne (Rys. 17c). Jak widać na Rys. 17c, dla najwyższego stężenia 1M jonów  $K^+$  zaobserwowano niższy sygnał niż dla stężenia 0.1M  $K^+$ , co wskazuje na wysycenie materiału dla pewnej progowej wartości stężenia jonów. Poprzez analizę otrzymanych stałe czasowych zaniku krzywych eksponencjalnych czułość systemu została rozszerzona do wyższych stężeń (Rys. 17d). Inny scenariusz analizy danych zakłada wykorzystanie jedynie kolejnych powtórzeń danego sygnału – w badanym przypadku analiza sygnału po dwóch obiegach pętli (sygnał przy 2.4s) umożliwia separację rozważanych stężeń.

Zgodnie z teorią SWEET, układ obliczania rezerwuarowego jest w ciągłym kontakcie z wykrywanym indywidualnym chemicznym. Pomimo wysycenia maksymalnej amplitudy otrzymanego sygnału, dynamika przenoszenia sygnału przez układ w pętli sprzężenia zwrotnego zmienia się w zależności od stężenia jonów  $K^+$ , tym samym umożliwiając wykrycie wyższych stężeń korzystając z innej reprezentacji analizowanych danych.

*D5. Dawid Przyczyna, Maria Szaciłowska, Marek Przybylski, Marcin Strzelecki, Konrad Szaciłowski „Recognition of Musical Dissonance and Consonance in a Simple Neuromorphic Computing System”, Int. J. Unconv. Comput. 2022, 17, 81*

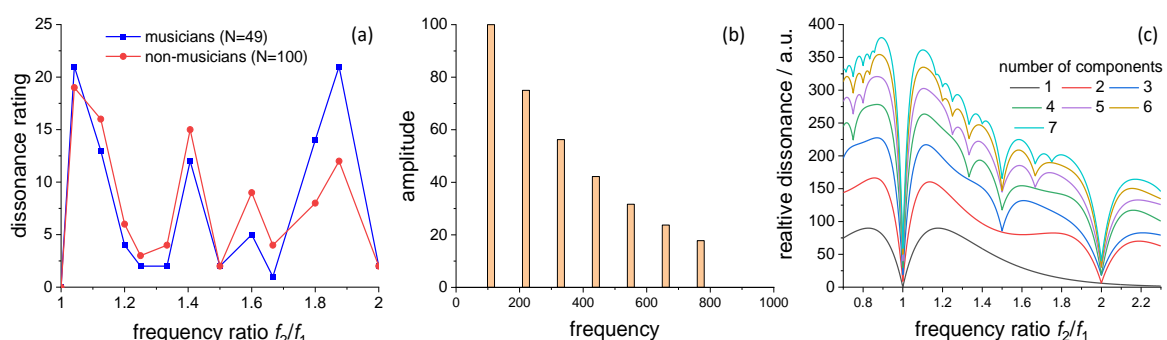




Muzyka i mowa są tworzone i przetwarzane przez różne struktury neuronalne, ale mają pewne cechy wspólne: są środkami komunikacji oraz mają specyficzną składnię – tzn. istnieje zbiór reguł określających właściwe połączenie ich elementów (słów lub nut). Muzyka jest dziedziną ludzkiej działalności artystycznej i rozrywkowej, ale także polem intensywnych badań. Najprostszy przekaz muzyczny, melodia, może być zdefiniowany jako odpowiednia sekwencja czasowa skwantyfikowanych częstotliwości. Częstotliwości te są nazywane stopniami skali muzycznej. Większość systemów muzycznych opiera się na koncepcji oktawy: przedziału między częstotliwościami  $f$  i  $2f$ . W muzyce pochodzenia europejskiego oktawa jest podzielona na 12 części (równomiernie rozmieszczonych w przypadku stroju temperowanego, zaś nierównomiernie w przypadku stroju naturalnego), zwanych półtonami. Dwa podstawowe pojęcia związane z harmonią muzyczną to konsonans i dysonans. Pojęcia te dotyczą wrażeń estetycznych wywoływanych przez dwa (lub więcej) dźwięki grane jednocześnie. Skala konsonansu i dysonansu pozwala scharakteryzować interwały muzyczne pod względem tego, jak bardzo brzmią przyjemnie lub nieprzyjemnie. O ile sama klasyfikacja jest doskonale znana i jednoznaczna, o tyle jej fizyczne i psychologiczne pochodzenie pozostaje co najmniej niejasne.

Plomp i Levelt (Plomp i Levelt 1965) oraz Sethares (Sethares 2005, 1993) wskazują w swoich badaniach na potencjalną rolę składowych harmonicznymi interwałów muzycznych na ich charakter konsonansowy/dysonansowy. W ich podejściu kombinacja tonów jest dysonansowa, jeśli w danym dźwięku istnieją dysonansowe stosunki między wyższymi harmonicznymi dwóch tonów, zaś stopień dysonansu zależy od liczby tych dysonansowych stosunków. Po odpowiednim przyporządkowaniu parametrów model daje bardzo wiarygodne wyniki, porównywalne z oceną stopnia dysonansu słyszanych dźwięków przez uczestników badania (Rys. 18).

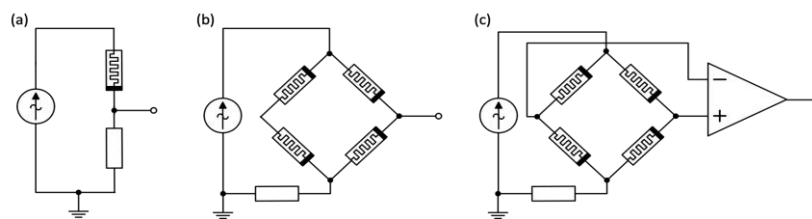
Na podstawie modelu zaproponowanego przez Setharesa, możliwa jest symulacja krzywych dysonansowych w zależności od występowania określonej liczby składowych harmonicznymi. Wyniki tych obliczeń są przedstawione na Rys. 18 b-c. Należy zauważyć, że to podejście opiera się na obecności składowych harmonicznymi w każdym tonie: w przypadku pojedynczych sygnałów sinusoidalnych można wyodrębnić tylko prymę, dodanie większej liczby składowych harmonicznymi powoduje wyodrębnienie oktawy (2 składowe), kwinty (3 składowe) i kwarty (4 składowe), jak pokazano na rysunku 18c.



**Rysunek 18.** Percepcja dysonansu przez osoby z (49 osób) i bez (100 osób) wykształcenia muzycznego, na podstawie danych z ref. (Lopresto 2015) (a). Dysonans muzyczny obliczony dla tonu podstawowego  $A_2 = 110$  Hz i zmiennej liczby składowych harmonicznymi: przykładowe widmo Fouriera tonu  $A_2$  (b) oraz obliczone na podstawie modelu Setharesa krzywe dysonansu sensorycznego dla zmiennej liczby składowych harmonicznymi (c).

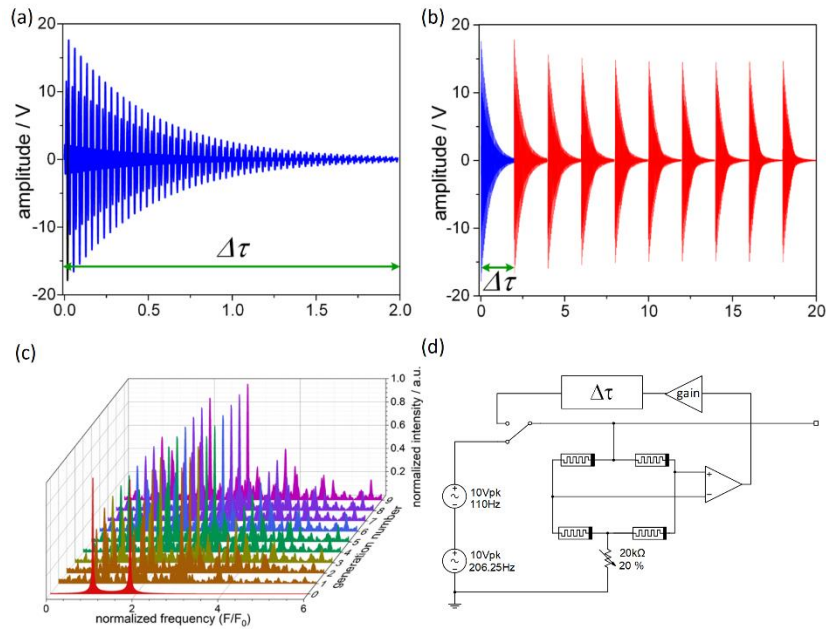
Wiele prowadzonych badań wskazuje na istotny komponent neurofizjologiczny w percepcji muzyki oraz na szczególną rolę konsonansu muzycznego. Podkreślają one również znaczenie muzyki na bardzo podstawowym poziomie neurofizjologicznym u ptaków, ssaków i ludzi. W związku z tym w ramach omawianej pracy postanowiono sprawdzić, czy proste urządzenie neuromorficzne działające w trybie uczenia nienadzorowanego będzie w stanie rozróżnić (bądź grupować) kombinacje tonów na konsonansowe i dysonansowe. Badania miały na celu przetestowanie tezy, że skoro percepcja muzyki jest procesem neurofizjologicznym, to urządzenie naśladujące dynamikę struktur nerwowych powinno wykazywać podobne zdolności.

Obliczenia rezerwuarowe z neuromorficznymi elementami synaptycznymi to nowe i wciąż niekonwencjonalne, lecz skuteczne podejście do przetwarzania i klasyfikacji różnych sygnałów. Można je opisać jako model obliczeń *przejściowych*, w którym wpływ danych wejściowych zmienia wewnętrzną dynamikę wybranego systemu obliczeniowego. Wybór odpowiedniego substratu obliczeniowego, który charakteryzuje się nieliniową odpowiedzią i bogatą dynamiką wewnętrzną, zapewnia realizację prostych protokołów odczytu stanu warstwy rezerwuaru. W poniższych badaniach zaimplementowano na platformie Multisim prosty neuromorficzny system obliczeniowy – synapsę mostkową – w układzie obliczania rezerwuarowego *Single Node Echo-State Machine* (SNESM) jako narzędzie do grupowania interwałów muzycznych według ich konsonansowego lub dysonansowego charakteru.



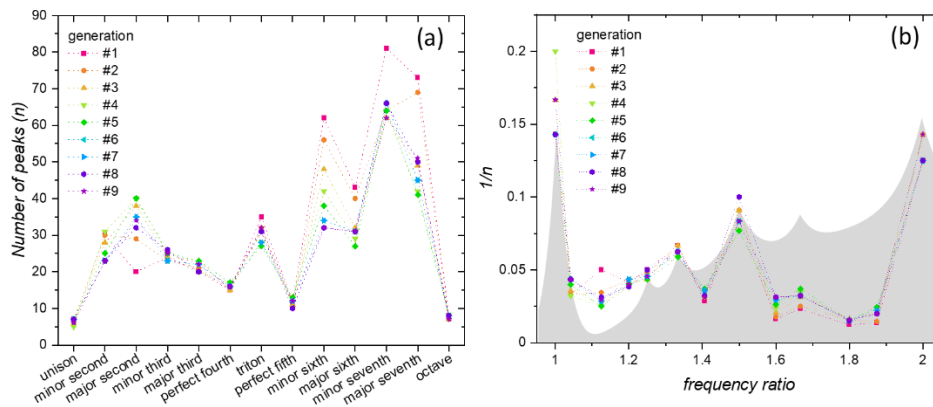
**Rysunek 19.** Rozpatrywane obwody memrystywne zaimplementowane na platformie MULTISIM. Obwody bazujące na pojedynczym memrystorze (a), synapsie mostkowej bez (b) oraz ze wzmacniaczem różnicowym (c).

Z uwagi na powyżej wspomnianą rolę wyższych harmonicznych w rozpoznaniu interwałów muzycznych, postanowiono przetestować kilka konfiguracji układów aby wybrać najbardziej odpowiedni do włączenia go do układu rezerwuarowego. Zmierzono odpowiedź elektryczną modelu pojedynczego memrystora, synapsy mostkowej bez oraz ze wzmacniaczem różnicowym, następnie obliczono transformaty Fouriera w celu określenia występowania wyższych harmonicznych w transformowanym przez dany układ sygnale. Wyselekcjonowano układ na bazie mostka synaptycznego ze wzmacniaczem różnicowym (Rys. 19c), gdyż układ wykazał najlepszą wydajność generacji wyższych harmonicznych.



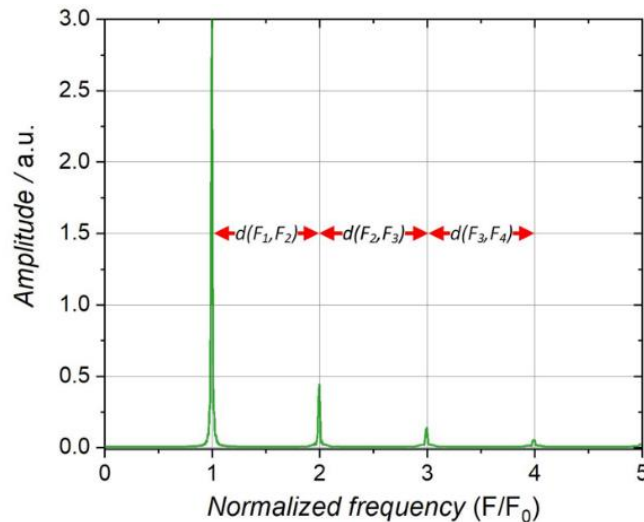
**Rysunek 20.** Przykład sygnałów wejściowych (a) i wyjściowych (b) zarejestrowanych w pętli sprzężenia zwrotnego układu SNESM: sygnał wejściowy – kwinta (A1-E1, niebieski) i echo wyjściowe (czerwony). Zielona strzałka wskazuje czas trwania każdej epoki. Przykładowe transformaty Fouriera dla ewolucji sygnału odpowiadającego septymie wielkiej C2-B2 (c). Schemat układu Single Node Echo-State Machine zaimplementowany na platformie MULTISIM (d).

Po całkowitym wzbudzeniu układu sygnałem wejściowym z dwóch generatorów, włączano przełącznik (Rys. 20d), który umożliwiał dalsze samowzbudzenie układu. W efekcie system generuje serię "epok" – obrazów sygnału wejściowego w kolejnych etapach jego ewolucji. W ramach analizy obliczono transformaty Fouriera wszystkich badanych interwałów muzycznych. Następnie policzono liczbę występujących (powyżej arbitralnej wartości progowej) składowych częstotliwościowych w każdym widmie Fouriera.



**Rysunek 21.** Liczba składowych częstotliwościowych dla różnych interwałów muzycznych dla kolejnych transformat Fouriera sygnału krążącego w pętli sprzężenia zwrotnego (a) oraz odwrotność liczby szczytów w funkcji stosunku częstotliwości dla różnych interwałów. Obszar zacieniony na szaro przedstawia symulowaną krzywą "konsonansu sensorycznego" (lustrzane odbicie krzywej dysonansu z Rys. 18c dla 5 harmonicznych). Punkty reprezentują dane eksperymentalne.

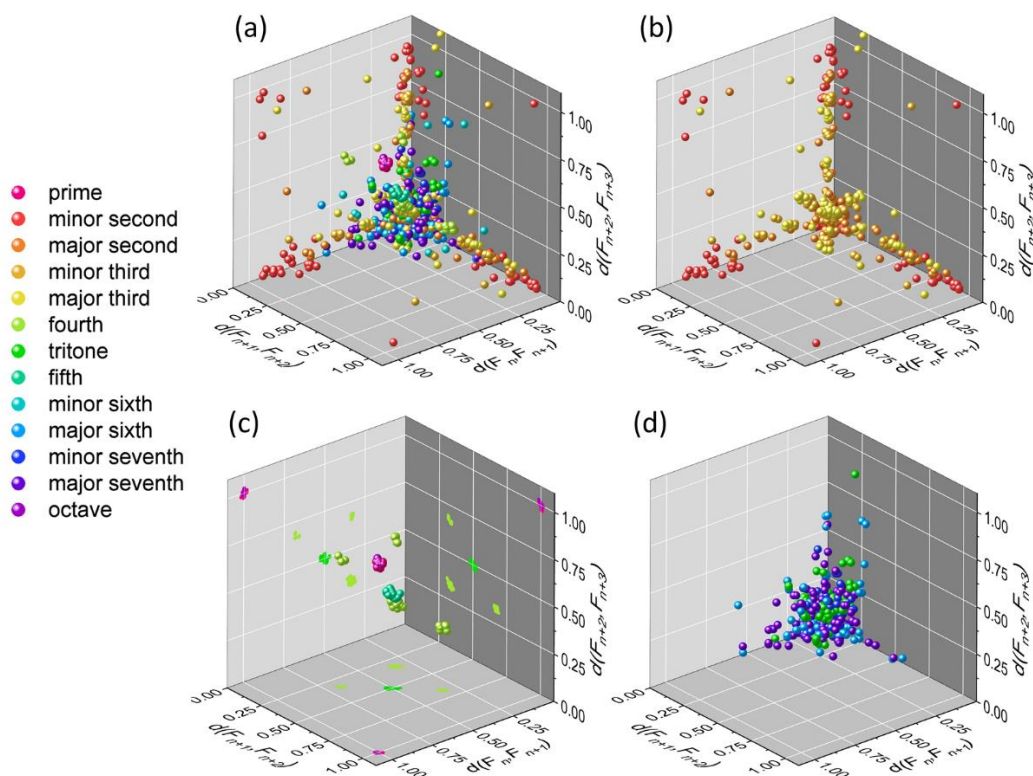
Warstwa odczytu oparta na zliczaniu składowych częstotliwościowych w widmach Fouriera umożliwia grupowanie interwałów muzycznych w sposób podobny do tego, w jaki robią to ludzie lub wyspecjalizowane algorytmy. Wynik ewolucji danych jest zbliżony do krzywej dysonansu sensorycznego (z kilkoma istotnymi różnicami, Rys. 21b).



**Rysunek 22.** Ilustracja metody analizy sygnału na podstawie odległości między składowymi częstotliwościowymi obecnymi w widmach Fouriera.

W celu zbadania zależności pomiędzy składowymi obecnymi w widmach częstotliwościowych, wykonano wizualizację danych – różnicę w odległościach pomiędzy daną składową częstotliwościową a składową ją poprzedzającym (Rys. 22). Następnie, skonstruowano trójwymiarowy "portret fazowy" z wykorzystaniem uzyskanych odległości – dla każdego interwału i dla każdej składowej obecnej w widmie częstotliwościowym (oznaczone tutaj jako  $F_n$ ) obliczono zestaw odległości do najbliższych sąsiadów:  $d(F_n, F_{n+1})$ ,  $d(F_{n+1}, F_{n+2})$  i  $d(F_{n+2}, F_{n+3})$ . Wartości te były wykorzystywane jako współrzędne kartezjańskie ( $x, y, z$ ) określające punkty w przestrzeni dla wszystkich kolejnych pików występujących w danym widmie. W reprezentacji danych dany punkt jest uzyskiwany na podstawie danej różnicy i dwóch kolejnych różnic częstotliwości. Każdy interwał jest więc reprezentowany jako zbiór punktów w przestrzeni trójwymiarowej.

Można zauważyć, że interwały traktowane jako absolutne – unison i oktawa – są skupione w jednym miejscu, wokół punktu  $(1,1,1)$ , ponieważ różnice między ich znormalizowanymi składowymi częstotliwościowymi zawsze będą wynosiły 1. Dodatkowo konsonanse doskonałe – kwarta i kwinta – są skupione w kilku obszarach w separacji od innych interwałów (Rys. 23c). Kwarta jest skupiona w 4 różnych regionach wokół punktów  $(\frac{1}{3}, \frac{1}{3}, \frac{1}{3})$ ,  $(\frac{1}{3}, \frac{1}{3}, \frac{2}{3})$ ,  $(\frac{1}{3}, \frac{2}{3}, \frac{1}{3})$  i  $(\frac{1}{3}, \frac{2}{3}, \frac{2}{3})$ , zaś kwintę można znaleźć w jednym większym skupisku w okolicy  $(\frac{1}{2}, \frac{1}{2}, \frac{1}{2})$ . Tylko punkty odpowiadające tym konsonansom interwałom są skupione w ograniczonych przestrzeniach. Sekundy i tereje zajmują miejsca wzdłuż osi (Rys. 23b), których skupisko znajduje się blisko początku układu współrzędnych. Trytony, seksty i septymy są rozproszone również w pobliżu początku układu współrzędnych (Rys. 23d). Większość interwałów postrzeganych jako dysonansowe można znaleźć w jednym dużym skupisku punktów w pobliżu punktu  $(0,0,0)$ .



**Rysunek 23.** Geometryczne przedstawienie różnych interwałów na podstawie odległości między kolejnymi składowymi widm Fouriera. Wszystkie interwały (a), sekundy i tercje (b), prymy, oktawy, kwinty i kwarty (c) oraz trytony, seksty i septymy (d).

Podsumowując, dwa różne sposoby reprezentacji danych wyjściowych z układu SNESM dają podobne wyniki – podejście oparte na zliczaniu występujących składowych częstotliwościowych pozwala na odwzorowanie krzywych dysonansowych, co jest ściśle związane ze słuchową klasyfikacją interwałów muzycznych. Podejście geometryczne, oparte na odległościach między kolejnymi pikami widma Fouriera, wyraźnie odróżnia konsonanse od dysonansów w ramach analizowanego portretu fazowego.

Ewolucja sygnałów oparta na bogatej dynamice synaptycznych układów opartych o memrystory pozwala uwypuklić różnice pomiędzy poszczególnymi sygnałami, umożliwiając ich grupowanie. Grupowanie przeprowadzono bez odwoływania się do teorii muzyki. Przeprowadzone badania sugerują duży potencjał w wykorzystaniu prostego systemu neuromorficznego do zaawansowanego przetwarzania informacji. Ponadto wskazują, że pojęcia konsonansu i dysonansu mogą mieć podłoże neurofizjologiczne.



*D6. Dawid Przychyna, Grzegorz Hess, Konrad Szaciłowski „KNOWM Memristors in a Bridge Synapse delay-based Reservoir Computing system for detection of epileptic seizures”, Int. J. Parallel Dist. Syst. 2022, 10.1080/17445760.2022.2088751.*





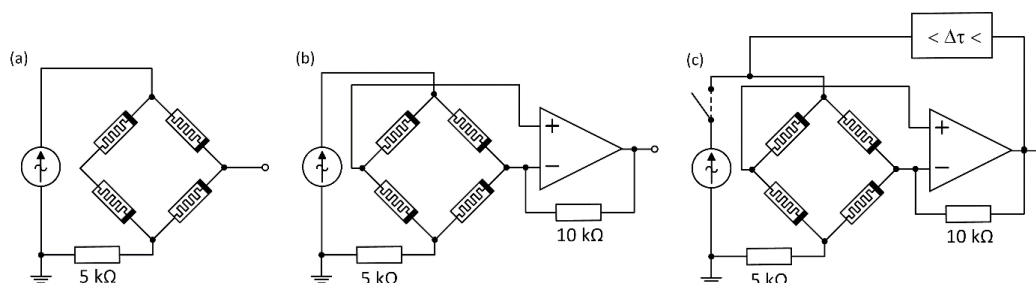
Nanourządzenia dokonujące nieliniowej transformacji sygnałów elektrycznych, a także prezentujące różne formy pamięci – m.in. urządzenia i obwody memrystyczne – mogą być wykorzystywane w nowych paradygmatach obliczeniowych, takich jak obliczenia neuromorficzne czy rezerwarowe, które mają na celu rozwiązywanie współczesnych problemów obliczeniowych. Dedykowane implementacje sprzętowe oparte na funkcjonalnych strukturach neuromorficznych zmniejszają zużycie energii i/lub zwiększają możliwości obliczeniowe danego systemu sztucznych sieci neuronowych.

Synapsa mostkowa to proste urządzenie neuromorficzne składające się z czterech memrystorów i wzmacniacza różnicowego. Charakteryzuje się ona zdolnością do reprezentacji wielu stanów analogowych oraz generacji wyższych harmonicznych, co może być korzystne z punktu widzenia bogatej *przestrzeni stanów* potrzebnej do efektywnego obliczania rezerwarowego. W poprzedniej pracy pokazano grupowanie interwałów muzycznych poprzez ewolucję sygnału w systemie obliczania rezerwarowego opartego na synapsie mostkowej działającej w pętli sprzężenia zwrotnego. W obecnej pracy przedstawiono sprzętową realizację tego systemu rezerwowego – *Single Node Echo-State Machine* (SNESM) – opartego na synapsie mostkowej jako substracie obliczeniowym używanym do wykrywania napadów padaczkowych. Ewolucja sygnału w systemie, a zwłaszcza tłumienie, akumulacja szumów i zniekształceń harmonicznych jak również nieliniowe filtrowanie wpływa na poprawę dokładności klasyfikacji wykorzystywanych sygnałów. Do określenia dokładności klasyfikacji wykorzystano F1-score – parametr analizy statystycznej używany do testowania dokładności klasyfikacji systemu w sposób zbalansowany. F1-score jest średnią harmoniczną między *precyzją* a *przywoływaniem*. Precyzja określa ułamek wystąpień klasy docelowej – w tym badaniu „padaczka” – spośród innych klas, natomiast przywoływanie określa ułamek docelowych klas, które zostały prawidłowo sklasyfikowane wśród innych wystąpień z tej samej klasy, które zostały pominięte. F1-score są obciążone najniższą wartością każdej wartości precyzji i przywoływania, więc gdy wynik F1-score rośnie, zarówno precyzja, jak i przywoływanie zwiększają się.

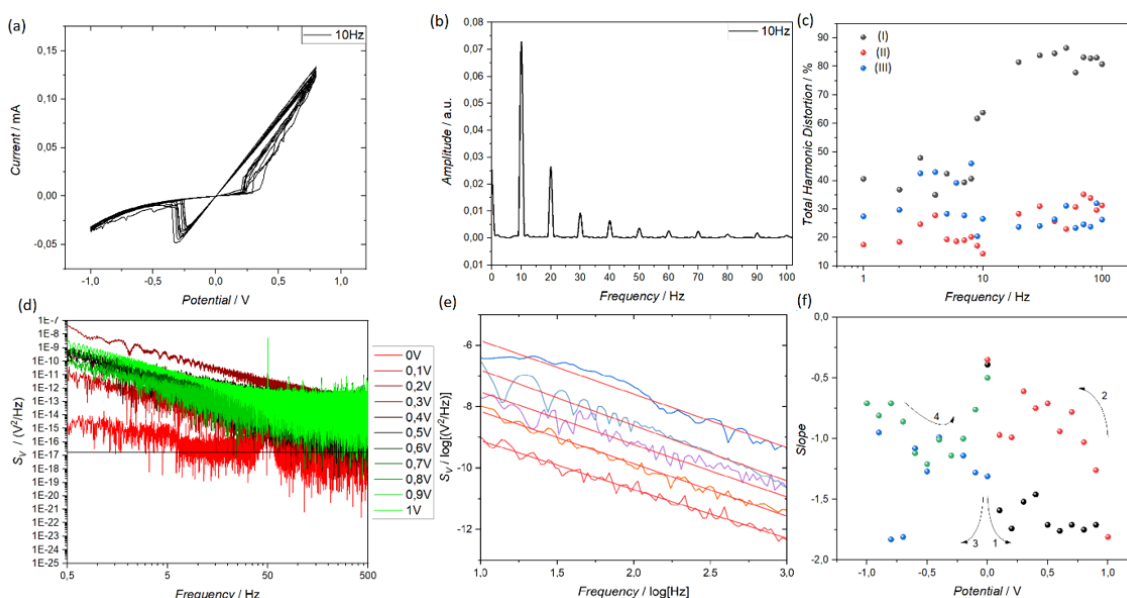
Zaletą systemów obliczania rezerwarowego jest ich zdolność do operowania na niewielkich, niekompletnych zestawach danych, bazując jedynie na najprostszych klasyfikatorach (w warstwie odczytu), takich jak regresja liniowa, metoda gradientu prostego czy drzewo binarne. Nie ma potrzeby stosowania wielowarstwowych sztucznych sieci neuronowych do uczenia warstwy odczytu SNESM, ponieważ rezerwar przeprowadza transformację danych, która ma na celu uproszczenie zadania klasyfikacji.

Padaczka to choroba, która dotyka około 50 milionów ludzi na całym świecie. Padaczkę rozpoznaje się na podstawie występowania napadów, które definiuje się jako przemijające oznaki i/lub objawy wynikające z nieprawidłowej aktywności populacji komórek nerwowych mózgu. Zatem padaczkę uważa się za przewlekłą chorobę mózgu, która charakteryzuje się trwałą skłonnością do nawracających, nieprovokowanych napadów oraz neurobiologicznymi, poznawczymi, psychologicznymi i społecznymi konsekwencjami tego stanu. Obecnie EEG w połączeniu z nagraniami wideo są najbardziej wiarygodnymi metodami wykrywania napadów padaczkowych, jednak są dostępne tylko w monitorowaniu ambulatoryjnym. Dlatego jako alternatywne rozwiązanie zaproponowano urządzenia do noszenia na ciele do wykrywania napadów padaczkowych.

Memrystory KNOWM Inc. to pół-komercyjne urządzenia memrystywne przeznaczone do badań naukowych. Proponuje się, aby mechanizm działania wywodził się z migracji jonów  $Ag^+$  tworzących aglomeraty umożliwiające nowe ścieżki przewodzenia, podobnie jak memrystory oparte na filamentach przewodzących. W niniejszej pracy przedstawiono charakterystykę (charakterystykę szumową i całkowite zniekształcenie harmoniczne) memrystorów KNOWM i opartej na nich synapsy mostkowej (Rys. 24). Parametr całkowitego zniekształcenia harmonicznego mówi nam o udziale wyższych harmonicznych sygnału względem częstotliwości podstawowej, może być zatem traktowany jako prosty eksperymentalny wskaźnik liniowości działania danego urządzenia. Woltamperometria sinusoidalna o dużej amplitudzie jest klasyczną elektrochemiczną techniką pomiarową, na podstawie której obliczono widma fourierowskie potrzebne do obliczeń całkowitego zniekształcenia harmonicznego. Pomiary woltamperometrii sinusoidalnej o dużej amplitudzie wykonano dla trzech scenariuszy: dla pojedynczego memrystora, dla synapsy mostkowej bez i ze wzmacniaczem różnicowym.



**Rysunek 24.** Schematy badanych układów. Synapsa mostkowa bez (a), ze wzmacniaczem różnicowym (b) oraz włączona do układu SNESM (c).



**Rysunek 25.** Przykładowy wynik woltamperometrii sinusoidalnej o dużej amplitudzie o prędkości skanu 10 Hz (a) oraz obliczone na jego podstawie widmo Fouriera (z prostokątną funkcją apodyzującą) (b). Całkowite zniekształcenie harmoniczne określone na podstawie transformaty Fouriera dla częstotliwości od 1 do 100 Hz (c). Przedstawiono wyniki dla pojedynczego memrystora (I), synapsy mostkowej bez wzmacniacza różnicowego (II) oraz ze wzmacniaczem różnicowym (III). Przykładowy szum mierzony dla pojedynczego memrystora

*KNOWM przedstawiony w domenie częstotliwości, dla potencjałów od 0V do 1V. Czarna linia wskazuje szum termiczny przy 0 V (d). Przykład dopasowania linii do kilku filtrowanych widm szumu (e). Zebrane wartości nachylenia widm szumu przy różnych potencjałach prądu stałego. Strzałki służą do wskazania kierunku przeprowadzania eksperymentu. Przykładowe wyniki dla pojedynczego memrystora KNOWM (f).*

Otrzymane widma częstotliwościowe wskazują na dwubiegunowy charakter badanych memrystorów, gdyż wszystkie parzyste i nieparzyste wyższe harmoniczne są w widmach równie dobrze reprezentowane (Rys. 25b) W przypadku pojedynczego memrystora KNOWM zaobserwować można wyższe wartości całkowitego zniekształcenia harmonicznego przy częstotliwościach powyżej 10 Hz, zaś w przypadku obwodów synaps mostkowych całkowite zniekształcenia harmoniczne są głównie stałe (poza kilkoma przypadkami w zakresie niższych częstotliwości, Rys. 25c). Jest to wyraźna różnica pomiędzy memrystorami KNOWM a raportowanymi modelami teoretycznymi, gdzie wprowadzenie wzmacniacza różnicowego do synapsy mostkowej skutkowało znacznym zwiększeniem całkowitego zniekształcenia harmonicznego.

W ramach określenia kolejnych aspektów charakterystyki elektrycznej memrystorów KNOWM wykorzystano metody chronoamperometryczne do scharakteryzowania szumu w zakresie  $\pm 1$  V (krok pomiarowy: 100mV). Następnie przeprowadzono transformację Fouriera dla każdego potencjału DC w celu obliczenia widm szumu. W celu porównania charakteru szumu przy różnych potencjałach wyznaczono ich nachylenia (Rys. 25d-f). Ze względu na to, że wyniki prezentowane są w skali logarytmicznej, w celu rzetelnego dopasowania linii, konieczna jest interpolacja zarejestrowanych przebiegów, zmniejszenie gęstości punktów w celu uzyskania równomiernego rozkładu punktów danych we wszystkich zakresach częstotliwości. Generalnie widma szumu obserwowane w przypadku urządzeń KNOWM mają charakter różowy, opisany prawem potęgowym postaci:

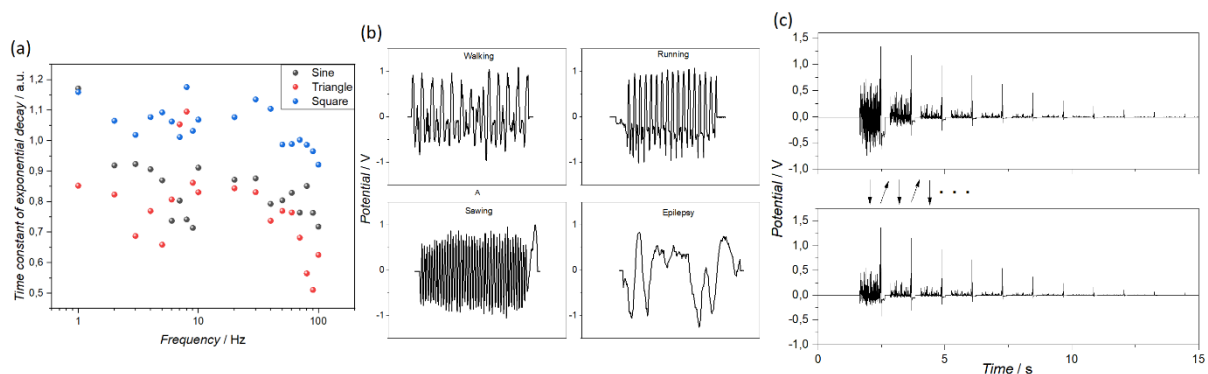
$$S_V(f) \propto \frac{1}{f^\gamma} \quad (15).$$

gdzie  $S_V(f)$  to widmowa gęstość mocy sygnału, a  $\gamma$  to parametr odzwierciedlający rodzaj szumu (0 dla białego szumu, -1 dla różowego i -2 dla brązowego). Widzimy, że szum termiczny memrystora KNOWM ewoluował od białego przez różowy do szumu brązowego, w zależności od przyłożonego potencjału DC i historii urządzenia. Podczas stopniowych zmian przyłożonego potencjału DC parametr  $\gamma$  zmieniał się od bliskiego zera przy niskich napięciach do -2 dla napięć wyższych niż ok. 0,5 V. Przy ok. 1 V (punkt przejścia z HRS do LRS) parametr szumu wzrasta stopniowo do zera wraz ze spadkiem napięcia (Rys. 25f). Zachowanie to sugeruje, że dynamika nośników ładunku w wielowarstwowych memrystorach KNOWM jest złożona i zależna od napięcia oraz od historii urządzenia. Zależność od napięcia może sugerować hoppingowe przewodnictwo elektronowe (co potwierdzało by przedstawiany powyżej mechanizm transportu elektronów poprzez aglomeraty Ag).

Warstwę rezerwurową analizowano bazując na pracy „Reservoir computing for sensing: an experimental approach”, gdzie porównywano stałe czasowe zaniku krzywych eksponencjalnych dopasowanych do uśrednionych wartości amplitudy wygaszanych sygnałów. Tym razem analizie poddano sygnały o trzech prostych kształtach (sinusoidalny, trójkątny oraz prostokątny). Otrzymany wynik potwierdza istnienie dwóch podstawowych wymagań dotyczących warstwy rezerwuaru: właściwości *separacji* i *uogólnienia* – sygnały o różnych

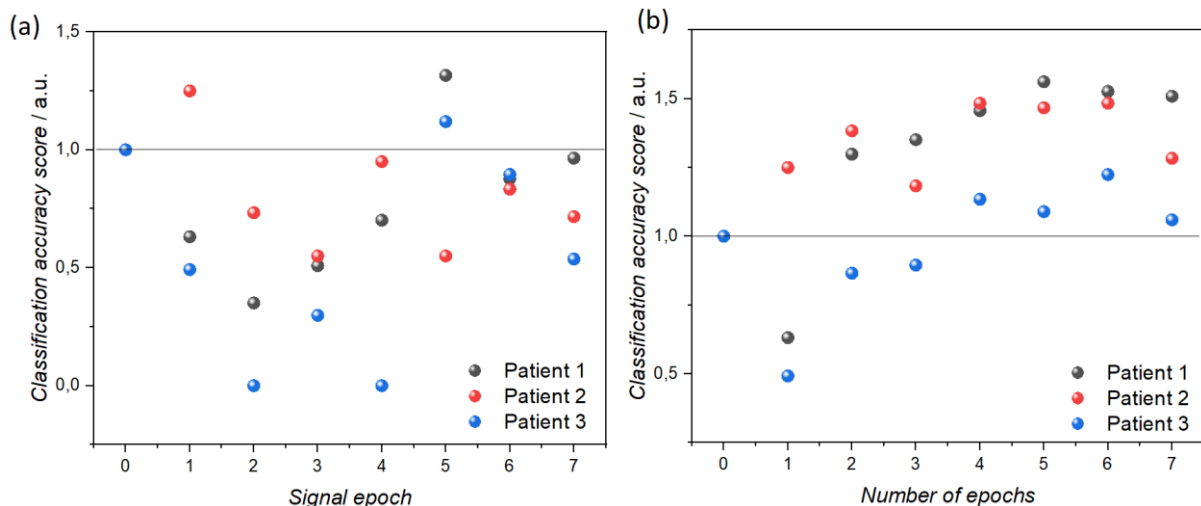
kształtach są rozdzielane przez system i ta separacja jest uogólniana w danym zakresie częstotliwości (z odchyleniami przy 1Hz oraz 5-9Hz).

Możliwości klasyfikacji i wpływ układu SNESM na ewolucję sygnału przetestowano w zadaniu mającym na celu rozpoznanie sygnałów reprezentujących napad padaczki. Analizowany zestaw danych (pobrane z repozytorium online) został zebrany od trzech różnych pacjentów za pomocą trójosiowego akcelerometru przymocowanego do dominujących dłoni, co jest powszechną techniką nieinwazyjnego i niezakłócającego życia sposobu monitorowania aktywności ruchowej. Zestaw danych zawiera 136 przypadków na pacjenta. Klasy zawarte w zbiorze danych to „chodzenie”, „bieganie”, „piłowanie” i „napad padaczkowy” (Rys. 26b). Zestaw danych zawiera szeregi czasowe o jednakowej długości. Celowo wykorzystano niewielki zestaw danych, ponieważ w przypadku podejścia polegającego na obliczaniu rezerwarowym system mógłby być kalibrowany indywidualnie dla każdego pacjenta.



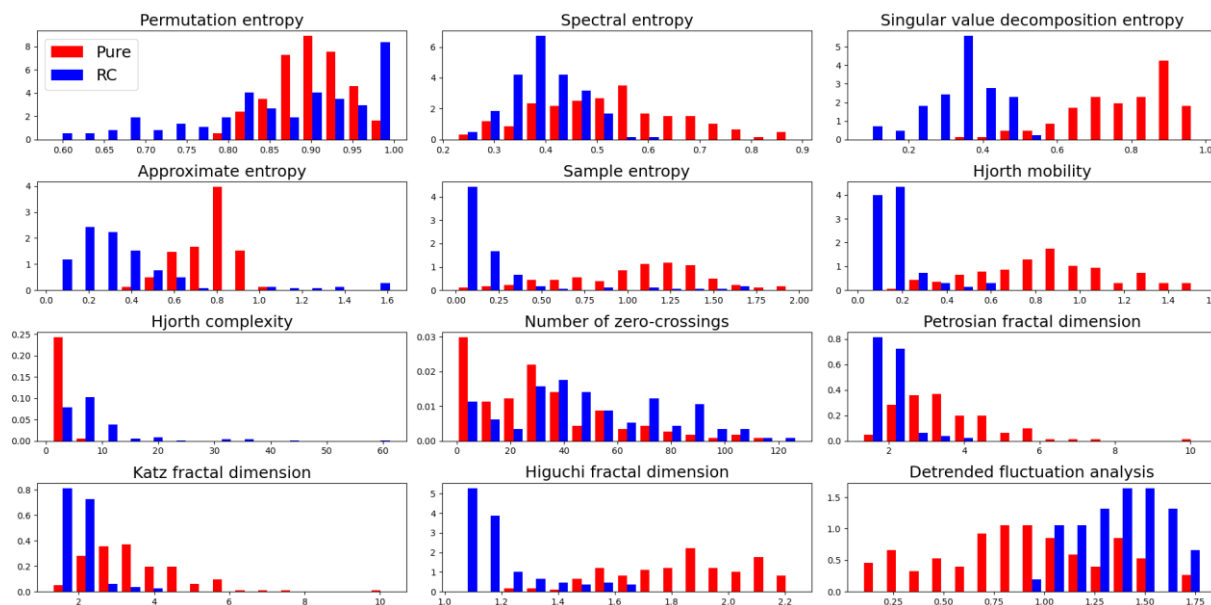
**Rysunek 26.** Zbiór wartości stałej czasowej zaniku wykładniczego dla trzech prostych kształtów sygnału tłumionych w układzie SNESM bazującym na synapsie mostkowej (a). Przykłady czterech klas sygnału z analizowanego zbioru danych (po standaryzacji) (b). Ewolucja sygnału w układzie SNESM (c). Najpierw sygnał sterujący przechodzi przez system, a następnie, po transformacji przez synapsę mostkową, jest opóźniony i zawracany ponownie na wejście układu. Strzałki wskazują kierunek przepływu danych.

Poszczególne echa sygnału (zwane epokami) otrzymane z układu SNESM (Rys. 26c) wykazują charakter stacjonarny, co zostało potwierdzone dwoma testami statystycznymi (*Augmented Dickey-Fuller* oraz *Kwiatkowski-Phillips-Schmidt-Shin*). Następnie na podstawie wszystkich poszczególnych epok sygnału obliczono 11 parametrów charakteryzujących jego złożoność, które posłużyły jako *cechy* do trenowania modelu uczenia maszynowego (dokładny opis parametrów złożoności sygnałów przedstawiono w materiałach dodatkowych do tej publikacji, jak również dokładniej w poprzedniej pracy „Towards Embedded Computation with Building Materials”). Zgodnie z założeniami obliczania rezerwarowego, wykorzystano prosty model klasyfikacyjny – drzewo binarne. Podobnie jak w przypadku pracy „Hardware realization of the pattern recognition with an artificial neuromorphic device exhibiting a short-term memory”, analizę powtórzono również dla nieprzetwarzanego sygnału wejściowego, który tak jak w poprzednim przypadku posłużył jako referencja.



**Rysunek 27.** Wynik oceny dokładności klasyfikacji (na podstawie parametru  $F$ -score) dla kolejnych epok sygnału (a) oraz dla kilku epok na raz (b). Liczba „0” symbolizuje nieprzetworzone dane wejściowe służące jako odniesienie.

Po kilku cyklach ewolucji sygnału system wykazuje poprawę dokładności klasyfikacji w porównaniu z danymi nieprzetworzonymi (epoka 5 dla pacjenta nr 1 i 3 oraz epoka 1 dla pacjenta nr 2, Rys. 27a). Gdy dane były analizowane zbiorczo, kilka epok na raz, uzyskano dalszą poprawę dokładności (Rys. 27b). Aby zilustrować i porównać działanie układu SNESM dla różnych pacjentów, wyniki znormalizowano w odniesieniu do dokładności klasyfikacji nieprzetworzonych danych, reprezentujących „1”. Ta metoda prezentacji danych pozwala na prostsze porównywanie zbiorów danych od różnych pacjentów, dla których początkowa dokładność klasyfikacji służąca jako odniesienie będzie się różnić.



**Rysunek 28.** Porównanie histogramów dla parametrów złożoności sygnału nieprzetworzonego („Pure”, zabarwiony na czerwono) i sygnału przetworzonego w układzie obliczania rezerwuarowego („RC”, zabarwiony na niebiesko) dla pacjenta nr. 1 (epoka nr 5 dla RC).

Aby zbadać zmiany w parametrach określających złożoność sygnału, porównano histogramy dwóch skrajnych przypadków – sygnału nieprzetworzonego i epokę nr 5 sygnału

przekształconego przez SNESM dla pacjenta nr. 1 (Rys. 28). Wybrano te sygnały, ponieważ dla tego przypadku można zaobserwować największą poprawę dokładności klasyfikacji dla pojedynczej epoki sygnału. Prawie wszystkie obliczone parametry złożoności wykazują wyraźne zmiany w ich rozkładzie (co za tym idzie, również w korelacji pomiędzy nimi), co może być jedną z głównych przyczyn usprawnienia omawianego zadania klasyfikacyjnego (poza zaletą rozszerzania zestawu danych przez system SNESM).

SNESM może okazać się przydatnym systemem przetwarzania sygnałów szeregów czasowych, zaprojektowanym w celu zwiększenia dokładności zadań klasyfikacyjnych. Wyniki charakterystyki memrystorów KNOWM i systemu SNESM opartego na synapsie mostkowej sugerują możliwość zastosowania takich systemów do innych zadań obliczeniowych i/lub klasyfikacyjnych (w warunkach skąpych zestawów danych i prostych modeli klasyfikacyjnych) ze względu na bogatą wewnętrzną dynamikę obecną w tych systemach wyrażoną zróżnicowanym całkowitym zniekształceniem harmonicznym oraz widmami szumowymi. Zróżnicowana filtracja i nieliniowa transformacja sygnałów o różnych kształtach w systemie SNESM to kolejna zaleta umożliwiająca klasyfikację sygnałów.

## Dorobek naukowy

Tabela 1. Publikacje naukowe

l.p.	Autorzy	Tytuł publikacji	Nazwa czasopisma	Numer tomu, strona (rok)
1.	Kacper Pilarczyk, Ewelina Właźlak, <b>Dawid Przyczyna</b> , Andrzej Blachecki, Agnieszka Podborska, Vasileios Anathasiou, Zoran Konkoli, Konrad Szaciłowski	Molecules, semiconductors, light and information: Towards future sensing and computing paradigms.	Coordination Chemistry Reviews	365, 23-40 (2018).
2.	Ewelina Właźlak, Andrzej Blachecki, Magdalena Bisztyga-Szklarz, Sylwia Klejna, Tomasz Mazur, Krzysztof Mech, Kacper Pilarczyk, <b>Dawid Przyczyna</b> , Maciej Suhecki, Piotr Zawal, Konrad Szaciłowski	Heavy pnictogen chalcogenides: the synthesis, structure and properties of these rediscovered semiconductors.	Chemical Communications	54 (86), 12133-12162 (2018)
3.	<b>Dawid Przyczyna</b> , Maria Lis, Kacper Pilarczyk, Konrad Szaciłowski	Hardware Realization of the Pattern Recognition with an Artificial Neuromorphic Device Exhibiting a Short-Term Memory.	Molecules	24(15), 2738 (2019)
4.	<b>Dawid Przyczyna</b> , Kacper Pilarczyk, Andrzej Blachecki, Vladimir Gorokh, Konrad Szaciłowski	New approaches towards chemosensing.	International Semiconductor Conference (CAS) IEEE	23-26 (2019)
5.	Andrew Adamatzky, Konrad Szaciłowski, Zoran Konkoli, Liss C Werner, <b>Dawid Przyczyna</b> , Georgios Ch. Sirakoulis	On Buildings that Compute. A Proposal.	From Astrophysics to Unconventional Computation, Springer	35, 311-335 (2019)
6.	<b>Dawid Przyczyna</b> , Sébastien Pecqueur, Dominique Vuillaume, Konrad Szaciłowski	Reservoir computing for sensing: an experimental approach.	International Journal of Unconventional Computing	14, 267-284 (2019)
7.	Ewelina Właźlak, <b>Dawid Przyczyna</b> , R. Gutierrez, G. Cuniberti, Konrad Szaciłowski	Towards synthetic neural networks: can artificial electrochemical neurons be coupled with artificial memristive synapses?	Japanese Journal of Applied Physics	59, S10801, 2020
8.	<b>Dawid Przyczyna</b> , Piotr Zawal, Tomasz Mazur, Marcin Strzelecki, Pierr-Luigi Gentili, Konrad Szaciłowski	In-materio neuromimetic devices: dynamics, information processing and pattern recognition.	Japanese Journal of Applied Physics	59, 050504 (2020)
9.	Ewelina Właźlak, Justyna Kalinowska-Tłuścik, <b>Dawid Przyczyna</b> , Piotr Zawal, Konrad Szaciłowski	Bismuth triiodide complexes: structure, spectroscopy, electronic properties, and memristive properties.	Journal of Materials Chemistry C	8 (18), 6136-6148 (2020)
10.	<b>Dawid Przyczyna</b> , Maciej Suhecki, Andrew Adamatzky, Konrad Szaciłowski	Towards Embedded Computation with Building Materials.	Materials	14 (7), 1724 (2021)
11.	<b>Dawid Przyczyna</b> , Maria Szaciłowska, Marek Przybylski, Marcin Strzelecki, Konrad Szaciłowski	Recognition of musical dissonance and consonance in a simple reservoir computing system.	International Journal of Unconventional Computing	17, (2022)
12.	Maria Lis, Shu Onuma, <b>Dawid Przyczyna</b> , Piotr Zawal, Tomasz Mazur, Kacper Pilarczyk, Pier Luigi Gentili, Seiya Kasai, Konrad Szaciłowski	From Oscillatory Reactions to Robotics: A Serendipitous Journey Through Chemistry, Physics and Computation.	Handbook of Unconventional Computing, World Scientific	1-79 (2022)
13.	<b>Dawid Przyczyna</b> , Grzegorz Hess, Konrad Szaciłowski	KNOWM Memristors in a Bridge Synapse delay-based Reservoir Computing system for detection of epileptic seizures.	International Journal of Parallel, Emergent and Distributed Systems	1-16, (2022)
14.	<b>Dawid Przyczyna</b> , Marcin Strzelecki, Gisy Abd, Lulu Alluhaibi, Kapela Pilaka, Konrad Szaciłowski	On communication, information, energy and music.	Unconventional Computing, Arts, Philosophy World Scientific	(2022)

Tabela 2. Udział w konferencjach

l.p.	Nazwa konferencji	Miejsce, termin	Tytuł prezentacji	Forma prezentacji	Autorzy
1.	6th International Conference on Multifunctional, Hybrid and Nanomaterials	Sitges, Hiszpania 11-5.03.2019	Photo-enhanced memristive effects realized in nanograined chrome yellow pigment	poster	<b>Dawid Przychyna</b> , Piotr Zawal, Kacper Pilarczyk, Konrad Szaciłowski
2.	23rd International Symposium on the Photochemistry and Photophysics of Coordination Compounds	Hong Kong 14-9.07.2019	Unusual photoelectrochemistry observed in photocatalytic 19th century yellow pigment	poster	<b>Dawid Przychyna</b> , Kacper Pilarczyk, Konrad Szaciłowski
3	2019 international semiconductor conference	Sinaia, Rumunia 9-1.09.2019	Artificial neuron as information pre-processing agent	talk	<b>Dawid Przychyna</b> , Maria Lisa, Kacper Pilarczyk, Konrad Szaciłowski
4	XIV Interdyscyplinarna Konferencja Naukowa TYGIEL 2022	Lublin, Polska 24-27.03.2022	Przetwarzanie sygnałów w układach rezerwurowego obliczania	talk	<b>Dawid Przychyna</b> , Konrad Szaciłowski

#### Kierowanie projektami naukowymi

- Grant NCN, PRELUDIUM 16, nr 2018/31/N/ST5/03112

Tytuł projektu: *“Roztwory stałe półprzewodnikowych tlenków potrójnych dla nowych struktur obliczeniowych - przełączanie rezystancyjne oraz właściwości synaptyczne”*

#### Zrealizowane staże naukowe

- Jednostka oraz osoba przyjmująca – University of the West of England UWE (Wielka Brytania, Bristol), prof. Andrew Adamatzky, dyrektor laboratorium obliczeń niekonwencjonalnych (08-29.05.2022)

#### Działania popularyzujące naukę

- Czynny udział w przygotowaniu pokazów podczas Festiwalu Nauki i Sztuki oraz Nocy Naukowców
- Współautorstwo artykułu popularnonaukowego w Biuletynie AGH 147/2020
- Współautorstwo artykułu popularnonaukowego w czasopiśmie LINKS (LINKs-series Special Edition 1 | Unconventional Computing) *„Information, communication and music”*
- Udział w koncercie muzycznym *„Oscylacje. Propagacje. Transformacje”* w ramach 45. Zjazdu Fizyków Polskich. Miejsce w przestrzeni publicznej: Opera Krakowska. Wystąpienie jako *The Nano Consort – Etiuda rezerwurowa nr 1* (członkowie zespołu: Kacper Pilarczyk, Dawid Przychyna, Marcin Strzelecki, Konrad Szaciłowski, Dominika Peszko, gościnnie – Piotr Zieliński)



## *Załączniki*

- Artykuły naukowe wchodzące w skład rozprawy
- Oświadczenia współautorów



*Artykuły naukowe wchodzące w skład rozprawy*





## Towards synthetic neural networks: can artificial electrochemical neurons be coupled with artificial memristive synapses?

Ewelina Wlazlak<sup>1\*</sup>, Dawid Przczyzna<sup>1,2</sup>, Rafael Gutierrez<sup>3\*</sup>, Gianaurelio Cuniberti<sup>3,4,5</sup>, and Konrad Szacilowski<sup>1\*</sup>

<sup>1</sup>Academic Centre for Materials and Nanotechnology, AGH University of Science and Technology, al. Mickiewicza 30, 30-059 Kraków, Poland

<sup>2</sup>Faculty of Physics and Applied Computer Science, AGH University of Science and Technology, al. Mickiewicza 30, 30-059 Kraków, Poland

<sup>3</sup>Institute for Materials Science and Max Bergmann Center of Biomaterials, Dresden University of Technology, D-01062 Dresden, Germany

<sup>4</sup>Dresden Center for Computational Materials Science (DCMS), TU Dresden, D-01062 Dresden, Germany

<sup>5</sup>Center for Advancing Electronics Dresden, TU Dresden, D-01062 Dresden, Germany

\*E-mail: ewlazlak@agh.edu.pl; rafael.gutierrez@tu-dresden.de; szacilow@agh.edu.pl

Received December 12, 2019; revised January 14, 2020; accepted March 9, 2020; published online March 30, 2020

The enormous amount of data generated nowadays worldwide is increasingly triggering the search for unconventional and more efficient ways of processing and classifying information, eventually able to transcend the conventional von Neumann–Turing computational central dogma. It is, therefore, greatly appealing to draw inspiration from less conventional but computationally more powerful systems such as the neural architecture of the human brain. This neuromorphic route has the potential to become one of the most influential and long-lasting paradigms in the field of unconventional computing. Memristive and the recently proposed memfractive systems have been shown to display basic features of neural systems such as synaptic-like plasticity and memory features, so that they may offer a diverse playground to implement synaptic connections. In this review, we address various material-based strategies of implementing unconventional computing hardware: (i) electrochemical oscillators based on liquid metals and (ii) mem-devices exploiting Schottky barrier modulation in polycrystalline and disordered structures made of oxide or perovskite-type semiconductors. Both items (i) and (ii) build the two pillars of neuromimetic computing devices, which we will denote as *synthetic neural networks*. We expect that the current review will be of great interest for scientists aiming at bridging unconventional computing strategies with specific materials-based platforms. © 2020 The Japan Society of Applied Physics

### 1. Introduction

In recent decades, we have witnessed an explosion of the amount of data accumulated in all spheres of human activity. The upcoming years may bring a new global problem, sometimes called “the information gap” or “information black hole”. It originates from the fact that mankind doubles the amount of stored data every two years, but processing and analysis involve only a small fraction of this collected data. The lack of analysis of this “information black holes” may bring to humanity many unexpected and poorly explained events.<sup>1,2</sup> The “Big Data” problem requires, therefore, effective theoretical and practical disruptive new methodologies of data processing and analysis. Contemporary silicon-based devices, based on the Turing architecture, cannot provide energy-efficient computing power to process this data.<sup>1,3</sup>

Today’s computer technologies, largely based on semiconductor materials, have an extraordinarily successful history. However, despite its unprecedented achievements, current classical computational paradigms encompass only a small subset of all computational possibilities.<sup>4</sup> There is a very broad class of computational substrates and environments, mainly physical systems, whose rich dynamics can be exploited as a computing medium.<sup>5</sup> Molecular electronics, which in principle should transfer classical electronics to the molecular scale and give unparalleled advantages as compared to silicon-based electronics, has not yielded any competitive technology so far; however, it has provided a unique insight into chemistry and physics at the single-molecule level.<sup>6,7</sup>

Therefore, alternative computing architectures and computational paradigms have to be explored, as well as different computational systems that can be combined into larger systems, an approach referred to as heterotic computing.<sup>8</sup> One of the most critical challenges for classical computing

today originates from the memory bottleneck and the high cost (in terms of time and energy) of constant data transfer from memory to CPU and vice versa, which is commonly termed as the von Neumann bottleneck. On the other hand, we encounter the extreme thermodynamic efficiency of the biological brain computing architecture, where information processing and storage are not physically separated processes. Therefore, the direct integration of information processing units and memory is an approach that would significantly reduce these bottlenecks, rendering computing much faster and more energy-efficient.

Unconventional methods of information processing are tempting, but their potential is not fully recognized yet. A special place among these new approaches is occupied by devices, systems, and ideas drawing inspiration from a highly sophisticated system: the brain. Neuromorphic solutions implemented by software engineers have started to revolutionize our world. Neural networks, machine learning, and artificial intelligence (AI) are in the main focus of the automotive and aviation industries as well as of companies specialized in Internet-related services. Whenever a large amount of data is produced and needs to be fast processed, neural energy-efficient deep learning algorithms and AI play a crucial role, e.g. in the aviation and automotive industry as autonomous control (Tesla, Porsche), or Internet applications as in face and speech recognition (Google Vision, Siri). These systems, however, are based on digital electronics, the neuromorphic computing features are realized software-wise, and they cannot mimic the extreme complexity of neural systems, neither in terms of structure nor complexity and performance. The hardware level is the next reasonable step which several companies: Hewlett-Packard (U.S.), IBM (U.S.), Intel Corporation (U.S.), Samsung Group (South Korea) are currently exploring.<sup>9–11</sup>

The current approach involving AI and deep learning algorithms, resembling the working of the human brain, is

based on traditional implementations on a software level, and sometimes also on CMOS implementations of neural architectures.<sup>12–16</sup> Deep learning relies on artificial neural networks that are typically executed on computers based on the conventional von Neumann architecture, operating mostly sequentially and based on Boolean logic.<sup>17</sup> In contrast, the brain's hardware operates in a massively parallel fashion through a densely interconnected physical network of neurons<sup>18</sup> and in an analog manner with diverse modes of information coding.<sup>19,20</sup>

## 2. Memristor-oscillator coupling: neuron-like hybrid system

The steps towards real AI should involve stochasticity and randomness, the prerequisites of creativity in natural systems. The stochasticity should be present at various levels of the neuromimetic structure—at the device and system level. It seems, therefore, that neuromorphic analog electronics, despite their noisy character, may turn out to be useful in numerous computing tasks. Among all elements, memristors and other memristive devices seem to be, at least temporarily, a viable computational alternative. Therefore, *in materio* computing, despite its drawbacks and obvious limitations, irrespectively of its implementation (memristive, spintronic, molecular), seems to be the only way to overcome various bottlenecks of conventional computing (Fig. 1).<sup>21–26</sup>

Memristors and other memristive (or memfractive, *vide infra*) devices bear memory features (volatile and non-volatile), synaptic-like plasticity, and nonlinear electric characteristics. These features are ideally suited for various information processing protocols, including neural networks, reservoir computers, random number generation, and cryptography, including physical unclonable functions. They are also suitable for electric signal transformations due to strongly nonlinear characteristics and the ability to generate higher harmonic frequencies. Their main drawback lies in their passive character—they can sink current and dissipate energy, but cannot source current, neither in a passive way (like capacitors and inductors) nor in an active way (like current sources).

Therefore, we propose here a hybrid information processing solution, which at the same time, will be functionally closer to the nervous system (Fig. 2). Along with memristive

synapses, we postulate the introduction of new types of elements that can source electric current in the form of pulses, either regular or chaotic/stochastic. Such elements should also respond to electrical signals applied in a way similar to living neurons, e.g. by changes in their pulsing frequency. A brief search over recent chemical literature brings candidates for this quest—electrochemical oscillatory processes.<sup>27,28</sup> Among the plethora of electrochemical oscillators those based on liquid metals: mercury, gallium and gallium-based alloys seem to be especially useful.<sup>29–32</sup>

The current perspective presents some ways of application of liquid metal-based artificial neurons and memristive synapses as two cornerstones of neuromimetic computing devices, for which we have coined the term *synthetic neural networks*. Liquid metal droplets are prone to both spontaneous and stimulated oscillations, which can be monitored by optical (change of shape and light reflectivity) and electrical (change in electrochemical potential, generation of galvanic current, etc.) methods. Due to the dynamic properties of these oscillations, we coined the term *synthetic neurons* to describe electrochemical oscillators, which are stimuli-responsive, as they may show neuron-like behavior. Furthermore, it was demonstrated (in the case of mercury) that oscillating metal droplets can be synchronized using a resistive coupling that regulates the degree of cooperation,<sup>33,34</sup> and these synchronized systems behave similarly to neural systems (e.g. they show various catastrophic synchronization modes).<sup>35</sup>

Both systems seem to be electrically compatible: memristors usually operate with voltages ranging from hundreds of millivolts with currents ranging from nanoamperes to milli-amperes, whereas electrochemical oscillators generate voltage amplitudes of hundreds of millivolts and can source at least microampere currents. The operating frequency of electrochemical oscillators reached hundreds of Hz at the maximum, so it is also well suited for semiconductor-based memristive devices.

The realization of the proposed hybrid devices and the synthetic neural networks requires three main building blocks: (i) memristors and (ii) electrochemical oscillators that operate in the specific time and potential scales, and (iii) theoretical models to describe the operation of the system. Significant work was already done in the topics mentioned above, especially in the field of memristive devices and

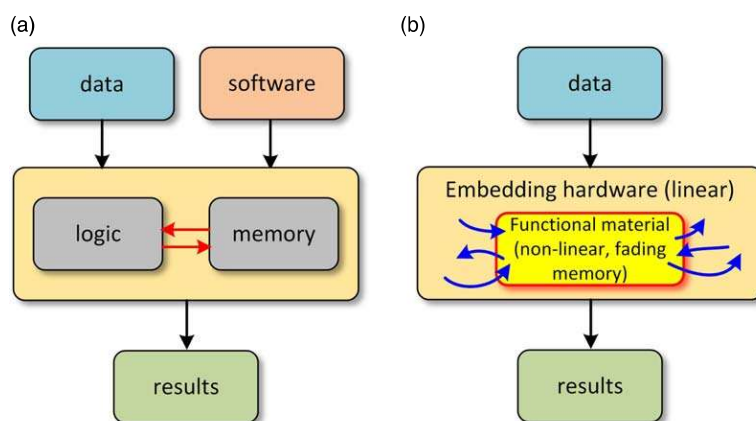


**Fig. 1.** (Color online) Cartoon representation of a classical von Neumann computing architecture (a) versus *in materio* computing system (b). Red arrows indicate the *von Neumann bottleneck* problem, whereas blue arrows show information transfer between the computing material and the interface/readout system.

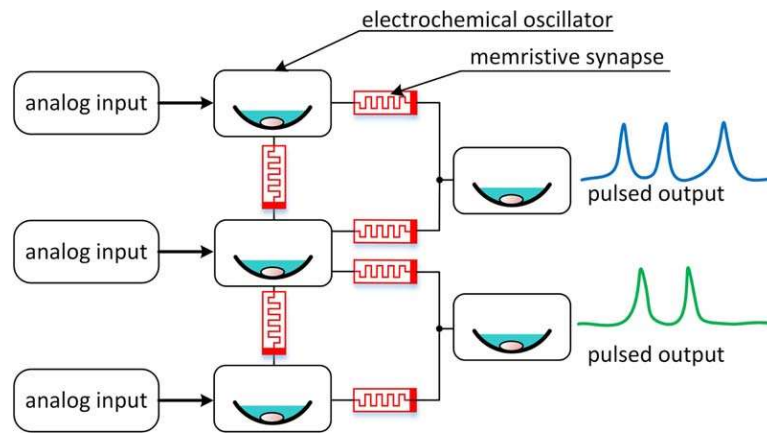


**Fig. 2.** (Color online) A tentative scheme of a memristively-coupled network of electrochemical oscillators. Depending on the state of the memristors (ON versus OFF), various coupling modes will be present in the network, leading to a plethora of time-varying output responses forced by analog inputs.

modeling of spiking neural networks. The main difficulty in the realization of the proposed concept will be the connection of all these pieces together. Attempts to create larger systems based on memristors or electrochemical oscillators have already been carried out (see Chap. 3). The analysis of this partial result is crucial in the design of memristor-oscillator coupled systems. Below, we briefly summarize the basics of essential elements that connected together should allow creating the new synthetic neural networks based on the neuron-like hybrid device.

**2.1. Memfractors, memristors and modeling**

A memristor is an element providing memory—a crucial factor in the *in materio* computing paradigm—and synapse-like plasticity to the hybrid memristor-oscillator device. A memristor, as the fourth fundamental passive electrical circuit element, was postulated by Leon Chua as early as 1971.<sup>36)</sup> For a long time it was considered only a scientific curiosity, but in 2008 for the first time, a physical device was linked to the memristor postulated by Leon Chua. R. S. Williams and coworkers at the HP labs presented a device based on a thin layer of TiO<sub>2</sub> sandwiched between Pt contacts,<sup>37)</sup> which showed the expected pinched hysteresis loop predicted in L. Chua’s work. A memristor (memcapacitor, meminductor, or, more generally, a memristive element) is a passive, nonlinear circuit element the properties (resistance, capacitance, or inductance) of which depend on the element’s history and the total electric charge that has passed through the element in particular. For instance, in the case of an ideal, current-driven memristor, its constitutive equations can be written in a generic way as (1)–(3):<sup>38)</sup>

$$U(t) = M[q(t)]I(t), \tag{1}$$

$$q(t) = \int_{-\infty}^t dF(\tau), \tag{2}$$

$$M[q(t)] = R_{OFF} \left( 1 - \frac{R_{ON}}{\beta} q(t) \right). \tag{3}$$

Here,  $U(t)$  is the voltage across the element,  $I(t)$  is the current,  $M$  is the *memristance* (charge-dependent resistance),  $q(t)$  is the electric charge that flew through the device up to time  $t$ , and  $R_{ON}$  and  $R_{OFF}$  are resistances in the so-called low-resistive and high-resistive conducting states, respectively. In this way, a

memristor can remember its history since its resistance is a function of the total charge that passed through the device. More importantly, if the current is switched off, the memristance value remains unchanged. The memristive properties displayed by various solid-state devices can be a consequence of several dynamical physical and chemical processes, including the formation of conductive filaments,<sup>39–41)</sup> the migration of ions and/or dopants,<sup>42)</sup> or the modulation of Schottky barrier heights.<sup>43,44)</sup> Hence, physically meaningful modeling of a memristor needs to take into account the specific underlying physical mechanism(s).

The latter of the cases mentioned above—Schottky barrier modulation—is especially relevant due to the simplicity of the Schottky junction fabrication; however, it is the rarest case of all memristive devices reported so far.<sup>44–46)</sup> The fabrication of a Schottky junction is a complex problem involving interactions between contacted materials at the atomic level.<sup>47,48)</sup> Therefore, previously proposed, simplistic models taking into account only macroscopic parameters (e.g. the work function<sup>47,48)</sup>) cannot yield reliable predictions of Schottky barrier parameters. For instance, the formation of metal-induced gap states (MIGS) within the bandgap can sensitively alter the local electronic structure at the interface. Thus, depending on the charge neutrality level, MIGS can exhibit both donor or acceptor-like properties.<sup>49–51)</sup> Mem-devices, based on a Schottky junction, have more complex characteristics than ideal memristors (Fig. 3). The main difference is usually observed as an asymmetry of the hysteresis loop. These devices display synaptic plasticity, but to the best of our knowledge, their dynamic is different from currently implemented devices in large neuromorphic systems.

Despite intensive experimental and theoretical works on memristive devices, they are still far from being fully understood and characterized, mostly due to the variability in the physical control parameters as well as in the underlying microscopic mechanisms leading to a display of memory effects in the devices. The most striking aspect is that the simple analytical description given by Eqs. (1)–(3), which originates from dopant diffusion mechanisms, as well as other analytical and numerical models of memristors reported so far, cannot accurately predict the  $I/V$  characteristics and features of real memristive devices.

This has been the motivation to attempt a further theoretical generalization of memristive elements, which promises

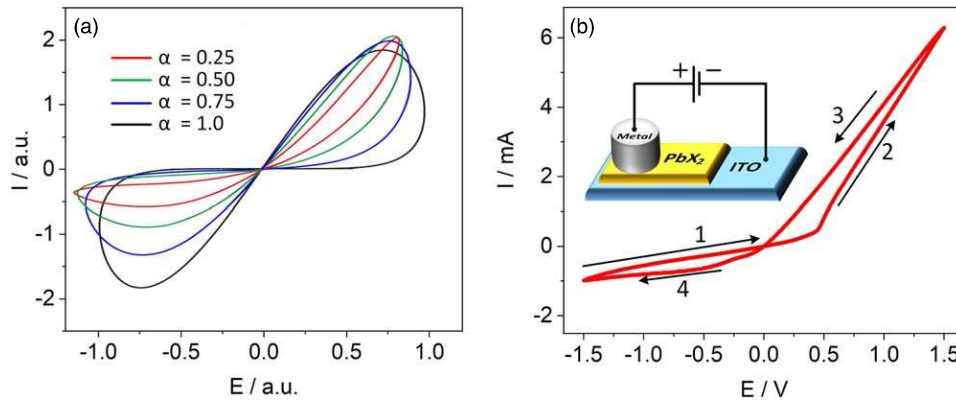


**Fig. 3.** (Color online) Pinched hysteresis loops for a charge controlled memristor for various values of the fractional-order  $\alpha$  and a constant  $\beta = 1$  value [cf. Eq. (6)], adapted from Ref. 52 (a). The case  $\alpha = 0.25$  (red curve) has a much closer similarity to the experimentally observed Schottky barrier in lead halide memristors (b). Adapted from Ref. 53.

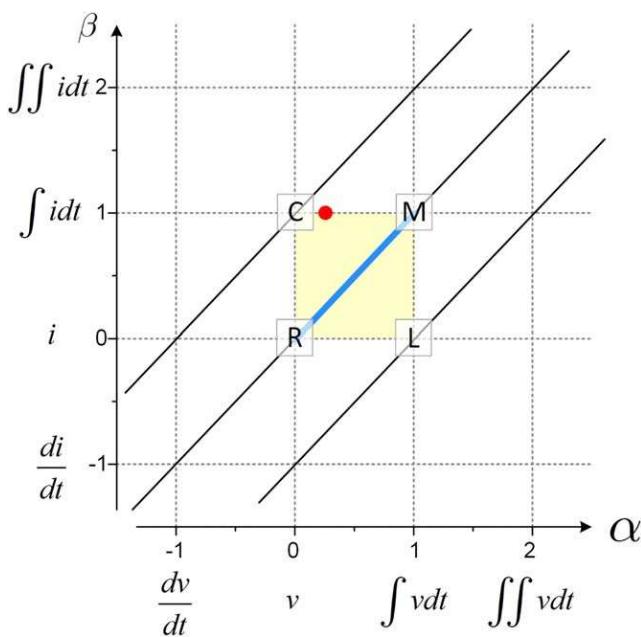


**Fig. 4.** (Color online) A fragment of a periodic table of memristive circuit elements defined on the space of the order of differential operators. *R* stands for a resistor, *C* for a capacitor, *L* for inductor, and *M* for memristor. The yellow area indicates the devices of interest discussed in this paper. The red dot indicates the position of a  $1/4$ -order memfractor from Fig. 3, whereas the thick blue line across the yellow area indicates the simplest memfractive elements that cannot accumulate energy; however, they still provide memory features significant for signal and information processing.

to achieve a closer connection with real experimental setups. This approach, presented by M. Abdelouahab, R. Lozi, and L. Chua, assumes non-integer order differential operators,<sup>54,55</sup> i.e. instead of using first-order ordinary differential equations it exploits the concept of fractional derivatives and fractional integrals to gain flexibility in the description of memory effects. Without entering into mathematical details, a fractional derivative (in the so-called Riemann–Liouville sense) is defined through the expression (4):<sup>56</sup>

$$a D_t^\alpha f(t) = \frac{1}{\Gamma(n - \alpha)} \frac{d^n}{dt^n} \int_a^t \frac{f(\tau)}{(t - \tau)^{1+\alpha-n}} d\tau, \quad (4)$$

with  $\alpha$  being the fractional order of the operator,  $n = \text{int}[\alpha]$ , and  $\Gamma(\cdot)$  is the Gamma function given by (5):

$$\Gamma(z) = \int_0^\infty x^{z-1} e^{-x} dx. \quad (5)$$

The range of temporal correlations can be tuned by the power-law integral kernel  $(t - \tau)^{-1-\alpha+n}$ .

Based on this approach, L. Chua<sup>55</sup> and others<sup>52,57</sup> extended the definition of memristors and other similar mem-devices, introducing the concept of memfractance  $F_M^{\alpha\beta}(t)$ , ( $\alpha, \beta \in \mathbb{R}$ ) and a generalized formulation of Ohm’s law in terms of fractional derivatives (6):

$$v(t) = D_t^{1-\alpha} (F_M^{\alpha\beta}(t) D_t^{\beta-1} i(t)). \quad (6)$$

Depending on the values of  $\alpha, \beta$  the standard capacitance, resistance, and inductance can be recovered as well as intermediate circuit elements displaying combinations of the previous basic elements (Fig. 4). Using fractional derivatives to describe the memristor dynamics (thus defining a fractional-order memristor or memfractor) makes the theory not only mathematically elegant, but it also provides much better control over the shape of the pinched hysteresis loop (see Fig. 3), i.e. it allows to achieve a more accurate description of memristive behavior in realistic devices.<sup>52,53</sup>

We remark that fractional calculus has also been extensively applied to describe anomalous diffusion processes in disordered media,<sup>58–60</sup> as well as to other natural phenomena displaying power-law scaling in their temporal behavior, see e.g. thereviews by Chen et al.<sup>61</sup> and B. J. West.<sup>62,63</sup> Fractional calculus is thus conceptually consistent with charge carrier transport in materials with randomly distributed charge traps, where power-law behavior may emerge in a natural way. We notice, however, that directly applying Eq. (4) to model memfractor behavior in specific materials seems rather difficult due to its very generic character, so that memfractive behavior has only been described in a very phenomenological way using e.g. simple series expansions in the powers of the electric charge, see Refs. 55, 64 for typical examples.

One of the possibilities of formal realization of memfractors involves networks of first-order memristors [cf. Eqs. (1)–(3) and Fig. 5], with a memfractance order  $\alpha$  depending on the network topology. In an example shown in Fig. 5, a  $1/2$ -order memfractor is built from first-order memfractors [i.e.  $(\alpha, \beta) = (1, 1)$  memristors].<sup>57,65,66</sup> More practically, an approach used for other types of fractional



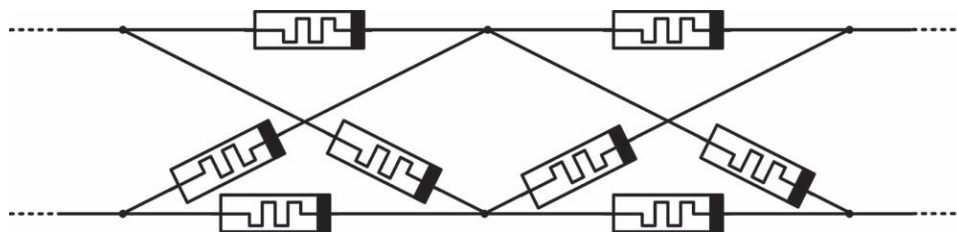


Fig. 5. (Color online) An equivalent circuit comprising of ideal memristors with a property of  $\frac{1}{2}$ -order memfractance. Adapted from Ref. 57.

circuit elements can be applied with modifications, e.g. capacitor-like devices containing conducting particles dispersed in adielectricmatrix or so-called constant phase elements realized in electrolyte-based devices.<sup>64)</sup>

Therefore, we expect that polycrystalline, highly disordered semiconducting materials with a complex conductivity mechanism or appropriate arrangement of trap states materials may display memfractive properties. Aspeci fic example of a material class where the concept of memfractance should find an immediate embodimentare polycrystalline and disordered structures based on oxide or perovskite-type semiconductors or other microcrystalline materials (Fig. 6). In such materials, each crystallite (especially if in contact with the metallic electrode) may work as an individual memristor. Therefore, the bulk of the materials may be considered as a complex, percolated network of memristive elements with complex charge transport properties,<sup>67–73)</sup> in which the memfractive properties should emerge. The observed discrepancies between experimentally recorded and simulated  $I$ - $V$  curves (cf. Fig. 3)<sup>74)</sup> may be a hint that the devices based on disordered structures are much closer to memristive networks (i.e. memfractors) than to ideal memristors.

Numerous semiconducting materials, including lead iodide,<sup>53)</sup> methylammonium iodobismuthates,<sup>75)</sup> and tin mixed ligand complex  $[\text{SnI}_4\{(\text{C}_6\text{H}_5)_2\text{SO}\}_2]$ <sup>76)</sup> display highly asymmetric hysteresis curves in ITO/semiconductor/Cu structures. Theses shapes are very similar to theoretically

obtained characteristic hysteresis curves of memfractive elements with  $\alpha = \frac{1}{4}$  and  $\beta = 1$  as defined by Eq. (6) (cf. Fig. 3). Furthermore, these junctions exhibit well-developed synaptic plasticity and follow typical Hebbian-like learning patterns, but their learning profiles are highly asymmetrical (an example shown in Fig. 7). In the studied case, the depression mode of synaptic weight change was by ca. one order of magnitude smaller than the corresponding synaptic weight increase in the potentiation mode.<sup>75)</sup>

Coming back to the modeling of memristive devices, most of the work carried out so far has primarily focused on representing memristors by general phenomenological models which reflect the electrical response of a memristive device regardless of its physical structure or material composition.<sup>77–80)</sup> Atomistic modeling has not been used very often and has mostly focused on the broad class of resistance switching related to vacancy migration in solid-state memristors, cf. Ref. 81 for an overview associated with valence change materials. Still, they have contributed to shed light on some microscopic, materials-related aspects of memristive behavior. Thus, Williams et al. used molecular dynamics (MD) simulations to investigate systems with oxygen vacancies driven by an external voltage.<sup>82)</sup> The obtained results showed a competition between short- and long-range interactions among the oxygen vacancies, leading short-range ordering and mimicking memristor polarity inversion. Similar MDsimulations highlighting other aspects of memristive behavior and ion dynamics can be found in

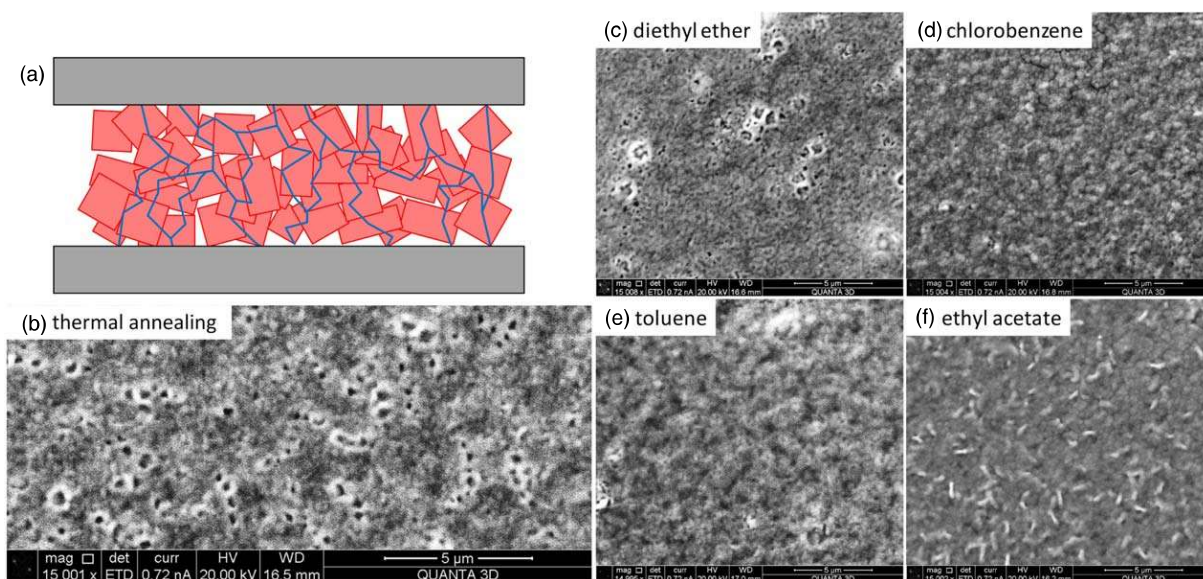
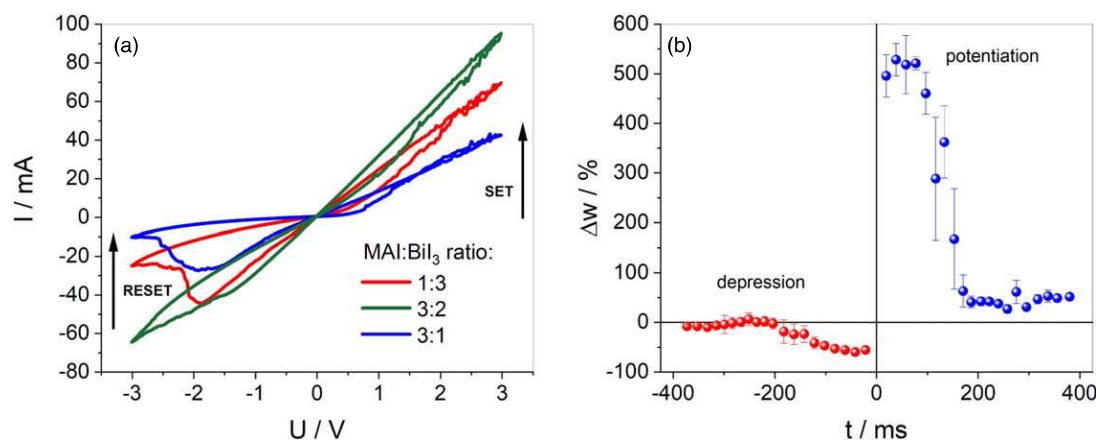


Fig. 6. (Color online) A cartoon illustrating the structure of a non-ideal memristor based on a polycrystalline material. Blue lines indicate some selected percolation pathways (a). SEM images on methylammonium triiodoplumbate thin layers on ITO glass obtained via thermal annealing (b) or in the presence of four different antisolvents (c)–(f). SEM images courtesy Tomasz Mazur and Piotr Zawal.



**Fig. 7.** (Color online) Asymmetrical pinched hysteresis loops recorded for methylammonium iodobismuthate layers with various methylammonium iodide (MAI) and bismuth iodide ratios (a) and the spike-timing-dependent plasticity for the 3:1 material (b). Adapted from Ref. 75 with permission of The Royal Society of Chemistry.

recent literature.<sup>83,84</sup> Access to longer time scales relevant for vacancy dynamics can be reached via kinetic Monte-Carlo (kMC) simulations. A kMC approach was used to investigate structural configurations of a  $\text{TiO}_2$  memristor, with a focus on oxygen vacancy migration under an externally applied voltage.<sup>85</sup> The authors found that vacancy hopping-induced localized electric fields seem to play an important role in the structural evolution of the filaments. Interestingly, using density-functional theory (DFT), they found that filament induced gap states can emerge, leading to an insulator-metal transition during the filament formation process. Further DFT-based investigations of structural and thermodynamic features of vacancies in various memristive systems were presented recently.<sup>86–89</sup>

Phenomenological models, on the other side, are clearly sufficient for circuit-level simulations but are limited to specific switching mechanism(s) of the memristor and include various physical parameters that describe the active material characteristics in the device, thus reflecting potentially different switching mechanisms. We believe that a thorough understanding of atomic-scale processes leading to memristive behavior is fundamental in order to optimize material properties and help in the design of memory-based devices. Moreover, bridging atomistic information, encoding material properties, with phenomenological memristor (or more general memfractor) models represents a formidable challenge to modeling approaches, which deserves to be addressed in order to open the road for rational materials design.

A fascinating aspect of memristive elements, going beyond their relevance in circuit design, is that they can be considered as an electronic equivalent of a synapse. With that in mind, various applications for signal processing and classification have been developed.<sup>90–92</sup> Memfractive devices should share similar features; moreover, they should exhibit much better flexibility and memory features, as the character of the hysteresis loop should be tunable by structural parameters of the material (cf. Fig. 2).

## 2.2. Electrochemical spiking neurons

The second part of the hybrid synthetic neuron is an electrochemical oscillator that connected to the memristor will modulate the resistive state of the former with periodic spikes. The famous Hollywood movie “Terminator 2:

Judgment day”<sup>93</sup> presents a science-fiction vision of liquid metal-based technology, soft robotics, and AI. Due to the unusual properties of room temperature liquid metals, they are the basis of emerging technology—liquid metal soft robotics.<sup>29</sup> This technology is based on mercury (the only room temperature liquid metallic element), gallium (melting point of  $29.7^\circ\text{C}$ ), and gallium-based alloys (Ga–In eutectic, galinstan) with melting points in the range of  $11^\circ\text{C}$ – $16^\circ\text{C}$ . The main features of liquid metals that are explored in this context are high electrical conductivity, low viscosity (only twice the viscosity of water), and variable surface tension: high for metals with pure surface and decreasing dramatically in the presence of oxidized layers at the surface. Along with the electrocapillarity effect, this creates the possibility of shape and movement control of metallic droplets due to changes in the properties of the metal-electrolyte interface.<sup>94–97</sup> Whereas the mechanical properties of liquid metal interfaces are deeply explored, and new technologies based on this foundation have emerged, the information-related aspects of these phenomena have remained, until recently, unexplored. Last year, a report on maze solving by liquid gallium droplets has been published.<sup>98,99</sup> The cited papers, remain, however, almost the single example of high-level information processing utilizing liquid metal “hardware”.

The relation between surface tension and the electric potential of the liquid metal surface was first described by Lippmann in 1873,<sup>100</sup> and the phenomenon is referenced as the electrocapillarity effect. The “mercury beating heart”—a classical chemical experiment is a beautiful and convincing demonstration of the electrocapillarity effect.<sup>32</sup> In this experiment, a mercury drop is placed in an acidic solution of an oxidizing agent (e.g. potassium chromate or potassium permanganate) and touched with an iron nail. The mercury droplet starts to shrink and spread periodically—the “mercury heart” starts to beat. The same process (but with a different rate or character of oscillations) can be observed in acidic electrolytes with dissolved oxygen and with other reactive metals, either in direct contact with a mercury drop or connected with it by tungsten wire. Two phases can be distinguished in the cycle: (i) oxidation in a moderately acidic medium result in the formation of mercury oxide islands (and subsequently a compact layer), which significantly reduces

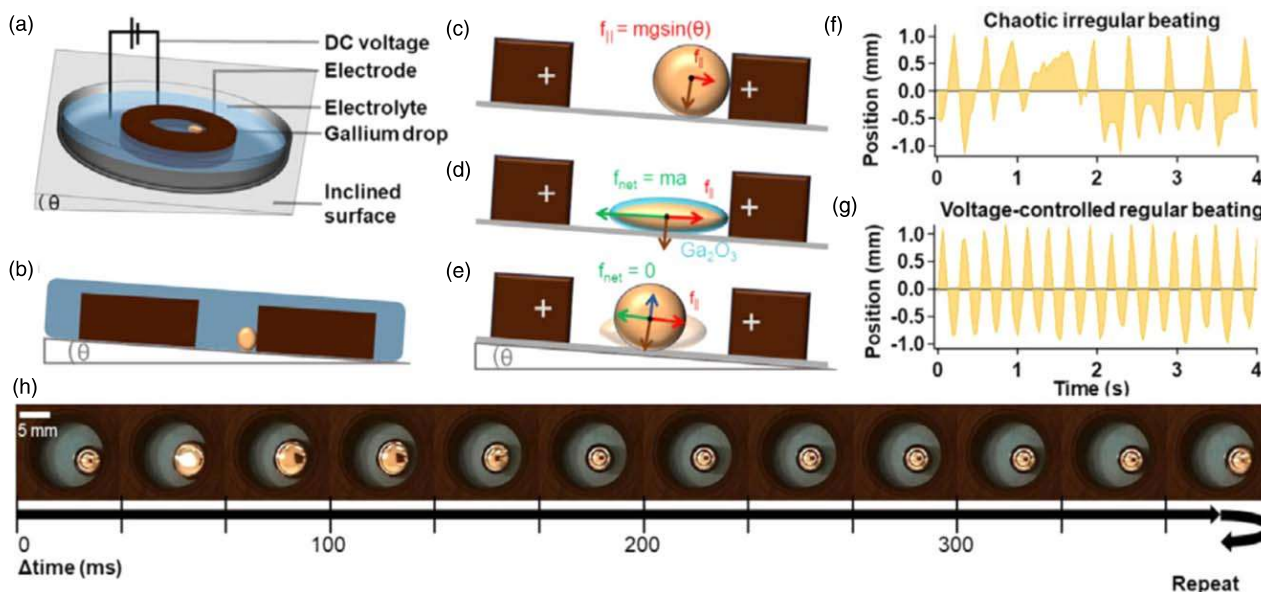
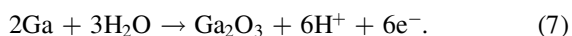


**Fig. 8.** (Color online) Schematic diagram of the experimental setup for the gallium oscillations (a). Cross-section of the inclined apparatus (b) and a force diagram of the gallium heartbeat sequence (c)–(e). Time course of chaotic motions occurring for certain drop sizes, or once the stabilizing voltage is removed (f). Regular periodic oscillations under a constant DC voltage observed for the 50 μl gallium drop (g). At the bottom, a series of photographs captured from the video shows the cycle of a heartbeat for the 50 μl drop (h). Reproduced from Ref. 101 with permission. Copyright American Physical Society, 2018.

the surface tension of a mercury drop, that gradually spreads at the bottom of the vessel. (ii) At some point, it touches a piece of iron (or other active metal), and the surface oxide layer undergoes rapid reduction. The reduction is accompanied by a swift increase in surface tension, which makes the drop to shrink. These spontaneous oscillations repeat until the reagents (oxidant in the solution and the reducing metal) are consumed. The frequency of oscillations strongly depends on several factors including the volume of the metal drop, the composition of the electrolyte, type of active metal and its exposed surface, temperature, etc.<sup>31,32</sup>

Placing of a mercury drop between graphite electrodes and applying an external potential difference is another way to induce electrochemical-mechanical oscillations.<sup>30</sup> Oscillating metal drops generate electrical signals of amplitude up to ca. 1 V because they serve at the same time as galvanic cells. Very recently, electrochemically induced oscillations were observed in the case of molten gallium,<sup>101,102</sup> whereas galinstan and gallium–indium eutectic alloys should behave similarly.<sup>103</sup>

Application of a constant DC bias to graphite ring electrode placed on inclined support induces strong and persistent oscillations of gallium droplets (Fig. 8).<sup>101</sup> In the first step, the gallium droplet stays in contact with the electrode. If the electrode potential is higher than the standard electrochemical potential of gallium, the droplet gets oxidized at the surface according to reaction (7):



The gallium oxide layer thus formed acts as a surfactant, significantly decreasing the surface tension of liquid gallium. This results in the rapid spreading of the droplet at the inclined bottom of the cell and loss of electrical contact with the ring graphite electrode. Subsequently, the oxide layer is etched by an acidic or basic electrolyte. Removal of the oxide layer restores the high surface tension of molten gallium, which retains spherical shape, comes into contact with the

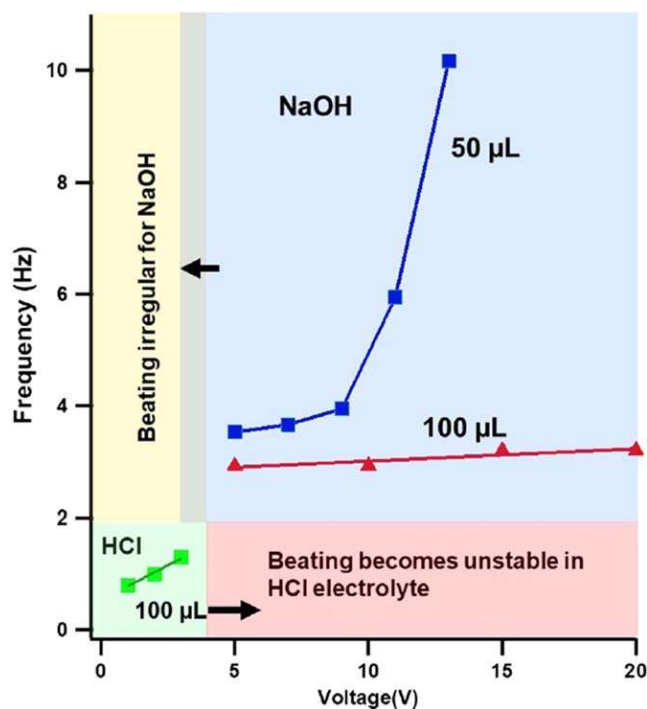


**Fig. 9.** (Color online) The beating frequency of a gallium droplet in NaOH and HCl electrolytes. Different threshold voltages are required to initiate beating in the acidic or basic electrolyte. Reproduced from Ref. 101 with permission. Copyright American Physical Society, 2018.

electrode, and the cycle starts over. The frequency of gallium DC voltage-forced oscillations strongly depends on the volume of the droplet, applied voltage, and electrolyte composition (Fig. 9). Depending on the applied forcing DC voltage and composition of the electrolyte, two different types of behavior can be observed: irregular, chaotic oscillations [Fig. 8(f)], and periodic oscillations [Fig. 8(g)]. The full map of various oscillatory modes is presented in Fig. 9. The most important feature of the studied system from the point

of view of neuromorphic information processing is the potential-induced controlled transition between chaotic and periodic modes. This allows us to define two dynamic states of the system. Furthermore, the periodic oscillations can be tuned over a certain frequency range. Such a feature makes the liquid metal electrochemical oscillator similar to a living neuron—the low-frequency background activity can be switched into periodic oscillation with a frequency depending on the intensity of the stimulus.

Upon application of an AC forcing signal, various oscillatory modes can be obtained, which are characterized by various shapes of oscillating metal drops and also accompanied by various electrical outputs.<sup>104)</sup> Different topological modes of these oscillations usually generate specific signal patterns, which are best reflected in the complex Fourier spectra of the recorded electrochemical signals.<sup>105)</sup> Moreover, electrically agitated liquid metal drops have already found application as unconventional circuit elements, but so far have not been coupled with the memristive device.<sup>106,107)</sup>

### 2.3. Models of neuronal information processing

The human brain is definitely the most complex information processing system. Its unprecedented complexity is a result of approximately  $10^{11}$  neurons connected into an extremely complex dynamic network with ca.  $10^{14}$  synapses.<sup>108)</sup> Each neuron collects information from numerous synapses, and depending on its own characteristics and the input (rate, amplitude, and time sequence of input spikes), it generates the output spike. Whereas the triggering of the action potential and propagation of signal along the axon is an electrical phenomenon, the information transfer and processing at synapses level relies on various chemical information carriers: neurotransmitters. Further complication originates from the fact that there are numerous types of neurons with various characteristics, and there are numerous types of synapses and neurotransmitters.

One of the goals of the proposed hybrid device is to create a more complex synthetic neural network. This system, due to the presence of a spiking oscillator and memristor introducing plasticity, will be considered as a neuromorphic hybrid device. The modeling of the operation of the new type of network is one of three crucial components in the road to the application of such a system.

The development of the modeling of neural processes involves three phases, with increasing complexity and accuracy of modeling. The simplest networks are feed-forward neural networks—systems mimicking the neural information processing based on a basic learning principle—modulation of synaptic weights between nodes and unidirectional information flow. The first, least advanced model is a perceptron—a first-generation neural network (Fig. 10). It contains one input layer and one or more processing nodes.

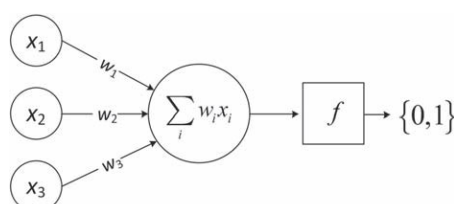


Fig. 10. Schematic structure of a single unit perceptron network.

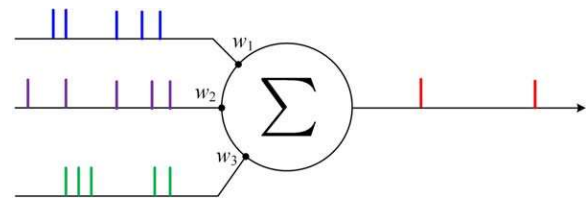


Fig. 11. (Color online) Schematic structure of single-unit spiking neural network.

Each node calculates the weighted sum of inputs (8) and uses a simple threshold function (9) to generate the output, which has a binary character. Learning of the perceptron is achieved by updating all weights when known data are fed into the input in order to minimize the classification errors.

$$s = \sum_i w_i x_i \tag{8}$$

$$f(s) = \begin{cases} 0, & \text{if } s > T \\ 1 & \text{otherwise} \end{cases} \tag{9}$$

A more advanced approach (second generation neural networks) is based on the same geometry (connectivity) as the perceptron, but (i) it may contain more layers and (ii) it uses as an activation a logistic function (10) instead of a threshold function:

$$f(s) = \frac{1}{1 + e^{-s}}. \tag{10}$$

This allows the generation of a continuum of output values and opens the possibility of multilayer architectures. Various activation functions can be used in different layers of the network; furthermore, a continuum of output states can be further processed using fuzzy logic approaches.<sup>109)</sup>

The third, most advanced model of neural information processing is based on spiking neuron models (Fig. 11).<sup>108)</sup> Whereas the former models operate with information encoded in the amplitudes of inputs, the third-generation model is sensitive to the duration and time sequence of events, with the role of synaptic weights similar to those of the previous two generations.

Numerous mathematical models of spiking behavior can be applied, from the Hodgkin–Huxley,<sup>110)</sup> leaky integrate-and-fire, Izhikevich,<sup>111)</sup> Thorpe, and spike response models.<sup>108)</sup> The common feature of all these models is their internal dynamics, leading to the generation of output spikes upon appropriate input conditions. These models also enable modeling of various coding approaches, such as the rate (frequency) coding and pulse coding. In the first approach, the number of spikes within a defined time window encodes relevant information. In the second one, the exact time interval between subsequent events is the main carrier of information. Spiking neural networks also offer spike-timing dependent plasticity and spiking-rate dependent plasticity—two main components of natural learning mechanisms within the Hebbian learning paradigm.<sup>112)</sup> These networks are not purely reactive, but also respond to the time sequence of events and therefore have a higher form of internal memory.

The highest level of performance can be achieved when the nodes of a network possess internal dynamics, e.g. when the activation function of the nodes varies in time. The simplest case of a dynamic neural network would be a

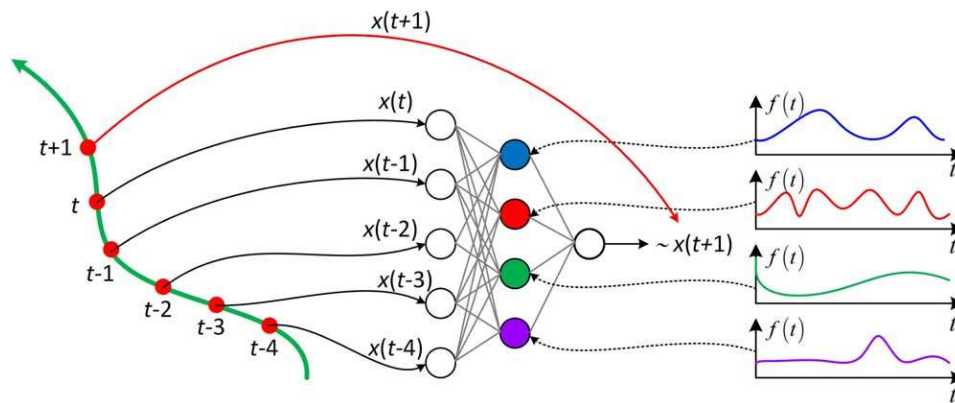


**Fig. 12.** (Color online) Schematic structure of a feed-forward neural network with nodes presenting time-dependent activation functions. Such a network can be used to predict the future dynamics of systems based on the system's history. Known trajectory at several points of time ( $t - 4, t$ ) serves a basis for approximate prediction of system dynamics at  $t + 1$ . Adapted from Ref. 114.

perceptron-like system with a periodic change in the activation function of a single node in the network. In this case, the network automatically would become a phase- and frequency-sensitive filter operation in a similar way to a comb filter.<sup>113</sup> Any time-dependent periodic input signal will be processed by nodes with a periodically varying activation function. Therefore, if the input frequency is commensurate with the eigenfrequency of the node, a positive interference will occur, and the two oscillations will be phase-matched. A network with numerous time-varying nodes would be capable of analysis of the time sequence of events and prediction of the future of input dynamics (Fig. 12).<sup>114</sup> In this case, each node can extract one characteristic dynamic feature, and the combination of these features at several different time scales (defined by the rate of activation function variability) will be used for trajectory prediction.

Taking into account the quality and reliability of software spiking neural networks, it seems reasonable to look for experimental approaches towards them. While perceptrons and feed-forward networks can relatively easily be implemented with memristors (for details of memristors and their models see Sect. 2.1 of this review), there are no physical realizations of artificial spiking neurons operating in a way similar to living neurons and based on hardware platforms different from standard CMOS technology. The photoelectrochemical neurons<sup>115</sup> reported so far have demonstrated their utility in certain pattern recognition tasks, including classification of hand-written digits.<sup>116</sup> Therefore there is an urgent need to develop spiking neuron hardware models based on unconventional substrates compatible with memristive synapses and other *in materio* computational systems.<sup>117</sup>

### 3. First steps toward larger systems

The idea of a hybrid memristor-electrochemical oscillator device is new, and up to our knowledge, it has not been realized so far at software or hardware level, neither as a single device nor in arrangements of individual components. Nonetheless, first attempts to create more complex systems with memristors or electrochemical oscillators have been made.

#### 3.1. Memristive reservoirs

Recently, the hardware implementation of complex memristive systems, especially reservoir systems, has attracted increasing attention.<sup>118,119</sup> The main advantage of reservoir

computers (as compared to, e.g. feed-forward and recurrent neural networks) is the randomness of internal connections. Another advantage of reservoir systems is their flexibility: they allow effective processing of time-varying inputs and extract different features from large data sets by application of appropriate driving signals. Moreover, the application of delayed feedback may also convert simple neural networks or even single node synaptic/memristive devices into echo state machines, which are a specific kind of reservoir computer, as shown in Fig. 13(b).

Primarily, reservoir computing (RC) was developed to address the issue of the high computational cost of recurrent network training. Two forms of RC were independently developed, namely Echo State Network (ESN)<sup>121</sup> and Liquid State Machine (LSM),<sup>122</sup> where authors suggested the importance of multidimensional and rich dynamical state space. Later, the RC paradigm went beyond ESN and LSM, becoming a general model for information processing using non-autonomous dynamical systems with rich state space possessing a set of well-defined properties (*vide infra*).<sup>123</sup>

In general terms, a reservoir is a complex dynamical nonlinear system, the state of which at any point in time is a complex and unknown function of its history and has fading memory. The signal (the data to be analyzed) is supplied at the input and undergoes dynamic evolution at the reservoir nodes. The reservoir essentially maps the input into a point in a new space (created by the internal dynamics of the reservoir), thus performs a nonlinear transformation of the input.<sup>124</sup> Computation performed by the reservoir is represented as the projection of the trajectory of progressive states in its internal configuration space. In order to maximize the computing performance of the reservoir system, the user provides an additional input signal (also termed as “drive”), which needs to be tailored to maximize the distance between different regions of the configuration space into which the reservoir is driven. Fundamentally, we should have freedom in choosing the right drive, depending on the computational task we want to perform and the complexity of the reservoir layer itself. For a suitably complex reservoir layer, a relatively simple drive should suffice.<sup>125</sup>

The obtained different reservoir states can then be analyzed by the second part of the system, the readout layer (usually a simple perceptron or related system), which can be trained and used to generate the final desired

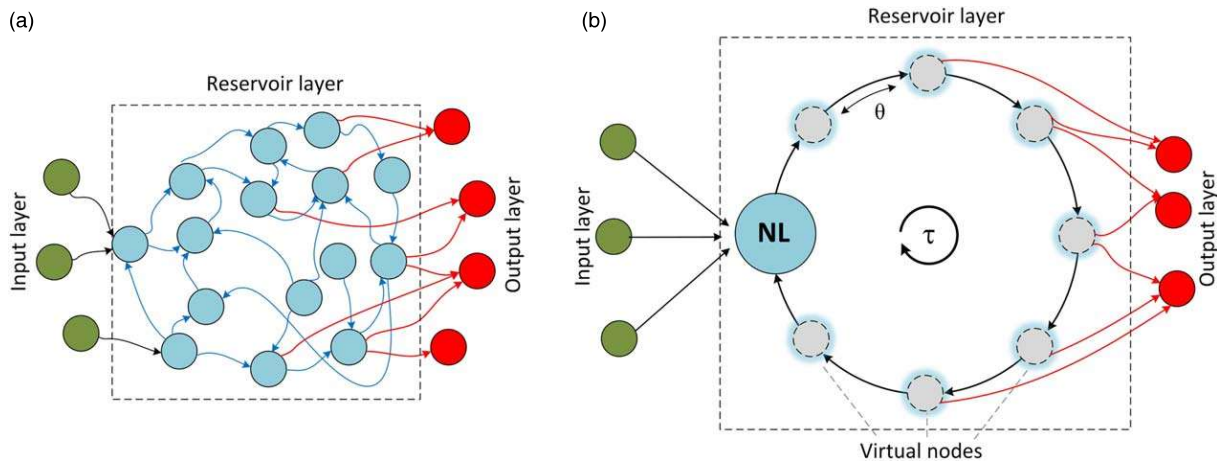


**Fig. 13.** (Color online) Schematic structure of a typical reservoir (a) of randomly, recursively and sparsely connected nodes, and the delayed feedback echo state machine (b) of circular topology. Green nodes represent different inputs acting upon the reservoir. Red nodes represent different readout functions, depending on which property of the reservoir we are interested in probing.  $\theta$ —denotes the time between virtual neurons, i.e. the full time of delay line,  $\tau$ —is the time needed for an efficient evolution of the system, NL—nonlinear node. Adapted from Ref. 120.

output. Training of the reservoir, in contrast to conventional neural networks, does not require any changes in the structure/synaptic weights inside the reservoir. The whole process involves only adjustments in the output layer and the drive. Therefore, reservoirs are considered as more efficient information processing devices than neural networks, their training and operation is, however, more challenging.<sup>124,126,127)</sup>

The dynamics of the internal reservoir state can be described with simple mathematical formulations.<sup>123)</sup> In simplified terms, the reservoir evolves and is updated in discrete time steps  $t$ . It depends on two factors—its initial condition  $x_{t-1}$  and input signal  $u_t$ , based on which current reservoir state  $x_t$  can be obtained, giving (11):

$$x_t = \mathfrak{F}(x_{t-1}, u_t), \tag{11}$$

where  $\mathfrak{F}$  is a function containing a description of the internal reservoir dynamics and its responsiveness to the input data. The readout layer can consist of any function  $\psi$ , depending on which reservoir parameter are we probing to obtain output information  $y_t$ , giving:

$$y_t = \psi(x_t). \tag{12}$$

The readout function  $\psi$  probes only current states of reservoir  $x_t$  (or just some fragments of it, cf. Fig. 13) and—as it was stated above—this is the only part of the whole computing system that needs to be trained.

RC systems only need to possess two very unrestrictive properties to achieve *universal computation power* for time-varying inputs: (i) the point-wise separation/generalization property (distant inputs signals should yield notable different states whereas close input signals should be mapped into similar reservoir states) and (ii) the approximation property for the readout function (readout function can map the current reservoir state to the desired current output with required accuracy).<sup>92)</sup> We refer the interested reader to recent review papers<sup>128,129)</sup> and specialized books.<sup>130–132)</sup>

Important and closely connected features of reservoirs are their *fading memory* and *echo state property*.<sup>133)</sup> Fading memory assures (through the fading-with-time impact of previous inputs on the current state of the reservoir) that

operation of the reservoir does not turn chaotic, as it was shown that RC systems tend to be most efficient when operating at the edge of chaos.<sup>134–136)</sup> The chaotic reservoir does not fulfill the generalization property so that even similar classes of the input signal are separated, and no classification can be performed. On the other hand, the echo state property—as the name implies—relies on the influence of the input signal on the dynamics of the reservoir, which is embedded in its future states. In other words, the current state of the reservoir configuration space depends on all previous input signals. In mathematical terms, the system of interest has an echo state property if there exists a function  $\varepsilon$  formulated as (13):

$$x_t = \varepsilon(u_t, u_{t-1}, u_{t-2}, \dots, u_{-\infty}) \tag{13}$$

which does not depend on the initial state of the reservoir, but only on the history of inputs. For an arbitrarily chosen systems, the existence of the  $\varepsilon$  function cannot be guaranteed. Finite-time probing of the echo states on the basis of Eq. (11) gives a recurrent recipe for the state of the reservoir (14):

$$x_t = \mathfrak{H}^{(h)}(u_t, u_{t-1}, u_{t-2}, \dots, u_{t-h+1}, x_{t-h}). \tag{14}$$

For a given number of steps, it gives relatively simple recipes, examples for  $h = 2$  and  $h = 3$  are shown (15)–(16):

$$\mathfrak{H}^{(2)} = \mathfrak{F}(\mathfrak{F}(x_{t-2}, u_{t-1}), u_t) \tag{15}$$

$$\mathfrak{H}^{(3)} = \mathfrak{F}(\mathfrak{F}(\mathfrak{F}(x_{t-3}, u_{t-2}), u_{t-1}), u_t). \tag{16}$$

Whereas the existence of the  $\varepsilon$  function cannot be guaranteed, the limit (17) can be safely taken for systems with an echo state property:

$$\varepsilon = \lim_{h \rightarrow \infty} \mathfrak{H}^{(h)}. \tag{17}$$

The fading memory feature allows simplification for a finite interval of time (18):

$$x_t = \tilde{\varepsilon}^{(h)}(u_t, u_{t-1}, u_{t-2}, \dots, u_{t-h+1}). \tag{18}$$

More detailed analysis of reservoir dynamics can be found in works of Jaeger and Konkoli.<sup>121,124,137–142)</sup>

Memristors, due to their nonlinear characteristics and internal memory, may play the role of a node in neural networks and reservoir systems. The hardware implementation of a particular type of reservoir system, i.e. Single Node Echo State Machine [SNESM, Fig. 13(b)], was recently presented.<sup>53)</sup> Figure 14(a) presents the experimental setup used to realize the idea of SNESM. The system, by definition, has only one physical node, and the feedback loop realized by incorporation of the delay line. The system also has a signal generator, a source-measure unit, and a recorder. The red arrows indicate the feedback loop created in the system. In general, both the signal and the state of the memristor change every time the signal passes through the device in each cycle.

The presented system performs signal processing: the symmetrical signal passing through the node changes due to the asymmetrical  $I$ - $V$  characteristics of the memristor. The signal is then delayed and returned to the same physical node several times. Figures 14(b)–14(c) show two possible scenarios to be observed during the experiment: the signal might circulate in the created loop several times and finally vanished. In the second scenario, the amplitude of the signal increases in each loop and can circulate in the system indefinitely. This feature of the presented Echo State Machine was used to perform a classification task. The set of sinusoidal signals of different amplitudes (in the range 1 to

2.2 Vpp, and 50 mVstep) was introduced to the system, one by one. As a result, the amplitudes were separated into two subgroups: with the amplitude higher and with amplitude lower than a specific threshold value [here 1.85 Vpp, see Fig. 14(b)].

### 3.2. Coupled electrochemical oscillators

The possibility of electrically forcing liquid metal oscillations along with their ability to generate alternating electrical signals of significant amplitude leads to a new research direction—studies in coupled electrochemical oscillators. There are numerous reports of coupling of mercury-based oscillators,<sup>30–35,104,143–146)</sup> but up to date, gallium-based systems were almost completely neglected. The behavior of gallium-based systems should be analogous to mercury-based systems, at least in terms of the dynamics and phenomenological description. It was demonstrated that two liquid metal electrochemical oscillators could be coupled via a resistive link (e.g. noble metal wires and resistor connecting two metal drops placed in the same<sup>33)</sup> or in different<sup>34)</sup> electrolyte baths). It was found in both cases that despite initial differences in drop volume (and hence differences in oscillating frequencies) the individual oscillators can couple in synchronous oscillation provided the coupling resistance is low ( $R \rightarrow 0$ ), show partial synchronization with various phase shifts ( $R \approx 40 \Omega$ ) or oscillate independently ( $R \approx 200 \Omega$ , Fig. 15).<sup>33)</sup>

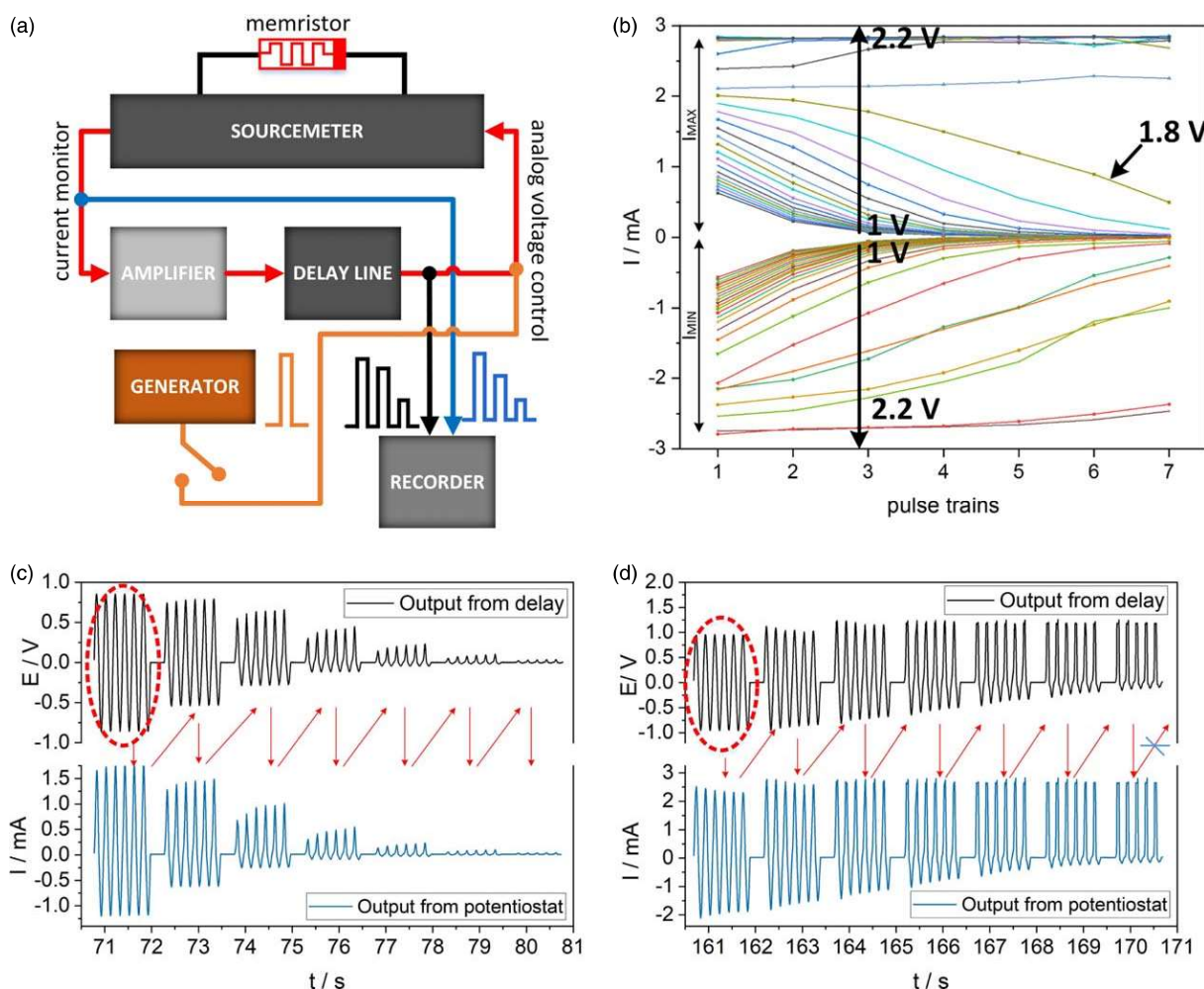


**Fig. 14.** (Color online) A scheme of the experimental system (a), the classification of the signal due to its amplitude (b), the two scenarios of signal circulating in the system (c), (d). Adapted from Ref. 53 with the permission of the American Chemical Society (ACS).

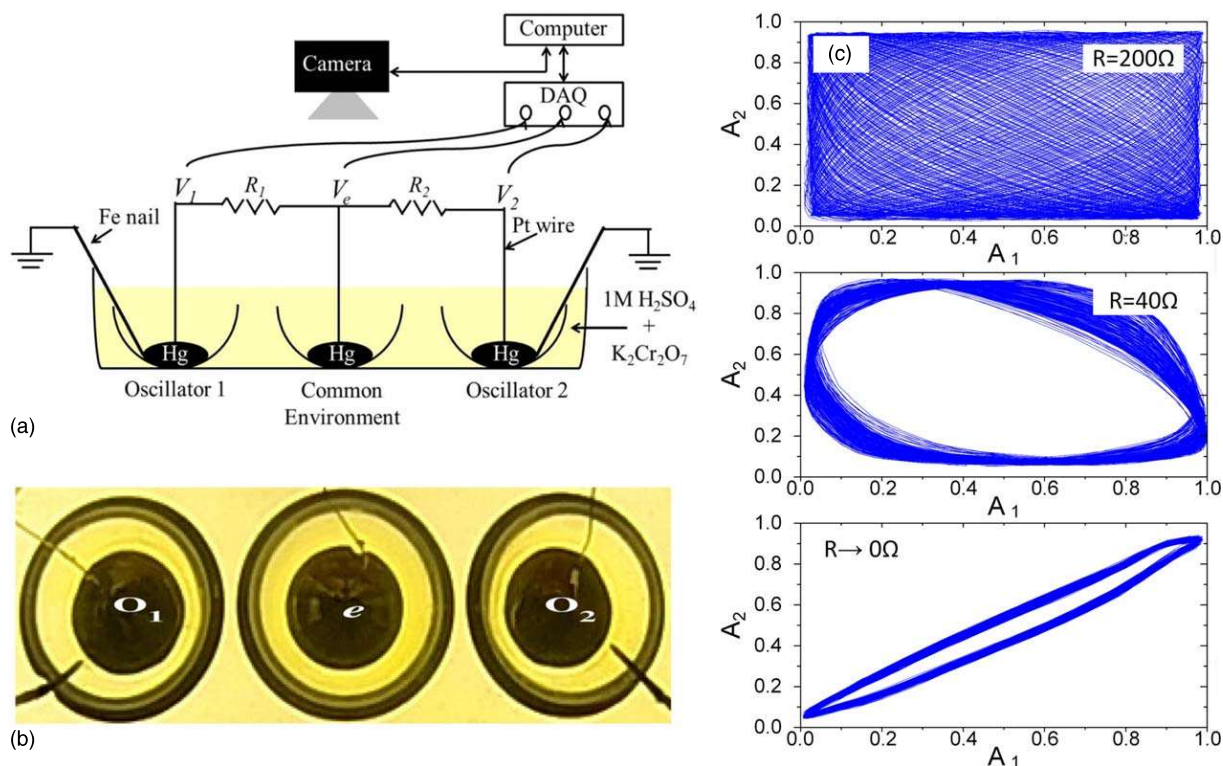


**Fig. 15.** (Color online) Schematic diagram of the experimental setup used to study the synchronization of individual electrochemical mercury beating heart system (a) and a top view of the experimental setup used to study the synchronization (b). State-space plots of the cross-sectional area of the Hg drop for different values of the coupling resistances (c). Reproduced from Ref. 33 with permission. Copyright American Institute of Physics 2016.

Application of operational amplifiers as coupling elements allows full control over the regulation of autonomous oscillatory activity of ensembles of oscillators,<sup>143)</sup> as well as precise control of the oscillatory dynamics of individual oscillators.<sup>147)</sup> Studies of larger assemblies of electrochemical oscillators with various connectivity indicated that these systems show various interesting phenomena. Depending on the frequency mismatch between individual oscillators and on their number, complex oscillatory patterns can be observed as a consequence of the local coupling of oscillators with small frequency mismatch.<sup>148,149)</sup> These partially synchronized networks may be regarded as functional analogs of polychronized oscillatory neural networks.<sup>150,151)</sup> In this type of neural networks, due to the interplay between delays in signal transmission and plasticity, neurons of similar activity spontaneously self-organize into groups. The number of those groups changes dynamically and can even exceed the number of individual neurons, resulting in unprecedented computational performance. Electrochemical, liquid metal-based oscillators, coupled via dynamic (plastic) memristive links, seem to be very well suited for computational purposes. This concept, however, has never been addressed, neither theoretically nor experimentally, despite its experimental simplicity. Furthermore, such ensembles of coupled electrochemical oscillators show other features characteristic for neural networks (or other networks of coupled oscillators): explosive synchronization<sup>144)</sup> and Kuramoto transitions.<sup>35)</sup> Mercury-based weakly coupled oscillators are also prone to transition between periodic and aperiodic oscillations,<sup>145,146)</sup> and show surprising sensitivity towards noise when maintained at specific oscillatory modes (e.g. triangular, cf. Refs. 104, 105).<sup>152)</sup> This phenomenon can be explained in terms of stochastic resonance<sup>153)</sup> and indicates the

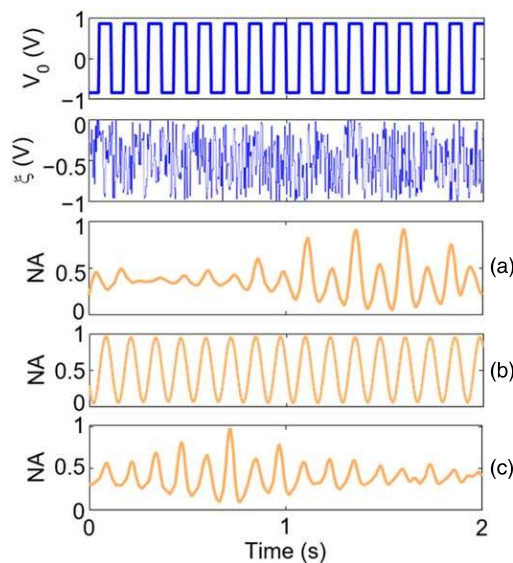


**Fig. 16.** (Color online) Demonstration of stochastic resonance in mercury beating heart system:  $V_0$  is the subthreshold forcing signal,  $\xi$  is the biased white noise signal. Lower curves show mercury drop oscillations (as a variation in normalized surface area of a drop) for various noise amplitudes: 0.2 V (a), 0.4 V (b), and 1.35 V (c), NA stands for “normalized amplitude”. Reproduced from Ref. 152 with permission. Copyright American Physical Society, 2019.

potential of liquid metal electrochemical oscillators as a sensing element (Fig. 16). Interestingly, similar features have been recently reported for a memristor-based reservoir system driven with single square voltage pulses.<sup>76)</sup> Furthermore, switching between various oscillatory modes can be potentially interesting from the IT technology point of view. This relevance is further supported by the specific features of weakly coupled



oscillators—so-called “cognitive modes”, which have been already demonstrated for the Belousov–Zhabotinsky system.<sup>154)</sup> The system of dynamically coupled oscillators can operate at the edge of chaos (the dynamic state, in which synchronization modes are highly unstable and can travel, in the phase space, between several basins of stability, or switch between various attractors).<sup>136,155,156)</sup>

On the basis of all the abovementioned features, especially the self-sustained oscillations, ability to couple with other oscillators, and responsiveness to external stimulation, electrochemical liquid metal-based oscillators seem to be ideal candidates for mimicking neural features in unconventional computing devices. In contrast to other unconventional computing systems, electrochemical oscillators should operate without external sources of power, as the oscillations are a consequence of electrochemical phenomena at the metal/electrolyte interface. The learning ability of such neurons will be, however, significantly limited. Therefore, they need to be coupled with synaptic devices with pronounced memory features. Whereas simple capacitive coupling can, in principle, mimic the short term memory,<sup>157)</sup> coupling of electrochemical oscillators with memristive (or more precisely memfractive) elements will bring new computational features.

#### 4. Towards autonomous robotics

Recent studies by S. Kasai and M. Aono have proven the utility of a simple, bioinspired computing device in the control of the autonomous robot.<sup>158)</sup> This study was inspired by remarkable features of a primitive ameboid organism—slime mould *Physarum polycephalum*,<sup>159,160)</sup> which is a model organism in unconventional computing studies.<sup>161)</sup> The *Physarum* pseudopods are sensitive to light and other stimuli

(e.g. food sources of chemical repellants) and change their geometry upon stimulation [Fig. 17(a)].

The electronic implementation of the ameboid-inspired robotic controller is based on a simple RC circuits with a FET transistor shorting the capacitor and an inverter serving as an output voltage source [Fig. 17(b)]. The controller maps the possible movements according to the Kirchhoff law according to current flow via the “pseudopods” of the circuit. Simple feedback from the touch sensors and application of the bounceback rule<sup>160)</sup> provides signals [Fig. 17(c)] that can control the movements of the robot [Fig. 17(d)] successfully avoiding obstacles via solving the constraint satisfaction problem.

Here we propose that a similar control level can be achieved in an alternative way using unconventional computing devices based on electrochemical oscillators and memristive synapses coupled in a reservoir-like circuit without any digital electronic components involved in information processing. A set of two antiphase coupled liquid metal electrochemical oscillators should provide periodic signals triggering movements of legs on the left and right side of the tetrapod—with an appropriate delay between the front and rear legs. This should provide stimulation of the forwarding motion of the robot. Coupling of two oscillators should be realized with a memfractive element in an ON state. This will ensure the stable operation of synchronized oscillations and, thus, the steady speed and trajectory of the robot. Any obstacle detected by touch sensors modifies the rate of oscillations in one of the oscillators by changing the metal drop electrical potentials. Application of external potentials should, at the same time, switch memristor to higher resistivity, thus decoupling oscillators responsible for left and right legs. Such a condition will switch an

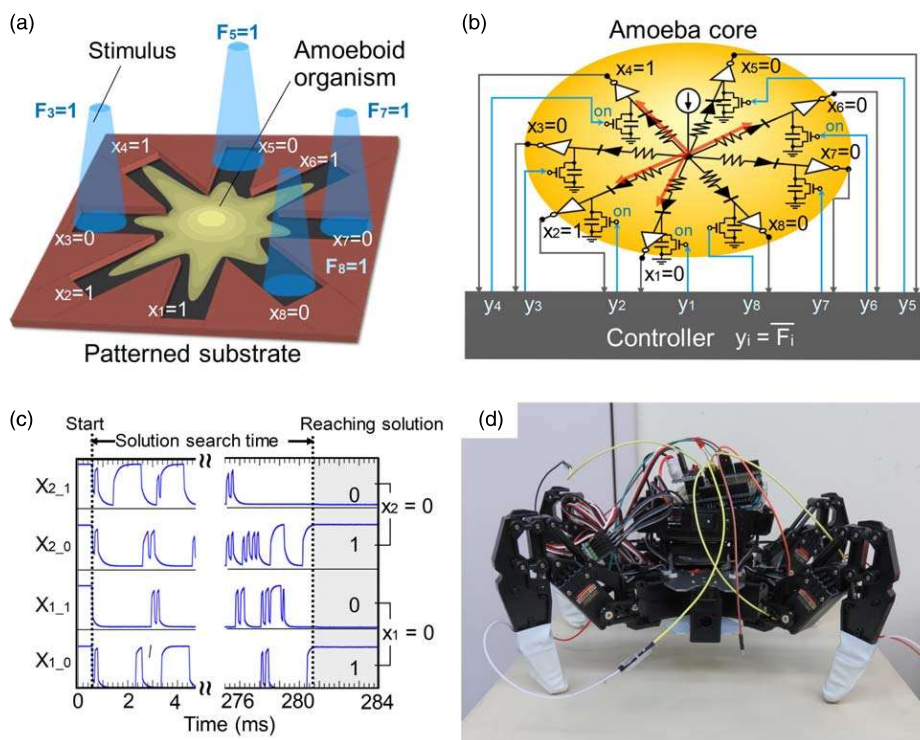


**Fig. 17.** (Color online) A basic concept of conversion of ameboid’s response to stimulation to system control parameters (a), its implementation in a classical electronic circuit (b), the electrical signal recorded during the search for the solution of a leg movement (c) and an autonomous walking robot with an ameboid-inspired controller onboard (d). Adapted from Ref. 158 with permission. Original figures courtesy Prof. Seiya Kasai.

autonomous robot into a foraging mode, in which it will explore the neighborhood in a series of quasi-random moves. They will continue as long as the touch sensors will be disturbed by the obstacles. Finally, when the free path is discovered, the speed and trajectory of the robot should be stabilized by the coupling of both oscillators.

The numerical simulations<sup>162,163</sup> indicate the possibility of the application of a memristive element as a coupler between two oscillators. Moreover, more detailed studies clearly demonstrate the dependence of the degree of coupling on the state of the memristor.<sup>164</sup> Most probably, this control proposal should be extended to more memristive “pseudo-pods”, like in Fig. 17(b). Constant phase shift, between oscillators, should be maintained by memristor-controlled all-pass filters. Details of this control paradigm will be developed in detail both on theoretical and experimental platforms. This concept is in line with the already explored field of LSM-based robotic controllers, which show higher fault tolerance than another neuromimetic system. Despite the low speed of operation (50–250 Hz) of studied controllers, they have proven their utility in the learning of spatiotemporal behavioral sequences. They have been used as a part of the autonomous robotic controller that was inspired by the structure and function of mushroom bodies—parts of insects’ neural systems responsible for sensory functions and learning.<sup>165</sup> Application of memfractive devices within reservoir systems and coupled with artificial spiking neurons is in line with the common approach towards robot learning.<sup>166</sup>

## 5. Closing remarks

The analysis of apparently unrelated systems: liquid metal-based electrochemical oscillators and memfractors (or other memristive elements) reveals their utility in advanced information processing. Furthermore, it seems that they exhibit complementary functionalities. Memfractors offer electrical nonlinearity, plasticity, and memory features. They present synaptic properties and can be elements of responsive artificial neural networks. On the other hand, electrochemical oscillators provide dynamic oscillatory signals, the features of which (time profile, amplitude, frequency) are sensitive to the external stimuli (e.g. applied forcing potential, the composition of the electrolyte). Their dynamics can be controlled at various levels and these oscillators can be easily coupled into larger systems, which exhibit criticality features similar to neural tissue.

Therefore, we postulate a novel unconventional computing platform combining these two realms: artificial memfractive synapses and electrochemical spiking neurons. As a test bench, we suggest autonomous robotics, mainly due to the appropriate time scale of both types of devices.

## Acknowledgments

Authors thank Andrew Adamatzky, Seiya Kasai, Gustavo Mello, and Zoran Konkoli for numerous stimulating discussions on unconventional computing and signal processing. Authors acknowledge the financial support from the Polish National Science Centre within the MAESTRO (grant agreement No. UMO-2015/18/A/ST4/00058) and PRELUDIUM (grant agreement No. UMO-2015/19/N/ST5/00533) projects. DP has

been partly supported by the EU Project POWR.03.02.00-00-I004/16.

- 1) M. Z. Zgurovsky and Y. P. Zaychenko, *Big Data: Conceptual Analysis and Applications* (Springer Nature, Cham, 2020).
- 2) A. J. Schuster (ed.) *Understanding Information: From the Big Bang to Big Data* (Springer, Cham, 2017).
- 3) A. K. Sangaiah et al. (ed.) *Cognitive Computing for Big Data Systems over IoT* (Springer, Cham, 2018).
- 4) S. Stepney, *Physica D* **237**, 1157 (2008).
- 5) C. Horsman, S. Stepney, R. C. Wagner, and V. Kendon, *Proc. R. Soc. A* **470**, 20140182 (2014).
- 6) R. M. Metzger, *Chem. Rev.* **115**, 5056 (2015).
- 7) D. Xiang, X. Wang, C. Jia, T. Lee, and X. Guo, *Chem. Rev.* **116**, 4318 (2016).
- 8) V. Kendon, A. Sebald, and S. Stepney, *Philos. Trans. A* **373**, 20150091 (2015).
- 9) Z. Wang et al., *Nat. Electron.* **1**, 137 (2018).
- 10) Z. Wang et al., *Nat. Mater.* **16**, 101 (2016).
- 11) C. Ríos, N. Youngblood, Z. Cheng, M. Le Gallo, W. H. P. Pernice, C. D. Wright, A. Sebastian, and H. Bhaskaran, *Sci. Adv.* **5**, eaau5759 (2019).
- 12) J. Pei et al., *Nature* **572**, 106 (2019).
- 13) J. Feldmann, N. Youngblood, C. D. Wright, H. Bhaskaran, and W. H. P. Pernice, *Nature* **569**, 208 (2019).
- 14) M. L. Schneider, C. A. Donnelly, S. E. Russek, B. Baek, M. R. Pufall, P. F. Hopkins, P. D. Dresselhaus, S. P. Benz, and W. H. Rippard, *Sci. Adv.* **4**, e1701329 (2018).
- 15) F. Akopyan, J. Sawada, A. Cassidy, R. Alvarez-Icaza, J. Arthur, P. Merolla, N. Imam, Y. Nakamura, P. Datta, and G.-J. Nam, *IEEE Trans. Comput. Aided Des. Integr. Circuits Syst.* **34**, 1537 (2015).
- 16) P. A. Merolla et al., *Science* **345**, 668 (2014).
- 17) J. Backus, *Commun. ACM* **21**, 613 (1978).
- 18) Y. van de Burggt, A. Melianas, S. T. Keene, G. Malliaras, and A. Saleo, *Nat. Electron.* **1**, 386 (2018).
- 19) A. Azarfar, N. Calcini, C. Huang, F. Zeldenrust, and T. Celikel, *Neurosci. Biobehavioral Rev.* **94**, 238 (2018).
- 20) R. Sarpeshkar, *Neural Comput.* **10**, 1601 (1998).
- 21) M. L. Schneider, C. A. Donnelly, and S. E. Russek, *J. Appl. Phys.* **124**, 161102 (2018).
- 22) S. Pecqueur, D. Vuillaume, and F. Alibert, *J. Appl. Phys.* **124**, 151902 (2018).
- 23) C. Sung, H. Hwang, and I. K. Yoo, *J. Appl. Phys.* **124**, 151903 (2018).
- 24) S. Fukami and H. Ohno, *J. Appl. Phys.* **124**, 151904 (2018).
- 25) M. Ziegler, C. Wenger, E. Chicca, and H. Kohlstedt, *J. Appl. Phys.* **124**, 152003 (2018).
- 26) D. Brunner, B. Penkovsky, B. A. Marquez, M. Jacquot, I. Fischer, and L. Larger, *J. Appl. Phys.* **124**, 152004 (2018).
- 27) M. Orlik, *Self-Organization in Electrochemical Systems II. Spatiotemporal Patterns and Control of Chaos* (Springer, Berlin, 2012).
- 28) M. Orlik, *Self-Organization in Electrochemical Systems I. General Principles of Self-Organization. Temporal Instabilities* (Springer, Berlin, 2012).
- 29) J. Liu, L. Sheng, and Z. Z. He, *Liquid Metal Soft Machines* (Springer Nature, Singapore, 2019).
- 30) M. Najdoski, V. Mirceski, V. M. Petruševski, S. Demiri, and D. Rosenberg, *J. Chem. Educ.* **84**, 1292 (2007).
- 31) C. W. Kim, I. H. Yeo, and W. K. Paik, *Electrochim. Acta* **41**, 2829 (1996).
- 32) S. W. Lin, J. Keizer, P. A. Rock, and H. Stensche, *Proc. Natl. Acad. Sci.* **71**, 4477 (1974).
- 33) T. Singla, F. Montoya, M. Rivera, S. Tajima, S. Nakabayashi, and P. Parmananda, *Chaos* **26**, 063103 (2016).
- 34) D. K. Verma, H. Singh, A. Q. Contractor, and P. Parmananda, *J. Phys. Chem. A* **118**, 4647 (2014).
- 35) D. K. Verma, H. Singh, P. Parmananda, and A. Q. Contractor, *Chaos* **25**, 064609 (2015).
- 36) L. O. Chua, *IEEE Trans. Circuit Theory* **CT-18**, 507 (1971).
- 37) D. B. Strukov, G. S. Snider, D. R. Stewart, and R. S. Williams, *Nature* **453**, 80 (2008).
- 38) O. Kavehei, A. Iqbal, Y. S. Kim, K. Eshraghian, S. F. Al-Sarawi, and A. Abbott, *Proc. R. Soc. A* **466**, 2175 (2010).
- 39) A. Younis, D. Chu, and S. Li, *Sci. Rep.* **5**, 13599 (2015).

- 40) Y. Yang, P. Gao, S. Gaba, T. Chang, X. Pan, and W. Lu, *Nat. Commun.* **3**, 732 (2012).
- 41) Y. Yang and W. Lu, *Nanoscale* **5**, 10076 (2013).
- 42) B. Hwang and J.-S. Lee, *Sci. Rep.* **7**, 673 (2017).
- 43) C. Baeumer et al., *Nat. Commun.* **7**, 12398 (2016).
- 44) A. Sawa, *Mater. Today* **11**, 28 (2008).
- 45) D. Ielmini, *Semicond. Sci. Technol.* **31**, 063002 (2016).
- 46) R. Waser, R. Dittmann, G. Staikov, and K. Szot, *Adv. Mater.* **21**, 2632 (2009).
- 47) R. T. Tung, *Mater. Sci. Eng. R* **35**, 1 (2001).
- 48) R. T. Tung, *Appl. Phys. Rev.* **1**, 011304 (2014).
- 49) W. Mönch, *J. Vac. Sci. Technol. B* **17**, 1867 (1999).
- 50) T. Nishimura, K. Kita, and A. Toriumi, *Appl. Phys. Lett.* **91**, 123123 (2007).
- 51) H. Vázquez, W. Gao, F. Flores, and A. Kahn, *Phys. Rev. B* **71**, 041306 (2005).
- 52) J. T. Machado, *Commun. Nonlinear Sci. Numer. Simul.* **18**, 264 (2013).
- 53) E. Wlazlak, M. Marzec, P. Zawal, and K. Szacilowski, *ACS Appl. Mater. Interfaces* **11**, 17009 (2019).
- 54) J. Tenreiro Machado, *Commun. Nonlinear Sci. Numer. Simul.* **18**, 264 (2013).
- 55) M.-S. Abdelouahab, R. Lozi, and L. Chua, *Int. J. Bifurc. Chaos* **24**, 1430023 (2014).
- 56) R. Herrmann, *Fractional Calculus* (World Scientific, Singapore, 2013), p. 500.
- 57) Y. F. Pu and X. Yuan, *IEEE Access* **4**, 1872 (2016).
- 58) R. Metzler and J. Klafter, *Phys. Rep.* **339**, 1 (2000).
- 59) E. K. Lenzi, M. A. F. dos Santos, M. K. Lenzi, D. S. Vieira, and L. R. da Silva, *J. King Saud Univ. Sci.* **28**, 3 (2016).
- 60) E. K. Lenzi, M. A. F. Dos Santos, M. K. Lenzi, and R. M. Neto, *Commun. Nonlinear Sci. Numer. Simul.* **48**, 307 (2017).
- 61) H. Sun, Y. Zhang, D. Baleanu, W. Chen, and Y. Chen, *Commun. Nonlinear Sci. Numer. Simul.* **64**, 213 (2018).
- 62) B. J. West, *Rev. Mod. Phys.* **86**, 1169 (2014).
- 63) B. J. West, *Fractional Calculus View of Complexity: Tomorrow's Science* (CRC Press, Boca Raton, FL, 2015).
- 64) K. Biswas, G. Bohannan, R. Caponetto, A. M. Lopes, and J. A. T. Machado, *Fractional Order Devices* (Springer Nature, Cham, 2017).
- 65) Y. Pu, *IEEE Access* **4**, 3379 (2016).
- 66) Y. Pu, *IEEE Access* **4**, 3398 (2016).
- 67) V. V. Uchaikin and R. T. Sibatov, *Commun. Nonlinear Sci. Numer. Simul.* **13**, 715 (2008).
- 68) K. Y. Choo, S. V. Muniandy, K. L. Woon, M. T. Gan, and D. S. Ong, *Org. Electron.* **41**, 157 (2017).
- 69) R. T. Sibatov and V. V. Uchaikin, *Usp. Fiz. Nauk* **179**, 1079 (2009).
- 70) K. Y. Choo and S. V. Muniandy, *Int. J. Mod. Phys. Conf. Ser.* **36**, 1560008 (2014).
- 71) X. Yang, J. Hu, S. Chen, and J. He, *Sci. Rep.* **6**, 30597 (2016).
- 72) J. C. Dyre and T. B. Schröder, *Rev. Mod. Phys.* **72**, 873 (2000).
- 73) S. Kirkpatrick, *Rev. Mod. Phys.* **45**, 574 (1973).
- 74) Y. Aoki, C. Wiemann, V. Feyer, H.-S. Kim, C. M. Schneider, H. Ill-Yoo, and M. Martin, *Nat. Commun.* **5**, 3473 (2014).
- 75) T. Mazur, P. Zawal, and K. Szacilowski, *Nanoscale* **11**, 1080 (2019).
- 76) E. Wlazlak, P. Zawal, and K. Szacilowski, *ACS Appl. Electron. Mater.* **2**, 329 (2020).
- 77) I. Abraham, *IEEE Access* **4**, 7747 (2016).
- 78) M. R. Rudra and R. J. Pieper, *IETE J. Res.* **61**, 440 (2015).
- 79) I. Abraham, *PLoS One* **9**, e111607 (2014).
- 80) H. O. Sillin, R. Aguilera, H.-H. Shieh, A. V. Avizienis, M. Aono, A. Z. Stieg, and J. K. Gimzewski, *Nanotechnology* **24**, 384004 (2013).
- 81) S. Ambrogio, B. Magyari-Köpe, N. Onofrio, M. Mahbulul Islam, D. Duncan, Y. Nishi, and A. Strachan, *J. Electroceram.* **39**, 39 (2017).
- 82) S. E. Savel'ev, A. S. Alexandrov, A. M. Bratkovsky, and R. Stanley Williams, *Nanotechnology* **22**, 254011 (2011).
- 83) N. Rajabiyoun and T. Karacali, *Appl. Phys. A* **125**, 296 (2019).
- 84) J. Lee, C. Du, K. Sun, E. Kioupakis, and W. D. Lu, *ACS Nano* **10**, 3571 (2016).
- 85) D. Li, M. Li, F. Zahid, J. Wang, and H. Guo, *J. Appl. Phys.* **112**, 073512 (2012).
- 86) J. Lee, W. D. Lu, and E. Kioupakis, *Nanoscale* **9**, 1120 (2017).
- 87) F. Raffone, F. Risplendi, and G. Cicero, *Nano Lett.* **16**, 2543 (2016).
- 88) A. Paris and S. Taioli, *J. Phys. Chem. C* **120**, 22045 (2016).
- 89) S. Prada, M. Rosa, L. Giordano, C. Di Valentin, and G. Pacchioni, *Phys. Rev. B* **83**, 245314 (2011).
- 90) G. Tanaka, R. Nakane, T. Yamane, S. Takeda, D. Nakano, S. Nakagawa, and A. Hirose, *Neural Information Processing* (Springer, Cham, 2017) Vol. 4.
- 91) C. Li et al., *Nat. Electron.* **1**, 52 (2018).
- 92) C. Du, F. Cai, M. A. Zidan, W. Ma, S. H. Lee, and W. D. Lu, *Nat. Commun.* **8**, 2204 (2017).
- 93) J. Cameron, *Terminator 2: Judgement Day* (TriStar Pictures, Culver City, CA, 1991).
- 94) A. Chiolerio and M. B. Quadrelli, *Adv. Sci.* **4**, 1700036 (2017).
- 95) Y. Yu and E. Miyako, *Chem. Eur. J.* **24**, 9456 (2018).
- 96) S. C. Tan, B. Yuan, and J. Liu, *Proc. R. Soc. A* **471**, 2015.0297 (2015).
- 97) C. B. Eaker and E. T. Dickey, *Appl. Phys. Rev.* **3**, 031103 (2016).
- 98) A. Adamatzky, A. Chiolerio, and K. Szacilowski, *Soft Matter* **16**, 1455 (2020).
- 99) A. Adamatzky, A. Chiolerio, and K. Szacilowski, (2019), arXiv:1907.11385v1.
- 100) G. Lippmann, *Ann. Phys.* **225**, 546 (1873).
- 101) Z. Yu, Y. Chen, F. F. Yun, D. Cortie, L. Jiang, and X. Wang, *Phys. Rev. Lett.* **121**, 024302 (2018).
- 102) H. Moellenkamp, H. Huntemann, and W. Jansen, *Monatsch. Chem.* **130**, 741 (1999).
- 103) J. Zhang, Y. Yao, L. Sheng, and J. Liu, *Adv. Mater.* **27**, 2648 (2015).
- 104) E. Ramirez-Alvarez, J. L. Ocampo-Espindola, F. Montoya, F. Yousif, F. Vazquez, and M. Rivera, *J. Phys. Chem. A* **118**, 10673 (2014).
- 105) D. K. Verma, A. Q. Contractor, and P. Parmananda, *J. Phys. Chem. A* **117**, 267 (2012).
- 106) Y. Ren and J. Liu, *Micromachines* **9**, 218 (2018).
- 107) J. Wissman, M. D. Dickey, and C. Majidi, *Adv. Sci.* **4**, 1700169 (2017).
- 108) S. Schliebs and N. Kasabov, *Springer Handbook of Bio-/Neuro-Informatics* (Springer, Dordrecht, 2014).
- 109) P. E. Stingu and F. L. Lewis, *Encyclopedia of Complexity and Systems Science* (Springer, New York, 2009).
- 110) M. Nelson and J. Rinzel, *The Book of Genesis* (Springer, Berlin, 1997).
- 111) E. M. Izhikevich, *IEEE Trans. Neural Networks* **14**, 1569 (2003).
- 112) D. O. Hebb, *The Organization of Behavior: A Neuropsychological Theory* (Wiley, New York, 1949) A Wiley Book in Clinical Psychology, p. xix.
- 113) C. Shuni and C. Burrus, *IEEE Trans. Circuits Syst.* **31**, 913 (1984).
- 114) J. R. Chung, J. Kwon, T. A. Mann, and Y. Choe, *The Relevance of The Time Domain To The Neural Network Models* (Springer, New York, 2012), p. ^pp.
- 115) K. Pilarczyk, A. Podborska, M. Lis, M. Kawa, D. Migdał, and K. Szacilowski, *Adv. Electr. Mater.* **2**, 1500471 (2016).
- 116) D. Przyczyna, M. Lis, K. Pilarczyk, and K. Szacilowski, *Molecules* **24**, 2738 (2019).
- 117) S. Stepney, S. Rasmussen, and M. Amos, *Computational Matter* (Springer, Cham, 2018).
- 118) J. Moon, W. Ma, J. H. Shin, F. Cai, C. Du, S. H. Lee, and W. D. Lu, *Nat. Electron.* **2**, 480 (2019).
- 119) C. Merkel, Q. Saleh, C. Donahue, and D. Kudithipudi, *Procedia Comput. Sci.* **41**, 249 (2014).
- 120) K. Pilarczyk, E. Wlazlak, D. Przyczyna, A. Blachecki, A. Podborska, V. Athanasiou, Z. Konkoli, and K. Szacilowski, *Coord. Chem. Rev.* **365**, 23 (2018).
- 121) H. Jaeger, "German National Research Center for Information Technology," GMD Technical Report 148 Bonn, Germany, 2001, p. 13.
- 122) W. Maass, T. Natschläger, and H. Markram, *Neural Comput.* **14**, 2531 (2002).
- 123) Z. Konkoli, S. Nichele, M. Dale, and S. Stepney, *Computational Matter* (Springer, Cham, 2018).
- 124) Z. Konkoli, *Int. J. Parallel Emergent Distrib. Syst.* **33**, 121 (2016).
- 125) V. Athanasiou and Z. Konkoli, *Int. J. Parallel Emergent Distrib. Syst.* **33**, 367 (2018).
- 126) V. Athanasiou and Z. Konkoli, *Int. J. Circ. Theor. Appl.* **46**, 1072 (2018).
- 127) H. Paugam-Moisy, R. Martinez, and S. Bengio, *Neurocomputing* **71**, 1143 (2008).
- 128) G. Tanaka, T. Yamane, J. B. Heroux, R. Nakane, N. Kanazawa, S. Takeda, H. Numata, D. Nakano, and A. Hirose, *Neural Networks* **115**, 100 (2019).
- 129) G. Van der Sande, D. Brunner, and M. C. Soriano, *Nanophotonics* **6**, 561 (2017).
- 130) A. Adamatzky et al. (ed.) *From Parallel to Emergent Computing* (CRC Press, Boca Raton, FL, 2019).
- 131) A. Adamatzky, *Advances in Unconventional Computing. Prototypes, Models and Algorithms* (Springer, Cham, 2017).
- 132) A. Adamatzky, *Advances in Unconventional Computing. Theory* (Springer, Cham, 2017).

- 133) H. Jaeger, "The 'echo state' approach to analysing and training recurrent neural networks," German National Research Center for Information Technology, GMD Technical Report 148, 2001.
- 134) L. O. Chua, *Nanotechnology* **24**, 383001 (2013).
- 135) J. Boedeker, O. Obst, J. T. Lizier, N. M. Mayer, and M. Asada, *Theory Biosci.* **131**, 205 (2012).
- 136) C. G. Langton, *Physica D* **42**, 12 (1990).
- 137) H. Jaeger, *Scholarpedia* **2**, 2330 (2007).
- 138) V. Athanasiou and Z. Konkoli, *From Parallel to Emergent Computing* (CRC Press, London, 2019).
- 139) Z. Konkoli, *Int. J. Parallel Emergent Distrib. Syst.* **33**, 121 (2018).
- 140) Z. Konkoli, *Unconventional Computing. A Volume of the Encyclopedia of Complexity and Systems Science* (Springer Nature, New York, 2018).
- 141) Z. Konkoli, *Advances in Unconventional Computing: Theory* (Springer, Cham, 2017) Vol. 1.
- 142) Z. Konkoli and G. Wendin, *Int. J. Unconv. Comput.* **10**, 405 (2013).
- 143) A. Biswas, P. Kumar, D. Das, and P. Parmananda, *Phys. Rev. E* **99**, 032223 (2019).
- 144) P. Kumar, D. K. Verma, P. Parmananda, and S. Boccaletti, *Phys. Rev. E* **91**, 062909 (2015).
- 145) P. Kumar and P. Parmananda, *Chaos* **28**, 045105 (2018).
- 146) P. Kumar, P. Parmananda, D. K. Verma, T. Singla, I. de Nicolás, and J. Escalona, *Chaos* **29**, 053112 (2019).
- 147) R. Phogat, I. Tiwari, P. Kumar, M. Rivera, and P. Parmananda, *Eur. Phys. J. B* **91**, 111 (2018).
- 148) P. Kumar and P. Parmananda, *Europhys. Lett.* **122**, 20002 (2018).
- 149) P. Kumar, D. K. Verma, and P. Parmananda, *Phys. Lett. A* **381**, 2337 (2017).
- 150) E. M. Izhikevich, J. A. Gally, and G. M. Edelman, *Cerebr. Cortex* **14**, 933 (2004).
- 151) E. M. Izhikevich, *Neural Comput.* **18**, 245 (2006).
- 152) P. Kumar, J. M. Cruz, and P. Parmananda, *Phys. Rev. E* **99**, 040201 (2019).
- 153) B. Kosko, *Noise* (Viking, New York, 2006).
- 154) V. K. Vanag, *Chaos* **29**, 033106 (2019).
- 155) L. Chua, *Int. J. Bifurc. Chaos* **15**, 3435 (2005).
- 156) K. Srinivasen, I. Tiwari, and P. Parmananda, *Europhys. Lett.* **123**, 60003 (2018).
- 157) S. Westerlund, *Phys. Scr.* **43**, 174 (1991).
- 158) K. Saito, N. Suefuji, S. Kasai, and M. Aono, *J. Appl. Logics* **5**, 1799 (2018).
- 159) S. Kasai, M. Aono, and M. Naruse, *Appl. Phys. Lett.* **103**, 163703 (2013).
- 160) M. Aono, M. Naruse, S.-J. Kim, M. Wakabayashi, H. Hori, M. Ohtsu, and M. Hara, *Langmuir* **29**, 7557 (2013).
- 161) A. Adamatzky (ed.) *Advances in Physarum Machines. Sensing and Computing with Slime Mold* (Springer, Cham, 2016).
- 162) C. K. Volos, I. M. Kyprianidis, I. N. Stouboulos, J. M. Muñoz-Pacheco, and V. T. Pham, *J. Eng. Sci. Technol. Rev.* **8**, 44 (2015).
- 163) C. K. Volos, I. M. Kyprianidis, I. N. Stouboulos, E. Tlelo-Cuautle, and S. Vaidyanatham, *J. Eng. Sci. Technol. Rev.* **8**, 157 (2015).
- 164) M. Ignatov, M. Hansen, M. Ziegler, and H. Kohlstedt, *Appl. Phys. Lett.* **108**, 084105 (2016).
- 165) L. Patané, R. Strauss, and P. Arena, *Nonlinear Circuits and Systems for Neuro-Inspired Robot Control* (Springer Nature, Cham, 2018).
- 166) J. Peters, D. D. Lee, J. Kober, D. Nguyen-Tuong, J. A. Bagnell, and S. Schaal, *Springer Handbook of Robotics* (Springer Nature, Berlin, 2016), p. 1.

Article

# Hardware Realization of the Pattern Recognition with an Artificial Neuromorphic Device Exhibiting a Short-Term Memory

Dawid Przyczyna <sup>†</sup>, Maria Lis <sup>†</sup>, Kacper Pilarczyk <sup>\*</sup> and Konrad Szaciłowski <sup>\*</sup>

Academic Centre for Materials and Nanotechnology, AGH University of Science and Technology, al. Mickiewicza 30, 30-059 Kraków, Poland

<sup>\*</sup> Correspondence: kpilarcz@agh.edu.pl (K.P.); szacilow@agh.edu.pl (K.S.)

<sup>†</sup> These authors contributed equally.

Received: 20 June 2019; Accepted: 26 July 2019; Published: 28 July 2019



**Abstract:** Materials exhibiting memory or those capable of implementing certain learning schemes are the basic building blocks used in hardware realizations of the neuromorphic computing. One of the common goals within this paradigm assumes the integration of hardware and software solutions, leading to a substantial efficiency enhancement in complex classification tasks. At the same time, the use of unconventional approaches towards signal processing based on information carriers other than electrical carriers seems to be an interesting trend in the design of modern electronics. In this context, the implementation of light-sensitive elements appears particularly attractive. In this work, we combine the abovementioned ideas by using a simple optoelectronic device exhibiting a short-term memory for a rudimentary classification performed on a handwritten digits set extracted from the Modified National Institute of Standards and Technology Database (MNIST)(being one of the standards used for benchmarking of such systems). The input data was encoded into light pulses corresponding to black (ON-state) and white (OFF-state) pixels constituting a digit and used in this form to irradiate a polycrystalline cadmium sulfide electrode. An appropriate selection of time intervals between pulses allows utilization of a complex kinetics of charge trapping/detrapping events, yielding a short-term synaptic-like plasticity which in turn leads to the improvement of data separability. To the best of our knowledge, this contribution presents the simplest hardware realization of a classification system capable of performing neural network tasks without any sophisticated data processing.

**Keywords:** photoelectrochemistry; wide bandgap semiconductor; artificial neuron; in materio computing; neuromorphic computing

## 1. Introduction

Pattern recognition is one of the basic cognitive functions, which, due to its complexity and required accuracy, has challenged researchers for decades in a strive to mimic it in an artificial setup. The development of such systems is fueled by various possible applications in medicine, security, economics and many other fields of human's activity. At the moment, the majority of available solutions are based on various software implementations of the machine learning approach, including above all the use of artificial neural networks (ANN) of different architectures. In most of the cases, the ANNs principle of operation is based on the optimization of weights associated with individual connections between nodes (neurons) and the information flow is inspired by the functions of biological structures found in the nervous system. It has been proven on numerous occasions that these algorithms provide an excellent efficiency in various classification tasks with both supervised and unsupervised learning procedures [1–3].

In spite of this, the use of software implementations for ANN algorithms often requires heavy pre- and post-processing of the analysed data and/or a high degree of network complexity translating into a high energy consumption [4]. The use of ANN-based methods may also be associated with a potentially low tolerance towards deliberate attacks [5], emphasized in the case of the one-pixel attack capable of deceiving certain deep neural networks [6]. To meet the discussed drawbacks, some researchers propose the development of hardware implementations for neural networks architectures, incorporating novel materials, non-classic electronic elements and unconventional computing paradigms, such as multi-valued and fuzzy logic systems [7].

The development of neuromorphic computing (NC) can be perceived as one of the manifestations of this trend. The key idea here is to design a brain-inspired hardware computing platform which is optimized towards the implementation of selected aspects of ANN algorithms [7,8]. Among the most advantageous concepts, the use of circuitry employing spiking artificial synapses has been proven to be more energy efficient than the implementation *in silico* [8]. The construction of these systems is currently being investigated in terms of new materials [9–11] which are applied within integrated networks capable of performing sophisticated information processing [12–14]. At the same time, a number of studies aim at simplifying the circuitry realizing the neuromorphic computations. Wang et al. [15] demonstrated a hybrid convolutional neural network with only one spiking synapse based on a HfO<sub>2</sub> memristor. The system was capable of recognizing handwritten digits with the efficiency of 784 neurons. It was achieved through the time division multiplexing access technique. Nonetheless, the “network” required multilayer information pre-processing and several thousands of software neurons to operate.

The research on photochemical and photoelectrochemical in materio computing devices indicates the possibility of their integration into larger computing systems with the use of optical [16,17] or electrical [18] signals. This can lead to the construction of more complex photoelectrochemical circuits [18], molecular arithmetic-logic units [17] or molecular-scale neural networks [16] and communication systems [19] capable of the sophisticated information processing. The studies on artificial photoelectrochemical synapses [20], devices that may realize elementary learning processes (e.g., paired pulse facilitation, PPF), stimulated further development of the neuromorphic systems combining the neuromimetic approach towards data processing with in materio computing concepts [21–25]. The operation principle of a photoelectrochemical synapse is based on the competition between light-induced charge carrier generation, charge carrier trapping and other interfacial processes affecting the photocurrent generation. Whereas the information processing realized with the use of unconventional molecular or nanoscale devices has several drawbacks compared to classic, silicon-based electronics (usually low speed, some problems with data encoding and concatenation) [26], its combination with classic techniques and algorithms seems to be promising. The term heterotic computation encompasses hybrid systems, in which information processing is performed on various platforms depending on the optimal scenario, utilizing the speed and maturity of *in silico* computing or the flexibility of the unconventional approaches [27,28].

Here, we present an extremely simplified, robust circuit made of only one photoelectrochemical element, the operation of which is similar to a simple classification system. In the discussed case an Modified National Institute of Standards and Technology Database (MNIST) set of handwritten digits serves as the input data under consideration [29]—without the use of any data pre-processing or software ANNs. The presented optoelectronic device realizes the paired-pulse facilitation (PPF)—a type of short-term plasticity (STP)—seen as an enhancement of the postsynaptic current resulting from the increase in stimulating events frequencies [30,31]. Therefore, we are testing the information processing capability of a single artificial neuron made of nanocrystalline cadmium sulfide. The obtained results show, that the use of a such simple system may improve the separation in the phase space based solely on the characteristics of the input data (unsupervised learning). It seems possible that the proposed approach could be scaled up and a network of similar, interconnected devices could

serve as a complex hardware neural network implementing the fuzzy logic formalism and selected concepts of reservoir computing [32].

## 2. Results and Discussion

### 2.1. Material Characterization

In order to determine the band gap width ( $E_g$ ) of cadmium sulfide (CdS), the reflectance spectrum was recorded. Kubelka–Munk's function  $F_{KM}$  was calculated based on the raw data and a Tauc plot was made (Figure 1a). CdS is typically considered a direct semiconductor with the  $E_g$  value equal to 2.42 eV for the hexagonal phase and 2.33 eV for the tetragonal polymorph. The value determined for the discussed material (2.33 eV, Figure 1a) may suggest the dominance of the latter polymorph, but this value is usually also observed for mixtures of both crystalline phases [33].

The powder X-ray diffraction measurements have been employed to assess the CdS sample composition. The obtained data was analyzed using HighScore Plus software [34] in which so called Rietveld refinement was applied [35]. This method allows evaluation of certain parameters including the volume fraction of phases. The analysis conducted for the diffraction pattern shown in Figure 1b indicates that both the tetragonal hawleyite [36] and hexagonal greenockite [37] phases are present in approx. 1:1 volume ratio. The energy dispersive X-ray spectroscopy (Figure 1c) indicates the absence of significant impurities, therefore electronic trap states (vide infra) most likely originate from CdS lattice defects. The SEM image (Figure 1d) reveals heavily agglomerated material, for which the particle size statistics were calculated using Image J software [38]. The distribution of crystalline diameters is relatively narrow, ranging from 25 to 110 nm, with an average diameter of  $71 \pm 3$  nm, whereas the distribution maximum is found at  $53 \pm 1$  nm.

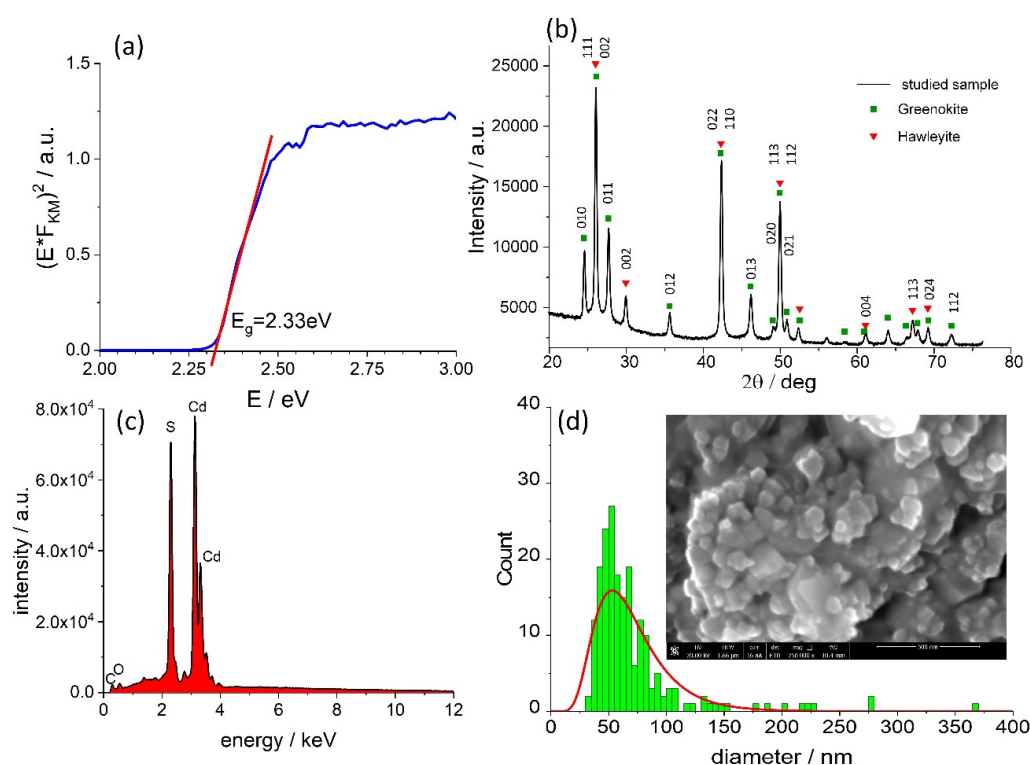


**Figure 1.** The Tauc plot (a), the powder X-ray diffractogram (b), the energy-dispersive X-ray spectrum (EDS) (c) and the crystallite diameter distribution of the CdS sample (d) discussed in this study. Inset shows the SEM image of the studied sample.

## 2.2. Plasticity of the Artificial Neuron

The composites of cadmium sulfide with multiwalled carbon nanotubes reported in our previous works exhibited memory features that can be functionally associated with the neuronal facilitation (particularly, the paired-pulse facilitation—PPF) in terms of the short-term synaptic plasticity [20]. In the neuroscience, the PPF is considered a neuronal enhancement mechanism which consists of four distinctive processes characterized by different time constants and different physiology [39]. The PPF causes an amplification of the postsynaptic response as a consequence of the increase in stimulating event frequencies at the presynaptic axon [40]. It is believed that the PPF is realized mainly through the accumulation of depolarizing  $\text{Ca}^{2+}$  ions in the presynaptic neuron [30]. High frequency components of the PPF mechanism (i.e., these characterized by low time constant values) may be useful from the point of view of information processing. These include the fast-decaying facilitation F1 and the slow-decaying facilitation F2 [30,39,41]. The influence of both components manifests itself in the double exponential decay of the postsynaptic response depicted in Figure 2.

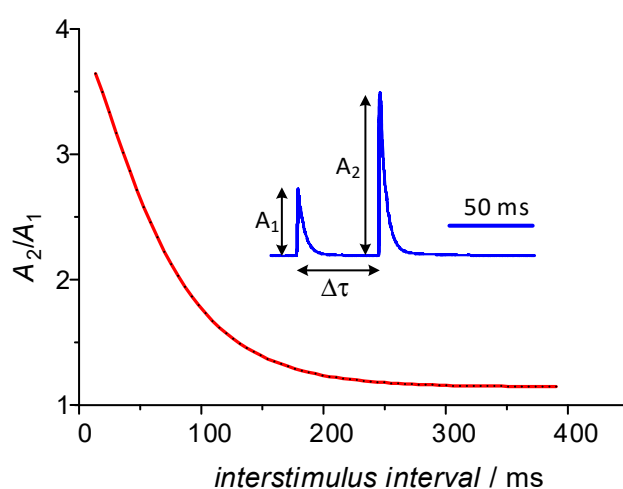


**Figure 2.** An example of the paired-pulse facilitation observed in nervous system. Adapted from [31].

A similar phenomenon was observed for the photoelectrodes made of nanocrystalline cadmium sulfide (Figure 3). Like in the case of multiwalled carbon nanotubes (MWCNT)-CdS composite [20], when the interval between light pulses is sufficiently long (over 300 ms for this study) the subsequent photocurrent spikes are unaffected by previous states the device was in. However, if the interval between irradiations becomes shorter (e.g., 80 ms) the amplification of the second photocurrent response becomes significant. Detailed analysis reveals that the ratio of pulse intensities (the facilitation rate) vs. the time interval between stimuli is best fitted with a biexponential function (1):

$$\frac{A_2}{A_1} = a_1 e^{-\frac{t}{\tau_1}} + a_2 e^{-\frac{t}{\tau_2}} + y_0 \quad (1)$$

which is fully consistent with the previous reports on MWCNT-CdS composite photoelectrodes [20]. The result of the fitting procedure is presented in Figure 3b and the parameters equal to:  $a_1 = 0.218 \pm 0.023$ ,  $a_2 = 0.340 \pm 0.014$ ,  $\tau_1 = 19.8 \pm 4.6$  ms,  $\tau_2 = 167 \pm 23$  ms and  $y_0 = 1.008 \pm 0.013$ . The time constants values, which are representative for polycrystalline CdS samples, are slightly higher than those obtained for CdS/MWCNT composites [20]. Interestingly, the determined values are consistent with the parameters typically observed in the case of biological structures [31].

The double exponential decay can be associated with two distinctive trapping/detrapping events characterized by two time constants  $\tau_1$  and  $\tau_2$ . This diversity may originate from the presence of two CdS polymorphs, of which charge trapping states most likely differ. At the same, through the comparison with selected natural learning processes, these two mechanisms may be associated



with two components of neuronal plasticity: the fast-decaying facilitation F1 and the slow-decaying facilitation F2. Alternatively, they can be described as manifestations of short- and long-term memory, respectively [42].

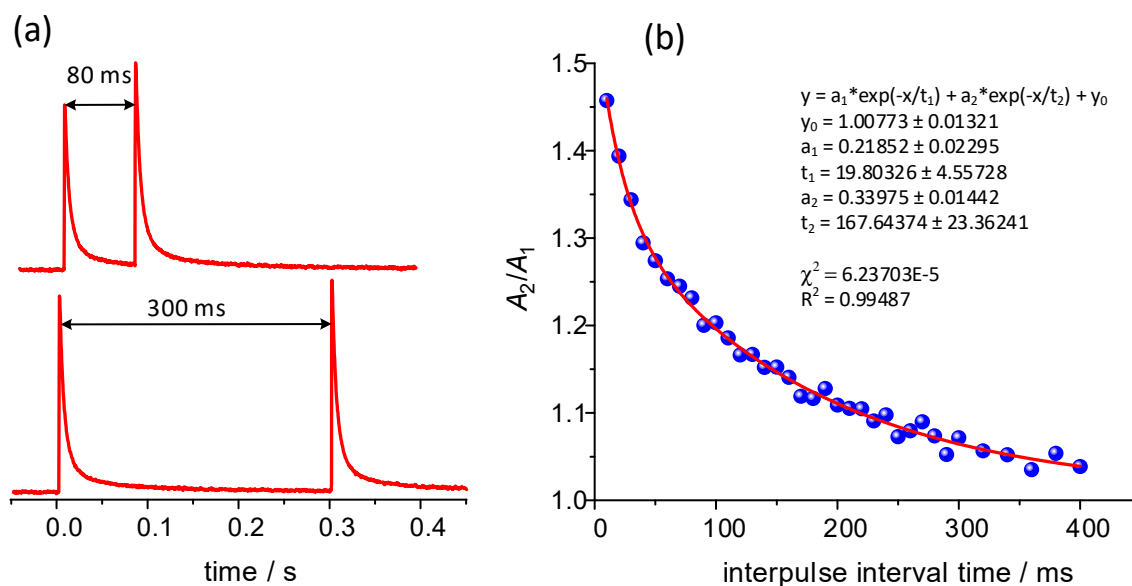


**Figure 3.** The photocurrent spikes resulting from the pulsed light illumination of CdS-based photoelectrodes (a) and the analysis of the photocurrent amplification vs. time interval between subsequent pulses (b).

The overall mechanism of photocurrent generation and spikes amplification is summarized in Figure 4. The photoexcitation leads to the electrons transition from the valence to the conduction band (1) and the electron-hole recombination occurs spontaneously afterwards (1'). Electrons in the conduction band can be subsequently transferred through the interface to the conducting substrate (2) and holes can migrate to the surface and react with redox mediators in the electrolyte (2'). At the same time a fraction of electrons from the conduction band becomes trapped within interband states in a very fast process (3). This process efficiently competes with the interfacial electron transfer (2), but once the traps are filled this pathway becomes inactive. The trapped electrons undergo relaxation with the time constants  $\tau_1$  (3') and  $\tau_2$  (3'').

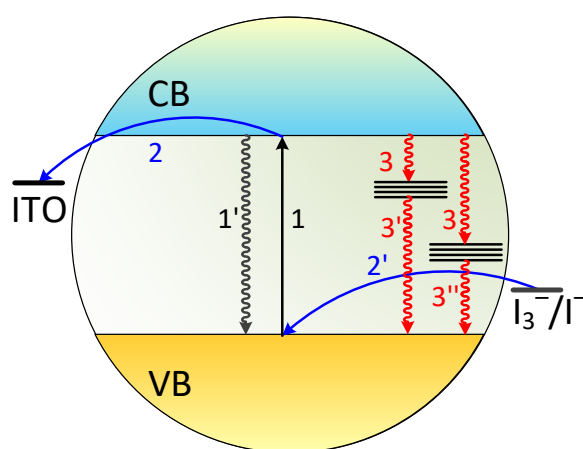


**Figure 4.** A tentative mechanism of the photocurrent generation and charge carriers trapping in the nanocrystalline CdS sample under consideration.

This simple mechanism provides a platform for the implementation of neuronal dynamics in an artificial, fully inorganic system. Due to its simplicity it can be applied for signal and pattern processing and could be integrated into larger neuromimetic systems. Furthermore, along with bioinspired neuromorphic computing, other information processing paradigms may be implemented within the same system: Boolean logic [43], ternary logic [44] and fuzzy logic [45]. The latter one is especially tempting, as it may contribute to the development of novel neuro-fuzzy information processing devices [46–48].

### 2.3. Recognition of Digits

A dataset containing 1000 handwritten digits (100 samples of each 0, . . . , 9 digit) was randomly selected from the MNIST database (Figure 5a). All the images were transformed into binary strings and used for the modulation of a light source. In order to eliminate possible errors resulting from the photoelectrode equilibration or photodegradation, first 20 and last 20 recorded photocurrent profiles were discarded and the remaining 60 patterns were subjected to further processing. First of all, a set of simple classification rules have been developed. These are based on pixel counting, therefore cannot provide a significant separation of the input data. In the first step, each sign (in a form of  $28 \times 28$ -pixel image, Figure 5a) was divided into four quadrants labelled  $\kappa_1, \dots, \kappa_4$  (Figure 5b) and the sum of black pixels confined within each quadrant was calculated. In other words, an individual character was associated with a vector  $[\Sigma\kappa_1, \Sigma\kappa_2, \Sigma\kappa_3, \Sigma\kappa_4]$  or a point in 4-dimensional space. Subsequently, four 3-dimensional projections were formulated in the following manner:  $[\Sigma\kappa_1, \Sigma\kappa_2, \Sigma\kappa_3]$ ,  $[\Sigma\kappa_1, \Sigma\kappa_2, \Sigma\kappa_4]$ ,  $[\Sigma\kappa_1, \Sigma\kappa_3, \Sigma\kappa_4]$  and  $[\Sigma\kappa_2, \Sigma\kappa_3, \Sigma\kappa_4]$ . For each type of input class (0, . . . , 9) an ellipsoid with the confidence level of 65% was fitted using 3D Confidence Ellipsoid toolbox in OriginPro 2019.

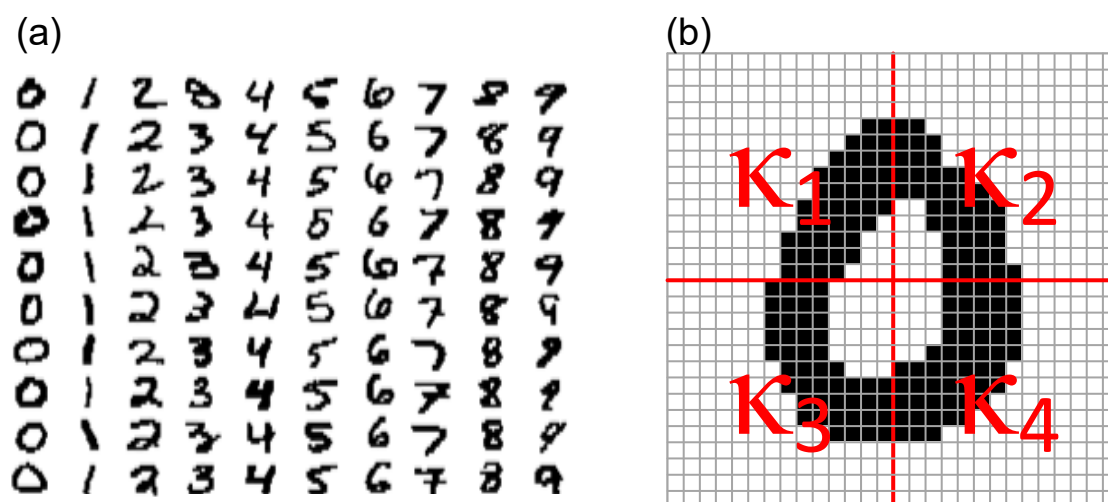


**Figure 5.** A small sample of the MNIST handwritten digits (a) and an image depicting the definition of quadrants for the  $28 \times 28$ -pixel image (b).

The collection of data points representing all 600 characters under consideration for  $[\kappa_1, \kappa_2, \kappa_3]$  combination of quadrants is shown in Figure 6a and the fitted ellipsoids in Figure 6b,c. It can be noticed, that the applied analysis procedure provides a rather poor separation, as the fitted ellipsoids excessively overlap in most of the cases, with the exception of “1” and “9” pair. This result is fully consistent with the initial assumption—simple pixels counting cannot serve as an efficient method for handwritten character recognition.

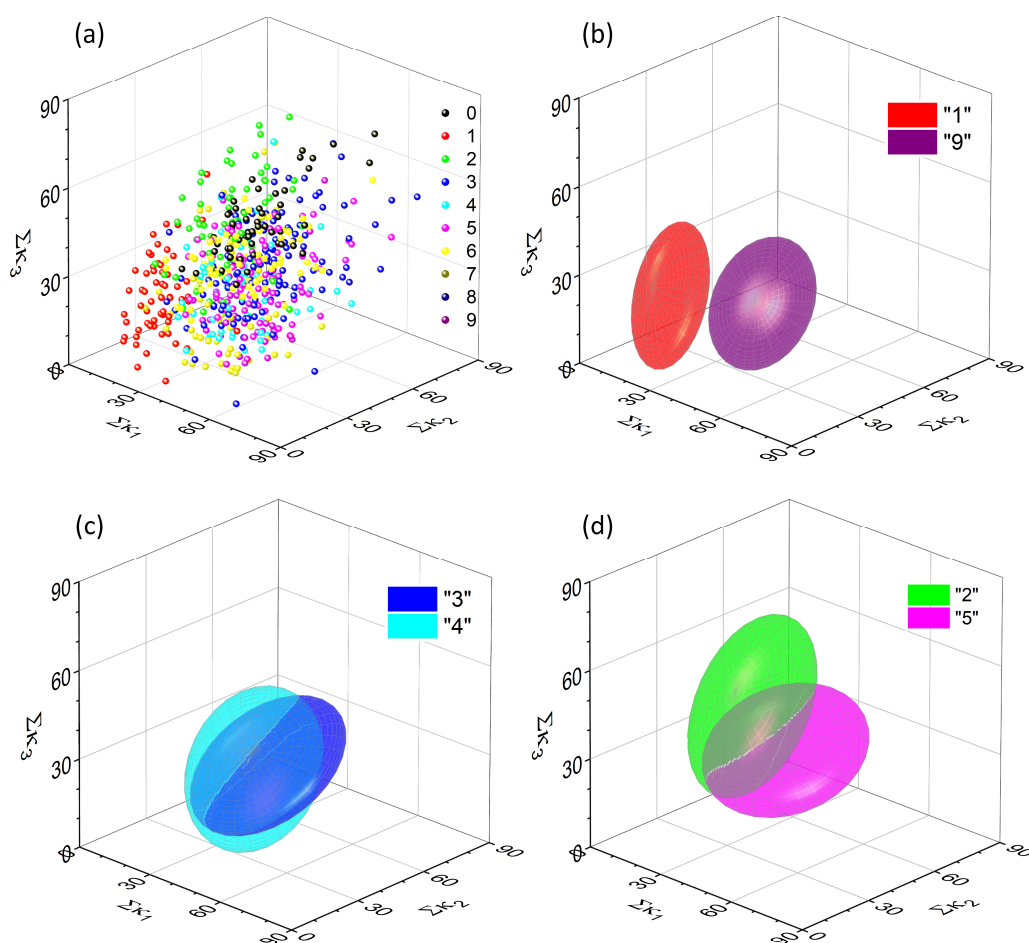


**Figure 6.** A complete collection of input data points (before feeding them into the single-node neural network) for a set of 600 handwritten digits in the one, arbitrary chosen 3D projection (a) and an example of a relatively well-separated pair, which is associated with digits “1” and “9” (b). Other ellipsoids overlap significantly, e.g., those for digits “3” and “4” (c) or “2” and “5” (d).

It can be noticed that only two pairs are completely separated, whereas three others are close to complete separation. Most of these cases concern digit “1” which is substantially different (when the symmetry and number of pixels are taken into account) from any other handwritten digit.

In order to quantify the efficiency of digits recognition in various scenarios, a separability index was defined. Let  $V(m(\kappa_i, \kappa_j, \kappa_k))$  be the volume of an ellipsoid fitted to the digit  $m$  representation in  $\kappa_i, \kappa_j, \kappa_k$  projection. Then the separability index of the digit  $m$  to  $n$  will be defined as a ratio between the relative complement of  $n$ -ellipsoid in  $m$ -ellipsoid to the volume of  $m$ -ellipsoid for  $m \neq n$  (2):

$$\xi_{m/n} = \frac{V(m(\kappa_i, \kappa_j, \kappa_k) \setminus n(\kappa_i, \kappa_j, \kappa_k))}{V(m(\kappa_i, \kappa_j, \kappa_k))} \quad (2)$$

The calculated separability indices for the input data in one of the possible projections are collected in Table 1. It is noteworthy that the matrix containing separability indices for a given combination of quadrants is not symmetrical, i.e.,  $\xi_{m/n} \neq \xi_{n/m}$ , since ellipsoids have different volumes. If  $m = n$  then  $\xi_{m/n} = 0$ .

**Table 1.** The collection of separability indices for the input data in  $\kappa_1, \kappa_2, \kappa_3$  projection. The efficiency of data separation is color coded (vide infra) from red (no separation,  $\xi = 0$ ) to green (perfect separation,  $\xi = 1$ ).

	0	1	2	3	4	5	6	7	8	9
0	0.000	1.000	0.753	0.971	0.889	0.812	0.677	0.927	0.838	0.984
1	1.000	0.000	0.963	0.977	0.959	0.996	0.982	0.895	0.999	1.000
2	0.346	0.900	0.000	0.699	0.556	0.563	0.518	0.617	0.569	0.738
3	0.942	0.953	0.770	0.000	0.395	0.360	0.721	0.584	0.523	0.386
4	0.781	0.916	0.668	0.406	0.000	0.505	0.685	0.364	0.558	0.080
5	0.600	0.991	0.649	0.325	0.469	0.000	0.455	0.689	0.355	0.597
6	0.395	0.964	0.659	0.741	0.702	0.520	0.000	0.806	0.692	0.831
7	0.841	0.763	0.684	0.550	0.298	0.680	0.773	0.000	0.694	0.179
8	0.592	0.998	0.590	0.405	0.438	0.236	0.587	0.648	0.000	0.541
9	0.982	1.000	0.890	0.661	0.482	0.789	0.899	0.581	0.797	0.000

In most of the cases the separation is insufficient to allow the unequivocal recognition of handwritten shapes. The exception is a pair {1, 9} for which the separability index is equal to one, as the corresponding ellipsoids do not overlap. It is due to the fact, that “1” differs significantly in terms of pixels distribution between the quadrants. Poor separation can be however greatly improved with the use of even the simplest, the single-node hardware neural network.

In the first step all the characters were converted row-by-row into a stream of bits (“0” for a white pixel and “1” for a black one) and used to modulate the light source according to the scheme presented in Figure 7a,b. The recorded photocurrent spikes (Figure 7c) reflected the sequence of light pulses, but their intensity varied according to the previous states the photoelectrode was in (the short-term memory, vide supra, Figure 3). The photocurrent patterns were subsequently normalized: the amplitude of each signal was divided by the highest intensity recorded for the particular character. The application of various threshold values (Figure 7c,d) acted as a filter for the photocurrent spikes depending on their amplitude. The obtained images with the lowest intensity pixels removed at different thresholds are shown in Figure 8.

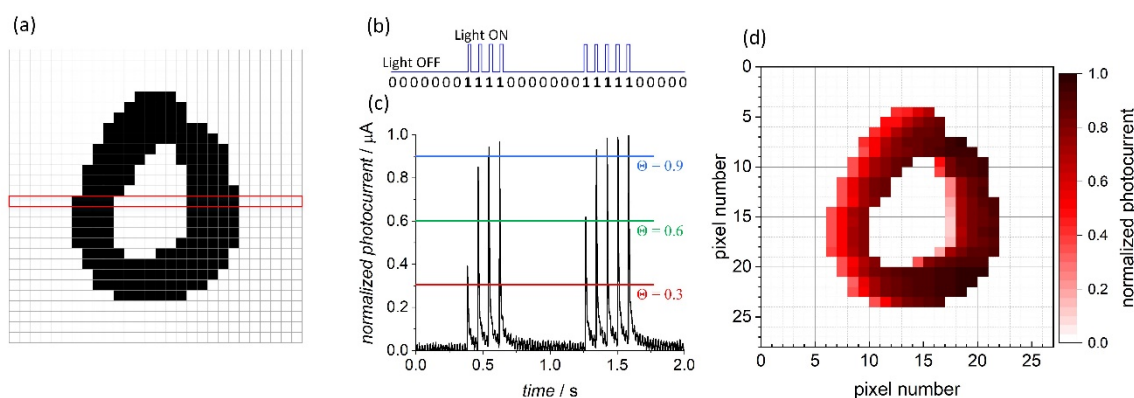


**Figure 7.** A  $28 \times 28$  pixels image of a handwritten character with a marked row (a) translated into a sequence of bits and corresponding light pulses (b). A pattern of photocurrent spikes for a given binary input with three thresholds indicated (c). An image of the character reconstructed from the normalized photocurrent amplitudes (d).

The application of different thresholds (from  $\Theta = 0.3$ , with virtually no signal filtration to  $\Theta = 0.9$ , corresponding to the removal of all but the most intense pixels) leads to the evolution of the character image, which depends directly on the neighbors of each particular pixel in the row. Significantly, the “distance” (formerly in space, translated into time intervals between the light pulses) from the closest preceding black pixel determines the weight of the subsequent photocurrent spike amplification. As

the result, a simple type of classification according to the scattering of pixels can be achieved. Like in the case of the input data, the output images are subjected to the evaluation of respective separability indices at various threshold values. An example is shown in Table 2.

Figure 9a shows a collection of all data points obtained for one selected projection ( $\kappa_1, \kappa_2, \kappa_3$ ) and one threshold value ( $\Theta = 0.7$ ). They seem to be equally scattered as points for unprocessed data (cf. Figure 6a), but the fitting procedure reveals significant differences. Some ellipsoids, that were initially well separated (e.g., the {1, 9} pair) overlap significantly (Figure 9b). Some other remain unchanged (Figure 9c). More interestingly there are numerous pairs (e.g., {2, 5}, Figure 9d) which are significantly separated upon the data processing with the neuromimetic element.

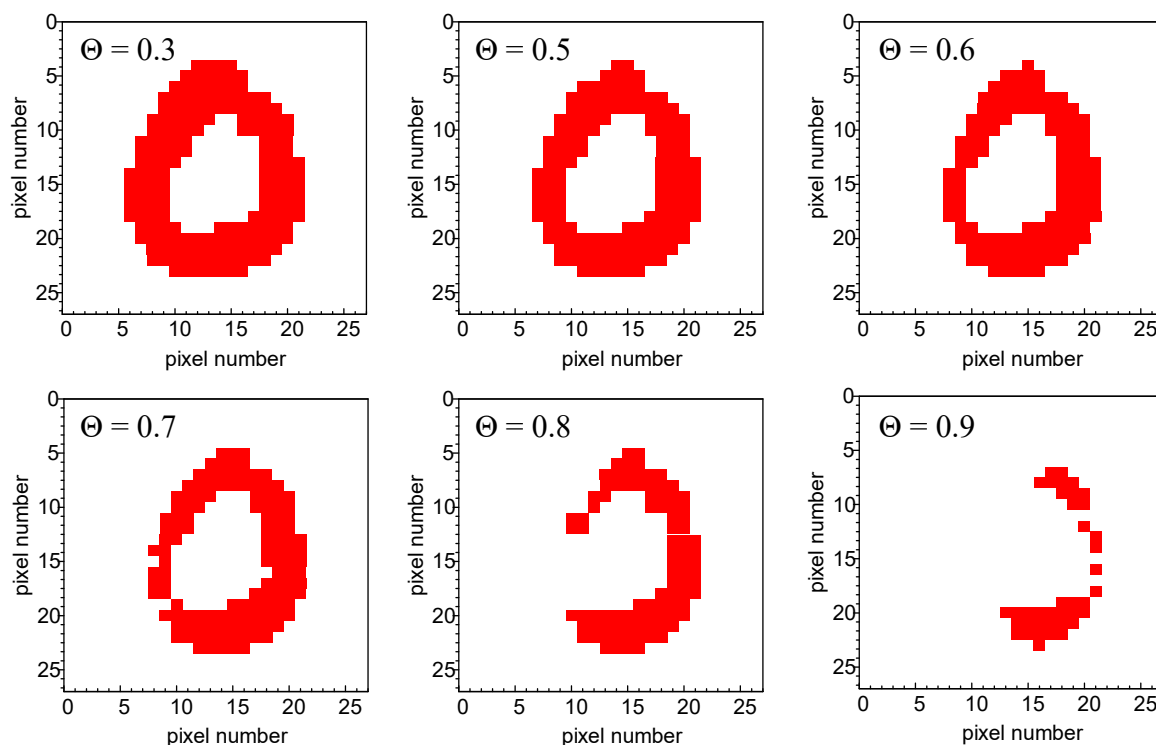


**Figure 8.** An image of the character from Figure 7 reconstructed from the normalized photocurrent spikes at different threshold values.

**Table 2.** The collection of separability indices for the output data in  $\kappa_1, \kappa_2, \kappa_3$  projection at the threshold  $\Theta = 0.7$ . The efficiency of data separation is color coded from red (no separation,  $\xi = 0$ ) to green (perfect separation,  $\xi = 1$ ).

	0	1	2	3	4	5	6	7	8	9
0	0.000	0.482	0.783	0.548	0.812	0.452	0.923	0.654	0.782	0.366
1	0.608	0.000	0.936	0.899	0.969	0.376	1.000	0.808	0.984	0.710
2	0.507	0.807	0.000	0.500	0.264	1.000	0.504	0.730	0.653	0.580
3	0.457	0.839	0.735	0.000	0.540	0.964	0.878	0.596	0.611	0.364
4	0.723	0.940	0.522	0.436	0.000	1.000	0.439	0.801	0.672	0.732
5	0.840	0.759	1.000	0.991	1.000	0.000	1.000	0.959	1.000	0.858
6	0.896	1.000	0.705	0.863	0.487	1.000	0.000	0.998	0.854	1.000
7	0.549	0.669	0.845	0.561	0.824	0.817	0.998	0.000	0.788	0.133
8	0.467	0.947	0.626	0.209	0.457	1.000	0.735	0.603	0.000	0.512
9	0.670	0.801	0.904	0.725	0.906	0.747	1.000	0.654	0.896	0.000

Upon data treatment with the neuromimetic element the separability is significantly improved. Six pairs of digits are completely separated and two others are close to complete separation. Furthermore, these pairs are different than those separated with the use of the pixel counting method (cf. Table 1).

The improvement of digits classification can be visually evaluated by the comparison of color-coded Tables 1 and 2. In order to perform a global quantitative evaluation of the separation efficiencies and to assess the improvement associated with the use of the single-node hardware neural device, a separability ratio ( $\Xi_{m/n}$ ) was defined as a ratio of the separability index calculated for the processed data to the separability index determined for the input data (for  $m \neq n$ ) (3):

$$\Xi_{m/n} = \frac{\xi_{m/n}^{output}}{\xi_{m/n}^{input}} \quad (3)$$

and  $\Xi_{m/n} = 0$  for  $m = n$ . Detailed analysis of calculated values provides information on the discussed procedure efficiency even in the case of significantly overlapped ellipsoids. Selected separability ratios for  $\kappa_1, \kappa_2, \kappa_3$  projection at the threshold  $\Theta = 0.7$  are presented in Table 3.

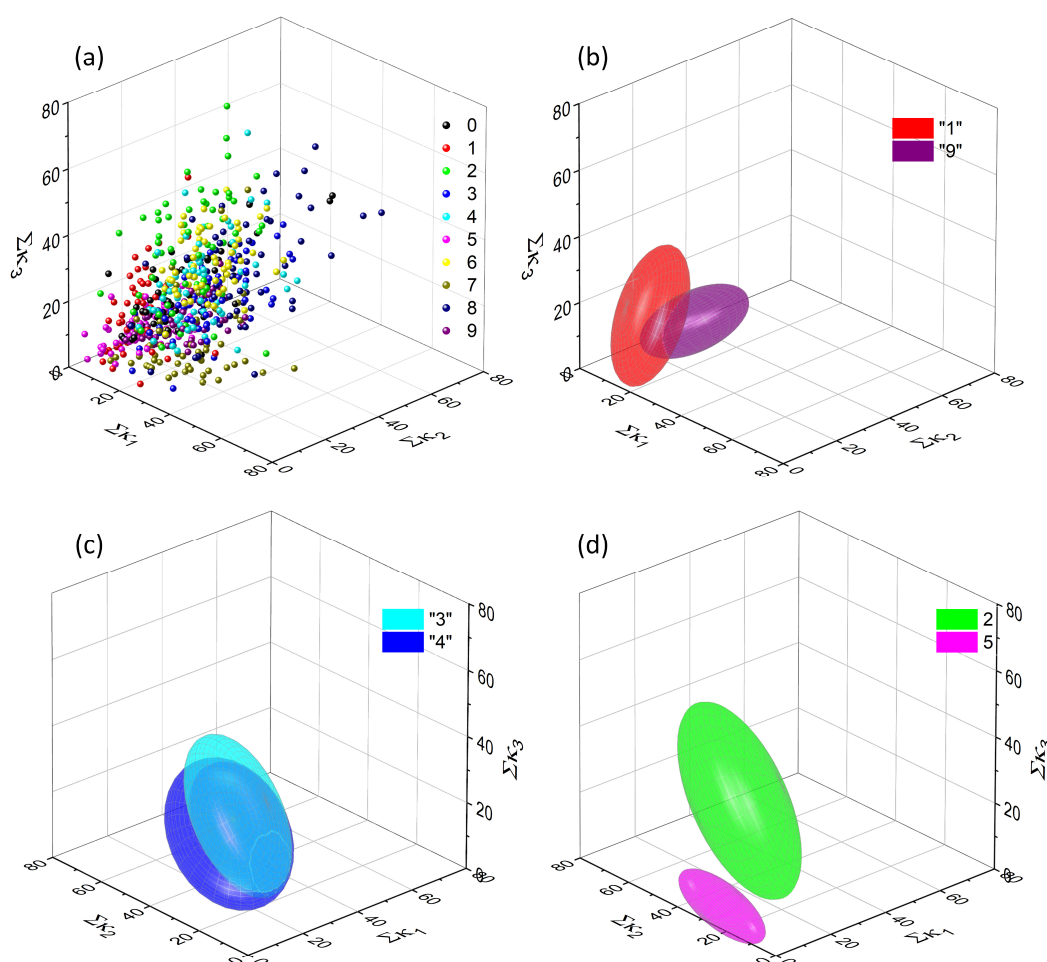


**Figure 9.** A complete collection of output data points (after feeding them into the single-node neural network) for a set of 600 handwritten digits in the one, arbitrary chosen 3D projection (corresponding to the one shown in Figure 6) (a) and an example of significantly overlapped ellipsoids, corresponding to digits “1” and “9” (b), “3” and “4” (c). The majority of other ellipsoids are separated better, than in the case of untreated data—e.g., those associated with digits “2” and “5” (d).

**Table 3.** The collection of separability ratios ( $\Xi_{m/n}$ ) for the output data in  $\kappa_1, \kappa_2, \kappa_3$  projection at the threshold  $\Theta = 0.7$ . The efficiency of data separation is color coded from red—significantly decreased separability ( $\Xi < 0.5$ ), through yellow—slightly decreased separability ( $0.5 < \Xi < 1$ ), green—moderately improved separability ( $1 < \Xi < 1.5$ ), blue—significantly improved separability ( $1.5 < \Xi < 2$ ) to navy blue—outstanding improvement of separability ( $\Xi > 2$ ).

	0	1	2	3	4	5	6	7	8	9
0	0.000	0.482	1.040	0.564	0.913	0.556	1.363	0.705	0.933	0.372
1	0.608	0.000	0.971	0.919	1.011	0.377	1.019	0.903	0.984	0.710
2	1.468	0.897	0.000	0.715	0.475	1.777	0.974	1.183	1.147	0.787
3	0.485	0.881	0.954	0.000	1.369	2.682	1.219	1.019	1.167	0.945
4	0.926	1.026	0.781	1.074	0.000	1.979	0.642	2.203	1.205	9.127
5	1.398	0.766	1.542	3.055	2.134	0.000	2.198	1.393	2.818	1.438
6	2.267	1.037	1.070	1.166	0.694	1.923	0.000	1.239	1.233	1.204
7	0.652	0.877	1.235	1.021	2.770	1.202	1.291	0.000	1.135	0.742
8	0.788	0.949	1.061	0.515	1.044	4.229	1.253	0.931	0.000	0.947
9	0.682	0.801	1.016	1.097	1.877	0.947	1.112	1.125	1.125	0.000

It can be noticed that the overall improvement of separability is achieved with at least twofold increase of the index value for 10 pairs compared to the twofold decrease in five instances. A similar situation is also observed for other projections at this threshold. This qualitative picture suggests an improvement of handwritten digits recognition upon application of a neuromimetic element in data processing. A quantitative estimation of classification improvement can be obtained through simple numerical analysis of output data. Due to the analysis complexity (four quadrant combinations for eight different threshold values), various separation scenarios (depending on the chosen threshold and projection) are possible. Their overall efficiency can be evaluated using an integral separability index  $\Omega$ , which acts as a global parameter indicating performance of the system for all of the above-mentioned variables. For each separation scenario it can be defined as follows (4):

$$\Omega(\kappa_i, \kappa_j, \kappa_k, \Theta) = \frac{\sum_m \sum_n \xi_{m/n}^{output}}{\sum_m \sum_n \xi_{m/n}^{input}}, m \neq n \quad (4)$$

The above-mentioned dependency of the  $\Omega$  function values is depicted in Figure 10. It can be noted, that in the majority of investigated separation scenarios the integral separability index after the treatment with the single-node hardware neural network is significantly higher than the value calculated for the unprocessed input data. In three cases the selection of a low threshold value (a situation which results in an insufficient filtration of pixels due to inadequate exploitation of memory features) leads to the inferior separation. On the other hand, when the short-term memory of the system is optimally utilized, the recognition of handwritten digits increases. For two quadrant combinations an optimal threshold value exists, which is fully consistent with the expectations—too deep filtration removes too many pixels and all the data points (cf. Figures 6a and 9a) interfuse at the origin of the coordinate system.

### 3. Conclusions

Surprisingly, even a primitive hardware realization of the neural network architecture based on a single-node exhibiting the short-term memory can significantly improve pattern recognition. Classification based solely on the number of black pixels encompassed by each of the four quadrants the character image is divided into (cf. Figure 5b) is insufficient—only a few characters of a specific symmetry (e.g., “1”) could be distinguished using this primitive procedure. The application of the optoelectronic element with PPF functionality enhances tremendously (for such a simple device) the classification efficiency. This change is based on the extraction of a new feature of the studied data—the

scattering of pixels within the  $28 \times 28$  matrix. The high dispersion leads to the negligible photocurrent amplification. On the contrary, the digits with large groups of pixels are characterized by a higher number of counts for relatively high thresholds, for which the short-term memory of the system and resulting photocurrent amplification is strongly pronounced.

The system presented in this work is a single node neural device, the operation of which is based on the unsupervised learning paradigm involving the short-term memory of the device. The simple pixel counting method gives precise information on the size of the characters (therefore digit “1” separates well in all of the cases) and indirectly on their symmetry (it can be achieved by an appropriate selection of quadrant combinations). Application of a neuromimetic element allows further information processing, particularly the extraction of information on pixel “agglomeration”, at least at the single row level. This process is analogous to Sammon mapping [49], but does not involve the reduction of data space dimensionality (Figure 11).

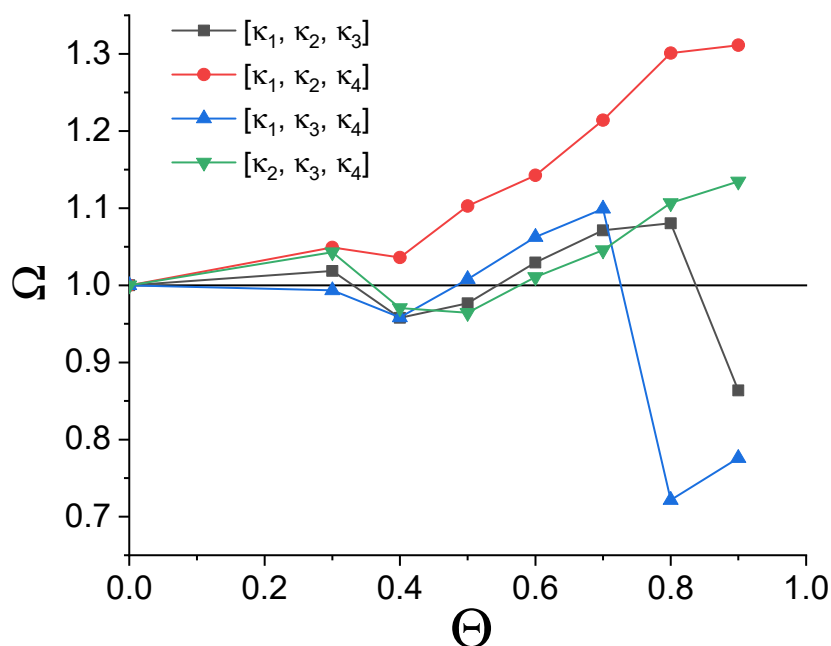


**Figure 10.** The dependence of the integral separability index  $\Omega$  vs. the threshold value  $\Theta$ . The horizontal line indicates the integral separability values determined for the input data. Threshold  $\Theta = 0$  corresponds to unprocessed input data.

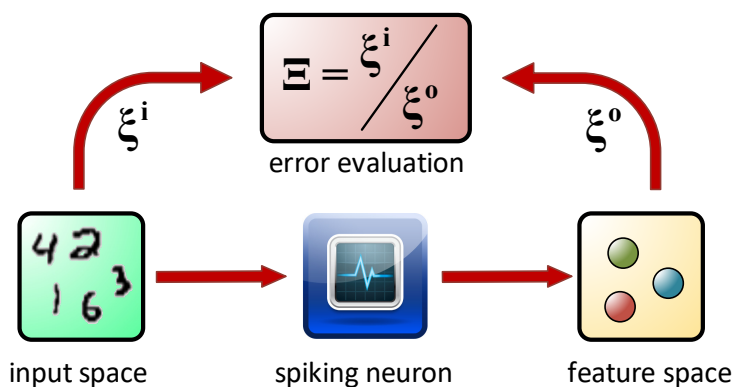


**Figure 11.** A diagram depicting the data flow and the efficiency evaluation of the unsupervised classification system under consideration.

The presented optoelectronic single-node neural device is superior compared to software implementations in terms of the error resistance and the energy efficiency. These features of the



discussed system make it a potential low-cost pre-processing unit. Furthermore, due to the operation based on time-series and the intrinsic short-term memory, it can be combined with selected aspects of the reservoir computing paradigm—in one of the possible scenarios, where a delayed feedback loop is used, the virtual neurons could significantly affect the system performance. At the same time, the analog character of the system allows the implementation of the fuzzy logic system, yielding a new class of hardware neuro-fuzzy devices.

The research presented in this paper supports the concept of heterodic computation [27,28]. It clearly shown that the performance of a simple numerical algorithm (classification based on pixel counting) can be improved by in-materio computational component, which itself cannot perform any classification tasks.

#### 4. Materials and Methods

Commercially available cadmium sulfide (POCH, Las Condes, Chile), potassium nitrate (Avantor, Radnor, PA, USA), potassium iodide (Aldrich, St. Louis, MO, USA) and iodine (Aldrich, St. Louis, MO, USA) were used as received.

Working electrodes were prepared from polyethylene terephthalate (PET, Camarillo, CA, USA) foil coated with indium tin oxide (Aldrich, St. Louis, MO, USA). These substrates were washed carefully with diluted detergent solution, deionized water and isopropanol. They were then dried in air. The cadmium sulfide was ground with deionized water in an agate mortar to a thick paste and deposited onto the freshly cleaned substrates using a screen-printing machine (MikMetal, Masis St, Yerevan, Armenia) equipped with a 80 mesh polymer grid.

The UV/Vis spectra were recorded using Lambda 750 spectrophotometer (Perkin Elmer, Waltham, MA, USA) within the wavelength range of 200–2000 nm. Barium sulfate of spectral purity was used as a reference material. The X-ray diffraction patterns were recorded with Empyrean ( $\text{Cu } \lambda_{\text{K}\alpha 1} = 1.54060 \text{ \AA}$ ) diffractometer (PANalytical, Malvern, UK) at room temperature with  $2\theta$  values ranging from 20 to 80 degrees. The scanning electron images were taken on Versa 3d (FEI, Lausanne, Switzerland) scanning electron microscope operating at 20 kV with an Everhart-Thornley detector. The chemical composition of the CdS sample was confirmed using the energy dispersive X-ray spectroscopy. All electrochemical measurements were performed with the use of SP-300 potentiostat (BioLogic, Cary, NC, USA). Luxeon Star/O Royal Blue diode (465 nm, the total radiometric power of 110 mW) was used as the light source. It was powered through the WA-301 wideband amplifier (Aim-TTI, Cambridgeshire, England). Pulse sequences were generated with TG2512A arbitrary function generator (Aim-TTI, Cambridgeshire, England) triggered with Arduino Uno R3 system.

The photoelectrochemical experiments were performed in air-equilibrated electrolytes using a three-electrode configuration. As the photoactive component the screen-printed CdS electrodes, immersed in an aqueous electrolyte containing 0.1 M  $\text{KNO}_3$ , 0.001 M KI and 0.0001 M  $\text{I}_2$ , were used. A saturated Ag/AgCl electrode was used as a reference electrode and a platinum wire as a counter electrode. The positive voltage (400 mV) was applied to the working electrode and the photocell was irradiated with short light pulses (300  $\mu\text{s}$ ).

The experiment automation was realized based on the program written in Arduino C++ language. All the necessary data processing was performed with the use of programs written in Python 3.7.2.

**Author Contributions:** M.L., D.P. and K.P. have performed all photoelectrochemical experiments. D.P. and K.P. have selected appropriate data sets. K.P. and K.S. have developed algorithms for data processing and designed the experimental setup. K.P. wrote the software necessary for data handling and measurements automation. All the authors contributed to the data analysis and the manuscript preparation.

**Funding:** This research was funded by National Science Centre (Poland) within the MAESTRO project, contract No. UMO-2015/18/A/ST4/00058. D.P. acknowledges partial support from European Union within the EU Project POWR.03.02.00-00-I004/16. K.P. was supported by the Foundation for Polish Science (FNP) and acknowledges partial support from National Science Centre within the PRELUDIUM project, contract No. UMO-2016/21/N/ST3/00469.

**Acknowledgments:** The authors thank Grzegorz Cios and Marianna Marciszko for the XRD measurements and Kapela Pilaka for countless discussions of an extremely fruitful character on the design of hardware neural networks.

**Conflicts of Interest:** The authors declare no conflict of interest.

## References

1. Perez, L.; Wang, J. The effectiveness of data augmentation in image classification using deep learning. *arXiv* **2017**, arXiv:1712.04621 2017.
2. Basheer, I.A.; Hajmeer, M. Artificial neural networks: fundamentals, computing, design, and application. *J. Microbiol. Methods* **2000**, *43*, 3–31. [[CrossRef](#)]
3. Querlioz, D.; Bichler, O.; Gamrat, C. Simulation of a memristor-based spiking neural network immune to device variations. In Proceedings of the 2011 International Joint Conference on Neural Networks, San Jose, CA, USA, 31 July–5 August 2011; pp. 1775–1781.
4. Liu, W.; Wang, Z.; Liu, X.; Zeng, N.; Liu, Y.; Alsaadi, F.E. A survey of deep neural network architectures and their applications. *Neurocomputing* **2017**, *234*, 11–26. [[CrossRef](#)]
5. Nguyen, A.; Yosinski, J.; Clune, J. Deep neural networks are easily fooled: High confidence predictions for unrecognizable images. In Proceedings of the IEEE Conference on Computer Vision and Pattern Recognition, Boston, MA, USA, 7–12 June 2015; pp. 427–436.
6. Su, J.; Vargas, D.V.; Sakurai, K. One pixel attack for fooling deep neural networks. *IEEE Trans. Evol. Comput.* **2019**. [[CrossRef](#)]
7. Nawrocki, R.A.; Voyles, R.M.; Shaheen, S.E. A mini review of neuromorphic architectures and implementations. *IEEE Trans. Electron. Dev.* **2016**, *63*, 3819–3829. [[CrossRef](#)]
8. Akopyan, F.; Sawada, J.; Cassidy, A.; Alvarez-Icaza, R.; Arthur, J.; Merolla, P.; Imam, N.; Nakamura, Y.; Datta, P.; Nam, G.-J. Truenorth: Design and tool flow of a 65 mw 1 million neuron programmable neurosynaptic chip. *IEEE Trans. Computer-Aided Des. Integr. Circ. Syst.* **2015**, *34*, 1537–1557. [[CrossRef](#)]
9. Wu, Y.; Yu, S.; Wong, H.-S.P.; Chen, Y.-S.; Lee, H.-Y.; Wang, S.-M.; Gu, P.-Y.; Chen, F.; Tsai, M.-J. AlOx-based resistive switching device with gradual resistance modulation for neuromorphic device application. In Proceedings of the 4th IEEE International Memory Workshop, Milan, Italy, 20–23 May 2012; pp. 1–4.
10. Jang, J.-W.; Park, S.; Burr, G.W.; Hwang, H.; Jeong, Y.-H. Optimization of conductance change in Pr 1–x Ca x MnO 3-based synaptic devices for neuromorphic systems. *IEEE Electron Dev. Lett.* **2015**, *36*, 457–459. [[CrossRef](#)]
11. Yu, S.; Wu, Y.; Jeyasingh, R.; Kuzum, D.; Wong, H.-S.P. An electronic synapse device based on metal oxide resistive switching memory for neuromorphic computation. *IEEE Trans. Electron. Dev.* **2011**, *58*, 2729–2737. [[CrossRef](#)]
12. Jin, X.; Rast, A.; Galluppi, F.; Davies, S.; Furber, S. Implementing spike-timing-dependent plasticity on SpiNNaker neuromorphic hardware. In Proceedings of the 2010 International Joint Conference on Neural Networks (IJCNN), Barcelona, Spain, 18–23 July 2010; pp. 1–8.
13. Qiao, N.; Mostafa, H.; Corradi, F.; Osswald, M.; Stefanini, F.; Sumislawska, D.; Indiveri, G. A reconfigurable on-line learning spiking neuromorphic processor comprising 256 neurons and 128K synapses. *Front. Neurosci.* **2015**, *9*, 141. [[CrossRef](#)]
14. Indiveri, G.; Linares-Barranco, B.; Legenstein, R.; Deligeorgis, G.; Prodromakis, T. Integration of nanoscale memristor synapses in neuromorphic computing architectures. *Nanotechnology* **2013**, *24*, 384010. [[CrossRef](#)]
15. Wang, J.; Hu, S.; Zhan, X.; Yu, Q.; Liu, Z.; Chen, T.P.; Yin, Y.; Hosaka, S.; Liu, Y. Handwritten-digit recognition by hybrid convolutional neural network based on hfo 2 memristive spiking-neuron. *Sci. Rep.* **2018**, *8*, 12546. [[CrossRef](#)]
16. Gentili, P.L.; Giubila, M.S.; Germani, R.; Romani, A.; Nicoziani, A.; Spalletti, A.; Heron, B.M. Optical Communication among Oscillatory Reactions and Photo-Excitable Systems: UV and Visible Radiation Can Synchronize Artificial Neuron Models. *Angew. Chem. Int. Ed.* **2017**, *56*, 7535–7540. [[CrossRef](#)] [[PubMed](#)]
17. Szaciłowski, K. Molecular Logic Gates Based on Pentacyanoferrate Complexes: From Simple Gates to Three-Dimensional Logic Systems. *Chem. Eur. J.* **2004**, *10*, 2520–2528. [[CrossRef](#)] [[PubMed](#)]
18. Mech, J.; Kowalik, R.; Podborska, A.; Kwolek, P.; Szaciłowski, K. Arithmetic device based on multiple Schottky-like junctions. *Aust. J. Chem.* **2010**, *63*, 1330–1333. [[CrossRef](#)]

19. Gentili, P.L.; Giubila, M.S.; Germani, R.; Heron, B.M. Photochromic and luminescent compounds as artificial neuron models. *Dyes Pigments* **2018**, *156*, 149–159. [[CrossRef](#)]
20. Pilarczyk, K.; Podborska, A.; Lis, M.; Kawa, M.; Migdał, D.; Szaciłowski, K. Synaptic Behavior in an Optoelectronic Device Based on Semiconductor-Nanotube Hybrid. *Adv. Electr. Mater.* **2016**, 1500471. [[CrossRef](#)]
21. Pilarczyk, K.; Wlazlak, E.; Przyczyna, D.; Blachecki, A.; Podborska, A.; Anathasiou, V.; Konkoli, Z.; Szaciłowski, K. Molecules, semiconductors, light and information: Towards future sensing and computing paradigms. *Coord. Chem. Rev.* **2018**, *365*, 23–40. [[CrossRef](#)]
22. Pilarczyk, K.; Daly, B.; Podborska, A.; Kwolek, P.; Silversen, V.A.D.; de Silva, A.P.; Szaciłowski, K. Coordination chemistry for information acquisition and processing. *Coord. Chem. Rev.* **2016**, *325*, 135–160. [[CrossRef](#)]
23. Horsman, C.; Stepney, S.; Wagner, R.C.; Kendon, V. When does a physical system compute? *Proc. Royal Soc. A* **2014**, *470*, 20140182. [[CrossRef](#)]
24. Stepney, S. The neglected pillar of material computation. *Physica D* **2008**, *237*, 1157–1164. [[CrossRef](#)]
25. Stepney, S.; Rasmussen, S.; Amos, M. (Eds.) *Computational Matter*; Springer: Cham, Switzerland, 2018.
26. Szaciłowski, K. *Infochemistry. Information Processing at the Nanoscale*; John Wiley & Sons: Chichester, UK, 2012.
27. Kendon, V.; Sebald, A.; Stepney, S. Heterotic computing: exploiting hybrid computational devices. *Phil. Trans. Royal Soc. A* **2015**, *373*, 20150091. [[CrossRef](#)] [[PubMed](#)]
28. Kendon, V.; Sebald, A.; Stepney, S. Heterotic computing: past, present and future. *Phil. Trans. Royal Soc. A* **2015**, *373*, 20140225. [[CrossRef](#)] [[PubMed](#)]
29. LeCun, Y.; Bottou, L.; Bengio, Y.; Haffner, P. Gradient-based learning applied to document recognition. *Proc. IEEE* **1998**, *86*, 2278–2324. [[CrossRef](#)]
30. Zucker, R.S.; Regehr, W.G. Short-term synaptic plasticity. *Annu. Rev. Physiol.* **2002**, *64*, 355–405. [[CrossRef](#)] [[PubMed](#)]
31. Jackman, S.L.; Regehr, W.G. The mechanisms and functions of synaptic facilitation. *Neuron* **2017**, *94*, 447–464. [[CrossRef](#)] [[PubMed](#)]
32. Appeltant, L.; Soriano, M.C.; Van der Sande, G.; Danckaert, J.; Massar, S.; Dambre, J.; Schrauwen, B.; Mirasso, C.R.; Fischer, I. Information processing using a single dynamical node as complex system. *Nat. Commun.* **2011**, *2*, 468. [[CrossRef](#)] [[PubMed](#)]
33. Zelaya-Angel, O.; Alvarado-Gil, J.J.; Lozada-Morales, R.; Vargas, H.; Ferreira da Silva, A. Bandgap shift in CdS semiconductor by photoacoustic spectroscopy: evidence of a cubic to hexagonal lattice transition. *Appl. Phys. Lett.* **1994**, *64*, 291–293. [[CrossRef](#)]
34. Degen, T.; Sadki, M.; Bron, E.; König, U.; Nénert, G. The HighScore suite. *Powder Diffr.* **2014**, *29*, S13–S18. [[CrossRef](#)]
35. Rietveld, H.M. A profile refinement method for nuclear and magnetic structures. *J. Appl. Cryst.* **1969**, *2*, 65–71. [[CrossRef](#)]
36. Skinner, B.J. Unit-cell edges of natural and synthetic sphalerites. *Am. Miner.* **1961**, *46*, 1399–1411.
37. Xu, Y.N.; Ching, W.Y. Electronic, optical and structural properties of some wurzite crystals. *Phys. Rev. B* **1993**, *48*, 4335–4351. [[CrossRef](#)] [[PubMed](#)]
38. Rasband, W.S. *ImageJ*; U.S. National Institutes of Health: Bethesda, MD, USA, 2012.
39. Fisher, S.A.; Fischer, T.M.; Carew, T.J. Multiple overlapping processes underlying short-term synaptic enhancement. *Trends Neurosci.* **1997**, *20*, 170–177. [[CrossRef](#)]
40. Salin, P.A.; Scanziani, M.; Malenka, R.C.; Nicoll, R.A. Distinct short-term plasticity at two excitatory synapses in the hippocampus. *Proc. Natl. Acad. Sci. USA* **1996**, *93*, 13304–13309. [[CrossRef](#)] [[PubMed](#)]
41. Wang, Z.; Joshi, S.; Savel'ev, S.E.; Jiang, H.; Midya, R.; Lin, P.; Hu, M.; Ge, N.; Strachan, J.P.; Li, Z. Memristors with diffusive dynamics as synaptic emulators for neuromorphic computing. *Nat. Mater.* **2017**, *16*, 101. [[CrossRef](#)] [[PubMed](#)]
42. Yu, Q.; Tang, H.; Hu, J.; Tan, K.C. *Neuromorphic Cognitive Systems. A Learning and Memory Centered Approach*; Springer International Publishing AG: Cham, Switzerland, 2017.
43. Szaciłowski, K.; Macyk, W.; Stochel, G. Light-driven OR and XOR programmable chemical logic gates. *J. Am. Chem. Soc.* **2006**, *128*, 4550–4551. [[CrossRef](#)] [[PubMed](#)]
44. Warzecha, M.; Oszejca, M.; Pilarczyk, K.; Szaciłowski, K. A three-valued photoelectrochemical logic device realising accept anything and consensus operations. *Chem. Commun.* **2015**, *51*, 3559–3561. [[CrossRef](#)] [[PubMed](#)]


45. Blachecki, A.; Mech-Piskorz, J.; Gajewska, M.; Mech, K.; Pilarczyk, K.; Szaciłowski, K. Organotitania-Based Nanostructures as a Suitable Platform for the Implementation of Binary, Ternary, and Fuzzy Logic Systems. *ChemPhysChem* **2017**, *18*, 1798–1810. [[CrossRef](#)]
46. Kasabov, N. From multilayer perceptrons and neurofuzzy systems to deep learning machines: which method to use? A survey. *Int. J. Inf. Technol. Security* **2017**, *9*, 3–24.
47. Kar, S.; Das, S.; Gosh, P.K. Applications of neuro fuzzy systems: A brief review and future outline. *Appl. Soft Comput.* **2014**, *15*, 243–259. [[CrossRef](#)]
48. Bavandpour, M.; Bagheri-Shouraki, S.; Soleimani, H.; Ahmadi, A.; Linares-Barranco, B. Spiking neuro-fuzzy clustering system and its memristor crossbar based implementation. *Microelectron. J.* **2014**, *45*, 1450–1462. [[CrossRef](#)]
49. Sammon, J.W. A nonlinear mapping for data structure analysis. *IEEE Trans. Computers* **1969**, *C18*, 401–409. [[CrossRef](#)]

**Sample Availability:** Samples of the polycrystalline CdS are available from the authors on request. The full set of output data with separability indices for all possible classification scenarios is available on request. The programs used for the data processing are available on request.



© 2019 by the authors. Licensee MDPI, Basel, Switzerland. This article is an open access article distributed under the terms and conditions of the Creative Commons Attribution (CC BY) license (<http://creativecommons.org/licenses/by/4.0/>).

# Towards Embedded Computation with Building Materials

Dawid Przychyna <sup>1,2,\*</sup>, Maciej Suchecki <sup>1,2</sup>, Andrew Adamatzky <sup>3</sup>  and Konrad Szaciłowski <sup>1,\*</sup> 

<sup>1</sup> Academic Centre for Materials and Nanotechnology, AGH University of Science and Technology, Mickiewiczza 30, 30-059 Krakow, Poland; suchecki@agh.edu.pl

<sup>2</sup> Faculty of Physics and Applied Computer Science, AGH University of Science and Technology, Mickiewiczza 30, 30-059 Krakow, Poland

<sup>3</sup> Department of Computer Science and Creative Technologies, Unconventional Computing Lab, University of the West of England, Bristol BS16 1QY, UK; andrew.adamatzky@uwe.ac.uk

\* Correspondence: dawidp@agh.edu.pl (D.P.); szacilow@agh.edu.pl (K.S.)

**Abstract:** We present results showing the capability of concrete-based information processing substrate in the signal classification task in accordance with *in materio* computing paradigm. As the Reservoir Computing is a suitable model for describing embedded *in materio* computation, we propose that this type of presented basic construction unit can be used as a source for “reservoir of states” necessary for simple tuning of the readout layer. We present an electrical characterization of the set of samples with different additive concentrations followed by a dynamical analysis of selected specimens showing fingerprints of memfractive properties. As part of dynamic analysis, several fractal dimensions and entropy parameters for the output signal were analyzed to explore the richness of the reservoir configuration space. In addition, to investigate the chaotic nature and self-affinity of the signal, Lyapunov exponents and Detrended Fluctuation Analysis exponents were calculated. Moreover, on the basis of obtained parameters, classification of the signal waveform shapes can be performed in scenarios explicitly tuned for a given device terminal.

**Keywords:** concrete; memristors; chaos; reservoir computing; signal classification



**Citation:** Przychyna, D.; Suchecki, M.; Adamatzky, A.; Szaciłowski, K. Towards Embedded Computation with Building Materials. *Materials* **2021**, *14*, 1724. <https://doi.org/10.3390/ma14071724>

Academic Editor: Moncef L. Nehdi

Received: 18 February 2021

Accepted: 27 March 2021

Published: 31 March 2021

**Publisher’s Note:** MDPI stays neutral with regard to jurisdictional claims in published maps and institutional affiliations.



**Copyright:** © 2021 by the authors. Licensee MDPI, Basel, Switzerland. This article is an open access article distributed under the terms and conditions of the Creative Commons Attribution (CC BY) license (<https://creativecommons.org/licenses/by/4.0/>).

## 1. Introduction

The upcoming era of the Internet of Things may require an energy-efficient pre-processing of signal in order to relieve microprocessors, especially in the case of relatively simple and routine processes. This part of computation can be delegated to solid state computational platforms based on materials, which are not associated with computation, e.g., various construction materials and other parts of the infrastructure. Here, we present a new approach towards unconventional in-materio computation using one of the most ubiquitous materials—Concrete. Small concrete blocks, containing admixtures of dopants (at micro and nanoscale) are demonstrated to present significant computational power to differentiate various waveforms utilizing the principles of reservoir computing. Complex dynamic response of concrete (doped and undoped) can be utilized for computation, and conversely—The dynamic response to known waveforms can be also used for detection of concrete defects, which, in far-fetched vision, can be used for self-monitoring of concrete structures and prevention of fatal accidents.

In developed countries, technology begins to encompass more and more aspects of life. Approximately 87% of humanity has access to electricity, according to the International Energy Agency [1]. In turn, less than half of the population has continuous access to the Internet [2]. Both these percentages increase every year, indicating progressing technological advancement of the human race. Nowadays, a technology that surrounds people with devices connected to the Internet—So-called Internet-of-things (IoT)—is beginning to gain increasing recognition [3]. It can take the form of “smart home”, with connected home appliances, heating, lighting, and wearables of inhabitants with a smartphone or smart speakers in an attempt to increase comfort and security of human life (e.g., in the form of

“elder care”). Other applications of IoT include healthcare, transportation, manufacturing, agriculture, or the military. The global market for IoT was valued at 164 mld \$ in 2018 [4] and it is predicted that the global market of “smart homes” can reach 58 mld \$ in 2020 [5]. At the same time, broadband access to the Internet as well as processing and storage of huge amount of data is extremely important. Fast information processing and storage, however, is an extremely energy-demanding technology. Therefore, at least some of the data processing should be delegated into substrates other than silicon, operating much slower, but at the same time consuming less energy. Alternatively, the waste heat produced during computing can be utilized for heating purposes in colder seasons. This may help to reduce the carbon footprint of computing, which nowadays accounts for 3.2% of the total anthropogenic carbon dioxide emissions [6].

Combination of ideas of *in materio* computing [7–11] and smart houses [12–15] immediately leads to the concept of computational concrete—Smart material combining construction and information processing features. If successful, such material should render each building an energy-efficient supercomputing device. What if walls would not only support the roof, but at the same time perform advanced, decentralized, and distributed computation? Each building block would sense itself and the environment, monitor safety of the construction, environmental pollution, and interact with humans in an intelligent way. This far-fetched vision has been already proposed and supported with some preliminary experimental and theoretical investigations [16]; however, long-term changes in concrete-based materials, which may lead to significant changes in electric properties of this material, should be taken into account in the case of out-of-lab applications. The selection of concrete as a computational medium seems shocking at the first glance. On the other hand, various unorthodox substrates have been already reported to perform advanced computation, including liquid marbles [17,18], slime molds [19,20], mycelia and fungi [21,22], algae [23], and photochromic solutions [24,25]. In principle, any physical system of sufficiently complex, structure, dynamics, and responsiveness to external stimuli can be utilized for information processing [26,27]. Because of the above, the choice of concrete as a ubiquitous computational medium seems reasonable. Furthermore, concrete is easily and readily prepared and fabricated in all sorts of shapes and structural systems. Its great simplicity lies in the fact that its constituents are ubiquitous and are readily available almost anywhere in the world. As a result of its ubiquity, functionality, and flexibility, it has become by far the most popular and widely used construction material in the world. It is particularly suitable for nano- or micro-modifications due to its peculiar internal structure. The ingredients can be selected, proportioned, and engineered to produce a concrete of specific strength and durability or other multifunctional properties, so it is “fit for purpose” for the job for which it is intended [28]. It can be produced in the form of precast products or as ready-mixed concrete, which is delivered in the familiar rotating concrete lorry. Currently, ingredients are optimized to make concrete strong, light-weight, low-thermally conductive, and durable when exposed to the environment. However new investigations are focused on concrete with embedded sensing [29–33].

Current IoT technology includes a broad set of topics such as sensors, embedded systems and machine learning (ML). ML methods can be used to improve the performance and security of intelligent infrastructure through the prediction of inhabitants’ actions based on their daily behavior [34,35]. This is realized by advanced network systems and software implementation of ML, whereas the building structure acts only as a skeleton to ensure its durability and insulation. Through the use of efficient ML methods, such as Reservoir Computing (RC), it becomes possible to develop intelligent infrastructure based on the building blocks capable of embedded, distributed information processing [16].

RC paradigm can be regarded as an extension of artificial neural networks (ANN) encompassing in its framework various physical substrates and processes [36–38]. Its main strength is the so-called “reservoir of states” possessing rich configuration state space of internal dynamics and performing nonlinear transformation of input signals. Thanks to its operation, simplification of the training process of ANN can be achieved, as probing of a

reservoir at the readout layer is the only part of the system that needs tuning [39,40]. Probing different features of the reservoir can enable the implementation of pattern recognition, assuming that the given configuration state space is diverse enough [41].

It has been shown by Wlaźlak et al. that a pure hardware RC system based on a single memristive nonlinear node operating in the delayed feedback loop can be used in the simple classification of signal amplitudes [42,43]. A more complex RC setup based on memristor array (supporting reservoir of states) with ANN software readout was studied as an image recognition system [44] and similar systems were considered for waveform recognition [45]. Therefore appropriate doping, which can induce memristive properties in concrete-based materials is desired. In our recent work, we have suggested the possibility of implementing RC concepts based on hybrid construction material—A “computing concrete” based infrastructure, that could potentially work as a massively interconnected parallel processor [16]. This assumption was drawn on the basis of rich and nonlinear responses of the device to the electrical stimulation. It was theorized that highly nonlinear response arose due to many different pathways for charge carriers and superimposition of capacitive behavior of the device with internal ionic movement. Buildings based on this type of embedded hardware could then possess multisensory properties and support forms of information processing.

This work is aimed at a demonstration that concrete, the most ubiquitous construction material can be used as a computational medium. While semiconducting materials, carbon nanomaterials and various polymers definitely offer better performance [46–48], concrete is the most ubiquitous construction material; therefore, despite very limited computational performance, it may be explored and ultimately utilized for some computational tasks. The inherent randomness of concrete seems to be a severe drawback, but materials with a certain degree of irreproducibility can be also studied as a computational medium [49]. Due to limited memristive properties and rather poor internal electrical dynamics, computational tasks in doped concrete can be performed only under a heterotic approach—*in materio* computation must be accompanied by advanced signal analysis using a conventional, software-based approach. Nevertheless, concrete proves to be a useful computational medium capable of basic signal classification.

## 2. Materials and Methods

The base material used in this experiment was ready-to-use concrete mix procured from Leroy Merlin and steel shavings supplied by POCh (Gliwice, Poland). Antimony sulfoiodide nanowires (SbSI) were synthesized in the following procedure. The reactants weighed and added in a ratio of 1 g Sb, 0.265 g S, and 1 g I<sub>2</sub>. All reactants were mixed in a 100 mL flask using 50 mL isopropanol as a solvent. The whole was placed in the ultrasonic bath previously heated to 50 °C for 6 h. The resulting product was isolated by centrifugation at 5000 rpm and washed three times with isopropanol and 2-fold with water after that product was left to dry.

The reference sample consisting of only concrete, as well as modified samples additionally containing 1%, 5%, and 10% of either SbSI, steel shavings, or half and half mixture by weight of both, were created using the following steps. In the bottom of a plastic container, holes 1cm apart were made, creating a 3 × 3 grid. Those holes served as an insertion point for silver wires that would go through the bulk of the material. After preparing the mold, the material was poured in. The whole was firmly shaken to remove pockets of air and allow content to settle within the container. Water was poured until all concrete was sufficiently saturated. Excessive water was drained through entry points of silver wires. The whole was repeatedly shaken to remove any air bubbles that might have appeared. The samples were left to settle and dry at ambient temperature for a week (Figure 1). Samples have been stored and measured in an air-conditioned room with constant temperature (22 °C) and humidity (25%) in order to prevent excessive drying or accumulation of moisture.

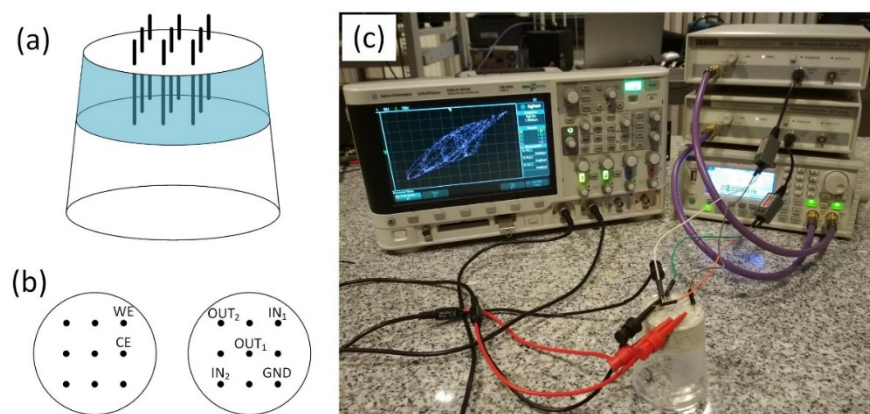


**Figure 1.** Schematic view of the computing concrete sample (a), pinouts for voltammetric (left) and signal processing experiments (b) and a real photo of an experimental setup (c). WE and CE stands for working and counter electrodes, respectively. IN1 and IN2 are signal input connectors, OUT1 and OUT2 output ones, GND is a common ground.

Voltammetric and spectroscopic measurements were performed on SP-300 potentiostat (BioLogic, Seyssinet-Pariset, France). Cyclic voltammetry was measured in a  $-5\text{ V}/5\text{ V}$  potential window with a scan rate of  $100\text{ mV/s}$ . Electrochemical impedance spectroscopy (EIS) was measured in the  $7\text{ MHz}-100\text{ mHz}$  frequency window, with  $50\text{ mV}$  AC perturbation.

To perform signal mixing in the computing concrete system, two separate arbitrary signals from a dual-channel arbitrary waveform generator (TG5012, Aim-TTi, Huntingdon, Cambridgeshire, UK) were applied via the WA301 waveform amplifier (Aim-TTi, Huntingdon, Cambridgeshire, UK) and impedance matching baluns (1VP-C, Top-View Tek, Shenzhen, Guangdong, China) to two chosen terminals of the sample as indicated in Figure 1. One channel was tuned to  $300\text{ Hz}$  with a sinusoidal wave shape, whereas the second channel was tuned to  $290\text{ Hz}$ ,  $280\text{ Hz}$ , and  $275\text{ Hz}$  with three different wave shapes for each of these frequencies (sinusoidal, triangular, and square). Application of symmetrical AC signals is crucial, as any DC component of potential higher than that of water electrolysis (approximately  $1.23\text{ V}$ ) may lead to irreversible changes in the material, even lower DC components may result in electrode corrosion. In that scenario, the sinusoidal signal could be perceived as a base probing signal to classify the second signal of unknown shape in a classification task. Both signals were  $10\text{Vpp}$  in amplitude. Processed waveforms were recorded on a digital oscilloscope (DSO-X2014A, Agilent Technologies, Santa Clara, CA, USA). Examples of recorded time series are shown in Figures S1 and S2 (Supplementary Materials).

Signals recorded at OUT1 terminal were of higher quality, less scattered and were used for further processing. Only in one case (Petrosian fractal dimension), the OUT2 signals were used along with OUT1 ones. Signal processing and analysis were performed in Python (Python Software Foundation, Beaverton, OR, USA). Nolitsa module was used for the time delay (Delayed Mutual Information method) and embedding dimension (False Nearest Neighbors and Average False Neighbors) estimation. By using Nolds (Python module for nonlinear dynamics study) Correlation Dimension, maximum Lyapunov exponent and Detrended fluctuation analysis (DFA) scores were calculated. Further study of dynamical parameters (Petrosian and Katz fractal dimensions, as well as sample and approximate entropy) was performed using the Entropy Python module for a one-dimensional time series analysis. All analysis was carried out for normalized time series.

### 3. Results

Initially, all obtained samples have been characterized with cyclic voltammetry within  $\pm 5\text{ V}$  window. All samples have shown moderate conductivity and currents up to  $2.5\text{ mA}$  have been recorded for samples doped with both semiconducting nanowires and metal shavings (Figure 2). It was found that undoped concrete, as well as concrete with low



content of any dopant, shows a predominant capacitive hysteresis loop (characteristic for ferroelectric materials) [50–53] superimposed on Ohmic current. This behavior should be expected for mixed oxide materials [54,55]. The strongest features characteristic for ferroelectric materials has been observed in the case of 10% of SbSI admixture, which is fully consistent with pronounced ferroelectric properties of this material [56–58], but this non-ideal capacitive behavior was observed in the majority of cases, the complex character of I/E curves may be interpreted in terms of mixed ferroelectric/antiferroelectric character of studied samples [59]. In light of the complex chemical and phase structure of samples, this may be fully justified.

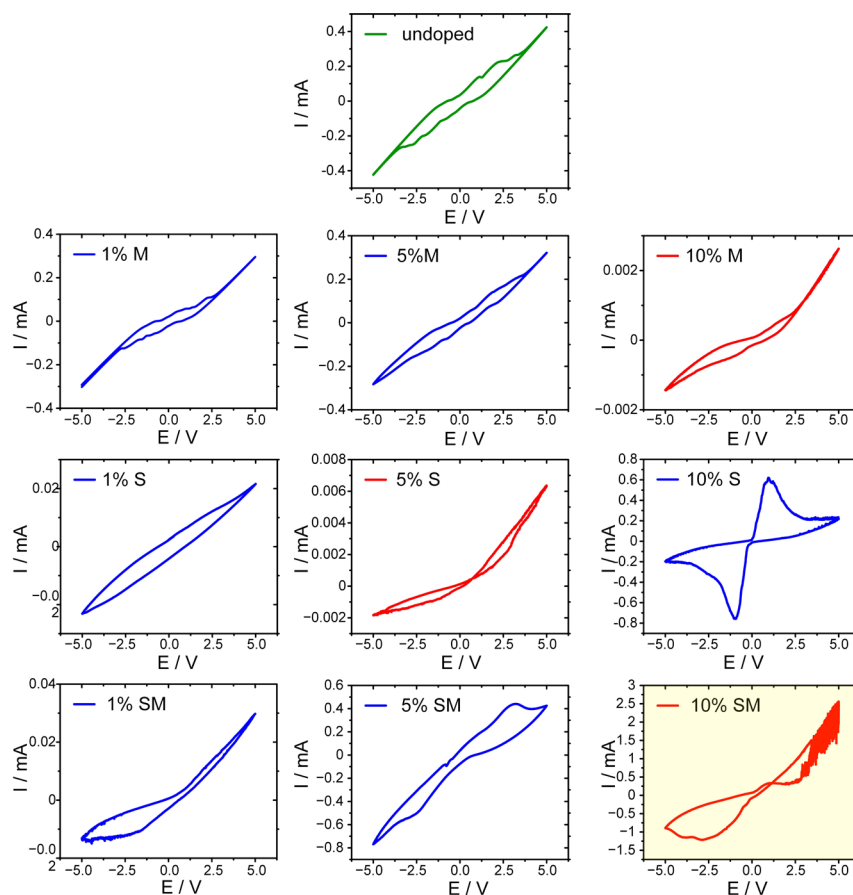


**Figure 2.** Voltamperometric characteristics of undoped concrete sample (top, dark green) and concrete containing various amounts of dopants: M—Metal shavings, S—Antimony sulfoiodide nanowires, SM—1:1 mixture of both dopants. Some samples show pinched hysteresis loops typical for memristive devices (red) whereas the others are of capacitive character (blue). The most pronounced memristive behavior was observed in the case of 10% SM sample, highlighted in yellow.

Detailed analysis of these phenomena is, however, out of scope of this study. In just few cases memristive behavior was observed, with the most pronounced resistive switching in the case of 10% SM sample (Figure 2). Therefore, this combination of both dopants was selected for further investigations and for the reservoir computing experiments.

Capacitive properties of selected samples were further addressed using impedance spectroscopy. The junction capacitances are low, which can be seen as a decrease of impedance at high frequency region. This effect is less pronounced for doped materials. Moreover, it was found that the Ohmic component increases with increasing concentration of the dopant (Figure 3a). Furthermore, undoped concrete show relatively high phase shift angle at low frequencies (Figure 3b), which can be associated with a Warburg impedance related to a slow diffusion process within a ceramic matrix. Increasing concentration of

dopant reduces this contribution because other transport mechanisms start to dominate (Figure 3c).

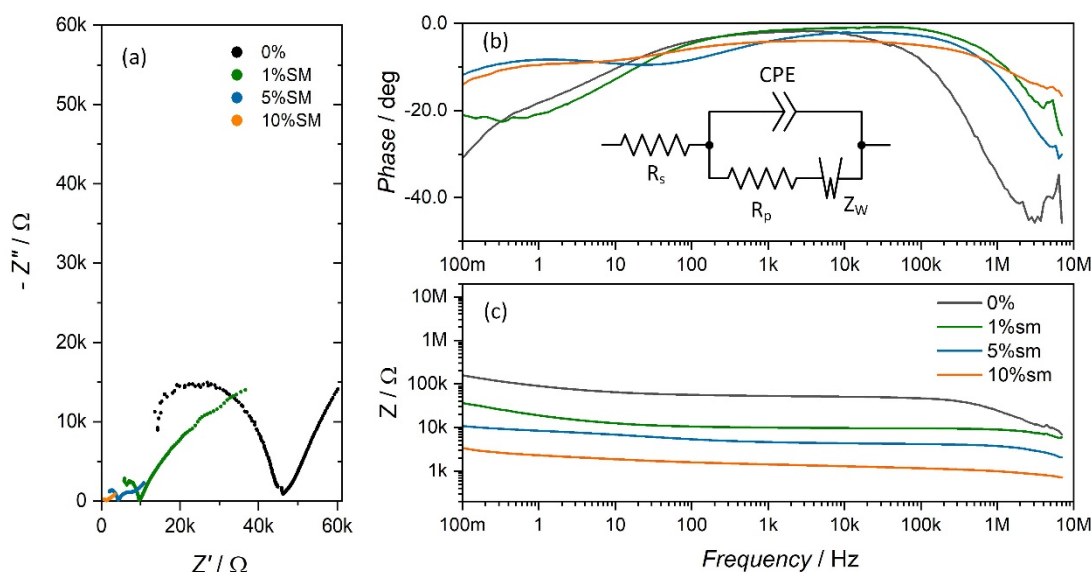


**Figure 3.** Impedance spectra of undoped and metal+semiconductor doped concrete samples: Nyquist plot (a) phase shift angles (b) and Bode plots (c). A simplified equivalent circuit is also shown. The linear Warburg component at low frequencies is visible only in the case of the undoped sample, whereas increased doping is correlated with a decrease of impedance results as well as with significant curvature of the low-frequency arm in Nyquist plots.

Based on registered signals (Figures S1 and S2), further information processing and analysis were performed based on several methods mentioned *vide supra*. Due to the lack of control over the spatial arrangement of 3d semiconductor/metallic grains suspended in a cement matrix, geometric change of the place from which we read the signals also changes to some extent the calculated parameters. For this reason, the signal readout layer must be properly calibrated to enable signal classification.

### 3.1. Estimation of Time Delay and Embedding Dimension Parameters

At first, Augmented Dickey–Fuller (ADF) test was calculated to check data stationarity. Results show that for a sample size  $T = 500$  the critical values were not exceeded in any case, the highest  $p$ -value was obtained for sin/square pair (no more than 1.25%), which means that the null hypothesis can be rejected (that the data possess “unit root” —the presence of stochastic trend) and the time series are in fact stationary [60].

According to the Taken’s theorem (which was also shown independently by Packard et al. [61]), single time series can be used to reconstruct so called “delay-coordinate map” based on chosen displacement (time delay) [62–64]. Reconstructed attractors possess the same mathematical properties (e.g., Lyapunov exponents, fractal dimensions of the attractor or eigenvalues of a fixed point) as the original manifolds of a given dynamical system (usually obtained on the basis of a set of ordinary differential equations). It comes down to the proper selection of a set of the adjacent coordinates with an equal time offset between them. Classical methods of determining the time delay measure the independence of subsequent points in the phase space. Basically, for infinite, noise-free time series, the selection of time delay can be chosen almost arbitrary [62], but for experimental data, it is good practice to determine its appropriate value. The time delay for the unfoldment of the attractor was estimated using the Delayed Mutual Information (DMI) [65] and Autocorrelation methods [64]. By applying information theory (for which Shannon provided mathematical formalism [66]) to strange attractors, we can quantify the degree of “surprise” new message provides—in the case of attractors these messages are in the form of values given attractor will take during measurement. The DMI method is based on the quantitative approach

to uncertainty about time delayed coordinates given the measure of a chosen coordinate. The first minima of calculated functional of joint probability distribution indicates the suitable  $\tau$  value (Figure 4a). In turn, the first zero of the autocorrelation function gives proper time delay. The autocorrelation method yields the most suitable delay value of three, whereas the DMI method, which is more reliable, yields  $\tau = 4$ . To inspect the validity of the calculated  $\tau$  value, several delay times were used to reconstruct attractors in the phase space for a randomly selected data set (Figure S3). It can be observed, that  $\tau = 4$  is optimal for the unfoldment of the attractors. It is good practice to choose the smallest time delay required, to avoid phenomena called the irrelevance and redundancy [64,67]. Irrelevance occurs when the reconstructed attractor folds over on itself thus making it more complicated than the original manifold, whereas redundancy means the concentration of attractor shape on the diagonal set. The plot of delayed mutual information versus time delay (Figure 4a) clearly indicates significant chaotic character of all recorded time series with a contribution of a stochastic component. These curves present oscillatory character (fingerprint of chaotic character) and a steep slope as small  $\tau$  values (stochasticity fingerprint) [68].

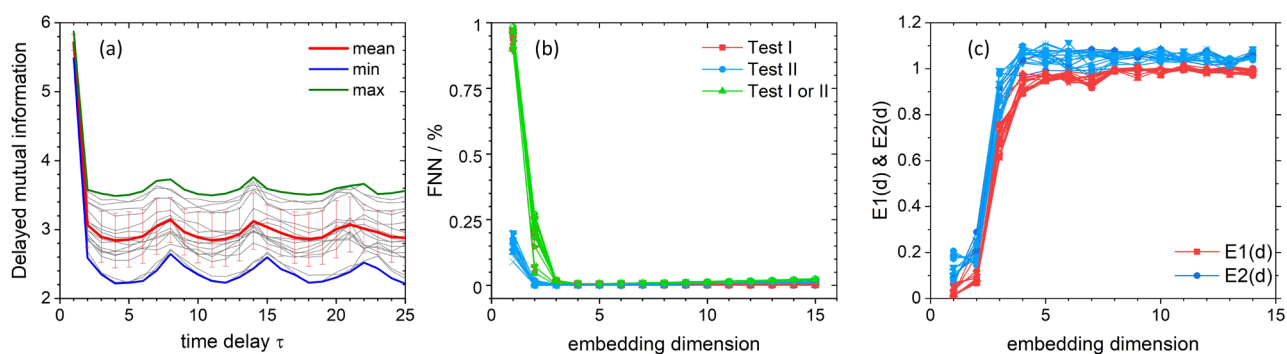


**Figure 4.** Results for time delay and embedding dimension calculations for all-time series recorded for pristine and doped (10%MS) concrete samples. Graphs present results from Delayed Mutual Information approach (a), False Nearest Neighbors test (b) and Average False Neighbors method (c). Calculated time delay  $\tau = 4$  (first minima of DMI, averaged over all data sets), whereas suitable embedding dimension equals four (0% of FNN in all tests and saturation of E1 & E2 in AFN). Descriptions of test criteria can be found in the text.

Based on a calculated time delay, time-delay embedded trajectories have been plotted (Figures S4 and S5) [68]. On both sets of trajectories, highly complex system dynamics can be observed. Frequency ratio of applied stimulation influences irregularities in observed traces, which is represented in beats present in the waveforms (Figures S2 and S3) and recurring decimal in these frequency ratios. For 300 Hz/290 Hz, recurrence of decimal place is observed for 28 digits, for 300 Hz/280 Hz for seven digits and for 300 Hz/275 Hz frequency ratio for two digits. The attractors are more regular for the cases where there is a smaller number of periodic digits, as well as for a smaller period of observed beats in the registered waveforms. Moreover, with the progressive deviation from the shape of the basic sinusoidal signal, more and more irregular trajectories can be observed (which may be associated with a greater number of harmonic components of the triangular and square wave signals).

In order to analyze the nonlinear dynamics of the recorded time series, the appropriate embedding dimension was determined using the False Nearest Neighbor (FNN) method proposed by Kennel et. al. [69] (Figure 4b) and the Average False Neighbors (AFN) method proposed by Cao [70] (Figure 4c). The FNN method tests whether neighboring points of a specific trajectory in a given embedding dimension are actually neighbors due to the system dynamics or whether they are next to each other only because of the insufficient dimensionality of the phase space. By examining how the number of neighbors changes as a function of dimension, one can determine the appropriate embedding dimension for

further analysis. To check the percentage of false neighbors relative to real neighbors, three criteria are used—the first criterion increases the embedding dimension and tests the ratio of Euclidean distance between pairs of points compared to the distance between points with previous embedding dimension value, the second criterion compare relation between reconstructed attractor in higher dimensions and its original size, whereas the third criterion uses both previous tests. Both criteria are compared to a heuristically chosen threshold, values of which are suggested in the original work of Kennel et al. The second condition tries to eliminate the situation where the limited amount of data and the noise present in them causes that the points that are not next to each other are treated as neighbors. To overcome possible problems with choosing proper threshold values in FNN test, Cao proposed his modified FNN method, called AFN or Cao’s test. The main difference is that instead of calculating relative distance ratios separately, a mean value of all of these distances is analyzed between a subsequent increase of embedding dimension (E1(d) in Figure 4c). Cao further defines another testing criterion (E2(d) in Figure 4c), where ratio of mean distances between subsequent embedding dimensions is calculated for the time delayed one dimensional time series and not for reconstructed vectors as in E1(d) criterion. Previously estimated time delay from DMI and autocorrelation methods was used to form time delayed vectors needed in FNN and AFN methods.

FNN results show that the number of false neighbors for all test criteria drops to 0% starting from the embedding dimension of 4 (Figure 4b). This outcome is consistent with the results obtained by the AFN method, where both criteria—E1 and E2—reach saturation starting from the same embedding dimension as in the one indicated in the FNN test (Figure 4c). For this reason, further analysis of nonlinear dynamics was made using the embedding dimension of 4. For a practical reason, however, the trajectories are depicted for embedding dimension of 3 (Figures S4 and S5). These figures can be considered as 3D projections of 4D trajectories obtained by the removal of the fourth coordinate.

The complex character of the recorded time series was further characterized with nonlinear dynamics methods (largest Lyapunov exponent), self-similarity methods (detrended fluctuation analysis, fractal dimensions), and disorder-based methods: dynamic (sample entropy) and structural (permutation entropy) entropy-based methods [71].

### 3.2. Analysis of Non-Linear Dynamics

Lyapunov exponents are one of the main indicators of chaos in the study of data possessing non-linear properties [72–74]. It probes the rate of divergence of concomitant trajectories in phase space. The exponential rate of divergence of two chaotic trajectories can be described as follows [75] Equation (1):

$$\Delta(t) \sim \Delta_0 e^{\lambda t} \quad (1)$$

where  $\lambda$  is the Lyapunov exponent, and  $\Delta_0$  is the initial separation vector. Due to differences in initial conditions based on a given separation vector, one can obtain a spectrum of Lyapunov exponents. It is common to refer to the largest one as the Maximum Lyapunov exponent (MLE) that is used to probe the predictability and stability of the given data sample. To characterize trajectory instability, MLE can be defined as follows Equation (2):

$$\lambda = \lim_{t \rightarrow \infty} \lim_{\Delta_0 \rightarrow 0} \frac{1}{t} \ln \frac{\Delta(t)}{\Delta_0} \quad (2)$$

Positive MLE strongly indicates the chaotic nature of system dynamics, especially the sensitivity to the initial conditions, which is known as the “Butterfly effect” [76]. Calculated MLE shows, that for seven cases, an un-doped sample presents chaotic behavior (positive MLE) in registered waveforms. In contrast, the doped sample exhibits chaotic behavior in five cases overall (Figure 5a). This is generally consistent with the delayed mutual information dependence on a time delay (Figure 4a), which also indicates chaotic features

of the recorded time series. An overall increase of MLE can be observed for sine waveforms, whereas an overall decrease in MLE is present for the square wave shapes.

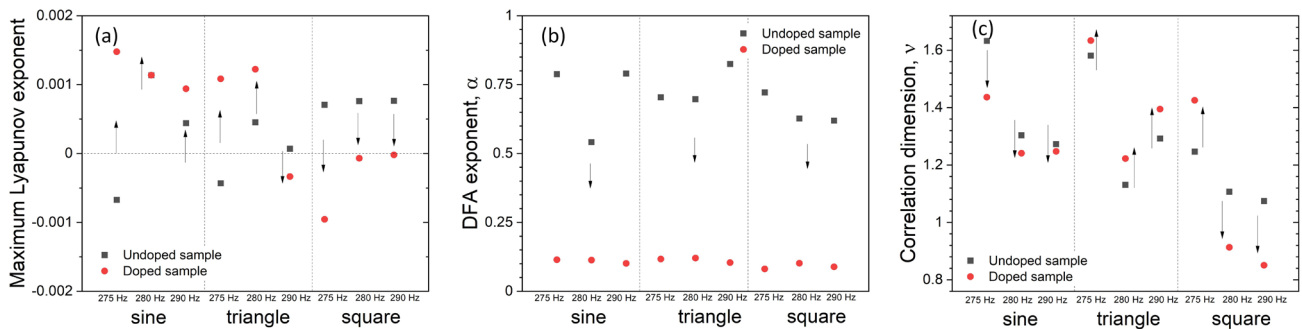


**Figure 5.** A set of dynamics indices for recorded time series. Maximum Lyapunov exponent for of a time series recorded for different input frequencies/waveforms (a). Detrended fluctuation analysis performed for time series recorded for different input frequencies/waveforms (b). Correlation dimension of a time series calculated for different input frequencies/waveforms (c). Arrows indicate the direction of changes upon doping.

Detrended Fluctuation Analysis (DFA) is a method for determining the statistical self-affinity of a signal [77,78]. Self-affinity can be regarded as a property of a fractal time series [79]. Using this parameter, one can easily distinguish whether the stimulated sample was doped or not (Figure 5b). Results indicate correlated ( $\alpha > 0.5$ ) and anti-correlated ( $\alpha < 0.5$ ) character of the registered time series for undoped and doped samples respectively. Both scaling factors  $\alpha$  lie between 0 and 1, indicating the stationary character of the time series (in accordance with ADF results, vide supra). Furthermore, those results indicate the presence of memory in registered time series, [77] which is consistent with the presence of measured memristive traces. The anti-correlated character of time series registered from doped samples may originate from the possibility of flipping resistive state, observed in CV measurements (Figure 2).

Another parameter used in the study of chaotic and dynamical systems is the correlation dimension ( $\nu$ ) [80]. It is used to probe dimensionality of the space occupied by a set of random points and is often referred to as a type of fractal dimension. For time series of points described as Equation (3):

$$\left\{ \overrightarrow{X(i)} \right\}_{i=1} \equiv \left\{ \overrightarrow{X(t+i\tau)} \right\}_{i=1} \quad (3)$$

where  $\tau$  is arbitrary, but fixed time increment. The correlation integral is defined as Equation (4):

$$C(r) = \lim_{N \rightarrow \infty} \frac{1}{N^2} \sum_{i,j=1}^N \Theta \left( r - \left| \overrightarrow{X(i)} - \overrightarrow{X(j)} \right| \right) \quad (4)$$

where  $\Theta(X)$  is a Heaviside step function. For small number  $r$ , correlation integral behaves according to a power law, Equation (5):

$$C(r) \sim r^\nu \quad (5)$$

where  $\nu$  is interpreted as a fractal dimension [80,81]. As can be seen in Figure 5c, the change of correlation dimension is strongly correlated with the shape of mixed signals. The correlation dimension is only shifting downwards for the mixing of sin/sin signals, only upwards for triangle signals, whereas for square (280–290 Hz) it shifts downwards and for 275 Hz  $\nu$  shifts upwards. Based solely on this fact, classification of signal shape can be performed (overall  $\nu$  decrease: sine, overall  $\nu$  increase: triangle, mixed  $\nu$  trend: square).

### 3.3. Classification of a Waveform on the Basis of the Decision Tree Method

As was already mentioned, changing the readout terminal influences obtained dynamical parameters. With this change, analysis of obtained parameters allows for different classification scenario. Analysis of Sample Entropy [82,83] and fractal dimensions (vide infra) gives an alternative approach towards signal classification. Sample entropy is a technique used for probing regularity/complexity (unpredictability of fluctuations) of time-series signals. It possesses desirable characteristics in the form of data length independence and relatively trouble-free implementation. It is defined as a negative natural logarithm of conditional probability between distances of two sets of points taken from template vector which acts as a representation of a given data sample.

For time series, Equation (6):

$$N = \{x_1, x_2, x_3, \dots, x_N\} \tag{6}$$

the template vector takes a form of Equation (7):

$$X_m(i) = \{x_i, x_{i+2}, x_{i+2}, \dots, x_{i+m-1}\} \tag{7}$$

where  $m$  is embedding dimension. Based on this, sample entropy can be described as Equation (8):

$$S_S = -\ln \frac{A}{B} \tag{8}$$

where  $A$  and  $B$  are numbers of template vector pairs having distance ( $d[X_{m+1}(i), X_{m+1}(j)]$  and  $d[X_m(i), X_m(j)]$ , for  $A$  and  $B$ , respectively) lower than given tolerance  $r$  (which is taken as a factor of standard deviation).

If analyzed data is ordered, then templates for  $m$  points are also similar for  $m+1$  points, and  $A/B$  approaches unity [83]. In that case, the negative logarithm will approach 0. Results show, that in most cases (Figure 6a, apart from 300 Hz/290 Hz sin-square), obtained time series are more ordered for doped sample, which may be associated with less noise present in the signal (cf. Figures S1 and S2).

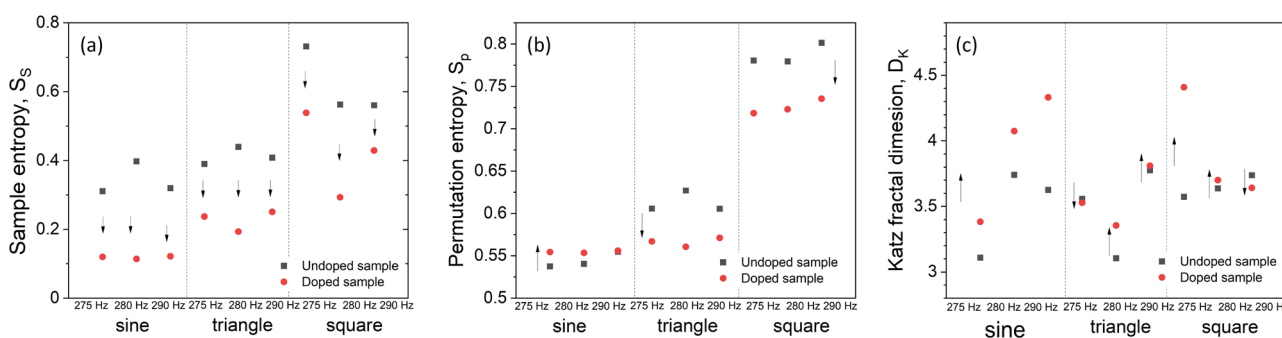


**Figure 6.** A set of dynamics indices for recorded time series. Sample entropy for different input frequencies/waveforms (a). Permutation entropy for different input frequencies/waveforms combinations (b). Values of Katz fractal dimension score for doped and un-doped sample different input frequencies/waveforms (c). Arrows indicate the direction of changes upon doping.

Trends observed in sample entropy changes (Figure 6a) do not allow unambiguous classification of waveforms, therefore other criteria must be used in parallel.

Permutation entropy is considered as a natural measure of time series complexity via reconstruction of a phase space of any dynamic system [84,85]. Here it was calculated according to Yan et al. [86] according to the Takens–Maine theorem. The phase space of a time series  $\{x(i), i = 1, 2, 3, \dots, N\}$  can be reconstructed as Equation (9):

$$\left\{ \begin{array}{l} X(1) = \{x(1), x(1 + \tau), \dots, x(1 + (m - 1)\tau)\} \\ \dots \\ X(i) = \{x(i), x(i + \tau), \dots, x(i + (m - 1)\tau)\} \\ \dots \\ X(N - (m - 1)\tau) = \{x(N - (m - 1)\tau), x(N - (m - 2)\tau), \dots, x(N)\} \end{array} \right. \quad (9)$$

where  $m$  is the embedded dimension and  $\tau$  is the time delay. Then, the  $m$  number of real values contained in each  $X(i)$  can be arranged in an increasing order as Equation (10):

$$\{x(i + (j_1 - 1)\tau) \leq x(i + (j_2 - 1)\tau) \leq \dots \leq x(i + (j_m - 1)\tau)\} \quad (10)$$

If there exist two or more elements in  $X(i)$  that have the same value, e.g.,  $x(i + (j_1 - 1)\tau) = x(i + (j_2 - 1)\tau)$ , their original positions can be sorted in such a way that for  $j_1 \leq j_2$  the relation  $x(i + (j_1 - 1)\tau) \leq x(i + (j_2 - 1)\tau)$  will be obtained. Hence, any vector  $X(i)$  can be mapped onto a group of symbols, Equation (11):

$$S(l) = (j_1, j_2, \dots, j_m) \quad (11)$$

where  $l = 1, 2, \dots, k \leq m!$ .  $S(l)$  is one of the  $m!$  symbol permutations, which is mapped onto the  $m$  number symbols  $(j_1, j_2, \dots, j_m)$  in  $m$ -dimensional embedding space. If  $P_1, P_2, \dots, P_k$  are used to denote the probability distribution of each symbol sequences, respectively, and the condition described by Equation (12):

$$\sum_{l=1}^k P_l = 1 \quad (12)$$

is fulfilled, the permutation entropy of a time series  $\{x(i), i = 1, 2, 3, \dots, N\}$  can be defined as a Shannon entropy for the  $k$  symbol sequence, Equation (13):

$$S_p(m) = -\sum_{l=1}^k P_l \ln P_l \quad (13)$$

As the maximum value of  $S_p(m)$  for a uniform probability distribution is equal to  $\ln m!$ , it is usually given as a normalized value, Equation (14):

$$S_p(m) = \frac{-\sum_{l=1}^k P_l \ln P_l}{\ln m!} \quad (14)$$

The values of permutation entropy serve as a measure of time series randomness. Smaller values indicate less chaotic behavior whereas values approaching the unity indicate highly chaotic behavior and thus unpredictability of time series. These data suggest that time series recorded for sine and triangle waveforms are significantly more ordered (i.e., less chaotic) than those for square waves, which may be utilized as a classification tool (Figure 6b).

Analysis of Petrosian [87] and Katz fractal dimensions [88] allows a different approach for signal classification. Katz fractal dimension ( $D_K$ ) calculates the fractal dimension of data directly from the waveforms without the need for their abstract representation. It is defined as Equation (15):

$$D_K = \frac{\log_{10} n}{\log_{10} \frac{d}{L} + \log_{10} n} \quad (15)$$

where  $d$  is calculated fractal dimension,  $n = L/a$  ( $n$  is used for normalization of distances — $L$  is the total sum of lengths of the successive points, and  $a$  is averaged distance between successive points) and  $d$  is the maximum distance between the first point and any other point within the data set.  $D_K$  is known to overestimate probed fractal dimension, hence large differences in obtained  $D_K$  and correlation dimension scores [89]. Figure 5c shows calculated Katz fractal dimensions of attractors for various waveform and frequency combinations.

Another approach in probing fractal dimension of time series was suggested by Petrosian [87]. Petrosian fractal dimension ( $D_P$ ) is calculated for binarized time series. It is defined as follows in Equation (16):

$$D_P = \frac{\log_{10} N}{\log_{10} N + \log_{10} \frac{N}{N+0.4N_\delta}} \quad (16)$$

where  $N$  is the length of the time series, and  $N_\delta$  is the number of sign changes in the signal derivative. It can be observed in Figure 7, that Petrosian fractal dimensions increase in the series sine<triangle<square for both output signals and both materials. There is, however, a significant change in the undoped/doped difference, as indicated by black arrows in Figure 7.

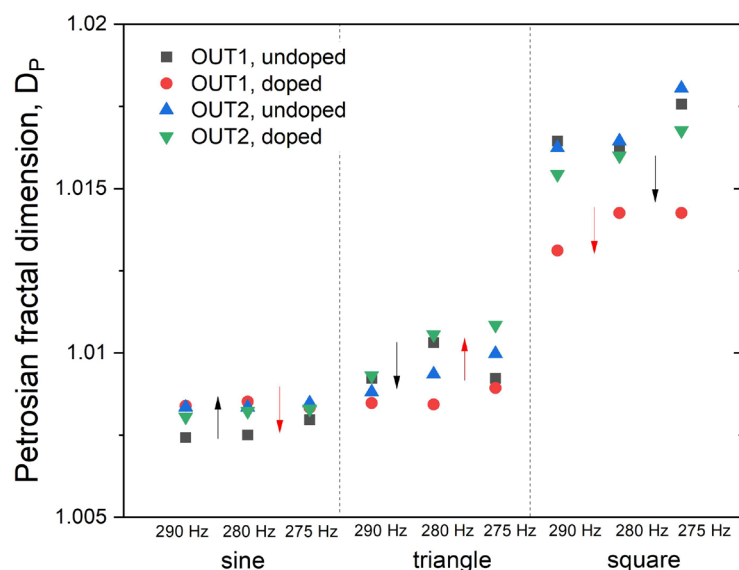


**Figure 7.** Petrosian fractal dimension for time series collected from OUT1 (a) and OUT2 (b) device terminals. Black arrows indicate trends for OUT1, whereas red arrows for OUT2 (cf. Figure 1 for terminal markings).

#### 4. Discussion

Each individual dynamics index cannot serve as a reliable classification index for waveform discrimination. Therefore, observed trends, taken collectively, constituted a set of criteria that can be used for waveform discrimination on the basis of the signal dynamics in pristine and heavily doped concrete blocks. These criteria, along with the dynamic analysis presented above, can be regarded as a readout layer of the reservoir computing system.

Based on different trends of change of the given parameter between doped and undoped samples (Table 1), one can classify signal shapes in a decision tree manner. A decision tree could be constructed as follows:

- ✓ If calculated permutation entropy decreases and Katz fractal dimension is of mixed trends, then the signal is of the triangle wave shape.
- ✓ If calculated Petrosian fractal dimension is increasing, then the signal is of sinusoidal shape, if its decreasing (and was increasing in the previous step), then it is of square shape.



**Table 1.** A list of trends observed between different shapes of mixed signals for different methods of analysis. Trends are shown for the doped sample in relation to the un-doped one.

Chaos Index	Sine	Triangle	Square
Permutation entropy	increases	decreases	increases
Katz fractal dimension	increases	mixed	increases
Petrosian fractal dimension	increases	decreases	decreases

As already mentioned, changing the readout terminal influences obtained dynamical parameters (*vide supra*). With this change, the analysis of obtained parameters allows for different classification scenarios. Based solely on the Petrosian fractal dimension of registered time series but analyzed from two different device terminals (OUT1 and OUT2, Figure 7) another classification variant of a decision tree manner can be obtained.

A decision tree based on trends summarized in Table 2 could be constructed as follows:

1. If the calculated Petrosian fractal dimension (OUT1) is increasing, then the signal is of sinusoidal shape, if its decreasing (and was increasing in the previous step), then it is of square or triangular shape.
2. If calculated Petrosian fractal dimension (OUT2) is increasing, then the signal is of triangular shape, if its decreasing (and was decreasing in the previous step), then it is of square shape.

**Table 2.** A list of trends observed between different shapes of mixed signals for different methods of analysis. Trends are shown for the doped sample in relation to the un-doped one.

Chaos Index	Sine	Triangle	Square
Petrosian fractal dimension (OUT1)	Increases	Decreases	Decreases
Petrosian fractal dimension (OUT2)	Decreases	Increases	Decreases

Along with various trends (changes in various dynamic parameters upon transition from pristine to doped concrete) another classification system, based on the whole collection of time series can be also derived (Figure 8). Three selected criteria provide the best classification of waveforms, and also provide means for the classification of concrete material. Interestingly, detrended fluctuation analysis yields exponent  $\alpha$ , which can differentiate between doped and undoped concrete, but does not provide means for signal classification. Time series recorded for pristine concrete are much higher ( $\alpha > 0.50$ ) than for doped concrete ( $\alpha < 0.25$ ). This indicates a statistically higher correlation of time series for pristine material and anticorrelation for doped one. This may be associated with quite different dielectric responses of both materials. Sample entropy ( $S_s$ ) is not a useful classification criterion, both due to the same trend over all samples (*vide supra*) and due to very scattered values (Figure 8). Petrosian fractal dimension for sine and triangular waveforms are significantly lower than for square signals, therefore it may serve as a crude criterion for detection of square wave signals. Finally, the permutation entropy provides a weak classification tool for all waveform shapes: sine waves yield the lowest values, triangular waves the intermediate ones, whereas square waves the highest values of  $S_p$ . This criterion should be considered as a fuzzy one, as the boundary between sine and triangular waves is not well defined.

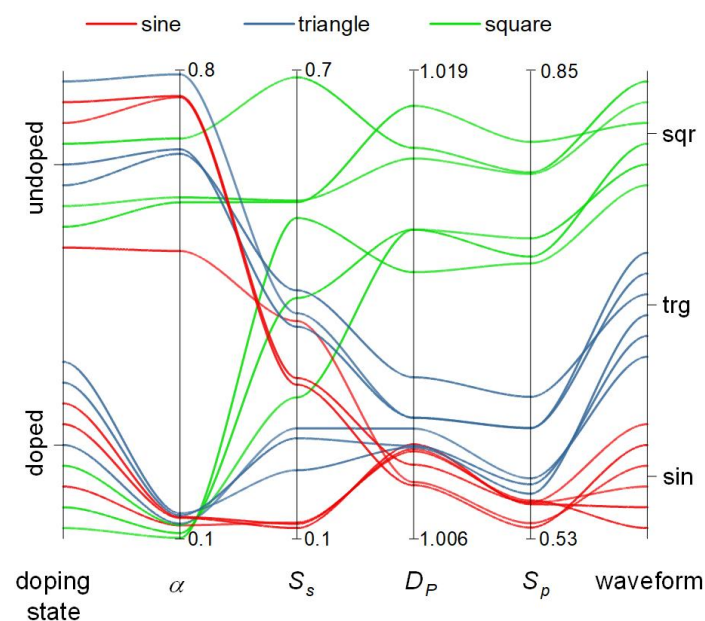


**Figure 8.** Parallel coordinate plot for all-time series and selected dynamic criteria: detrended fluctuation exponent ( $\alpha$ ), sample entropy ( $S_s$ ), Petrosian fractal dimension ( $D_p$ ) and permutation entropy ( $S_p$ ). Detrended fluctuation exponent can serve as a classification factor for the concrete doping state, whereas permutation entropy significantly classifies time series according to their waveforms.

Despite the requirement of a complex numerical processing of the data in order to extract the classification parameters the results presented here clearly indicate that computation with appropriately prepared concrete blocks is possible. Surprisingly, concrete—one of the most ubiquitous construction materials—shows complex chaotic dynamics when stimulated with acoustic frequency electrical signals. Moreover, these dynamics can serve as a classification tool. The selection of a wider range of frequencies and waveforms should lead to more complex classification patterns. It seems, that concrete itself presents internal electrical dynamics so complex, that in principle it should be capable of much more complex computational tasks in real-time. Recently reported speech recognition in coupled nano vortex oscillators [90] is based on a system of comparable dynamics (however shifter to radio frequency range). Therefore, any classification of acoustic signals required their mapping into radio frequencies. The system presented here performs complex classification tasks directly on amplified signals.

The device presented in this paper (Figure 9) can be regarded as a heterotic reservoir computing system. The heteroticity originates from combination of *in materio* reservoir processing of input signals followed by software algorithms for post-processing. In a far-fetched vision, an alternative, *in materio*-based readout should be considered, but the required complexity of signal processing seems to exceed the state of the art of *in materio* reservoir computers. The observed features indicate, that the small concrete blocks with silver wire electrodes show a set of features sufficient for reservoir computing. The fading memory feature is represented by capacitive and memristive character of the device, whereas internal dynamics are provided by the drive signal. It shows the echo state property, as the output at the selected point reflects features on inner electrical dynamics. The dynamic response of the system is complex enough to provide sufficient separability (in the sense of Stone–Weierstrass theorem [91]) of the input data [92]. It also presents some generalization features, as the observed output space (trends of several criteria) is much smaller than the (infinite) input space of various signals. Due to the specific task and material properties of pristine and doped concrete the output layer, especially the post-processing part, is relatively complex. It should be noted, however, that this was the requirement for a relatively hard task for memristive reservoir computing systems and that the memristive properties of deliberately chosen materials were very poor. Despite

this, the classification task is successfully performed. Future upgrade of this system may involve fuzzy logic inference engine (or multinary logic), as the output trends are not crisp values, and therefore the fuzzy descriptors may be more adequate. Interestingly, multinary and fuzzy logic may be also implemented in related materials [93–95].

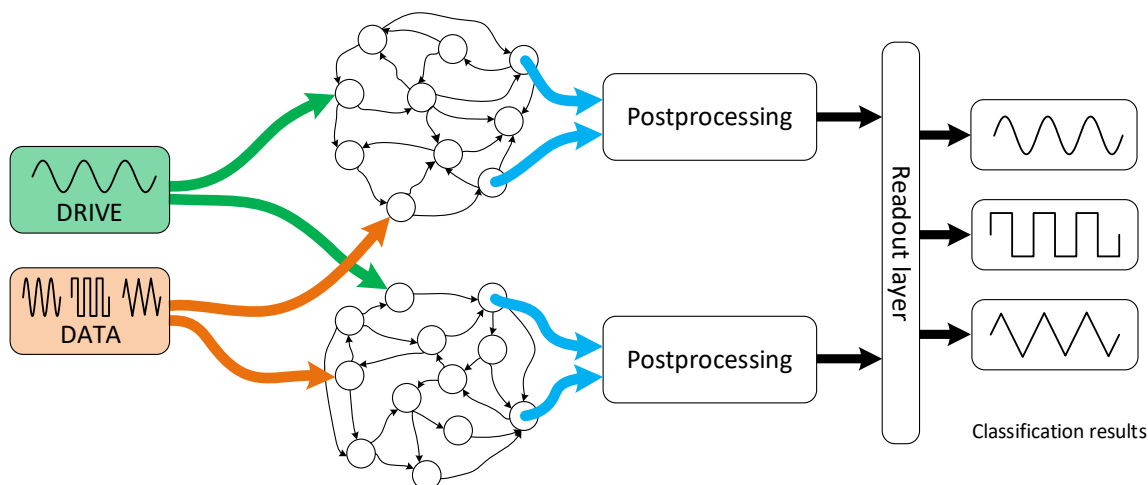


**Figure 9.** A scheme of a dual concrete-based reservoir computing system used for waveform classification.

The computational performance of concrete would depend, however, not only on the doping state but many other factors: humidity, temperature, and the age of samples. The dependence of performance on environmental factors can be used for various sensing purposes, while aging processes may irreversibly change the computing performance of concrete artifacts. Although this may not be beneficial from an information processing point of view, it is very interesting in itself and may also find applications in the future as a tool for monitoring the status of concrete structures.

Aging of concrete involved both chemical changes (hydrolysis and corrosion of silicate network) as well as self-weight consolidation of the granular skeleton. This leads to changes of hydro-mechanical properties and displacements of the ensembles of functional nanoparticles. If the “computing circuits” (i.e., the assemblies of metallic and/or semiconducting particles) in concrete were fixed the ageing would be detrimental to the computational properties of the concrete. However, the computing circuits prototypes presented in this work are highly distributed (hence can be regarded as amorphous), and therefore deformations or even topological modifications of the ensembles of functional particles should not significantly affect the computing abilities of the concrete materials. The interfacial and external computing elements will be continuously adjusting to the ever-changing morphologies of the concrete. Moreover, a reconfiguration of the embedded computing circuits during concrete ageing might be advantageous because novel computational properties will emerge. This may be taken as a distant analogy to the nervous system, which at different stages of development shows different functionalities: intensive learning abilities at an early age, peaking classification in adulthood, and slowly declining memory in older age.

Along with the classification of signals, the concrete-based reservoir computing device can be used in a reversed way (cf. Figure 8). One can consider the doping state as the input and the specific responses to electrical stimulation as the output. Due to the fact that the fading memory echo state machines are universal approximators, as analyzed in detail by Ortega et al. [91,96,97], they can operate easily in a reversed way. This reversed operation of reservoir computer may be ultimately used to infer the state of the concrete sample. This would require a set of standard stimulation protocols along with a database of responses corresponding to the different states of concrete samples. Although this has not been addressed experimentally, there are numerous reports on the use of electrical measurements

(e.g., impedance spectroscopy) for monitoring of concrete elements [98–100]. We can envision, that combination of classical electrical measurements with signal-processing features of concrete can lead to more efficient concrete monitoring techniques and may contribute to increased safety and prevention of fatal accidents. However, this far-fetched vision requires years of further intense studies in the fields of concrete technologies and reservoir computing.

## 5. Conclusions

In this article, the classification of signal shapes was shown based on *in materio* computing concrete hardware system. Samples present a highly non-linear response in regard to data transformation, possess rich configuration state space, and their dynamics (when stimulated with a simple sine wave drive) are represented in the form of four-dimensional trajectories. These features make them a suitable platform for reservoir computing implementation. Depending on used terminals for the readout layer, different classification scenarios can be achieved. Moreover, as it can be seen in the case of the detrended fluctuation exponent, some of the chaos indices can be used for the classification of the doping state of concrete. Whereas this feature has not been explored deeply in this study, in principle it may constitute a new tool for real-time monitoring of concrete structures, detection of structural degradation and prevention of fatal accidents. The presented results can be treated as proof of the concept for the possibility of information processing and classification tasks performed by appropriately doped ubiquitous construction materials.

It should be noted, however, that the performance of concrete-based computing devices is very limited. Classification of waveforms in concrete can be performed only with the support of time-series processing algorithms operating at classical computers. Therefore, the presented results can be regarded as an approach towards concrete-based heterotic computing. On the other hand, the same numerical algorithms cannot perform signal classification due to fundamental reasons: chaos indices (like Lyapunov exponents, signal entropies and fractal dimensions) are not suited for the classification of smooth periodic signals. The concrete samples themselves also cannot perform this type of classification. Combination of two apparently incompatible approaches results in successful computation. It also illustrates the theoretical concept addressing the balance between the complexity of the information processing systems and the interface. In the studied case the processing system is simplified to the extreme (almost a piece of stone); therefore, the post-processing and readout must be more complex [41].

Further development of the concept can bring the realization of more aspects of a multisensory infrastructure capable of information processing based on its embedded hardware and intelligent computing houses as a far-fetched vision.

**Supplementary Materials:** The following are available online at <https://www.mdpi.com/article/10.3390/ma14071724/s1>, Figure S1: Registered timeseries for undoped concrete sample, Figure S2: Registered timeseries for doped concrete sample, Figure S3: 2D projections of trajectories (return plots) of the signal obtained for two sine waves (275 and 300 Hz) in undoped concrete, Figure S4: Embedded time-delay trajectories of time series recorded for un-doped concrete sample for various input waveforms and frequencies, constructed with time delay  $\tau = 4$ , Figure S5: Embedded time-delay trajectories of time series recorded for doped sample (10% SM) for various input waveforms and frequencies, constructed with time delay  $\tau = 4$ .

**Author Contributions:** D.P. conducted most of the experimental data (EIS, time series, part of the CVs), performed the time-series analysis, developed decision-tree based classification approach, and wrote large sections of the manuscript. M.S. prepared the samples, performed nanowire synthesis, and performed some electrochemical experiments. A.A. formulated the idea of concrete computation, contributed to the discussion of results, and revised the manuscript. K.S. formulated the general experimental approach, performed analysis of electrochemical data, wrote several sections of the manuscript, and developed the second classification approach, as well as integrated and revised the whole manuscript. All authors have read and agreed to the published version of the manuscript.

**Funding:** The authors acknowledge the financial support from the Polish National Science Centre within the MAESTRO and PRELUDIUM projects (grant agreement No. UMO-2015/18/A/ST4/00058 and UMO-2018/31/N/ST5/03112). DP has been partly supported by the EU Project POWR.03.02.00-00-I004/16.

**Institutional Review Board Statement:** Not applicable.

**Informed Consent Statement:** Not applicable.

**Data Availability Statement:** The data that support the findings of this study are available from the corresponding author upon reasonable request. All time series as well as electrochemical and impedance spectroscopy data are available as asci as well as instrument-specific binary files.

**Acknowledgments:** Authors thank Grzegorz Kulinowski for his assistance in maintaining the constant environmental conditions during sample preparation and measurements.

**Conflicts of Interest:** The authors declare no conflict of interest.

## References

1. Richter, F. Electricity Access Keeps Climbing Globally. Available online: <https://www.statista.com/chart/16552/electricity-access-worldwide/> (accessed on 26 March 2020).
2. De Silva, A.P.; McClenaghan, N.D.; McCoy, C.P. *Handbook of Electron Transfer*; Balzani, V., de Silva, A.P., Gould, E.J., Eds.; WILEY-VCH: Weinheim, Germany, 2000; Volume 5, p. 156.
3. Kraeling, M.; Brogioli, M.C. Optimizing Embedded Software for Power. In *Software Engineering for Embedded Systems*; Oshana, R., Kraeling, M., Eds.; Newnes: Newton, MA, USA, 2019; pp. 465–499. [CrossRef]
4. Global IoT Market Report, History and Forecast 2013–2025, Breakdown Data by Companies, Key Regions, Types and Application. Available online: <https://www.itintelligencemarkets.com/reports/Global-IoT-Analytics-Market-Report--History-and-Forecast-2013-2025--Breakdown-Data-by-Companies--Key-Regions--Types-and-Application-2619> (accessed on 10 February 2021).
5. Total Market Value of the Global Smart Homes Market in 2014 and 2020. Available online: <https://www.statista.com/statistics/420755/global-smart-homes-market-value/> (accessed on 26 March 2020).
6. Truemann, C. Why Data Centres are the New Frontier in the Fight against Climate Change. Available online: <https://www.computerworld.com/article/3431148/why-data-centres-are-the-new-frontier-in-the-fight-against-climate-change.html> (accessed on 10 January 2020).
7. Miller, J.F.; Downing, K. Evolution in materio: Looking beyond the silicon box. In Proceedings of the 2002 NASA/DoD Conference on Evolvable Hardware, Washington, DC, USA, 15–18 July 2002; pp. 167–176.
8. Harding, S.; Miller, J.F. Evolution in Materio. In *Encyclopedia of Complexity and Systems Science*; Meyers, R.A., Ed.; Springer: New York, NY, USA, 2009; pp. 3220–3233. [CrossRef]
9. Miller, J.F.; Harding, S.L.; Tufte, G. Evolution-in-materio: Evolving computation in materials. *Evol. Intell.* **2014**, *7*, 49–67. [CrossRef]
10. Dale, M.; Miller, J.F.; Stepney, S. Reservoir Computing as a Model for In-Materio Computing. In *Advances in Unconventional Computing: Volume 1: Theory*; Adamatzky, A., Ed.; Springer International Publishing: Cham, Switzerland, 2017; pp. 533–571. [CrossRef]
11. Miller, J.F.; Hickinbotham, S.J.; Amos, M. In Materio Computation Using Carbon Nanotubes. In *Computational Matter*; Stepney, S., Rasmussen, S., Amos, M., Eds.; Springer International Publishing: Cham, Switzerland, 2018; pp. 33–43. [CrossRef]
12. Yassine, A.; Singh, S.; Hossain, M.S.; Muhammad, G. IoT big data analytics for smart homes with fog and cloud computing. *Future Gener. Comput. Syst.* **2019**, *91*, 563–573. [CrossRef]
13. Shuhaiber, A.; Mashal, I. Understanding users' acceptance of smart homes. *Technol. Soc.* **2019**, *58*, 101110. [CrossRef]
14. Mokhtari, G.; Anvari-Moghaddam, A.; Zhang, Q. A New Layered Architecture for Future Big Data-Driven Smart Homes. *IEEE Access* **2019**, *7*, 19002–19012. [CrossRef]
15. Fedotov, D.; Matsuda, Y.; Minker, W. From Smart to Personal Environment: Integrating Emotion Recognition into Smart Houses. In Proceedings of the 2019 IEEE International Conference on Pervasive Computing and Communications Workshops (PerCom Workshops), Kyoto, Japan, 11–15 March 2019; pp. 943–948.
16. Adamatzky, A.; Szaciłowski, K.; Konkoli, Z.; Werner, L.C.; Przczyzna, D.; Sirakoulis, G.C. On buildings that compute. A proposal. In *From Astrophysics to Unconventional Computation*; Adamatzky, A., Kendon, V., Eds.; Springer Nature Switzerland AG: Cham, Switzerland, 2020.
17. Adamatzky, A.; Chiolerio, A.; Szaciłowski, K. Liquid metal droplet solves maze. *Soft Matter* **2020**, *16*, 1455–1462. [CrossRef] [PubMed]
18. Fullarton, C.; Draper, T.C.; Phillips, N.; Mayne, R.; de Lacy Costello, B.P.J.; Adamatzky, A. Evaporation, Lifetime, and Robustness Studies of Liquid Marbles for Collision-Based Computing. *Langmuir* **2018**, *34*, 2573–2580. [CrossRef] [PubMed]
19. Adamatzky, A. A would-be nervous system made from a slime mold. *Artif. Life* **2015**, *21*, 73–91. [CrossRef]
20. Adamatzky, A. *Advances in Physarum Machines. Sensing and Computing with Slime Mold*; Springer International Publishing: Cham, Switzerland, 2016.

21. Adamatzky, A. Towards fungal computer. *Interface Focus* **2018**, *8*, 20180029. [[CrossRef](#)] [[PubMed](#)]
22. Adamatzky, A. On spiking behaviour of oyster fungi *Pleurotus djamor*. *Sci. Rep.* **2018**, *8*, 7873. [[CrossRef](#)]
23. Phillips, N.; Draper, T.C.; Mayne, R.; Adamatzky, A. Marimo machines: Oscillators, biosensors and actuators. *J. Biol. Eng.* **2019**, *13*, 72. [[CrossRef](#)] [[PubMed](#)]
24. Gentili, P.L.; Micheau, J.-C. Light and chemical oscillations: Review and perspectives. *J. Photochem. Photobiol. C* **2019**, 100321. [[CrossRef](#)]
25. Szaciłowski, K.; Stasicka, Z. Molecular switches based on cyanoferrate complexes. *Coord. Chem. Rev.* **2002**, *229*, 17–26. [[CrossRef](#)]
26. Horsman, C.; Stepney, S.; Wagner, R.C.; Kendon, V. When does a physical system compute? *Proc. R. Soc. A* **2014**, *470*, 20140182. [[CrossRef](#)]
27. Stepney, S.; Rasmussen, S.; Amos, M. *Computational Matter*; Springer: Cham, Switzerland, 2018.
28. Dimov, D.; Amit, I.; Gorrie, O.; Barnes, M.D.; Townsend, N.J.; Neves, A.I.S.; Withers, F.; Russo, S.; Craciun, M.F. Ultrahigh Performance Nanoengineered Graphene–Concrete Composites for Multifunctional Applications. *Adv. Funct. Mater.* **2018**, *28*, 1705183. [[CrossRef](#)]
29. Downey, A.; D’Alessandro, A.; Laflamme, S.; Ubertaini, F. Smart bricks for strain sensing and crack detection in masonry structures. *Smart Mater. Struct.* **2017**, *27*, 015009. [[CrossRef](#)]
30. Li, H.; Ou, J.P. Smart Concrete, Sensors and Self-Sensing Concrete Structures. *Key Eng. Mater.* **2008**, *400*, 69–80. [[CrossRef](#)]
31. Han, B.; Ding, S.; Yu, X. Intrinsic self-sensing concrete and structures: A review. *Measurement* **2015**, *59*, 110–128. [[CrossRef](#)]
32. Materazzi, A.L.; Ubertaini, F.; D’Alessandro, A. Carbon nanotube cement-based transducers for dynamic sensing of strain. *Cem. Concr. Compos.* **2013**, *37*, 2–11. [[CrossRef](#)]
33. Quinn, W.; Kelly, G.; Barrett, J. Development of an embedded wireless sensing system for the monitoring of concrete. *Struct. Health Monit.* **2012**, *11*, 381–392. [[CrossRef](#)]
34. Mahdavejad, M.S.; Rezvan, M.; Barekatin, M.; Adibi, P.; Barnaghi, P.; Sheth, A.P. Machine learning for internet of things data analysis: A survey. *Digit. Commun. Netw.* **2018**, *4*, 161–175. [[CrossRef](#)]
35. Xiao, L.; Wan, X.; Lu, X.; Zhang, Y.; Wu, D. IoT security techniques based on machine learning: How do IoT devices use AI to enhance security? *IEEE Sign. Proc. Mag.* **2018**, *35*, 41–49. [[CrossRef](#)]
36. Konkoli, Z. Reservo On Reservoir Computing: From Mathematical Foundations to Unconventional Applications. In *Advances in Unconventional Computing*; Springer: Cham, Switzerland, 2017; pp. 573–607.
37. Konkoli, Z.; Nichele, S.; Dale, M.; Stepney, S. Reservoir computing with computational matter. In *Computational Matter*; Springer: Cham, Switzerland, 2018; pp. 269–293.
38. Athanasiou, V.; Konkoli, Z. On using reservoir computing for sensing applications: Exploring environment-sensitive memristor networks. *Int. J. Parallel Emergent Distrib. Syst.* **2018**, *33*, 367–386. [[CrossRef](#)]
39. Jaeger, H. The “echo state” approach to analysing and training recurrent neural networks—with an erratum note. *Bonn Ger. Ger. Natl. Res. Cent. Inf. Technol. GMD Tech. Rep.* **2001**, *148*, 13.
40. Maass, W.; Natschläger, T.; Markram, H. Real-time computing without stable states: A new framework for neural computation based on perturbations. *Neural Comput.* **2002**, *14*, 2531–2560. [[CrossRef](#)] [[PubMed](#)]
41. Konkoli, Z.; Stepney, S.; Broersma, H.; Dini, P.; Nehaniv, C.L.; Nichele, S. Philosophy of computation. In *Computational Matter*; Stepney, S., Rasmussen, S., Amos, M., Eds.; Springer: Cham, Switzerland, 2018.
42. Właźlak, E.; Marzec, M.; Zawal, P.; Szaciłowski, K. Memristor in a Reservoir System—Experimental Evidence for High-Level Computing and Neuromorphic Behavior of PbI<sub>2</sub>. *ACS Appl. Mater. Interfaces* **2019**, *11*, 17009–17018. [[CrossRef](#)] [[PubMed](#)]
43. Właźlak, E.; Zawal, P.; Szaciłowski, K. Neuromorphic Applications of a Multivalued [SnI<sub>4</sub> ((C<sub>6</sub>H<sub>5</sub>)<sub>2</sub>SO)<sub>2</sub>] Memristor Incorporated in the Echo State Machine. *ACS Appl. Electron. Mater.* **2020**, *2*, 329–338. [[CrossRef](#)]
44. Du, C.; Cai, F.; Zidan, M.A.; Ma, W.; Lee, S.H.; Lu, W.D. Reservoir computing using dynamic memristors for temporal information processing. *Nat. Commun.* **2017**, *8*, 2204. [[CrossRef](#)] [[PubMed](#)]
45. Tanaka, G.; Nakane, R.; Yamane, T.; Takeda, S.; Nakano, D.; Nakagawa, S.; Hirose, A. Waveform Classification by Memristive Reservoir Computing. In *Neural Information Processing*; Liu, D., Xie, S., Li, Y., Zhao, D., El-Alfy, E.M., Eds.; Springer: Cham, Switzerland, 2017; Volume 4.
46. Tanaka, G.; Yamane, T.; Héroux, J.B.; Nakane, R.; Kanazawa, N.; Takeda, S.; Numata, H.; Nakano, D.; Hirose, A. Recent advances in physical reservoir computing: A review. *Neural Netw.* **2019**, *115*, 100–123. [[CrossRef](#)]
47. Przyczyna, D.; Zawal, P.; Mazur, T.; Strzelecki, M.; Gentili, P.L.; Szaciłowski, K. In-materio neuromimetic devices: Dynamics, information processing and pattern recognition. *Jpn. J. Appl. Phys.* **2020**, *59*, 050504. [[CrossRef](#)]
48. Przyczyna, D.; Pecqueur, S.; Vuillaume, D.; Szaciłowski, K. Reservoir Computing for Sensing—An Experimental Approach. *Int. J. Unconv. Comput.* **2019**, *14*, 267–284.
49. Bose, S.K.; Lawrence, C.P.; Liu, Z.; Makarenko, K.S.; van Damme, R.M.J.; Broersma, H.J.; van der Wiel, W.G. Evolution of a designless nanoparticle network into reconfigurable Boolean logic. *Nat. Nanotechnol.* **2015**, *10*, 1048–1052. [[CrossRef](#)]
50. Tian, B.; Liu, L.; Yan, M.; Wang, J.; Zhao, Q.; Zhong, N.; Xiang, P.; Sun, L.; Peng, H.; Shen, H.; et al. A Robust Artificial Synapse Based on Organic Ferroelectric Polymer. *Adv. Electron. Mater.* **2019**, *5*, 1800600. [[CrossRef](#)]
51. Oh, S.; Hwang, H.; Yoo, I.K. Ferroelectric materials for neuromorphic computing. *APL Mater.* **2019**, *7*, 091109. [[CrossRef](#)]
52. Robert, G.; Damjanovic, D.; Setter, N. Preisach modeling of ferroelectric pinched loops. *Appl. Phys. Lett.* **2000**, *77*, 4413–4415. [[CrossRef](#)]

53. Park, M.H.; Lee, Y.H.; Kim, H.J.; Kim, Y.J.; Moon, T.; Kim, K.D.; Müller, J.; Kersch, A.; Schroeder, U.; Mikolajick, T.; et al. Ferroelectricity and Antiferroelectricity of Doped Thin HfO<sub>2</sub>-Based Films. *Adv. Mater.* **2015**, *27*, 1811–1831. [[CrossRef](#)] [[PubMed](#)]
54. Böske, T.S.; Müller, J.; Bräuhaus, D.; Schröder, U.; Böttger, U. Ferroelectricity in hafnium oxide thin films. *Appl. Phys. Lett.* **2011**, *99*, 102903. [[CrossRef](#)]
55. Jin, L.; Li, F.; Zhang, S. Decoding the Fingerprint of Ferroelectric Loops: Comprehension of the Material Properties and Structures. *J. Am. Ceram. Soc.* **2014**, *97*, 1–27. [[CrossRef](#)]
56. Audzijonis, A.; Grigas, J.; Kajokas, A.; Kvedaravičius, S.; Paulikas, V. Origin of ferroelectricity in SbSI. *Ferroelectrics* **1998**, *219*, 37–45. [[CrossRef](#)]
57. Mistewicz, K.; Nowak, M.; Stróż, D. A Ferroelectric-Photovoltaic Effect in SbSI Nanowires. *Nanomaterials* **2019**, *9*, 580. [[CrossRef](#)] [[PubMed](#)]
58. Sotome, M.; Nakamura, M.; Fujioka, J.; Ogino, M.; Kaneko, Y.; Morimoto, T.; Zhang, Y.; Kawasaki, M.; Nagaosa, N.; Tokura, Y.; et al. Spectral dynamics of shift current in ferroelectric semiconductor SbSI. *Proc. Nat. Acad. Sci. USA* **2019**, *116*, 1929. [[CrossRef](#)] [[PubMed](#)]
59. Pintilie, L.; Boldyreva, K.; Alexe, M.; Hesse, D. Coexistence of ferroelectricity and antiferroelectricity in epitaxial PbZrO<sub>3</sub> films with different orientations. *J. Appl. Phys.* **2008**, *103*, 024101. [[CrossRef](#)]
60. Fuller, W.A. *Introduction to Statistical Time Series*; John Wiley & Sons: Hoboken, NJ, USA, 2009; Volume 428.
61. Packard, N.H.; Crutchfield, J.P.; Farmer, J.D.; Shaw, R.S. Geometry from a time series. *Phys. Rev. Lett.* **1980**, *45*, 712. [[CrossRef](#)]
62. Takens, F. Detecting strange attractors in turbulence. In *Dynamical Systems and Turbulence*, Warwick 1980; Springer: Cham, Switzerland, 1981; pp. 366–381.
63. Sauer, T.; Yorke, J.A.; Casdagli, M. Embedology. *J. Stat. Phys.* **1991**, *65*, 579–616. [[CrossRef](#)]
64. Bradley, E.; Kantz, H. Nonlinear time-series analysis revisited. *Chaos* **2015**, *25*, 097610. [[CrossRef](#)]
65. Fraser, A.M.; Swinney, H.L. Independent coordinates for strange attractors from mutual information. *Phys. Rev. A* **1986**, *33*, 1134. [[CrossRef](#)] [[PubMed](#)]
66. Shannon, C.E. *The Mathematical Theory of Communication*, by CE Shannon (and Recent Contributions to the Mathematical Theory of Communication), W. Weaver; University of Illinois Press: Urbana, IL, USA, 1949.
67. Casdagli, M.; Eubank, S.; Farmer, J.D.; Gibson, J. State space reconstruction in the presence of noise. *Phys. D Nonlinear Phenom.* **1991**, *51*, 52–98. [[CrossRef](#)]
68. Daw, C.S.; Finney, C.E.A.; Tracy, E.R. A review of symbolic analysis of experimental data. *Rev. Sci. Instrum.* **2003**, *74*, 915–930. [[CrossRef](#)]
69. Kennel, M.B.; Brown, R.; Abarbanel, H.D. Determining embedding dimension for phase-space reconstruction using a geometrical construction. *Phys. Rev. A* **1992**, *45*, 3403. [[CrossRef](#)] [[PubMed](#)]
70. Cao, L. Practical method for determining the minimum embedding dimension of a scalar time series. *Phys. D Nonlinear Phenom.* **1997**, *110*, 43–50. [[CrossRef](#)]
71. Tang, L.; Lv, H.; Yang, F.; Yu, L. Complexity testing techniques for time series data: A comprehensive literature review. *Chaos Solitons Fractals* **2015**, *81*, 117–135. [[CrossRef](#)]
72. Eckmann, J.-P.; Kamphorst, S.O.; Ruelle, D.; Ciliberto, S. Liapunov exponents from time series. *Phys. Rev. A* **1986**, *34*, 4971–4979. [[CrossRef](#)]
73. Kantz, H. A robust method to estimate the maximal Lyapunov exponent of a time series. *Phys. Lett. A* **1994**, *185*, 77–87. [[CrossRef](#)]
74. Vallejo, J.C.; Sanjuan, M.A.F. *Predictability of Chaotic Dynamics*; Springer Nature: Cham, Switzerland, 2017.
75. Vulpiani, A. *Chaos: From Simple Models to Complex Systems*; World Scientific: Singapore, 2010; Volume 17.
76. Lorenz, E. The butterfly effect. *World Sci. Ser. Nonlinear Sci. Ser. A* **2000**, *39*, 91–94.
77. Hardstone, R.; Poil, S.-S.; Schiavone, G.; Jansen, R.; Nikulin, V.V.; Mansvelder, H.D.; Linkenkaer-Hansen, K. Detrended fluctuation analysis: A scale-free view on neuronal oscillations. *Front. Physiol.* **2012**, *3*, 450. [[CrossRef](#)] [[PubMed](#)]
78. Peng, C.-K.; Buldyrev, S.V.; Havlin, S.; Simons, M.; Stanley, H.E.; Goldberger, A.L. Mosaic organization of DNA nucleotides. *Phys. Rev. E* **1994**, *49*, 1685. [[CrossRef](#)] [[PubMed](#)]
79. Mandelbrot, B. How long is the coast of Britain? Statistical self-similarity and fractional dimension. *Science* **1967**, *156*, 636–638. [[CrossRef](#)] [[PubMed](#)]
80. Grassberger, P.; Procaccia, I. Characterization of strange attractors. *Phys. Rev. Lett.* **1983**, *50*, 346. [[CrossRef](#)]
81. Nerenberg, M.; Essex, C. Correlation dimension and systematic geometric effects. *Phys. Rev. A* **1990**, *42*, 7065. [[CrossRef](#)] [[PubMed](#)]
82. Richman, J.S.; Moorman, J.R. Physiological time-series analysis using approximate entropy and sample entropy. *Am. J. Physiol. -Heart Circ. Physiol.* **2000**, *278*, H2039–H2049. [[CrossRef](#)]
83. Richman, J.S.; Lake, D.E.; Moorman, J.R. Sample entropy. In *Methods in Enzymology*; Elsevier: Amsterdam, The Netherlands, 2004; Volume 384, pp. 172–184.
84. Bandt, C.; Pompe, B. Permutation Entropy: A Natural Complexity Measure for Time Series. *Phys. Rev. Lett.* **2002**, *88*, 174102. [[CrossRef](#)] [[PubMed](#)]
85. Riedl, M.; Müller, A.; Wessel, N. Practical considerations of permutation entropy. *Eur. Phys. J. Spec. Top.* **2013**, *222*, 249–262. [[CrossRef](#)]

86. Yan, R.; Liu, Y.; Gao, R.X. Permutation entropy: A nonlinear statistical measure for status characterization of rotary machines. *Mech. Syst. Signal Process.* **2012**, *29*, 474–484. [[CrossRef](#)]
87. Petrosian, A. Kolmogorov complexity of finite sequences and recognition of different preictal EEG patterns. In Proceedings of the Eighth IEEE Symposium on Computer-Based Medical Systems, Lubbock, TX, USA, 9–10 June 1995; pp. 212–217.
88. Esteller, R.; Vachtsevanos, G.; Echauz, J.; Litt, B. A comparison of waveform fractal dimension algorithms. *IEEE Trans. Circ. Syst.* **2001**, *48*, 177–183. [[CrossRef](#)]
89. Raghavendra, B.; Dutt, D.N. A note on fractal dimensions of biomedical waveforms. *Comput. Biol. Med.* **2009**, *39*, 1006–1012. [[CrossRef](#)] [[PubMed](#)]
90. Romera, M.; Talatchian, P.; Tsunegi, S.; Abreu Araujo, F.; Cros, V.; Bortolotti, P.; Trastoy, J.; Yakushiji, K.; Fukushima, A.; Kubota, H.; et al. Vowel recognition with four coupled spin-torque nano-oscillators. *Nature* **2018**, *563*, 230–234. [[CrossRef](#)] [[PubMed](#)]
91. Gonon, L.; Ortega, J. Reservoir Computing Universality With Stochastic Inputs. *IEEE Trans. Neural Netw. Learn. Syst.* **2020**, *31*, 100–112. [[CrossRef](#)]
92. Athanasiou, V.; Konkoli, Z. On mathematics of universal computation with generic dynamical systems. In *From Parallel to Emergent Computing*; Adamatzky, A., Akl, S.G., Sirakoulis, G.C., Eds.; CRC Press: London, UK, 2019.
93. Blachecki, A.; Mech-Piskorz, J.; Gajewska, M.; Mech, K.; Pilarczyk, K.; Szaciłowski, K. Organotitania-Based Nanostructures as a Suitable Platform for the Implementation of Binary, Ternary, and Fuzzy Logic Systems. *ChemPhysChem* **2017**, *18*, 1798–1810. [[CrossRef](#)] [[PubMed](#)]
94. Pilarczyk, K.; Daly, B.; Podborska, A.; Kwolek, P.; Silversson, V.A.D.; de Silva, A.P.; Szaciłowski, K. Coordination chemistry for information acquisition and processing. *Coord. Chem. Rev.* **2016**, *325*, 135–160. [[CrossRef](#)]
95. Warzecha, M.; Oszejca, M.; Pilarczyk, K.; Szaciłowski, K. A three-valued photoelectrochemical logic device realising accept anything and consensus operations. *Chem. Commun.* **2015**, *51*, 3559–3561. [[CrossRef](#)] [[PubMed](#)]
96. Gonon, L.; Ortega, J.-P. Fading memory echo state networks are universal. *Neural Netw.* **2021**, *138*, 10–13. [[CrossRef](#)]
97. Grigoryeva, L.; Ortega, J.-P. Echo state networks are universal. *Neural Netw.* **2018**, *108*, 495–508. [[CrossRef](#)] [[PubMed](#)]
98. Cosoli, G.; Mobili, A.; Giulietti, N.; Chiariotti, P.; Pandarese, G.; Tittarelli, F.; Bellezze, T.; Mikanovic, N.; Revel, G.M. Performance of concretes manufactured with newly developed low-clinker cements exposed to water and chlorides: Characterization by means of electrical impedance measurements. *Constr. Build. Mater.* **2021**, *271*, 121546. [[CrossRef](#)]
99. Hassi, S.; Ebn Touhami, M.; Boujad, A.; Benqlilou, H. Assessing the effect of mineral admixtures on the durability of Prestressed Concrete Cylinder Pipe (PCCP) by means of electrochemical impedance spectroscopy. *Constr. Build. Mater.* **2020**, *262*, 120925. [[CrossRef](#)]
100. Yu, J.; Sasamoto, A.; Iwata, M. Wenner method of impedance measurement for health evaluation of reinforced concrete structures. *Constr. Build. Mater.* **2019**, *197*, 576–586. [[CrossRef](#)]



## **Electronic supplementary information**

### **Towards embedded computation with building materials**

Dawid Przychyna<sup>ab\*</sup>, Maciej Suchecki<sup>ab</sup>, Andrew Adamatzky<sup>c</sup>, Konrad Szaciłowski<sup>a\*</sup>

<sup>a</sup>AGH University of Science and Technology, Academic Centre for Materials and Nanotechnology, al. Mickiewicza 30, 30-059 Kraków, Poland

<sup>b</sup>AGH University of Science and Technology, Faculty of Physics and Applied Computer Science, al. Mickiewicza 30, 30-059 Kraków, Poland

<sup>c</sup>University of the West of England, Unconventional Computing Lab, Department of Computer Science and Creative Technologies, Bristol BS16 1QY, United Kingdom

\*Corresponding authors: dawidp@agh.edu.pl, szacilow@agh.edu.pl

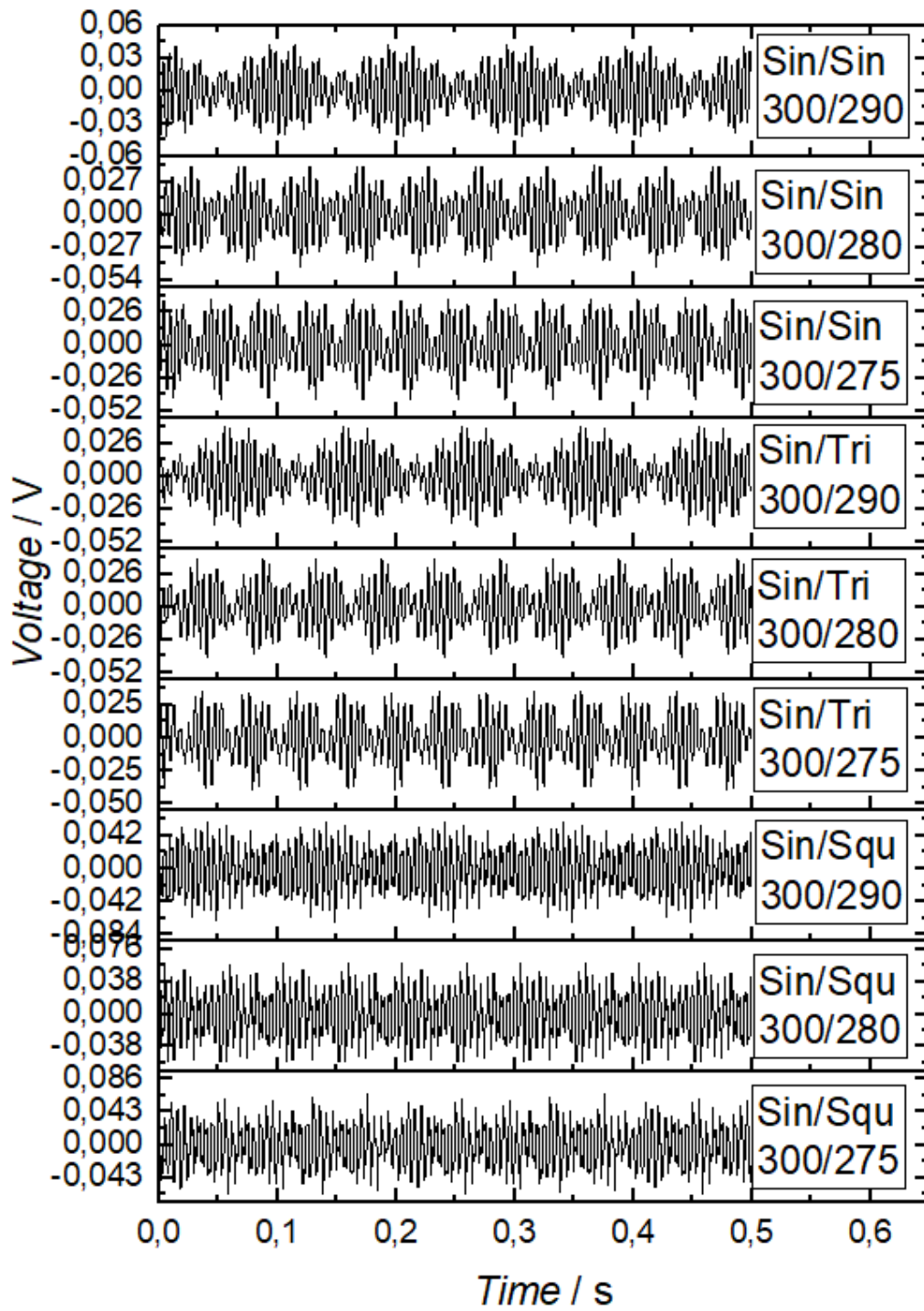


Figure S1. Registered timeseries for undoped concrete sample (Sin – sinusoidal, tri – triangular, squ – square wave form). Frequencies are given in Hz.

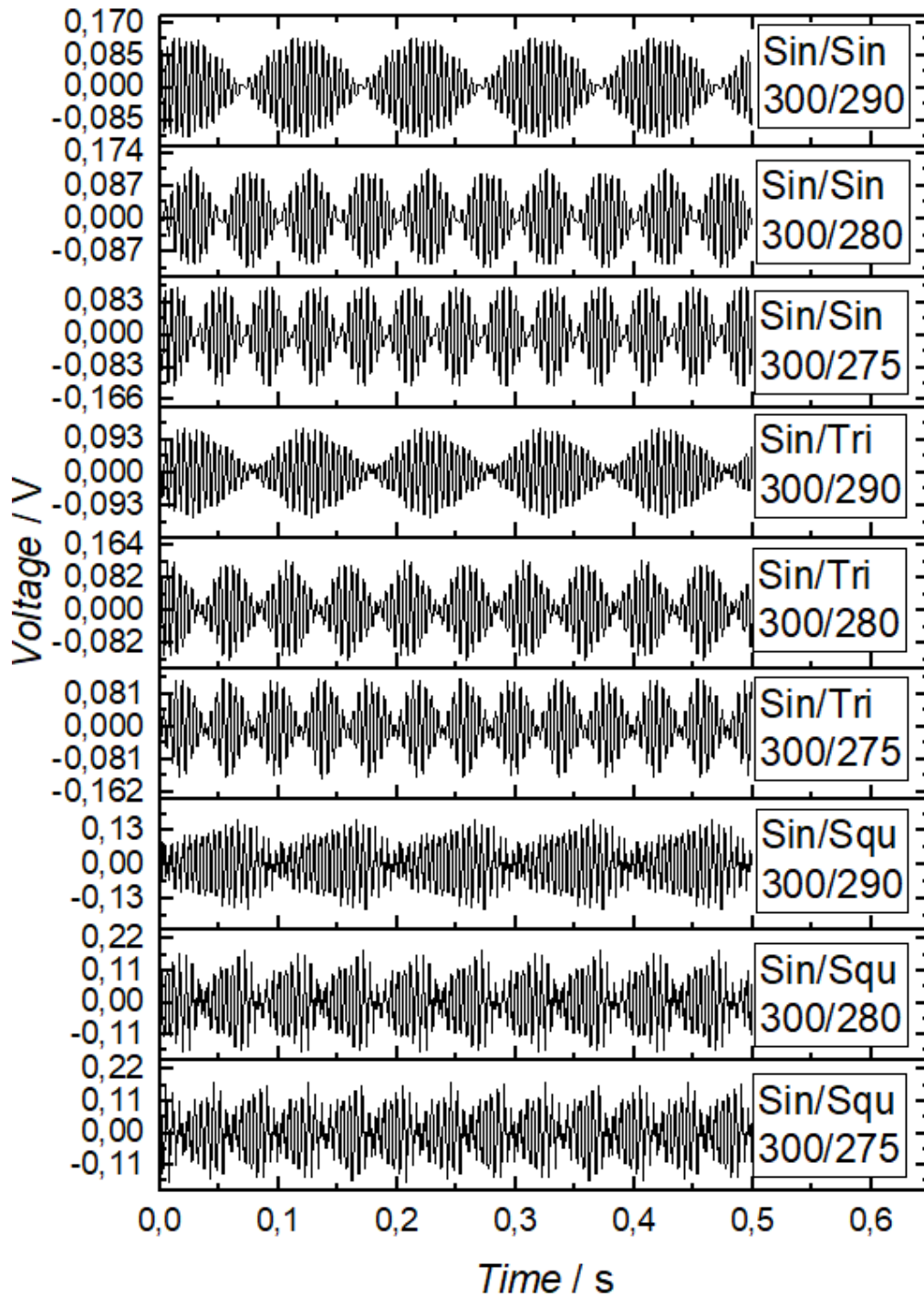


Figure S2. Registered timeseries for doped concrete sample (Sin – sinusoidal, tri – triangular, squ – square wave form). Frequencies are given in Hz.

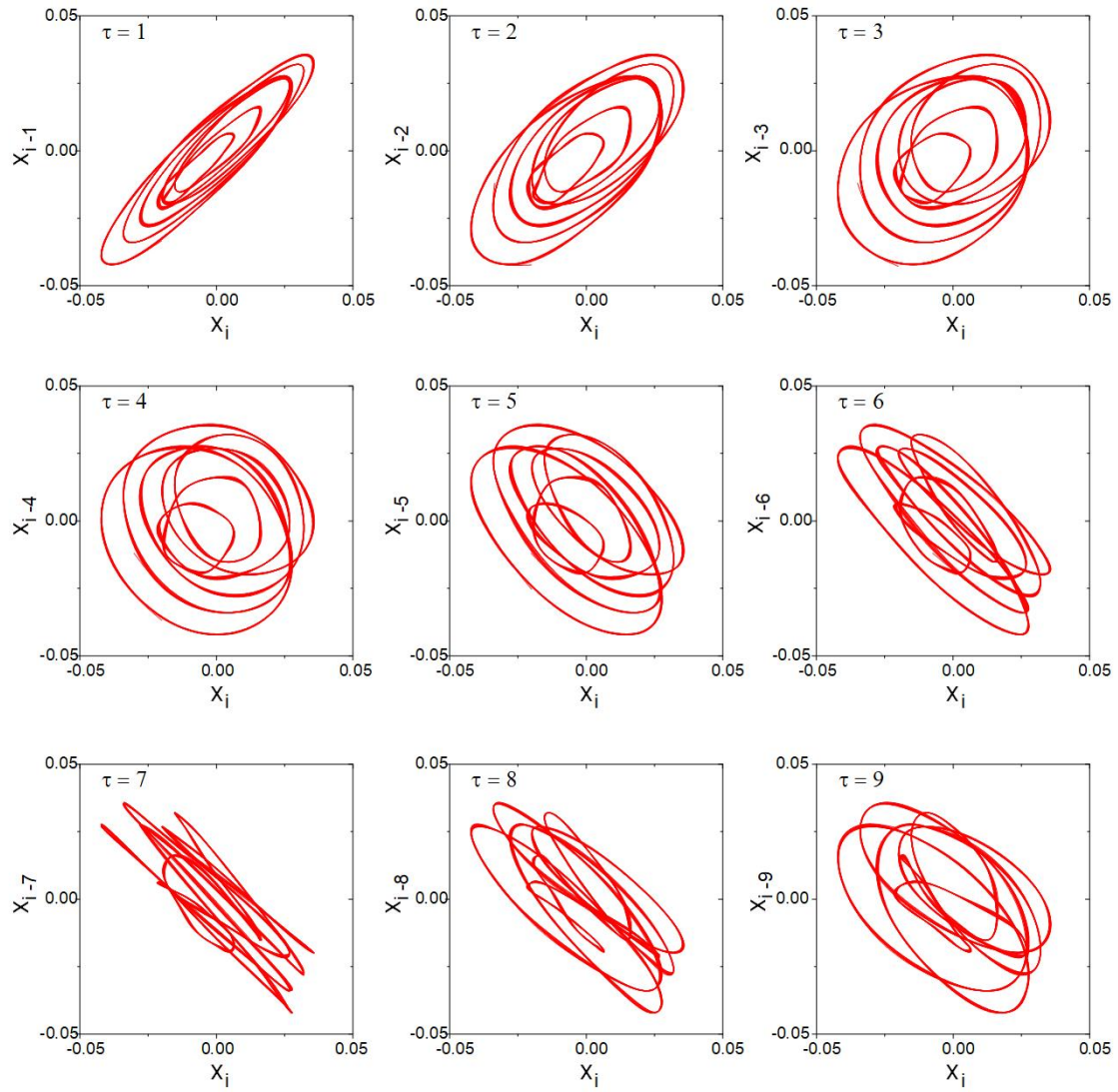


Figure S3. 2D projections of trajectories (return plots) of the signal obtained for two sine waves (275 and 300 Hz) in undoped concrete. The case of  $\tau = 4$  does not show any diagonal stretching.

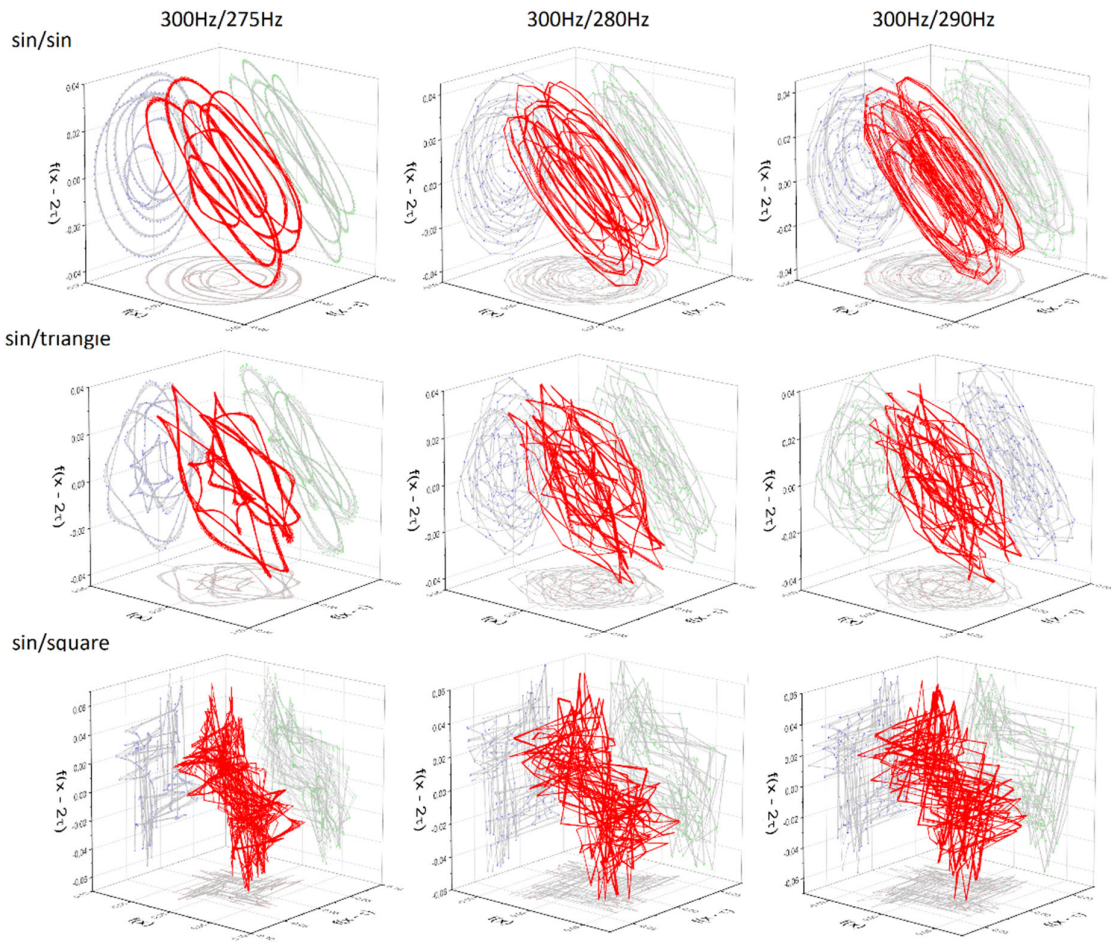


Figure S4. Embedded time-delay trajectories of time series recorded for un-doped concrete sample for various input waveforms and frequencies, constructed with time delay  $\tau = 4$ . It should be noted that the  $f(x)$  vs  $f(x-\tau)$  projections are free from diagonal distortions, which supports the evaluated  $\tau$  value.

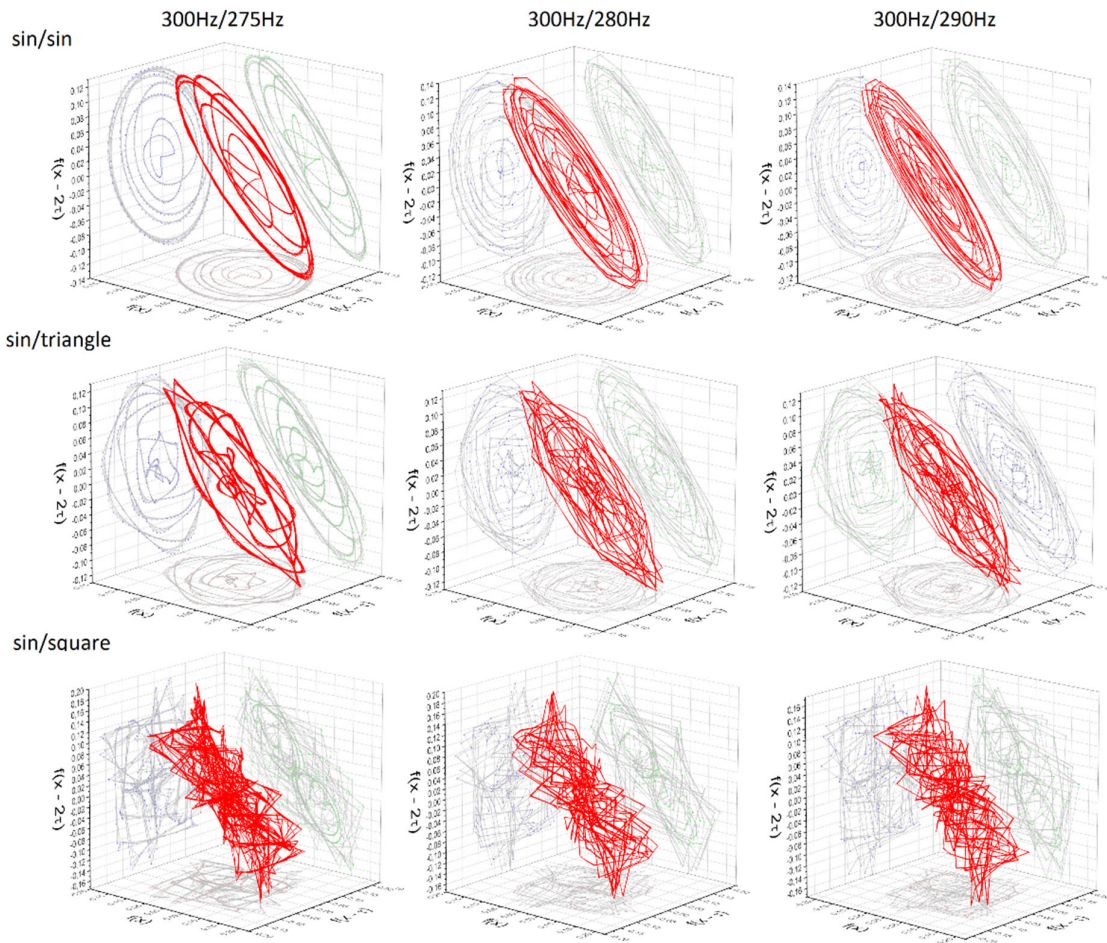


Figure S5. Embedded time-delay trajectories of time series recorded for doped sample (10% SM) for various input waveforms and frequencies, constructed with time delay  $\tau = 4$ . It should be noted that the  $f(x)$  vs  $f(x - \tau)$  projections are free from diagonal distortions, which supports the evaluated  $\tau$  value.

# Reservoir Computing for Sensing – an Experimental Approach

DAWID PRZYCZYNA,<sup>1,2</sup> SÉBASTIEN PECQUEUR,<sup>3</sup> DOMINIQUE VUILLAUME<sup>3</sup>  
AND KONRAD SZACIŁOWSKI<sup>1\*</sup>

<sup>1</sup>Academic Centre for Materials and Nanotechnology, AGH University of Science and Technology, Al. Mickiewicza 30, 30-059 Kraków Poland

<sup>2</sup>Faculty of Physics and Applied Computer Science, AGH University of Science and Technology, Al. Mickiewicza 30, 30-059 Kraków Poland

<sup>3</sup>Institut d'Électronique, Micro-électronique et de Nanotechnologie, CNRS, CS 60069, Av. Poincaré, 59652, Cedex, Villeneuve d'Ascq, France

The increasing popularity of machine learning solutions puts increasing restrictions on this field if it is to penetrate more aspects of life. In particular, energy efficiency and speed of operation is crucial, inter alia in portable medical devices. The Reservoir Computing (RC) paradigm poses as a solution to these issues through foundation of its operation – *the reservoir of states*. Adequate separation of input information translated into the internal state of the reservoir – whose connections do not need to be trained – allow to simplify the readout layer thus significantly accelerating the operation of the system. In this paper, the theoretical basis of RC was first described, followed by a description of its individual variants, their development and state-of-the-art applications in chemical sensing and metrology: detection of impedance changes and ion sensing. Presented results indicate applicability of reservoir computing for sensing and validating the SWEET algorithm experimentally.

*Keywords: Reservoir computing, chemical sensing, SWEET algorithm, conducting polymers*

## 1 INTRODUCTION

Problems of all civilizations arise and develop when the flow of one of the three fundamental components of systems is disturbed: matter, energy or information [1].

---

\*Corresponding author's E-mail: szacilow@agh.edu.pl

Insufficient resources or non-effective transportation of any of the above components can catastrophically affect prosperity of any social system. The rise and fall of complex civilizations as well as difficult situation in various regions of today's world can be explained on this basis [1, 2]. It is not surprising that there is intensive research carried out in each of these areas in the context of refining conventional solutions as well as discovering new, unconventional methods.

In information driven world, its effective acquisition and energy efficient processing is crucial. It seems, that silicon based computers are reaching their development potential, as miniaturisation reaches its economical validity [3]. For this reason, many studies are being carried out on new hardware architectures for specific applications as well as on new, faster and more efficient software solutions.

Algorithms from the machine-learning paradigm [4], in particular neural network algorithms are gaining increasing interest in recent years. They are used in the topics such as quantum chemistry [5], pattern recognition [6], medical diagnosis [7], finance [8], social media [9], data mining [10] and even game-playing [11]. The structure of the classic neural network is depicted in Figure 1a.

When a neural network contains more than one hidden layer then it is called a deep neural network. Data flow through hidden layers is then a multistep process. Each layer can be trained on further refinements of features with an increasing complexity and abstraction of the output. Such network can be used in variety of topics, for example for searching new materials for photovoltaics [12], in autonomous vehicles [13], or for human-to-computer

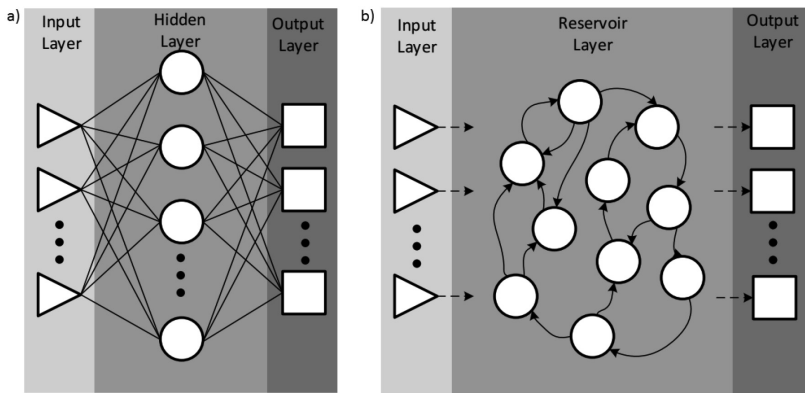


FIGURE 1

Schematic structure of classical neural network divided into layers. The input layer, hidden layer and output layer are connected through connections which are optimized during the work of the algorithm. The share in transmission of data through connections (synapses) between nodes (neurons) is modifiable with its real-valued weight (a). Schematic framework of Reservoir Computing. Classically, Reservoir layer consist of randomly connected nodes with recurrent connections. Connections of inputs and nodes in reservoir are rigid, only connections to output layer are trained (b).



interface [14]. One of the breakthroughs in the field of machine learning was success of AlphaGo – computer program based on deep neural network and Monte Carlo Tree search, who managed to beat the world champion in go [11]. The strength of the algorithm was its recursive action, optimizing the steps taken in each move, simultaneously updating all possible paths as the game moved on. Achievements of such algorithms is undeniable, but it comes with a cost - to work fast, they require powerful supercomputing platform with huge energy inputs.

## 2 RESERVOIR COMPUTING THEORY

In the area of recurrent neural networks (RNN), Reservoir Computing (RC) paradigm opens a new field for the development of software and hardware systems [15]. It addresses the problem of energy inefficient operation of RNN. RC operation principle is based on a non-linear dynamical system called *reservoir* (Figure 1b). Input layer feeds the data into reservoir layer where it is mapped onto high dimensional state space (Figure 2). Obtained versatility of states can be used for processing of non-linear dynamical sys-

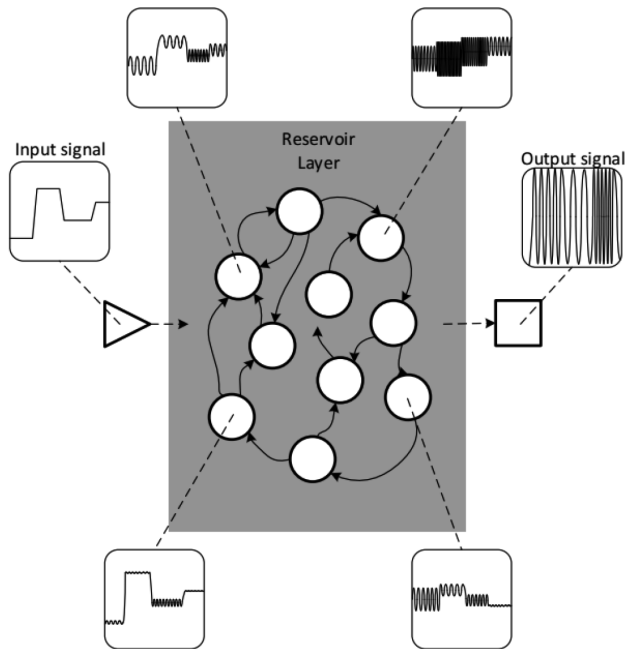


FIGURE 2

Versatility of states of dynamical reservoir presented on the example of the frequency generation. Adapted from [18].

tems with time-varying inputs and for linear separation of non-linear data through an increment of dimensionality [16]. Output signals consist of linear combination of internal states of reservoir at a given time, which depend on the system internal dynamics and the input data [15]. Therefore a reservoir computing system can be regarded, from the point of view of signal engineering, as a filter ( $\mathfrak{F}$ ) [17] which maps the space of input time series  $\Omega$  into the space of output time series  $\Omega'$  (1):

$$\mathfrak{F} : \Omega \rightarrow \Omega' \quad (1)$$

If the configuration space of the reservoir is large enough and the input can move the system into various regions of this space, then the dynamic system can perform computation. In this context, the input layer can be understood as an interface translating the input signal into a form that can influence the internal dynamics of the reservoir, whereas the readout layer is an interface probing the internal state of the reservoir and extracting information which is stored there [17]. Huge advantage of RC is that connection weights are deliberately optimised only at the output layer, whereas reservoir layer is left to evolve freely according to its own dynamic properties and its interactions with the input data and/or the environment. In principle any dynamic system, which is responsive to some external stimulation can be used for reservoir computing. Good reservoirs (i.e. systems capable of information processing according to their internal dynamics and filter property) should provide separability (i.e. small difference in the input should result in significant change in the output and different inputs should result in different outputs), the echo state property (output layer reflects the internal dynamics of the system) and fading memory (the state of the reservoir depends on its history for a non-infinite period of time). This approach provides fast and energy efficient operation both for software and hardware solutions.

Generally, by using a mathematical formalism, the operation of the reservoir can be described on the basis of a set of equations [19, 20]. The description of updating state of reservoir system is governed by discrete time equation:

$$x(n+1) = (1-a)x(n) + f\left(\mathbf{W}x(n) + \mathbf{W}^{in}u(n+1) + \mathbf{W}^{fb}y(n)\right) \quad (2)$$

where  $n$  is discrete time,  $x(n)$  is the N-dimensional reservoir state,  $f$  is an activation function,  $\mathbf{W}$  is the reservoir internal weight matrix,  $\mathbf{W}^{in}$  is the input weight matrix,  $u(n)$  is the K-dimensional input signal,  $\mathbf{W}^{fb}$  is the output feedback matrix and  $\mathbf{y}(n)$  is the L-dimensional output signal.  $\mathbf{W}^{int}$ ,  $\mathbf{W}^{in}$  and  $\mathbf{W}^{fb}$  matrices determine connection among nodes. Commonly, the logistic sigmoid, hyperbolic tangent or rectifying linear unit functions are used as an

activation function of neurons. The first part of the equation  $(1 - \alpha) x(n)$  is added only if leaky-fire-and-integrate model of neurons is used for a different dynamic behaviour [15].

The output of the reservoir can be formulated as follows:

$$y(n+1) = \mathfrak{F}(\mathbf{W}) = f_{out} \left( \mathbf{W}^{out} \left( u(n+1), x(n+1), y(n) \right) \right) \quad (3)$$

where  $y(n)$  is the readout output signals,  $f_{out}$  is a linear continuous function,  $\mathbf{W}^{out}$  is output weight matrix, and  $(u(n+1), x(n+1), y(n))$  is the concatenation of inputs, reservoir state and previous output vectors.

Readout of the reservoir is obtained by linear combination of reservoir states. Because state of each node will change upon inputs feed to the reservoir, the state matrix  $\mathbf{S}$  is a combination of  $\mathbf{K}$  input vectors and  $\mathbf{N}$  nodes states matrices, giving  $\mathbf{S} = \mathbf{N} \times \mathbf{K}$ . As an operation principle of RC is based on multidimensional states of reservoir layer,  $\mathbf{W}^{out}$  matrix weights are defined as combination of L-dimensions of N nodes states,  $\mathbf{W}^{out} = \mathbf{L} \times \mathbf{N}$ . The calculation of actual output  $\mathbf{Y} = \mathbf{W}^{out} \times \mathbf{S}$  being as close to  $\hat{\mathbf{Y}}$  desired “target” output as possible (in the least squared sense) is a linear problem; solution is based on Moore-Penrose pseudo inverse  $\mathbf{S}^+$  of the  $\mathbf{S}$  state matrix:

$$\mathbf{S}^+ = \left( \mathbf{S}^T \mathbf{S} \right)^{-1} \mathbf{S}^T \quad (4)$$

$$\mathbf{W}^{out} = \left( \hat{\mathbf{Y}} \mathbf{S}^+ \right)^T \quad (5)$$

On the other hand, common practice in obtaining a readout layer is usage of various regression function, e.g. Ridge, Least Mean Squares or Recursive Least Squares regressions [21]. The choice of proper algorithms depends on structure of the reservoir and the activation functions of neurons.

### 3 COMPUTATIONAL VARIANTS

Generally, RC comprises within its conceptual framework echo-state networks (ESN) and Liquid State Machine (LSM) algorithms that belong to the RNN group [15]. In a similar approach, computational structures can be realised on a delay-based system with feedback [16]. Additionally, the state weaving environment echo tracker (SWEET) algorithm has been recently proposed for sensing applications [22]. The main concepts are presented below along with the latest developments of algorithms along with state-of-

the-art application strategies. Other approaches, although functional, due to niche applications (or other limitations) are not as widely used as ESN, LSM or delay-based algorithms and have not been reviewed.

### 3.1 Echo state networks

ESN algorithm first proposed in 2001 by Jaeger [19] is one of the two pioneering RC. Since then, a great amount of work has been done in regard of software and hardware implementations employing this computational variant. Recently, it has been used for various diagnostic purposes, e.g. for blood vessel segmentation in retinal images [23], dynamical detection of steady state visual evoked potentials [24], diagnosis of Parkinson's disease [25], determination of ADHD biomarker [26] or for fetal QRS detection [27]. Other applications regarding non-linear systems modelling are also explored [28, 29].

In this computational variant, neurons within reservoir layer are connected randomly and have recurrent loops in their connection pathways. Additionally, connection between neurons is sparse, commonly less than 20%. Activation function of neurons is generally a sigmoidal in character (e.g. tanh), but hybrid applications of Leaky integrator neuronal model had also been used [30]. States of dynamical reservoir are dependent on its history of inputs, so called *echo* of its states.

Essentially, the ESN reservoir is randomly created, but sometimes it can lead to poor performance with too much computational complexity on one side and too little computing power to reach the desired target on the other. To increase performance of ESN, Dingyuan *et al.* [28] proposed optimisation algorithm of the network structure by removing insignificant synapses. Modified ESN achieved better results in chaotic time series prediction than non-optimised ESN. In turn, Abdelbari *et al.* [31] proposed employment of evolutionary algorithms to optimise network design and achieved the intended results in modelling several different complex systems. Dolinský *et al.* [32] explored optimisation of a readout layer through locally regularized orthogonal forward regression. The results indicate that modified readout can improve robustness to noise and accuracy of ESN. On the other hand, Sun *et al.* [33] incorporated deep learning methodology in ESN modelling of time-series benchmarks. The obtained results indicate very good prediction accuracy (low normalized root mean-square error) with acceptable training time.

### 3.2 Liquid State Machine

The LSM proposed in 2002 by Maas [34] is other pioneering RC solution. Initially, LSM was developed on the basis of the neuroscience to explain the main computational properties of neuronal microcircuits [35]. The difference between ESN and LSMs are a different activation function of neurons in the reservoir: sigmoid activations are replaced with threshold functions (spiking or digital) – each neuron is modelled on the basis of “leaky fire-and-inte-

grate” neuron model, so LSM is a type of spiking neural network [36]. Once the activation threshold is reached, neuron releases its energy to neighbouring neurons. This principle is similar to spatially distributed biological neurons [37]. The second difference is that LSM mainly employs biologically inspired structures in formation of reservoir layer. Recent advancements in regard to applications of LSM include: speech recognition [38], control of the movements of robots [39] and EEG seizure detection [40].

As improvements of the LSM algorithm, Schliebs *et al.* [41] showed that using dynamic activation function (high sensitivity for weak stimuli; low sensitivity for overstimulation) for spiking of neurons can improve the separation capabilities and efficiency of the network. On the other hand, Roy *et al.* [42] presented a new approach to the construction of the LSM structure along with an improved algorithm for the readout layer. Obtained results showed less errors and a better efficiency than other state-of-the art upgrades to LSM algorithm. Enhancement of computational capabilities of LSM has been shown by Li *et al.* in [43] by introduction of spike timing depended plasticity process along with intrinsic plasticity to the neurons in reservoir. Synchronous activation of neurons improved energy efficiency of LSM systems and improved computational performance due to self-organising property.

### 3.3 Delay-based systems

In order to meet the hardware challenges of too many components of the RC system, Appeltant *et al.* [16] and Pacquot *et al.* [44] have introduced an alternative approach in construction of the reservoir. Here, the reservoir layer consists of only one, nonlinear node operating in a delayed feedback mode, which fulfils the condition of minimizing complexity of necessary hardware for operation. The principle of operation of delay-based RC is based on *virtual neurons* (Figure 3). First, operations of sample and hold of an input signal are performed. Then, a so called masking operation is performed in order to obtain a higher versatility of states in the reservoir. The pre-processing by masking consists in modification of the input signal, which functions as diversification of the reservoir response, thus increasing its dimensionality in the state-space. The applied mask can take a form of digital binary values [45] or simple sinusoidal wave. It has been shown by Nakayama *et al.* that an analog mask with chaotic values is also efficient (Fig. 13) [46]. Multiplication of the input data with the masking function is the most commonly applied approach. Creation of virtual neurons involves dividing a given delay line into parts by time-multiplexing of obtained signal. Number of obtained virtual neurons is given by (6):

$$N = \frac{\tau}{\theta} \quad (6)$$

where  $\tau$  is time duration of a delay line and  $\theta$  is constant distance between each virtual neuron, i.e. the time interval in which output layer probes the

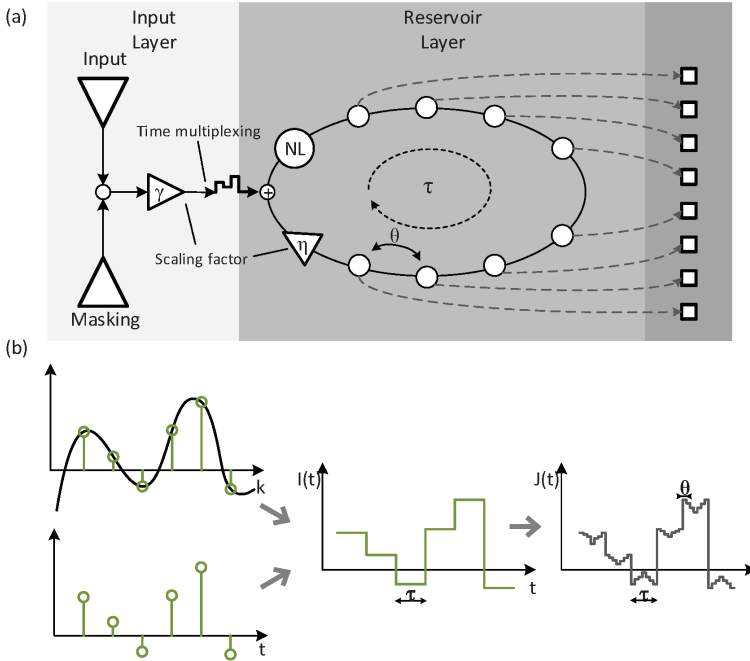


FIGURE 3

A schematic structure of the delay-based reservoir computing device.  $\tau$  is the length of the delay line,  $\theta$  is the distance between neighbouring nodes. Masked input is scaled by scaling factor  $\gamma$ , as well as signal in the delay line, which is scaled by feedback strength  $\eta$ . Scaling operations are often required to ensure that the signals in the reservoir are not saturated nor suppressed. Determination of scaling factors is optimised through numerical methods or scanning through their different values to ensure proper system operation in regard to the given task or used non-linear node (NL). For the sake of simplicity, the output layer was constructed directly from the states of all virtual neurons. Adapted from [47] (a). Schematic visualisation of masking procedure. In the first place sampling of continuous (or discrete) input data is performed, which are then kept at a given level by the „hold” operation. After sample and hold operations, masking function is acting on the signal with specified time-multiplexed windows ( $\theta$ ). Those operations create virtual neurons (through time multiplexing) and ensure high versatility of their states (b). Adapted from [48].

state of the reservoir (Fig. 3). Based on the above, the structure of delay-based RC is classified as belonging to circular connection topology with discrete reservoir.

Due to limitation of operation speed of delay-based systems, they are mainly implemented in fast photonic systems. A state-of-the-art result in the topic of words classification task were shown by Larger *et al.* in [49]. Authors investigated two approaches to increase the functionality of the optical RC. Extended delay memory (EDM) procedure has been explored, which involved the scaling between the length of the input information and the duration of the delay line. This approach departed from the classical assumption that the

input information must be equal to the length of the feedback loop. As a result, EDM enables temporal mixing of inputs in delayed line. Additionally, authors explored desynchronization of readout function (in relation to clock used to inject input information), proving numerically and experimentally the increase of functionality of reservoir by more than 1 order of magnitude. The investigated photonic RC enabled classification rate of stunning 1 million words per second.

On the other hand, Antonik *et al.* [50] examined the use of photonic RC in chaotic time series modelling and prediction. Authors presented first experimental hardware system capable of emulating Mackey-Glass series and Lorentz series with good agreement of Lyapunov exponents. However, the noise generated by system components (which are amplified in the feedback loop and weaken the accuracy of prediction after crossing specific threshold) is still a challenge to increase the functionality of the system.

#### **4 IMPLEMENTATION OF RESERVOIR COMPUTING FOR SENSING**

Conventional chemosensing usually deals with noisy signals (electrical or optical) coming from sensors, i.e. sensing devices that have to respect figure of merits as an individual element (selectivity, signal-to-noise ratio, drift): In classical electrochemical sensors a change in electrode potential (in the case of potentiometric sensors, e.g. glass electrodes for pH measurements), electrode current (in the case of amperometric sensors, e.g. electrogalvanic oxygen sensors [51]). In the case of some chemosensors, the signal comes from light absorption or emission by specific sensor molecules [52, 53]. Some electrochemical sensors combine these two approaches. These sensors use electrodes modified with appropriate molecular species which contribute to the generation of analytical signal [48]. In the classic sensing approach, information about given environment is contained within variable response to stimuli of a given sensory platform, which is in contact with that environment. Comparison of the output data with the calibration curve gives us information about the content of the given environment. In an attempt to improve performance of a sensory platform, machine learning algorithms (including RC) can be used to enhance classification of its responses [54-56]. In this configuration, machine learning (or other advanced information processing routine) is used only as a post processing unit. The first step towards significant improvement of sensor performances (without engineering of the sensing material itself) was the so called heterodyne sensing [57-59]. In this sensing approach, frequency mixing in nanoscale materials induced by surface dipoles is recorded.

A completely novel approach was suggested recently by Zoran Konkoli [22]. The recently proposed SWEET algorithm adopts a reservoir which is

weakly coupled with the environment under study. The difference can be highlighted in statements: ‘*reservoir computing for sensing*’ in case of SWEET and ‘*reservoir computing and sensing*’ for other approaches. This approach utilizes subtle changes in the internal dynamics of the reservoir due to interaction with the environment (i.e. the concentration or the flux of the analyte).

It can be argued that this is a new interpretation and extension of the RC paradigm, where intrinsic properties of the reservoir allow it to additionally act as a sensing platform and not merely as information processing unit. In the SWEET setup, the addition of a delayed feedback loop to the reservoir enhances its sensing potential due to the gradual build-up of even the smallest changes in its state, similarly to chaotic system. This means that the interaction of the reservoir with the environment can be very small, without compromising the quality of the detection. In principle, due to the high complexity of the reservoir-environmental layer, separation of internal states is achieved by adjusting input signal (drive) under different environment conditions. After finding proper drive that enables high separation of states in the phase space, relatively simple readout function suffices in probing reservoir internal states [22]. In contrast to classical sensing devices, the SWEET-based sensing devices can yield answers to any questions about the analyte concentrations – not only their actual values, but also their dynamic changes, or meeting a defined concentration threshold (Fig. 4).

The implementation of the SWEET concept was presented in a theoretical work in which the reservoir layer was constructed on the basis of one memristor (model was taken from literature) [60]. Basically, a memristor is a passive and non-linear circuit element, possessing switchable conductance states and non-volatile memory of its previous state [61]. A reservoir constructed this way was subjected to analysis and parameter optimisation. Two distinct drive signals were tested – one which was chosen arbitrarily based on scientific guess and the other optimised through *genetic algorithm*. Results show that both approaches allows for separation of different environmental conditions but the second approach is more robust towards potential scalability of memristor network constituting reservoir. It was discovered, that larger drive leads to faster operation at the cost of accuracy and should be optimised in regard to specific application. In addition, the authors introduced the “*Quality of sensing index v*”, which can be used to determine the quality of sensing by examining the degree of separation of reservoir states in the phase space.

A first crude experimental verification of the reservoir computing for sensing approach was demonstrated to detect monolayers of lipoic acid on gold surfaces (Fig. 5). Lipoic acid reacts with gold surfaces forming stable monolayers. The impedance of these monolayers is higher than those of bare gold electrodes due to the higher charge-transfer resistance through the molecular layer. Application of a delayed feedback device (Fig. 5a) demonstrates the idea of reservoir computing for sensing. The increase of the impedance can



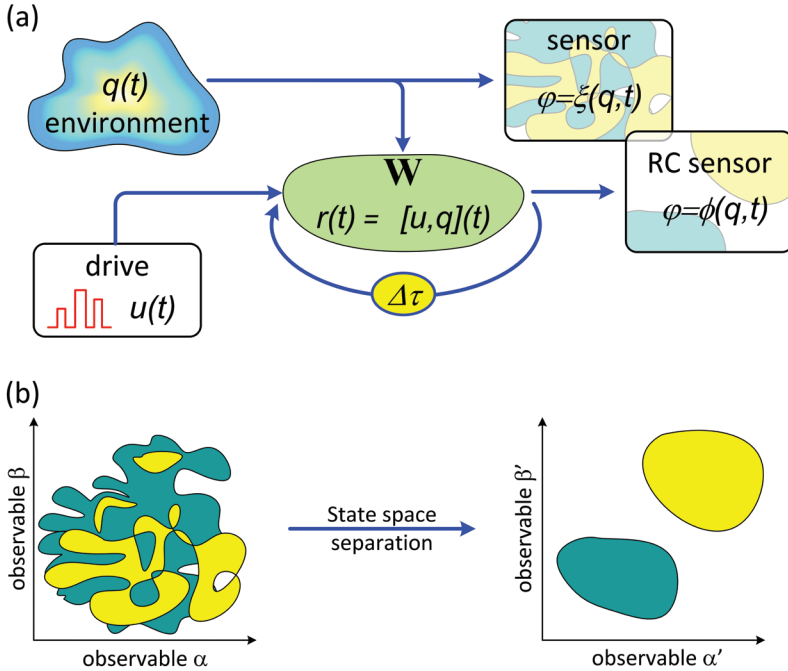


FIGURE 4

The overview of the SWEET sensing setup. The environment-sensitive reservoir is used to obtain information about the environment. This can be done on a direct pathway, which yields unprocessed information about the environment,  $\xi(q, t)$ , or through indirect sensing by studying the response of the reservoir  $\phi(q, t)$  to user-provided queries – the drive signal  $u(t)$ . The delayed feedback  $\Delta\tau$  is added to increase the complexity of the configuration space and achieve better reservoir computing properties (a). Symbolic representation of a complex sensing problem. A sensor has to detect the state of the system (yellow or green) on the basis of measurement of the observables  $\alpha$  and  $\beta$ . On the left, the case of a low phase space separation in which the sensing problem is hard and prone to errors. Application of reservoir computing-based sensor with an appropriate drive signal performs domain separation of the system and yields much more reliable information. In this scenario, a relatively simple readout layer can be used to infer the state of the environment. Most of the computation is performed by the device, and not the readout layer. Adapted from Ref. [48].

be observed as a decrease of AC-signal amplitude (the first pulse of red vs blue tracks in Fig. 5b) or more convincingly, as an alteration of signal evolution in the feedback loop. Accumulation of small amplitude changes results in much faster signal decay in the system, so instead of amplitude changes, the analytical signal may be based on the time constant of the system, which means that the signal was transferred into a different domain.

Implementation of a similar type and architecture has also been developed on the basis of Organic Electrochemical Transistor (OECT) arrays covered with glycol-side-chain polythiophene. Instead than using networks of several OECTs as already reported [62], a unique OECT was used as single dynamical

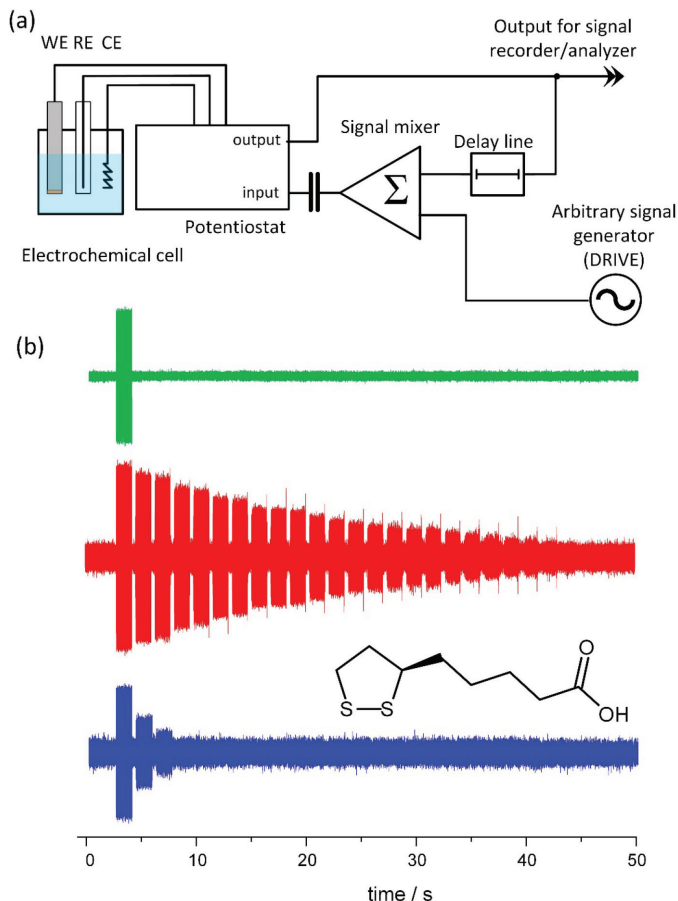


FIGURE 5

The block diagram of a reservoir sensor: WE stands for working electrode, RE for reference electrode and CE for counter electrode (a) and the response recorded with this device (b). The upper green curve presents the drive signal (2s, 100 Hz), the middle red one depicts the signal evolution in the absence of analyte (i.e. bare gold in potassium nitrate solution, pH = 7). The bottom blue curve presents the output of the device upon deposition of lipoic acid monolayer at the gold surface. Inset shows the molecular structure of the lipoic acid molecule. Potentiostat input controls the working electrode potential, the output is the analog current monitor.

cal node operating in feedback loop employed for  $K^+$  metal ions detection (Fig. 6). The channel of the OECT device was fabricated from a thin layer of PEDOT:PSS conducting polymer.

The source-drain current was followed by a potentiostat in two electrode configuration, serving as an analog sourcemeter. Platinum wire placed in the electrolyte served as the gate of the transistor. The gate of the transistor was connected to the feedback loop containing also the drive generator (Fig. 7).

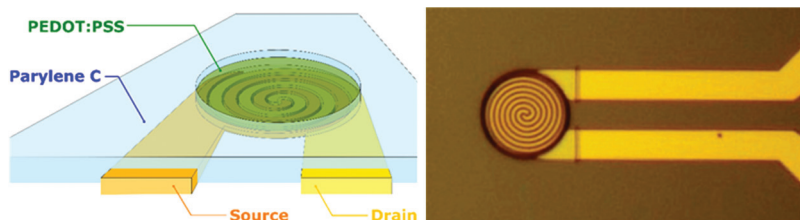


FIGURE 6 Design (left) and optical microscopy image (right) of PEDOT:PSS organic electrochemical transistor.

Current between source-drain (S-D) electrodes was forced by 100 mV DC potential. When the sinusoidal voltage (980 mV, 20 Hz, duration 1 s, interval between pulses 0.2 s) was applied to the gate electrode of OEET, ions present in the electrolyte were injected into the channel, hence modulating the observed S-D current. Resulting signal was then delayed and applied to the gate electrode through the feedback loop with a capacitive coupling until the amplitude was insufficient to induce any response of the S-D electrodes (Fig. 8 a). Signal analysis was performed with Fourier transform to overcome noise present in the system. With increasing ion concentration, the obtained currents from the S-D electrodes were increased, which ultimately influenced

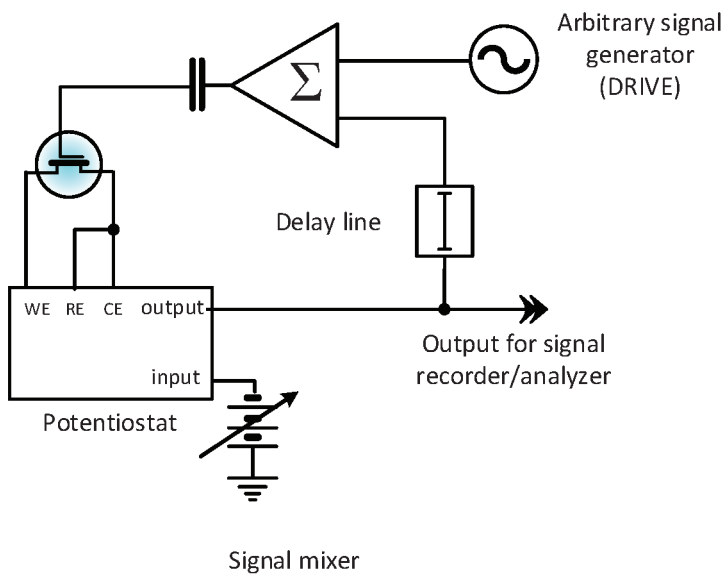


FIGURE 7 Connection diagram of a reservoir sensing system with OEET as an active element. Potentiostat input controls the potential source, the output is the analog current monitor.

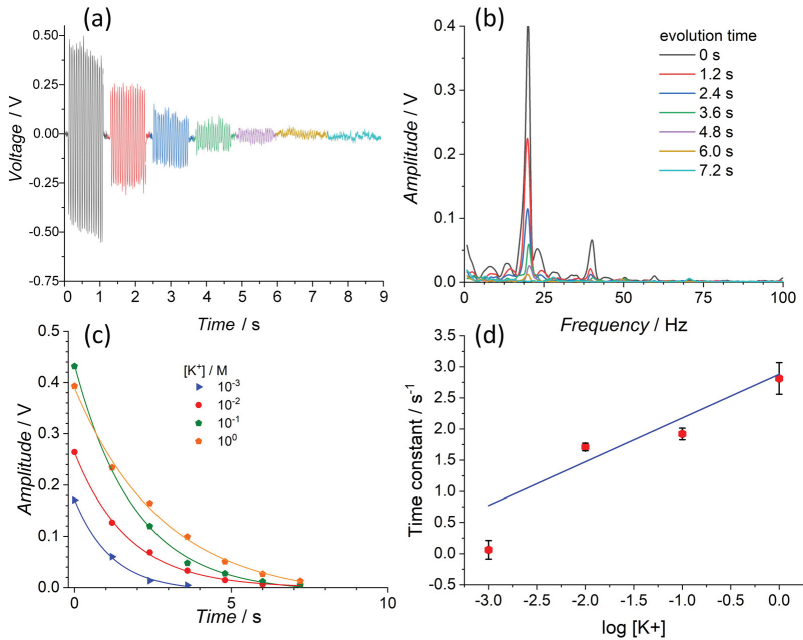


FIGURE 8

Exemplary response of the studied reservoir computing sensing system with feedback loop at high  $K^+$  ion concentration (a). Fourier transform spectra of each and every repeated signal package as a function of evolution time (b). Signal amplitudes of the first component (20 Hz) as a function of evolution time and potassium ion concentration (c), which enabled calibration of the time constants as a function of potassium concentration (d).

the number of received signal packs. By plotting amplitudes of peaks from Fourier transforms versus time, one can analyse time constant of fitted exponential curves, again, changing representation of the signal to a different state space (Figure 8 b). As a result, sensitivity of the system has been extended to higher concentrations, as it can be seen on the Figure 8 c. This promising preliminary results (Fig. 8 d) can be a starting point for more advanced studies of reservoir sensing with electrodes covered with specific molecular receptors or materials offering more complex dynamic behaviour (e.g. conducting polymers or semiconducting nanoparticles).

The OECT-based reservoir sensing system again demonstrates the utility of the SWEET approach towards chemical sensing. The information on the concentration of the analyte was transduced by the ion sensitive polymer and subsequently transformed from a simple voltage output signal into an evolution of a dynamic system. Small nonlinearities in the circuitry resulted in a significant harmonic distortion of the drive and generation of higher harmonics. This in turns allows facile filtering of the drive signal and may contribute to increased accuracy of signal analysis. Furthermore, concomitant analysis

of the evolution in time and frequency domains may be used to extract more information from electrochemical measurements.

## 5 CONCLUSIONS

Reservoir computing is a modern unconventional approach towards various problems associated with data classification, pattern recognition, and other applications that otherwise require high computational power. For numerous applications, it can be implemented in hardware. It is especially tempting to implement reservoir computing in various materials, e.g. assemblies of crystallites or nanoparticles, or thin molecular layers deposited at conducting substrates. Despite simplicity of the experimental approach, the computational performance may be useful for numerous practical applications, e.g. in chemical and biochemical sensing, environmental monitoring and other areas that may not necessarily require precise information of concentration, but rather binary classifications on specific thresholds of concentration.

## 6 EXPERIMENTAL

Lipoic acid-modified gold electrodes were prepared as follows. Gold disc electrodes (1 mm diameter) were polished with 1  $\mu\text{m}$  alumina suspension on soft cloth, etched in Piranha solution for one minute, washed with deionized water and dried in air. 50  $\mu\text{l}$  of saturated solution of lipoic acid in ethanol was poured over the electrode surface and left until all solvent evaporated. Subsequently each electrode was immersed in 100 ml of ethanol for 3 hours.

The fabrication of the OECTs was based on the methods described elsewhere [63, 64]: The Pt source and drain electrodes have an interdigitated spiral geometry for a total active surface of 615  $\mu\text{m}^2$  and 1.2  $\mu\text{m}$  channel length [62]. The PEDOT:PSS polymer was spin-coated and structured using a lithographically-patterned Parylene mask [64, 65]. A first 2  $\mu\text{m}$ -thick Parylene C layer was deposited as a passivation layer to prevent direct interfacing of the gold track with the analyte (3-acryloxypropyl trimethoxysilane was used as an adhesion promoter on the  $\text{SiO}_2$  substrate). A second 2<sup>o</sup>  $\mu\text{m}$ -thick Parylene C layer was used to pattern the semiconductor as a mask (Micro-90 was used as a surfactant to prevent the adhesion between both Parylene-C layers). The structuring of the cavities over the active area of the OECT was performed at once through both Parylene-C layers by e-beam lithography and reactive ion etching. The PEDOT:PSS formulation was subsequently spin-coated on the device after a short  $\text{UV-O}_3$  cleaning of the opened cavities.

Custom-built analog potentiostat “Kacper” (Instytut Fotonowy, Poland) was used in all experiments as a sourcemeter, with Ag/AgCl reference electrode and platinum wire counter electrode, which also served as a gate in

OECT experiments. 0.1 M  $\text{KNO}_3$  was used as a supporting electrolyte. G-Major/2 signal processing device (TC Electronics, Denmark) was used as a delay line, whereas audio signal mixer ZED Sixty 14 FX (Allen&Heath, UK) was used as mixing amplifier. Signals were recorded on Crimson 3 audio USB interface (Sound Performance Lab, Germany). Arbitrary function generator TG2512A (Aim-TTI, UK) was used as a source of a drive signal.

## 6 ACKNOWLEDGEMENTS

Authors thank dr. Ewelina Wlazlak for her help during SWEET experiments and data analysis.

Furthermore, authors thank professor Kapela Pilaka for his friendly support, spiritual atmosphere in our laboratory and numerous discussion over sushi. The authors wish to acknowledge a series of discussions with all the partners of the RECORD-IT consortium. This work has received funding from the European Union's Horizon 2020 research and innovation programme under grant agreement No. 664786 and National Science Centre (Poland) under grant agreement No. UMO-2015/18/A/ST4/00058. DP has been partly supported by the EU Project POWR.03.02.00- 00-I004/16.

## LITERATURE

- [1] G.E. Mabus, M.C. Kalton, Principles of systems science, Springer, 2016.
- [2] J. Tainter, The collapse of complex societies, Cambridge University Press, 1988.
- [3] K. Rupp, S. Selberherr, IEEE Transactions on Semiconductor Manufacturing 24 (2011) 1-4.
- [4] G.A. Tsihrintzis, D.N. Sotiropoulos, L.C. Jain, Machine Learning Paradigms. Advances in Data Analytics, Springer International Publishing AG, Cham, 2019.
- [5] R. Ramakrishnan, P.O. Dral, M. Rupp, O.A. von Lilienfeld, Journal of chemical theory and computation 11 (2015) 2087-2096.
- [6] N.M. Nasrabadi, Journal of electronic imaging 16 (2007) 049901.
- [7] Z. Obermeyer, E.J. Emanuel, The New England journal of medicine 375 (2016) 1216.
- [8] J. Heaton, N. Polson, J.H. Witte, arXiv preprint arXiv:1602.06561 (2016).
- [9] K. Lee, J. Caverlee, S. Webb, in: Proceedings of the 33rd international ACM SIGIR conference on Research and development in information retrieval, ACM, 2010, pp. 435-442.
- [10] I.H. Witten, E. Frank, M.A. Hall, C.J. Pal, Data Mining: Practical machine learning tools and techniques, Morgan Kaufmann, 2016.
- [11] D. Silver, J. Schrittwieser, K. Simonyan, I. Antonoglou, A. Huang, A. Guez, T. Hubert, L. Baker, M. Lai, A. Bolton, Nature 550 (2017) 354.
- [12] J. Wei, P. De Luna, Y. Bengio, A. Aspuru-Guzik, E. Sargent, Nature 552 (2017) 23-25.
- [13] M. Bojarski, D. Del Testa, D. Dworakowski, B. Firner, B. Flepp, P. Goyal, L.D. Jackel, M. Monfort, U. Muller, J. Zhang, arXiv preprint arXiv:1604.07316 (2016).
- [14] A. Kapur, S. Kapur, P. Maes, in: 23rd International Conference on Intelligent User Interfaces, ACM, 2018, pp. 43-53.
- [15] M. Lukoševičius, H. Jaeger, Computer Science Review 3 (2009) 127-149.
- [16] L. Appeltant, M.C. Soriano, G. Van der Sande, J. Danckaert, S. Massar, J. Dambre, B. Schrauwen, C.R. Mirasso, I. Fischer, Nature communications 2 (2011) 468.

- [17] Z. Konkoli, On reservoir computing: From mathematical foundations to unconventional applications, in: A. Adamatzky (Ed.) *Advances in unconventional computing*, Vol. 1: Theory, Springer International Publishing, Cham, Switzerland, 2017.
- [18] H. Jaeger, *Scholarpedia* 2 (2007) 2330.
- [19] H. Jaeger, Bonn, Germany: German National Research Center for Information Technology GMD Technical Report 148 (2001) 13.
- [20] I.B. Yildiz, H. Jaeger, S.J. Kiebiel, *Neural Networks* 35 (2012) 1-9.
- [21] B. Schrauwen, D. Verstraeten, J. Van Campenhout, in: *Proceedings of the 15th European Symposium on Artificial Neural Networks*. p. 471-482 2007, 2007, pp. 471-482.
- [22] Z. Konkoli, *International Journal of Parallel, Emergent and Distributed Systems* 33 (2018) 121-143.
- [23] A. Souhailia, A. Belatreche, A. Benyettou, K. Curran, in: *Advanced Computational Intelligence (ICACDI), 2017 Ninth International Conference on, IEEE, 2017*, pp. 91-98.
- [24] D. Ibanez-Soria, A. Soria-Frisch, J. Garcia-Ojalvo, G. Ruffini, *bioRxiv* (2018) 268581.
- [25] S.E. Lacy, S.L. Smith, M.A. Lones, *Artificial intelligence in medicine* 86 (2018) 53-59.
- [26] D.I. Soria, A. Soria-Frisch, J. Garcia-Ojalvo, J. Picardo, G. Garcia-Banda, M. Servera, G. Ruffini, *bioRxiv* (2018) 271858.
- [27] M. Lukoševičius, V. Marozas, *Physiological measurement* 35 (2014) 1685.
- [28] L. Dingyuan, L. Fu, Q. Junfei, L. Rong, in: *Control And Decision Conference (CCDC), 2017 29th Chinese, IEEE, 2017*, pp. 4350-4353.
- [29] S.I. Han, J.M. Lee, *IEEE Transactions on Industrial Electronics* 61 (2014) 1099-1112.
- [30] S.-X. Lun, X.-S. Yao, H.-Y. Qi, H.-F. Hu, *Neurocomputing* 159 (2015) 58-66.
- [31] H. Abdelbari, K. Shafi, *Journal of Artificial Intelligence and Soft Computing Research* 8 (2018) 133-154.
- [32] J. Dolinský, K. Hirose, S. Konishi, *Journal of Applied Statistics* 45 (2018) 740-762.
- [33] X. Sun, T. Li, Y. Li, Q. Li, Y. Huang, J. Liu, *Neurocomputing* 275 (2018) 1333-1349.
- [34] W. Maass, T. Natschläger, H. Markram, *Neural computation* 14 (2002) 2531-2560.
- [35] W. Maass, T. Natschläger, H. Markram, in: *Advances in neural information processing systems*, 2003, pp. 229-236.
- [36] N. Soures, C. Merkel, D. Kudithipudi, C. Thiem, N. McDonald, *IEEE Consumer Electronics Magazine* 6 (2017) 67-73.
- [37] W. Gerstner, W.M. Kistler, *Spiking neuron models: Single neurons, populations, plasticity*, Cambridge university press, 2002.
- [38] Y. Zhang, P. Li, Y. Jin, Y. Choe, *IEEE transactions on neural networks and learning systems* 26 (2015) 2635-2649.
- [39] R. de Azambuja, A. Cangelosi, S.V. Adams, in: *Neural Networks (IJCNN), 2016 International Joint Conference on, IEEE, 2016*, pp. 1134-1142.
- [40] A. Polepalli, N. Soures, D. Kudithipudi, in: *Rebooting Computing (ICRC), IEEE International Conference on, IEEE, 2016*, pp. 1-8.
- [41] S. Schliebs, M. Fiasché, N. Kasabov, in: *International Conference on Artificial Neural Networks*, Springer, 2012, pp. 604-611.
- [42] S. Roy, A. Banerjee, A. Basu, *IEEE transactions on biomedical circuits and systems* 8 (2014) 681-695.
- [43] X. Li, W. Wang, F. Xue, Y. Song, *Physica A: Statistical Mechanics and its Applications* 491 (2018) 716-728.
- [44] Y. Paquot, J. Dambre, B. Schrauwen, M. Haelterman, S. Massar, in: *Nonlinear Optics and Applications IV, International Society for Optics and Photonics, 2010*, pp. 77280B.
- [45] B. Schneider, J. Dambre, P. Bienstman, *IEEE Trans. Neural Netw. Learn. Syst.* 27 (2016) 2748-2753.
- [46] J. Nakayama, K. Kanno, A. Uchida, *Opt. Express* 24 (2016) 8679-8692.
- [47] G. Van der Sande, D. Brunner, M.C. Soriano, *Nanophotonics* 6 (2017) 561-576.
- [48] K. Pilarczyk, E. Wlazlak, D. Przczyzna, A. Blachecki, A. Podborska, V. Anathasiou, Z. Konkoli, K. Szaciłowski, *Coord. Chem. Rev.* 365 (2018) 23-40.
- [49] L. Larger, A. Baylón-Fuentes, R. Martinenghi, V.S. Udaltsov, Y.K. Chembo, M. Jacquot, *Physical Review X* 7 (2017) 011015.

- [50] P. Antonik, M. Haelterman, S. Massar, *Cognitive Computation* 9 (2017) 297-306.
- [51] A. Sieber, Oxygen sensor technology for rebreathers, in: R.D. Vann, P.J. Denoble, N.W. Pollock (Eds.) *Rebreather Forum 3. Proceedings, Divers Alert Network, Durham, 2012.*
- [52] K. Pilarczyk, B. Daly, A. Podborska, P. Kwolek, V.A.D. Silverson, A.P. de Silva, K. Szaciłowski, *Coord. Chem. Rev.* 325 (2016) 135-160.
- [53] A. Hierlemann, R. Gutierrez-Osuna, *Chem. Rev.* 108 (2008) 563-613.
- [54] R.A. Potyrailo, *Chem. Rev.* 116 (2016) 11877-11923.
- [55] A. Legin, S. Makarychev-Mikhailov, O. Goryacheva, D. Kirsanov, Y. Vlasov, *Anal. Chim. Acta* 457 (2002) 297-303.
- [56] A. Hierlemann, R. Gutierrez-Osuna, *Chem. Rev.* 108 (2008) 563-613.
- [57] G.S. Kulkarni, W. Zang, Z. Zhong, *Acc. Chem. Res.* 49 (2016) 2578-2586.
- [58] G.S. Kulkarni, K. Reddy, W. Zang, K. Lee, X. Fan, Z. Zhong, *Nano Lett.* 16 (2015) 695-700.
- [59] G.S. Kulkarni, K. Reddy, Z. Zhong, X. Fan, *Nat. Commun.* 5 (2014) 4376.
- [60] V. Athanasiou, Z. Konkoli, *International Journal of Parallel, Emergent and Distributed Systems* 33 (2018) 367-386.
- [61] L. Chua, *Semiconductor Science and Technology* 29 (2014) 104001.
- [62] S. Pecqueur, M. Mastropasqua Talamo, D. Guérin, P. Blanchard, J. Roncali, D. Vuillaume, F. Alibart, *Adv. Electron. Mat.* 4 (2018) 1800166.
- [63] M. Sessolo, J. Rivnay, E. Bandiello, G.G. Malliaras, H.J. Bolink, *Adv. Mater.* 26 (2014) 4803-4807.
- [64] S. Pecqueur, S. Lenfant, D. Guérin, F. Alibart, D. Vuillaume, *Sensors* 17 (2017) 570.
- [65] M. Sessolo, D. Khodagholy, J. Rivnay, F. Maddalena, M. Gleyzes, E. Steidl, B. Buisson, G.G. Malliaras, *Advanced Materials* 25 (2013) 2135-2139.



# Recognition of Musical Dissonance and Consonance in a Simple Neuromorphic Computing System

DAWID PRZYCZYNA,<sup>1,2</sup> MARIA SZACIŁOWSKA,<sup>3</sup> MAREK PRZYBYLSKI,<sup>1,2</sup>  
MARCIN STRZELECKI<sup>4</sup> AND KONRAD SZACIŁOWSKI<sup>1,\*</sup>

<sup>1</sup>*AGH University of Science and Technology, Academic Centre for Materials and Nanotechnology, al. Mickiewicza 30, 30-059 Kraków, Poland*

<sup>2</sup>*AGH University of Science and Technology, Faculty of Physics and Applied Computer Science, al. Mickiewicza 30, 30-059 Kraków, Poland*

<sup>3</sup>*Prince Józef Poniatowski School in Bolechowice, ul. Szkolna 7, 32-082 Bolechowice, Poland*

<sup>4</sup>*Faculty of Composition, Interpretation and Musical Education, Krzysztof Penderecki Academy of Music in Kraków, ul. Św. Tomasza 43, 31-027 Kraków, Poland*

*Received: September 8, 2021. Accepted: September 13, 2021*

Reservoir computing with neuromorphic synaptic elements is an emerging, but very successful approach towards processing and classification of various signals. It can be described as a model of a transient computation, where the influence of input changes the internal dynamics of a chosen computational system. Trajectory of these changes represents computation performed by the system. The selection of a suitable computational substrate capable of non-linear response and rich internal dynamics ensures the implementation of simple readout protocols. Signal evolution based on the rich dynamics of the memristive synapse layer helps to emphasize differences between given signals thus enabling their clustering. Here we present a simple neuromorphic computing system (single node echo-state machine based on the memristive synaptic bridge) implemented on the Multisim platform as a tool for clustering of musical intervals according to their consonant or dissonant character. The system generates a series of “epochs” – images of input signal at different stage of evolution. A readout layer based on peak counting in their Fourier spectra allows clustering of musical intervals in a way similar to human subjects or specialized algorithms. The result of this data evolution closely resembled the sensory dissonance curve, with some significant differences. Interestingly, clustering is performed without any reference to the theory of music. This study shows a high potential for exploiting a simple neuromorphic system for advanced

---

\* Contact author: E-mail: szacilow@agh.edu.pl

information processing. Furthermore, they indicate that the notions of consonance and dissonance may have the neurophysiological background.

*Keywords:* Dissonance, consonance, neuromorphic computing, memristor, memristive synapse, music modeling

### 1 INTRODUCTION

Music and speech are created and processed by distinctively different neural structures, but they have some common features: they are means of communication, have specific syntax – *i.e.* there exists a set of rules defining proper combination of elements (words or notes) [1]. Music is the only form of natural communication, that is created and perceived only by humans (however studies on animals indicate some aspects of sensitivity to music) [2, 3]. Music belongs to human universals, *i.e.* elements, patterns, features, or notions that are common to all human cultures worldwide [4], however, according to some opinions, it does not convey any biologically-relevant information [5]. According to Guerino Mazzola “*music embodies meaningful communication and mediates physically between its emotional and symbolic layers*” [6]. Music is a domain of human artistic and entertaining activity, but also a field of vigorous research. Dislike speech, music seems not usually meant for direct communication purposes, especially of biological importance [5].

The simplest musical message, melody, can be defined as an appropriate time sequence of quantized frequencies. These frequencies are called steps in musical scale. Most musical systems are founded on a concept of the octave: an interval between frequencies of  $f$  and  $2f$ . In the music of European origin, an octave is divided into 12 steps (evenly spaced the case of equal temperament, but unevenly spaced in the case of natural tuning), called semitones (Figure 1).

A characteristic feature of European music is the specific concept of musical harmony, which originates from geometrical foundations [6, 7] and may

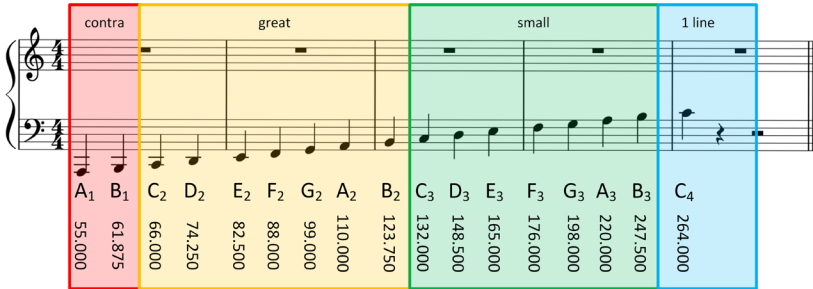


FIGURE 1 Sounds of the C-major scale used in this paper, frequencies of each tone are calculated according to the natural tuning with the reference tone A<sub>4</sub> tuned to 440 Hz.

be considered as a key component of theory and practice. Musical harmony is a complex notion related to the perception of individual and superimposed sounds. The notion of musical harmony includes: (i) the pure content of the set of frequencies heard at given time (including their harmonic components responsible for a timbre of an individual note), (ii) mutual relation of a set of simultaneously played notes (*i.e.* the verticality of the chord), (iii) the tonal context and context of adjacent chords which determine the quality (called harmonic function) of particular chord [8], and (iv) the position and relation of a chord in relation to the melody at given moment [9, 10].

The two fundamental notions associated with musical harmony are consonance and dissonance [11, 12]. This notion concerns the aesthetic feeling evoked by two (or more) sounds played simultaneously [13]. The consonance-dissonance scale allow characterization of musical intervals by how pleasing or disagreeable they are and dividing them into aesthetic classes of perfect consonance (unison, octave, fifth, fourth), imperfect consonance (major sixth, major third, minor third and minor sixth) and dissonance (major second, major seventh, minor seventh, minor second, tritone) [7]. Whereas the classification itself is perfectly well-known and unequivocal, the physical and psychological origin of this classification remains at least unclear [5]. The first detailed study on dissonance and consonance comes from works of Pythagoras of Samos, who related consonant and dissonant combination of tones with the ratio of the lengths of strings. Octave, perfect fifth and perfect fourth were recognized as consonant intervals and founded the basis in Pythagorean philosophy and cosmology [14]. Further works of physicists and music theorists (including Gioseffo Zarlino, Vincenzo and Galileo Galilei, Marin Mersenne, René Descartes, Daniel Bernoulli, and others) came to conclusion that the feeling of consonant and dissonant combinations of sounds relied on the ratios of frequencies [15]. Further works of French composer Jean-Philippe Rameau associated the ratios of harmonic overtones with musical intervals and concluded that harmonic series are foundations of musical harmonies [16]. It was further developed by Jean Rond d'Alembert, Leonhard Euler and Jean Baptiste Joseph Fourier, who provided a complete description of harmonic series for string, air columns and other physical systems. Later on Hermann von Helmholtz has focused on the sense of audition and have developed theory which is based on interaction of acoustic waves in human ear. Dissonance was associated with sound 'roughness' and 'beating' being a result of interference of acoustic waves, especially when two tones are of similar frequencies [17]. This theory has been falsified by recent experiments reported by Mc Dermott et al. [18]. It was found that the feeling of dissonance and consonance can be easily separated from the feeling of sound roughness. Furthermore, dissonance and consonance can be easily distinguished when sounds are played diotically (two tones to the ears) or dichotically (one tone to one ear). This, however does not falsify the role of harmonic components in the sound, as discussed by Plomp and Levelt [19] and recently by Sethares [10, 20], but may indicate other

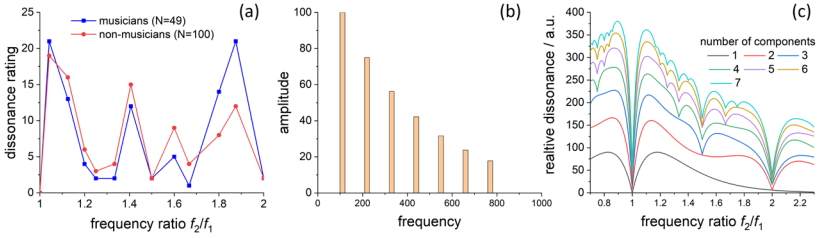


FIGURE 2

Perception of dissonance by human subjects with (49 persons) and without (100 persons) musical training, based on data from Ref. [21] (a). Musical dissonance calculated for a base tone  $A_2 = 110$  Hz and variable number of harmonic components: Fourier spectrum of the tone (b) and the calculated sensory dissonance curves for variable number of harmonic components (c).

physical background of dissonance perception. The approaches mentioned above state, that the tone combination is dissonant if there are dissonant ratios between higher harmonics of two tones and the degree of dissonance depends on the number of dissonant ratios. Upon proper assignment of parameters, the model gives very reliable results, comparable with the auditory evaluation of dissonance (Figure 2a).

The dissonance function between two sine waves of frequencies  $f_1$  and  $f_2$  ( $f_1 < f_2$ ) and corresponding amplitudes of  $l_1$  and  $l_2$  is defines as (1):

$$d(f_1, f_2, l_1, l_2) = l_2 \left( c_1 e^{-b_1 s (f_2 - f_1)} + c_2 e^{-b_2 s (f_2 - f_1)} \right), \quad (1)$$

where

$$l_{12} = \min(l_1, l_2), \quad (2)$$

$$s = \frac{x}{s_1 f_1 + s_2} \quad (3)$$

and the parameters have the following values:  $b_1 = -3.51$ ,  $b_2 = -5.75$ ,  $c_1 = 5.00$ ,  $c_2 = -5.00$ ,  $s_1 = 0.0207$ ,  $s_2 = 18.96$  and  $x = 0.24$  [10]. The dissonance of complex sounds being a collection of sine wave components  $f_0 \dots f_n$  ( $f_k = k f_0$ ) of amplitudes  $l_1 \dots l_n$  can be thus calculated as (4):

$$D = \sum_{i=1}^n \sum_{j=1}^n d(f_i, f_j, l_i, l_j) \quad (4)$$

The results of these calculations are presented in Figure 2 b-c. It should be noted, that this approach relies on the presence of harmonic components in each tone: for single sine signals only unison can be detected, addition of higher number of components results in isolation of octave (2 components), fifth (3 components) and fourth (4 components), as shown in Figure 2c.

Despite the well-established musical theories [7, 9, 22-24] the automated classification of intervals, chords and clusters and recognition of consonance and dissonance has not been achieved in any system without prior training on the basis on the theory of harmony (or incorporating the theory of harmony into the classification algorithm). Recent studies show, however, that this task can be performed in trained plastic neural networks [25]. Furthermore, the understanding of physical nature of dissonance and consonance is still not fully established [5], but it seems that it may have a background hidden deeply in natural processes [26], most probably in neuronal dynamics [27-30]. It was found in a series of independent studies that infants prefer consonant over dissonant sound combinations [31]. A significant preference of musical consonance was observed in numerous animal studies, *e.g.* infant chimpanzees (*Pan troglodytes*) [32], maccacs (*Macaca fascicularis*) [33], tamarins (*Saguinus oedipus*) [34], chickens (*Gallus gallus*) [35] and Java sparrows (*Padda oryzivora*) [36], determined either in behavioural or electrophysiological studies using implanted electrodes. Some adult primates also show the preference of musical consonance [37]. All these considerations point out the fact that the basic understanding of the phenomenon of musical consonance and dissonance is still missing. The notions of consonance and dissonance are antagonistic, and the dissonance can be described as a lack of consonance, or *vice versa*, depending on personal preferences. In music, transitions between dissonance and consonance usually are carriers of emotions and are of a great aesthetic value [23, 38, 39].

All the studies mentioned above indicate an important neurophysiological component to the perception of music and the special role of musical consonance. They also underline the significance of music at very basic neurophysiological level in birds, mammals and humans. Therefore, we intend to check, if a simple neuromimetic device operating in unsupervised learning mode will be able to differentiate combinations of tones into consonant and dissonant categories. If perception of music is a neurophysiological process, then a device that mimics the dynamics of brain structures should show similar ability.

One of the emerging computational paradigms that utilize neuromorphic components and their systems' dynamics for information processing is Reservoir Computing (RC) [40-43]. The basic notion of RC is reservoir – a dynamical system with specific set of properties which render it useful for computation. The reservoir interacts with its environment via the input layer and yields the results of computation via the readout layer. Computation in a reservoir systems consists of two major steps: (i) evolution (for a given time  $\Delta\tau$ ) of the inner state

of the reservoir upon interaction with input signal and (ii) assessment of the state of the reservoir and generation of the results by the output layer [44]. The main advantage of RC, as compared with feedforward artificial neural networks, consists in the lack of training of the reservoir: the only trainable part is the output layer, which decreases the costs of computation. The dynamics of the reservoir is usually represented as a trajectory in a configurational phase space. The input data modifies the internal dynamics and moves the trajectory to a different region of the phase space. The separation property of the reservoir is a simple consequence of this process – different inputs push the reservoir dynamics into different regions of the phase space. In order to perform computation, the dynamics of the reservoir should be sufficiently rich and it should not depend on initial conditions. The first condition is related to the size (not in geometrical sense but in terms of the size and dimensionality of the configuration space) of the reservoir, whereas the latter is associated with the fading memory feature [45-49]. As a consequence of the sensitivity of the reservoir internal dynamics to the applied input, an interplay between classification and clustering of input data is observed: reservoirs of high sensitivity tends to separate the inputs, whereas lower sensitivity leads to data clustering. Detailed formal analysis of this issue, described as “*terra incognita* of practical theorems” has been recently presented by Athanasiou and Konkoli [50].

The interested reader is referred to the literature on the RC subject presenting a rigorous mathematical description [40, 43, 50-53] along with precise description of prerequisites for reservoir layer [52, 54-57] as well as some practical examples of reservoir-like systems applied for signal processing and classification [58-60].

A useful simplification of RC systems engages a single nonlinear node dynamically coupled to itself via an appropriate delay (Fig. 3) [61]. In this

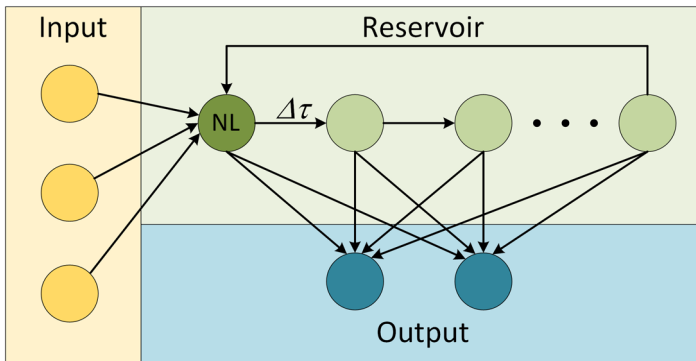


FIGURE 3

Schematics of reservoir computing with a single nonlinear node and a delayed feedback loop. The hidden layer (here referred to as reservoir layer) consists of a single nonlinear (NL) node that evolves in a feedback loop. Delay time  $\Delta\tau$  determines the time between consecutive steps of its evolution until the signal vanishes.

approach the signal package circulates in a closed feedback loop and each round in the loop generates an epoch, which can be considered as a state of a virtual node of the reservoir. This approach simplifies experimental realization of RC and is ideal for time series analysis. Even complex microelectronic systems such as photonic chips or memristor crossbars can be used as a single non-linear node [55, 62, 63]. Reduction of reservoir to a single physical node, however, usually limits their operation to a single data input [58-60] or requires appropriate signal masking and time multiplexing [64].

The search for a system capable of advanced signal processing has turned authors attention towards reservoir computing and especially single-node echo state machines (SNESM), a subclass of RC systems with delayed feedback. These systems are usually reported as mimicking the neural dynamics, furthermore, they can be relatively easy implemented both in hardware and in software. Recent findings in the field of SNESM show a possibility of discrimination signal and pulse amplitudes without prior training [58, 59] as well as application of simple photoelectrochemical dynamic systems for the recognition of handwritten characters [65] and improvement of chemical sensor performance [51, 60, 66]. It suggests that dynamic systems with appropriate feedback, fading memory and internal dynamics should be capable of advanced signal classification. These properties fit well into the notion of RC paradigm, where richness of possible states and their appropriate sensitivity/fading after stimulation can be used as effective platform for information processing. After ensuring that given computational substrate (or readout process) [67] presents appropriate dynamic conditions, simple readout processes should suffice in probing concomitant reservoir states thus performing computation (as the evolution of reservoir internal state represents its computing capabilities). By incorporating suitable substrate – for example a simple neuromimetic device as in this work – in the SNESM reservoir system, its information processing capabilities can be enhanced.

The applicability of this approach to time-series analysis, therefore can be, in principle, used for analysis and/or classification of acoustic frequency signal, *e.g.* heartbeat [68], speech or music. Whereas there were several attempts to apply RC to speech analysis [69-74], musical structures have attracted much less attention. There is only one report of RC-inspired music [75], but any musical objects itself have not been considered as a subject of RC or related studies. Therefore, current study uses musical intervals as input data and attempts their clustering according to their harmonic (consonant *vs* dissonant) quality.

The goal of this study is to verify the utility of neuromorphic computing approach towards unsupervised recognition and clustering (a first step towards classification) of musical intervals. As numerous literature reports (*vide supra*) indicate the ability of reservoir and related neuromorphic systems to process information (partly due to its memory features) and possibility for its simple implementation, it seems to be a good candidate for the classification tasks in which we rely on the simplest input signals (a sum of

two sine waves). As shown above, much more sophisticated RC circuits capable of analyzing complex signals can be found in the literature, but in this work the main focus in circuit design was simplicity. We used the most simplified neuromorphic systems: a single node recurrent neural network (also referred as SNESM), which has the ability of non-linear data transformation and high efficiency of higher harmonics generation to carry out complex and non-trivial signal classification. Even the use of a single memristor - let alone a synaptic bridge - has been shown to be a better solution for generating higher harmonics than other non-linear electronic components [76]. Moreover, the use of a neuromorphic device as a computing substrate also seems to be a natural step due to its ability to generate higher harmonics and the undeniable neurological factors related to the perception of music. A series of musical intervals from tones belonging to natural scale has been constructed and subjected processing by the memristive synapses in a feedback loop *in silico*. Based on the analysis of the signal evolution in the obtained Fourier transforms two different post-processing readout operation have been designed and their performance is compared.

## 2 RESULTS AND DISCUSSION

### 2.1 Selection of the best model

Initial tests have involved three model circuits of synapse, on the basis of which the most promising circuit has been selected for construction of a SNESM. A single sine input signal of  $A_1 = 55$  Hz frequency has been selected as a test signal. The response of all test circuits has been recorded and compared according to two factors: (i) the depth of the hysteresis curve, *i.e.* the difference in current between the high and low resistive states upon dynamic stimulation and (ii) the richness of the Fourier spectrum of the resulting spectrum, *i.e.* the total harmonic distortion. All three circuits (cf Methods, Figure 13) provide a significant signal transformation, however each of them presents distinct features, which are used to select the most promising circuit for further investigations.

A simple memristive circuit comprising one memristor and one resistor of  $2\text{ k}\Omega$  (cf. Figure 13 a) yields a classical, significantly asymmetric pinched hysteresis loop (Figure 4a). The surface areas of lobes are:  $54.99\text{ a.u.}^2$  (positive lobe) and  $37.06\text{ a.u.}^2$  (negative lobe). The asymmetry of both lobes is a result of numerical instability of the model circuit at low frequencies in MULTISIM environment. Fourier analysis indicates the presence of progressive formation of higher harmonics, the intensity of which decreases exponentially with increasing input frequency (Figure 4 b). Whereas the generation of a complex Fourier pattern is satisfactory and should be beneficial for dissonance/consonance discrimination, the asymmetry of the lobes may bring additional, undesired distortions of symmetric sine signals. Therefore, more complex circuits have been designed and tested for signal processing.



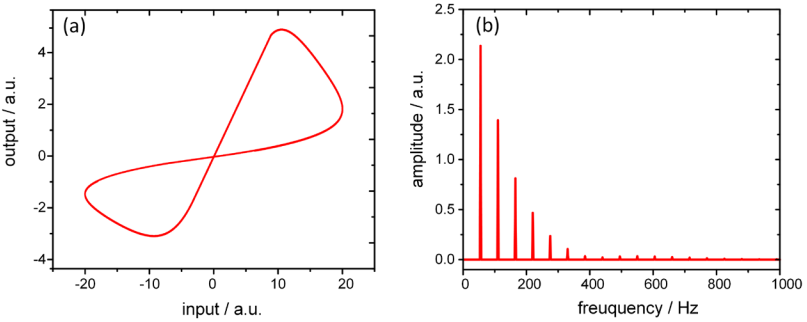


FIGURE 4  
Pinched hysteresis loop (a) and a Fourier spectrum of an output signal for calculated for a simple memristive circuit from Figure 13 a with input frequency  $A_1=55$  Hz.

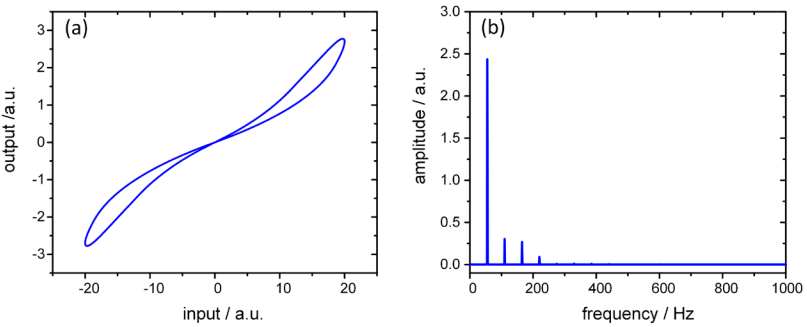


FIGURE 5  
Pinched hysteresis loop (a) and a Fourier spectrum of an output signal for calculated for a memristor bridge circuit from Figure 13 b with input frequency  $A_1=55$  Hz.

A memristor Wien bridge-like circuit with an additional resistor of  $2\text{ k}\Omega$  (cf. Figure 13 b) generates much less pronounced hysteresis loop, however it has much higher symmetry (Figure 5 a). Both lobes have exactly the same area of  $7.04\text{ a.u.}^2$ , which is over 5 times less than in the previous case. The high symmetry observed here is a result of specific connectivity within the bridge. The two memristors in each branch have opposite polarizations, and the two branches are oppositely polarized as well. As a consequence, both branches should have almost the same (within the numerical accuracy) resistance irrespectively of their history. Applied signal induce changes of the resistance ratios in each branch depending on their polarities [77]. The small discrepancies within each branch are reflected in small lobes of the pinched hysteresis loop with lower current values at each memristor, which should result in more reliable results due to elimination of numerical instabilities. Fourier analysis indicates the presence of progressive formation of higher harmonics, however their intensities are very low (Fig. 5 b). In comparison

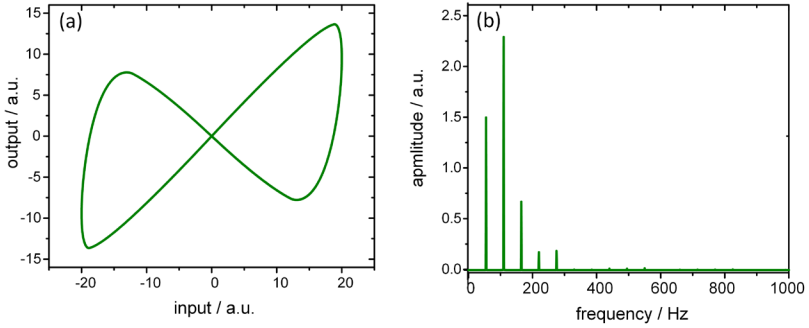


FIGURE 6

Pinched hysteresis loop (a) and a Fourier spectrum of an output signal for calculated for a memristor synaptic circuit from Figure 13 c with input frequency  $A_1=55$  Hz.

with the previous system higher symmetry of hysteresis loop is a significant advantage, however small harmonic distortion (*i.e.* low intensity of higher Fourier components) should be considered as a drawback.

Incorporation of a differential amplifier to the memristor Wien bridge circuit (cf. Figure 13 c) results in dramatic increase of the hysteresis loop area, and at the same time the symmetry of the pinched loop is preserved (Figure 6 a). The areas of lobes of  $239.50 \text{ a.u.}^2$  and  $239.51 \text{ a.u.}^2$  (for 55 Hz/20V input) is the largest one among all tested circuits. This circuit also provides very high harmonic distortion – the intensity of the first harmonic component (110 Hz) is higher than the input signal (Figure 6 b). Therefore, this circuit was used as a nonlinear node in the SNESM (cf Figure 14). The stability of the circuit is a result of reversed-polarity arrangement of memristors in each branch of the bridge. Whereas the total resistance of each branch remains virtually constant, the resistance ratios of upper and lower memristor in each branch change. Therefore, the potential difference between the two apices strongly depends on the history of the system and is also polarity dependent. The high symmetry observed here is a consequence of the mirror symmetry of the bridge. Furthermore, lower current values at each memristor (due to partition of the current within two branches of the bridge) should result in more reliable results due to elimination of numerical instabilities.

## 2.2 Evolution of summed sine signals

AC signals applied as the input to the SNESM circuit (cf. Figure 14) undergo gradual changes due to a nonlinear character of the memristive node. Single sine signal (*e.g.* 55 Hz, Figure 7) is transformed within a SNESM circuit into a complex signal with numerous overtones, the intensity of which varies from one generation to the other. Interestingly the ratio of overtone intensities varies among different epochs (generations), but the spectral composition of the signal remains unchanged.

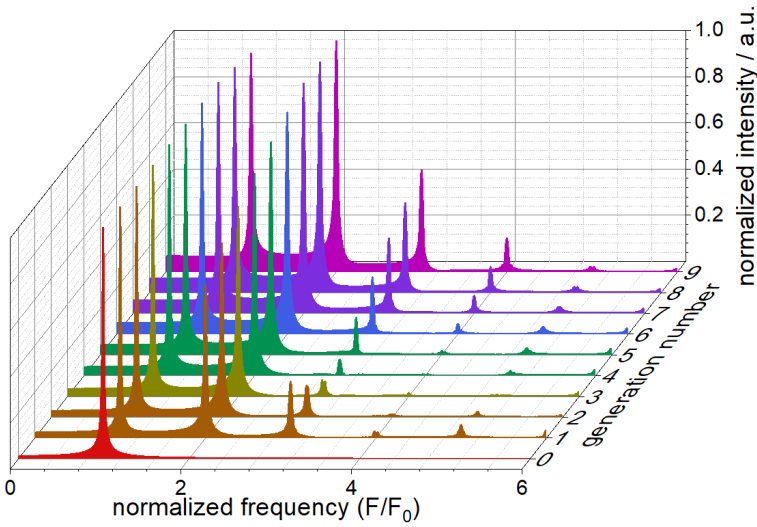


FIGURE 7

$A_1$  (55 Hz) input evolution within a single node echo state machine from Figure 14. Each spectrum corresponds to subsequent step in evolution, called generation. The 0<sup>th</sup> generation is the input signal.

More complex behavior can be observed in the case of musical intervals, *i.e.* signals being a sum of two sine waves of different frequencies applied as the input to the SNESM circuit (Figure 8). The case of octave is the simplest one. Qualitatively the octave ( $A_1$ - $A_2$  in this example) is undistinguishable from unison  $A_1$ . In the case of unison, the first harmonics appears in the first generation signal and slowly increases its intensity. In the case of octave signal the first harmonics is already present in the input, but the higher harmonics appear from the first generation. All spectra contain only integer-value harmonics, *i.e.*  $f_0, 2f_0, 3f_0$ , etc...

Regular patterns of Fourier components, however with different distance between subsequent peaks can be also observed in the case of perfect fourth and perfect fifth. In perfect fifth the intervals between subsequent peaks are identical and equal to  $\frac{1}{2}f_0$ , whereas in the case of perfect fourth its  $\frac{1}{3}f_0$ . Importantly, the same pattern is stable in all generations, higher harmonics slowly increase with the evolution time. Interestingly, in both cases low frequency components, *i.e.*  $\frac{1}{2}f_0$  (in the case of perfect fifth) and  $\frac{1}{3}f_0$  and  $\frac{2}{3}f_0$  (in the case if fourth) can be observed, especially in higher generation signals. This implies that the nonlinear memristive node acts as a frequency mixer, producing both sum and difference frequencies (eqs. 5-6):

$$f_+^1 = f_2 + f_1 \quad (5)$$

$$f_-^1 = f_2 - f_1 \quad (6)$$

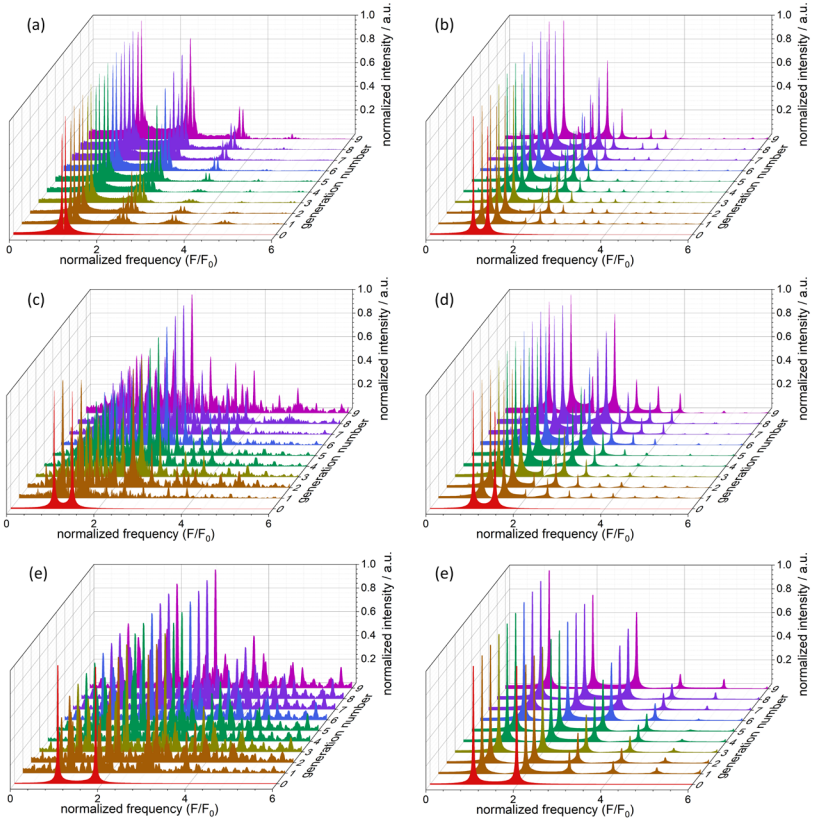


FIGURE 8

Evolution of signals corresponding to selected musical intervals: minor second  $B_1-C_2$  (a), perfect fourth  $C_2-F_2$  (b), tritone  $B_1-F_2$  (c), perfect fifth  $A_1-E_2$  (d), major seventh  $C_2-B_2$  (e) and octave  $A_1-A_2$  (f). In each case the  $F_0$  frequency is the frequency of lowest tone in the interval. Each spectrum corresponds to subsequent step in evolution, called generation. The  $0^{\text{th}}$  generation is the input signal. See Figure 2 for frequency values for each tone.

Taking into account relations between frequencies in perfect fifth (eq. 7) and perfect fourth (eq. 8) in natural scale [10]:

$$f_2 = \frac{3}{2} f_1 \quad (7)$$

or

$$f_2 = \frac{4}{3} f_1 \quad (8)$$

the observed low frequency signal, as well as high frequency components with non-integer spacings are obvious.

In the first generation signal additional components within perfect fifth (eqs. 9-10) and perfect fourth (eqs. 11-12) can be found:

$$f_+^1 = \frac{3}{2}f_1 + f_1 = \frac{5}{2}f_1 \quad (9)$$

$$f_-^1 = \frac{3}{2}f_1 - f_1 = \frac{1}{2}f_1 \quad (10)$$

or

$$f_+^1 = \frac{4}{3}f_1 + f_1 = \frac{7}{3}f_1 \quad (11)$$

$$f_-^1 = \frac{4}{3}f_1 - f_1 = \frac{1}{3}f_1 \quad (12)$$

In the second generation additional components are formed due to frequency mixing of input tones and the first generation ones. In the case of perfect fifth two new frequencies are equal either input tones or the first generation ones, as well as some 2<sup>nd</sup> generation frequencies are identical (only combination yielding positive differential frequency are listed, 13-20):

$$f_1^2 = f_1 + f_-^1 = f_1 + \frac{1}{2}f_1 = \frac{3}{2}f_1 = f_2 \quad (13)$$

$$f_2^2 = f_1 - f_-^1 = f_1 - \frac{1}{2}f_1 = \frac{1}{2}f_1 = f_-^1 \quad (14)$$

$$f_3^2 = f_1 + f_+^1 = f_1 + \frac{5}{2}f_1 = \frac{7}{2}f_1 \quad (15)$$

$$f_4^2 = f_2 + f_-^1 = \frac{5}{2}f_1 + \frac{1}{2}f_1 = \frac{6}{2}f_1 \quad (16)$$

$$f_5^2 = f_2 - f_-^1 = \frac{5}{2}f_1 - \frac{1}{2}f_1 = \frac{4}{2}f_1 \quad (17)$$

$$f_6^2 = f_2 + f_+^1 = \frac{5}{2}f_1 + \frac{5}{2}f_1 = \frac{10}{2}f_1 \quad (18)$$

$$f_7^2 = f_+^1 + f_-^1 = \frac{5}{2}f_1 + \frac{1}{2}f_1 = \frac{6}{2}f_1 = f_4^2 \quad (19)$$

$$f_8^2 = f_+^1 - f_-^1 = \frac{5}{2}f_1 - \frac{1}{2}f_1 = \frac{4}{2}f_1 = f_5^2 \quad (20)$$

Numerous iterations of the composite signal in the feedback loop result in accumulation of various frequencies with the spacing of  $\frac{1}{2}f_0$  (perfect fifth) or  $\frac{1}{3}f_0$  (perfect fourth). Thus, the feedback loop is utilized to recursively process signal and utilize some concepts of RC, namely the recursive information processing [44, 52, 55, 60, 78-80] for attempted classification of signals in terms of harmonic quality.

Other intervals generate much more complex patterns within the SNESM circuit and their evolution results in continuously increasing number of Fourier components with intercomponent spacings smaller than  $\frac{1}{3}f_0$ . Furthermore, large number of overlapping differential frequencies results in uneven distribution of most intense spectral components (cf. Fig. 8c, e). This observation may be already considered as a simple classification criterion: consonant tone combinations result in outputs with relatively small number of spectral components, and these components are evenly spaced. Whereas this is a useful criterion of preliminary classification, but it does not allow rating of degree of dissonance, as is it usually performed by listeners (Figure 3 a). Therefore, two different classification protocols have been suggested to classify musical intervals according to their dissonance/consonance levels and to unambiguously measure the degree of dissonance of a given tone combination: (i) counting a total number of peaks in Fourier spectrum in each generation and (ii) measuring distances between neighboring peaks in Fourier spectrum in each generation. These two approaches are briefly discussed below

### 2.3 Analysis of the number of peaks in the Fourier transform

A simple peak count analysis was performed to examine if any patterns were present in the obtained data (OriginPro2019 Peak Analyzer tool was used for this task, with following parameters: positive peaks, local maximum, point range = 4, threshold = 0.005). Detection of peaks was based on searching of the local maxima in a given point range by simple comparison of neighboring values. It was decided that the peaks should consist of at least 4 points from base to base as an arbitrary “peak” criterion – smaller number of points resulted in peak detection in the background, whereas bigger number resulted in omitting of peaks. This type of peak detection was carried out for all Fourier transforms for all epochs. The results are shown for individual intervals as peak count as a function of repetition of the feedback loop in order to examine data for deviations and anomalies (Figure 9).

Whereas initial input (generation #0) contains always two Fourier components, the higher generations contain variable number of peaks, moreover it also evolves in time, as expected from recurrent character of the SNESM circuit and Equations (9)-(20) as shown in Figure 9 a. It can be noticed that generally the number of peaks for consonant intervals (unison, perfect fourth, perfect fifth and octave) are significantly lower than for the dissonant intervals. Therefore, in order to reproduce the sensory dissonance curve (cf. Figure 3 a), the reciprocal number of Fourier components was plotted against the frequency ratios of

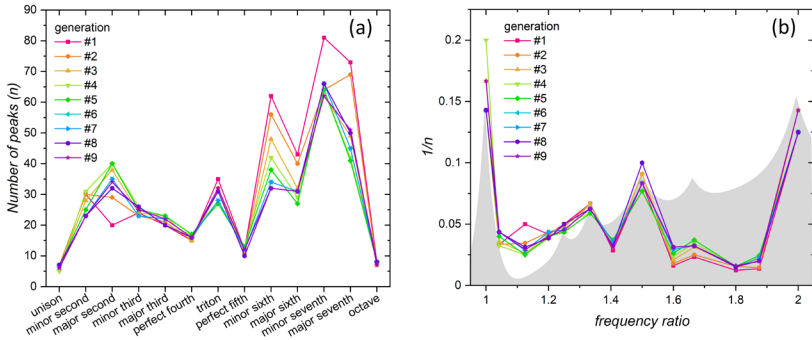


FIGURE 9

Number of peaks for various music intervals for subsequent Fourier transforms of the signal circulating in the feedback loop (a) and a reciprocal number of peaks as a function of frequency ratio for various intervals. Area shaded in grey represents simulated “sensory consonance” curve (mirror image of the dissonance curve from Fig. 3c for 5 harmonics). Points represent experimental data, whereas solid lines serve as eye guides.

various intervals (Figure 9 b). Surprisingly, it resembles the Helmholtz curve of consonances and dissonances, with exception of minor and major thirds, which form a local minimum on experimental curve, but are usually recognized as weak consonances (cf. Figure 3 a). The other discrepancy is minor sixth, which, along with major sixth constitutes a local minimum, as is again recognized as a weak consonance. Despite these small discrepancies, the neuromorphic system with a memristor bridge synapse shows unexpectedly good performance in discrimination of musical dissonance without prior training.

### 2.4 Analysis of the distance between peaks in the Fourier transform

In order to examine the relationship between the normalized frequencies of the peaks present in the Fourier transforms, an analysis was performed using the difference of normalized frequencies between a given peak and the peak preceding it (Figure 10). Then to visualize and analyze obtained data, a three-dimensional “phase portrait” was constructed using the obtained frequency differences. For each interval and for each peak (denoted here as  $F_n$ ) a set of distances to the nearest neighbors:  $d(F_n, F_{n+1})$ ,  $d(F_{n+1}, F_{n+2})$  and  $d(F_{n+2}, F_{n+3})$  were calculated.

These values were used as Cartesian coordinates (x, y, z) defining points in space for all subsequent peaks present in a given spectrum. In the data representation, the given point is obtained on the basis of given difference and two successive frequency differences. Each interval is thus represented as a set of points in three dimensional space (Figure 11). In order to enrich the constructed phase portrait all signal generations – *i.e.* the whole history of signal evolution – have been used. Due to this method of data visualization, the intervals possessing greater number of peaks in the Fourier spectra are represented by a greater number of points in the obtained phase space (*i.e.* the cardinality of their set is

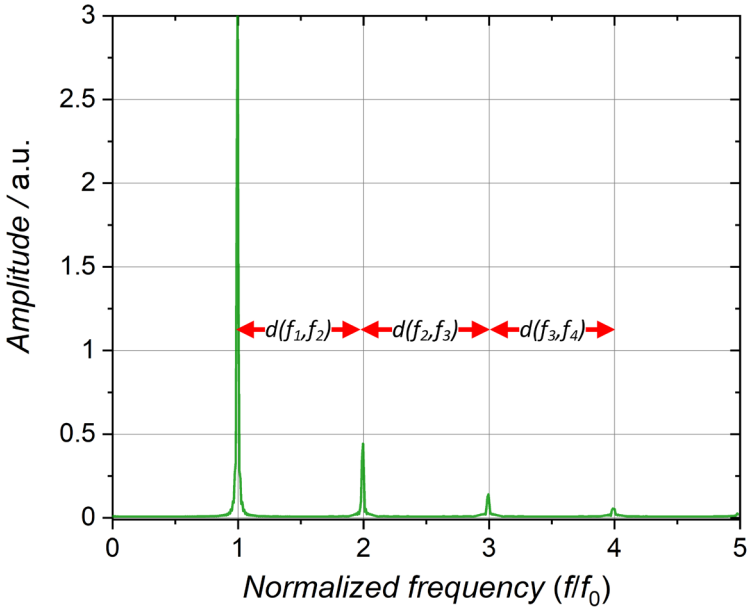


FIGURE 10  
A principle of signal analysis based on distances between peaks in Fourier spectra.

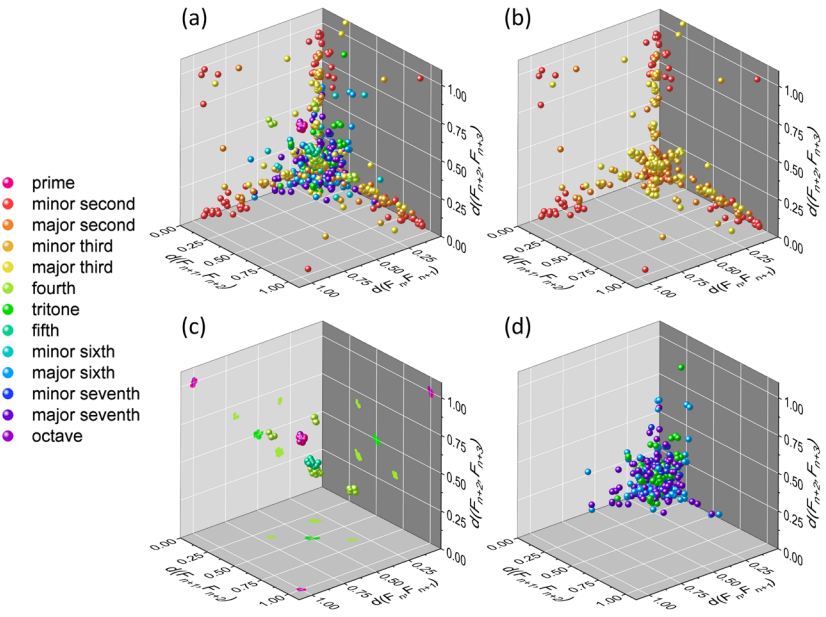


FIGURE 11  
Geometrical representation of various intervals on the basis of distances between subsequent components in Fourier spectra. All intervals (a), seconds and thirds (b), unisons, octaves, fourths and fifths (c) and tritones, sixths and sevenths (d).



greater). It can be observed, that intervals regarded as absolute consonances – unison and octave – are clustered in one place, around the (1,1,1) point, which is obvious, because the differences between the peaks of normalized frequencies for these intervals will always be 1. In turn, the intervals treated as perfect – fourth and fifth – are clustered in separation from other intervals.

Perfect fourth is clustered in 4 different regions around points  $(\frac{1}{3}, \frac{1}{3}, \frac{1}{3})$ ,  $(\frac{1}{3}, \frac{1}{3}, \frac{2}{3})$ ,  $(\frac{1}{3}, \frac{2}{3}, \frac{1}{3})$  and  $(\frac{1}{3}, \frac{2}{3}, \frac{2}{3})$ . Perfect fifth can be found in one bigger cluster at  $(\frac{1}{2}, \frac{1}{2}, \frac{1}{2})$ . This observation is consistent with the previous analysis of the distance of generated harmonics (equations 9-20). Only points corresponding to these consonant intervals are clustered in very limited spaces. Other intervals, usually considered dissonant, are localized in different regions of the phase space and corresponding points are more scattered. Seconds and thirds occupy places along axes with a cluster close to the origin of the coordinate system. Tritones, sixths and sevenths together are scattered as well close to the origin of the coordinate system. Most intervals perceived as dissonant can be found in one big cluster of points near the (0,0,0) point. Apart from absolute and perfect intervals, the other intervals are usually clustered in several separate areas, but their points can also be found mixed with other intervals in different parts of the graph.

The two different clustering schemes based on various processing of the SNESM output present very similar results. The approach based on peak counting yields consonance recognition closely related to the auditory classification of musical intervals. The geometrical approach, based on distances between subsequent peaks in Fourier spectra clearly differentiates consonances and dissonances. Furthermore, it clusters consonances into two categories (ideal – unison and octave and perfect – fourth and fifth). In the case of dissonant intervals, this method also provides some kind of differentiation, in which seconds and thirds are, at least partially, separated from sixths, sevenths and tritone.

### 3 CONCLUSIONS

The computational example presented in this paper show that a simple neuro-morphic computing circuit for RC system – a single node echo state machine with appropriately designed nonlinear node: a memristive bridge synapse with differential amplifier, is capable of advanced signal processing. Even such an abstract task as clustering of musical intervals according to their harmonic quality can be performed in a simple circuit without prior training or engaging any element of the theory of harmony into the algorithm. The system generates a family of higher frequency components in the case of single sine input, and a series of differential frequencies in the case of two sine inputs. Analysis of harmonic components showed the highest performance of the selected non-linear element among other similar variants for the computational node. Surprisingly, the results are very similar to the evaluation of

sound samples by human subjects (Figure 3 a) and theoretical dissonance analysis using the Plomp-Levelt [19] approach and Sethares algorithm [10]. The nonlinearity of the node is a key for successful performance – the input signals, devoid of higher harmonics, cannot be clustered. Therefore, memristors are the simplest passive elements that can be used in this application.

In a typical musical context (with an exception of electronic music) single sine waves are very uncommon. As it can be seen from the numerical dissonance analysis (eq. 1-4, Figure 3), the notion of sensory consonance and dissonance makes sense only in the case of higher harmonics: the interval of octave becomes distinguishable from the whole acoustic spectrum with at least one harmonics, the perfect fifth requires at least two harmonics. Interestingly, the system presented here can deal with single sine waves and classifies the notes in a similar way as human subjects and established numerical algorithms.

Recognition of consonance and dissonance as well as clustering of musical intervals according to their harmonic quality is performed on the basis of two simple post-processing protocols based on analysis of the obtained Fourier spectra. By simple peak counting and measuring distance between them it is possible to reproduce the sensory dissonance curve and also to cluster intervals in three-dimensional space according to the spectral characteristics of signal processed in the SNESM. In the obtained phase-space it is possible to separate absolute intervals (unison and octave), individual perfect intervals (fourth and fifth) and dissonant intervals (and to some extent seconds and thirds). Interestingly, this clustering scheme yields results very similar to other numerical models, but in this case completely devoid of any preliminary bias/training based on theory of music, in a purely unsupervised manner.

The presented data demonstrate the power of simple SNESM in solving difficult tasks without any training related to the nature of the input data. The results of this paper also indicate that the notions of musical consonance and dissonance may have neurophysiological background. It can be also speculated that neural processes involved in perception of music may be related to the RC principles.

## 4 METHODS

A simple numerical model of memristor was taken from the literature and used without any modifications as shown in Table 1 [81]. Figure 12 shows an equivalent circuit of this memristor. Two current sources  $G_{r1}$  and  $G_{r2}$  which have opposed polarities and operate in such a way so that  $G_{r2}$  is responsible for charging the capacitor, and  $G_{r1}$  for discharging it. Their operation is controlled by the necessary step functions used to determine which source is active each time, according to the applied voltage. Moreover, the problem of limiting the boundaries of  $r(V_M, t)$  is addressed by using elementary SPICE diodes and DC voltage sources. Their role is summarized as follows: if  $V_r$ , *i.e.* the voltage

```

.SUBCKT mem1 plus minus

.SYNTAX PSSpice
*Parameters` values
.param rmin = 100
.param rmax = 390
.param rinit = 390
.param alpha = 40000
.param beta = 10
.param gamma = 0.2
.param VtR = 1.5
.param VtL = -1.5
.param yo=0.0001
.param m = 82
.param fo = 310
.param Lo = 4
.param Dbreak = 1
.param Dbreak = 1

Gr1 0 r value = {dr_dt(V(plus)-V(minus))*st_f(-(V(plus)-
V(minus)))}
Gr2 0 r value = {dr_dt(V(plus)-V(minus))*st_f(V(plus)-
V(minus))}

D1 k r {Dbreak}
V1 k 0 {rmin}
D2 r g {Dbreak}
V2 g 0 {rmax}
Cr r 0 1 IC={rinit}

*Current equation Imem = V / R(L)
Gpm plus minus value={ (V(plus)-V(minus)) / ((fo*exp(2*L(V(r)))) /
L(V(r))) }

*Func. for non-linear threshold-based behavior
.func dr_dt(y)={-alpha*((y-VtL)/(gamma+abs(y-VtL)))*st_f
(-y+VtL)-beta*y*st_f(y-VtL)*
+st_f(-y+VtR)-alpha*((y-VtR)/(gamma+abs(y-VtR)))*st_f(y-VtR)}

*smoothing function
.func st_f(y)={1/(exp(-y/yo)+1)}
*L(V) function
.func L(y)={Lo-Lo*m/y}

.ends mem1

```

TABLE 1

A memristor description in PSSpice syntax according to [81].

across the capacitor  $C_r$  (which is described by the value of parameter  $r(V_M, t)$ ) falls below  $V_1$  (rises above  $V_2$ ) then diode  $D_1$  ( $D_2$ ) is forward biased and thus  $V_r$  is maintained equal to  $V_1$  ( $V_2$ ). In this setup the values of the DC sources are set equal to the boundary values of  $r(V_M, t)$ ; *i.e.*  $V_1 = r_{MIN}$  and  $V_2 = r_{MAX}$  [81].

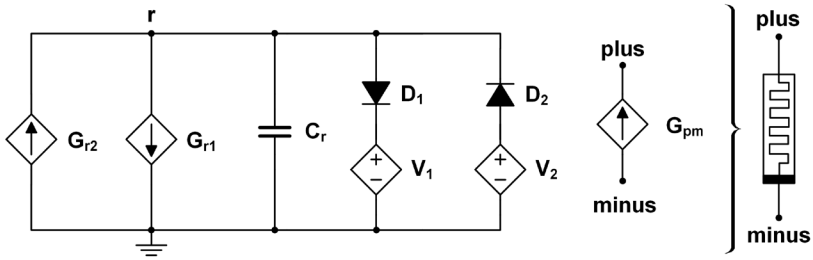


FIGURE 12 An equivalent circuit of the memristor model used in this study. Adapted from Ref. [81].

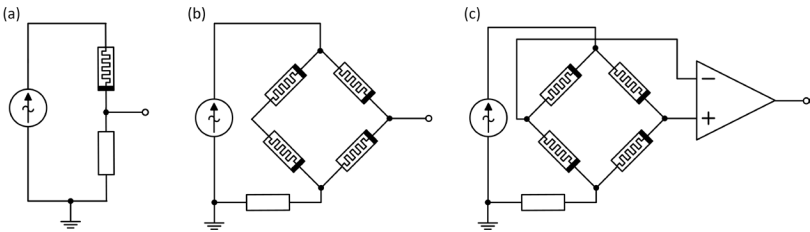


FIGURE 13 Memristor-based circuits implemented on the MULTISIM platform.

Four different memristor-based circuits were constructed on MULTISIM platform: a simple memristor-resistor circuit (Figure 13 a), memristor-based Wien bridge (Figure 13 b) and a bridge synapse (Figure 13 c). The latter was also incorporated in a feedback loop of the single node echo state machine (Figure 14).

The performance of the circuits was initially tested with sine wave signals of 55, 110 and 220 Hz frequencies (referred to musical notes  $A_1$ ,  $A_2$  and  $A_3$ , as named in Scientific/International Pitch Notation [82]). Subsequently various musical intervals (ranging from unison up to octave) were constructed in C-major scale spanning ca.  $2\frac{1}{2}$  octaves in natural tuning (cf Figure 2). Each tone was represented by a single sine wave pulse of given frequency lasting 2 s with a damping factor of  $2\text{ s}^{-1}$  (Figure 15 a). Signal damping was necessary to avoid effects associated with abrupt signal truncation. After the system was fully excited by the input signal from two generators, a switch was activated (Figure 14), which enabled further self-excitation of the system. A single signal epoch (here lasting two seconds) after by the delay (marked as  $\Delta\tau$  in Figures 1 and 14) was then returned to the system to excite it, which allowed signal evolution. Each simulation was run for 20 s, which allows recording on an input and 9 echoes generated by the feedback loop (Figure 15 b).

Recorded signals were imported to OriginPro2019 software package for further processing. Fourier transform spectra were calculated using the rectangle window function independently for each signal package.

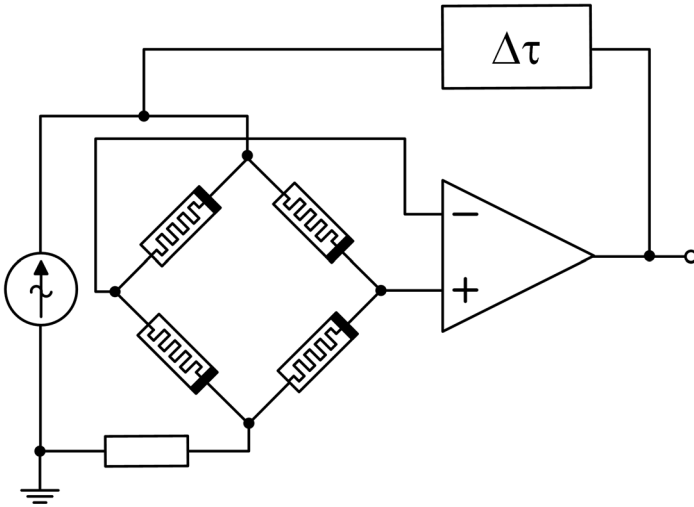


FIGURE 14 Single-node echo state machine (SNESM) implemented on the MULTISIM platform. An appropriate gain was set to eliminate premature fading of the signal in higher epochs.

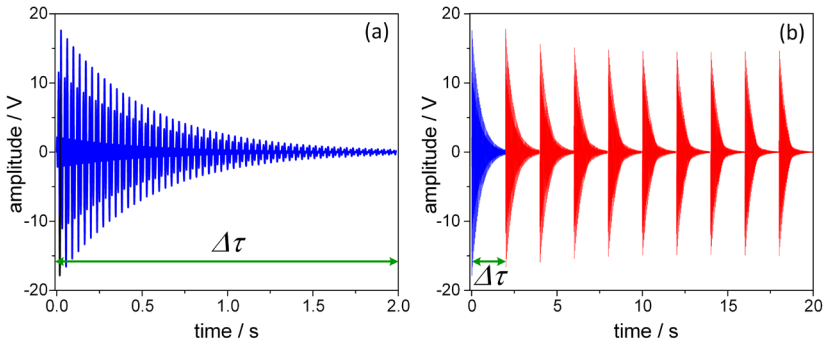


FIGURE 15 An example of the input (a) and output (b) signals recorded for the SNESM feedback loop: input perfect fifth ( $A_1$ - $E_1$ , 55 and 82.5 Hz, blue) and output echoes (red). Green arrow indicates duration of each epoch (generation).

## ACKNOWLEDGEMENTS

Authors acknowledge the financial support from the Polish National Science Centre within the MAESTRO (grant agreement No. UMO-2015/18/A/ST4/00058) and PRELUDIUM (grant agreement No. UMO-2018/31/N/ST5/03112) projects. DP has been partly supported by the EU Project POWR.03.02.00-00-I004/16.

### Data availability

The data that support the findings of this study are available from the corresponding author upon request.

### Conflicts of interest/Competing interests

Authors declare no conflicts of interest.

### Code availability

No special codes have been developed, all computations were done with commercial software packages (Multisim, OriginPro). The modified QBasic code (based on original code by W.A. Sethares and modified to the QBasic syntax) for dissonance calculation is available electronic supplementary information.

### Author contributions

Dawid Przyczyna has conducted most data analysis and has written large fragments of the manuscript. Maria Szaciłowska has performed most of numerical experiments in Multisim. Marcin Strzelecki has prepared sections of musical context of the research, contributed in the discussion of the results and revised the whole manuscript. Marek Przybylski has contributed in the discussion of results and has partially revised the manuscript. Konrad Szaciłowski has formulated the leading idea, has designed the Multisim calculation schemes, performed most of the raw data processing and has written large sections of the manuscript.

## REFERENCES

- [1] N.M. Weinberger, *Sci. Am.* 291(5) (2004) 88–95.
- [2] W. Apel, *Bird Song*, in: W. Apel (Ed.) *Harvard Dictionary of Music*. Second Edition, Revised and Enlarged., Harvard University Press Cambridge, Massachusetts, 1974.
- [3] M.J. West, A.P. King, M.H. Goldstein, *Singing, socializing, and the music effect*, in: P. Marler, H. Slabbekoorn (Eds.) *Nature's music: The science of bird song*, Academic Press, New York, 2004.
- [4] D.E. Brown, *Human universals*, McGraw-Hill, New York, 1991.
- [5] J.G. Roederer, *The physics and psychophysics of music*, Springer Science+Business, New York, 2008.
- [6] G. Mazzola, M. Mannone, Y. Pang, M. O'Brien, N. Torunski, *All about music. The complete Ontology: Realities, Semiotics, Communication and Embodiment*, Springer Nature, Cham, 2016.
- [7] G. Loy, *Musimatics*, MIT Press, Cambridge MA, 2006.
- [8] E. Bigand, R. Parncutt, F. Lerdahl, *Perception Psychophys.* 58 (1996) 125–141.
- [9] D. Paret, S. Sibony, *Musical Techniques*, John Wiley & Sons, Hoboken, 2017.
- [10] W.A. Sethares, *Tuning, Timbre, Spectrum, Scales*, Springer Verlag, London, 2005.
- [11] M.C. LoPresto, *Phys. Educ.* 44 (2009) 145–150.
- [12] J. Nordmark, L.E. Fahlén, *Speech Trans. Lab. Quart. Progr. Res. Stat. Rep.* 29 (1988) 111–122.
- [13] D.J. Benson, *Music. A Mathematical Offering*, Cambridge University Press, Cambridge, 2007.
- [14] J.L. Snyder, *Music Theory Spectrum* 5 (1983) 110–120.
- [15] R.M. Grant, *Music Theory Spectrum* 35 (2013) 62–76.
- [16] D.E. Cohen, *Music Theory Spectrum* 23 (2001) 139–169.
- [17] D.L. Bowling, D. Purves, *Proc. Natl. Acad. Sci.* 112 (2015) 11155–11160.

- [18] J.H. McDermott, A.J. Lehr, A.J. Oxenham, *Curr. Biol.* 20 (2010) 1035–1041.
- [19] R. Plomp, W.J.M. Levelt, *J. Acoust. Soc. Am.* 38 (1965) 548–560.
- [20] W.A. Sethares, *J. Acoust. Soc. Am.* 94 (1993) 1218–1228.
- [21] M.C. Lopresto, *Phys. Teacher* 53 (2015) 225–229.
- [22] D. Meredith, *Computational Music Analysis*, Springer International Publishing AG, Cham, 2016.
- [23] P.Y. Chan, M. Dong, H. Li, *Research* 2019 (2019) 2369041.
- [24] D. Tymoczko, *A Geometry of Music*, Oxford University Press, Oxford, 2011.
- [25] T. Pankovski, E. Pankovska, *Biologically Inspired Cognitive Architectures* 22 (2017) 82–94.
- [26] A. Schneider, Pitch and pitch perception, in: R. Bader (Ed.) *Springer Handbook of Systematic Musicology*, Springer International Publishing AG, Cham, 2018.
- [27] P. Crespo-Bojorque, J. Monte-Ordoño, J.M. Toro, *Neuropsychologia* 117 (2018) 188–198.
- [28] G.M. Bidelman, A. Krishnan, *J. Neurosci.* 29 (2009) 13165–13171.
- [29] L.L. Trulla, N. Di Stefano, A. Giuliani, *Front. Psychol.* 9 (2018).
- [30] P. Virtala, M. Tervaniemi, *Music Perception* 34 (2017) 387–404.
- [31] L.J. Trainor, B.M. Heinmiller, *Inf. Behav. Devel.* 21 (1998) 77–88.
- [32] T. Sugimoto, H. Kobayashi, N. Nobuyoshi, Y. Kiriya, H. Takeshita, T. Nakamura, K. Hashiya, *Primates* 51 (2010) 7–12.
- [33] Y.I. Fishman, I.O. Volkov, M.D. Noh, C. Garell, H. Bakken, J.C. Arezzo, M.A. Howard, M. Steinschneider, *J. Neurophysiol.* 86 (2001) 2761–2788.
- [34] J. McDermott, M. Hauser, *Cognition* 94 (2004) B11–B21.
- [35] C. Chiandetti, G. Vallortigara, *Psychol. Sci.* 22 (2011) 1270–1273.
- [36] S. Watanabe, M. Uozumi, N. Tanaka, *Behav. Processes* 70 (2005) 203–208.
- [37] A. Izumi, *J. Acoust. Soc. Am.* 108 (2000) 3073–3078.
- [38] C.L. Krumhansl, *Music Theory Spectrum* 17 (1995) 53–80.
- [39] J. Robinson, R.S. Hatten, *Music Theory Spectrum* 34 (2012) 71–106.
- [40] H. Jaeger, German National Research Center for Information Technology GMD Technical Report 148 (2001).
- [41] W. Maass, *Theor. Comput. Sci.* 261 (2001) 157–178.
- [42] T. Natschläger, W. Maass, H. Markram, *Telematic* 8(1) (2002) 39–43.
- [43] W. Maass, T. Natschläger, H. Markram, *Neural Comput.* 14 (2002) 2531–2560.
- [44] Z. Konkoli, Reservoir computing, in: A. Adamatzky (Ed.) *Unconventional computing. A volume of the encyclopedia of complexity and systems science*, Springer Nature, New York, 2018.
- [45] S. Boyd, L. Chua, *IEEE Trans. Circ. Syst.* 32 (1985) 1150–1161.
- [46] T.S. Lee, *IEEE Trans. Circ. Syst.* 35 (1988) 474–477.
- [47] A. Borys, *Int. J. Electron. Telecom.* 61 (2015) 377–280.
- [48] I. Farkaš, R. Bosák, P. Gergeľ, *Neural Networks* 83 (2016) 109–120.
- [49] A. Lazar, G. Pipa, J. Triesch, *Neural Networks* 20 (2007) 312–322.
- [50] V. Athanasiou, Z. Konkoli, On mathematics of universal computation with generic dynamical systems, in: A. Adamatzky, S.G. Akl, G.C. Sirakoulis (Eds.) *From Parallel to emergent computing*, CRC Press, London, 2019.
- [51] Z. Konkoli, *Int. J. Parallel Emergent Distrib. Syst.* 33 (2018) 121–143.
- [52] Z. Konkoli, On reservoir computing: From mathematical foundations to unconventional applications, in: A. Adamatzky (Ed.) *Advances in unconventional computing. Vol. 1: Theory*, Springer International Publishing, Cham, Switzerland, 2017.
- [53] D. Verstraeten, B. Schrauwen, M. D’Haene, D. Stroobandt, *Neural Networks* 20 (2007) 391–403.
- [54] M. Lukoševičius, H. Jaeger, *Comput. Sci. Rev.* 3 (2009) 127–149.
- [55] G. Tanaka, T. Yamane, J.B. Héroux, R. Nakane, N. Kanazawa, S. Takeda, H. Numata, D. Nakano, A. Hirose, *Neural Networks* 115 (2019) 100–123.
- [56] J.B. Butcher, D. Verstraeten, B. Schrauwen, C.R. Day, P.W. Haycock, *Neural Networks* 38 (2013) 76–89.

- [57] L. Grigoryeva, J.-P. Ortega, *Neural Networks* 108 (2018) 495–508.
- [58] E. Właźlak, P. Zawal, K. Szaciłowski, *ACS Appl. Electron. Mater.* 2 (2020) 329–338.
- [59] E. Właźlak, M. Marzec, P. Zawal, K. Szaciłowski, *ACS Appl. Mater. Interf.* 11 (2019) 17009–17018.
- [60] D. Przychyna, S. Pecqueur, D. Vuillaume, K. Szaciłowski, *Int. J. Unconv. Comput.* 14 (2019) 267–284.
- [61] J. Schumacher, H. Toutounji, G. Pipa, An analytical approach to a single node delay-coupled reservoir computing, in: V. Mladenov, P. Koprinkova-Hristova, G. Palm, A.E.P. Villa, B. Appollini, N. Kasabov (Eds.) *Artificial Neural Networks and Machine Learning*, Springer, Berlin, 2013.
- [62] M. Nakajima, K. Tanaka, T. Hashimoto, *Communications Physics* 4 (2021) 20.
- [63] Y. Zhong, J. Tang, X. Li, B. Gao, H. Qian, H. Wu, *Nat. Commun.* 12 (2021) 408.
- [64] L. Appeltant, G. Van der Sande, J. Danckaert, I. Fischer, *Sci. Rep.* 4 (2014) 3629.
- [65] D. Przychyna, M. Lis, K. Pilarczyk, K. Szaciłowski, *Molecules* 24 (2019) 2738.
- [66] K. Pilarczyk, E. Właźlak, D. Przychyna, A. Blachecki, A. Podborska, V. Anathasiou, Z. Konkoli, K. Szaciłowski, *Coord. Chem. Rev.* 365 (2018) 23–40.
- [67] K. Vandoorne, P. Mechet, T. Van Vaerenbergh, M. Fiers, G. Morthier, D. Verstraeten, B. Schrauwen, J. Dambre, P. Bienstman, *Nat. Commun.* 5 (2014) 3541.
- [68] M. Deng, T. Meng, J. Cao, S. Wang, J. Zhang, H. Fan, *Neural Networks* 130 (2020) 22–32.
- [69] F. Abreu Araujo, M. Riou, J. Torrejon, S. Tsunegi, D. Querlioz, K. Yakushiji, A. Fukushima, H. Kubota, S. Yuasa, M.D. Stiles, J. Grollier, *Sci. Rep.* 10 (2020) 328.
- [70] A. Smerieri, F. Duport, Y. Paquot, M. Haelterman, B. Schrauwen, S. Massar, *AIP Conf. Proc.* 1479 (2012) 1892–1895.
- [71] M.R. Salehi, L. Dehyadegari, *Opt. Quant. Electron.* 48 (2016) 281.
- [72] A. Alalshkumbarak, L.S. Smith, On Improving the Classification Capability of Reservoir Computing for Arabic Speech Recognition, in: S. Wermter (Ed.) *Artificial Neural Networks and Machine Learning*, Springer, Cham, 2014.
- [73] L.E. Suarez, J.D. Kendall, J.C. Nino, *Neural Networks* 106 (2018) 223–236.
- [74] M.D. Skowronski, J.G. Harris, *Neural Networks* 20 (2007) 414–423.
- [75] D. Przychyna, P. Zawal, T. Mazur, M. Strzelecki, P.L. Gentili, K. Szaciłowski, *Jpn. J. Appl. Phys.* 59 (2020) 050504.
- [76] G.Z. Cohen, Y.V. Pershin, M. Di Ventra, *Appl. Phys. Lett.* 100 (2012) 133109.
- [77] H. Kim, M.P. Sah, C. Yang, T. Roska, L.O. Chua, *Proc. IEEE* 100 (2012) 2061–2070.
- [78] L.F. Seoane, *Phil. Trans. B* 374 (2019) 20180377.
- [79] J.D. Hart, L. Larger, T.E. Murphy, R. Roy, *Phil Trans. A* 377 (2019) 20180123.
- [80] Z. Konkoli, S. Nichele, M. Dale, S. Stepney, Reservoir computing with computational matter, in: S. Stepney, S. Rasmussen, M. Amos (Eds.) *Computational Matter*, Springer, Cham, Switzerland, 2018.
- [81] I. Vourkas, G.C. Sirakoulis, *Memristor-based nanoelectronic computing circuits and architectures*, Springer International Publishing, Heidelberg, 2016.
- [82] R.W. Young, *J. Acoust. Soc. Am.* 11 (1939) 134–139.



RESEARCH ARTICLE



# KNOWM memristors in a bridge synapse delay-based reservoir computing system for detection of epileptic seizures

Dawid Przczyzna<sup>a,b</sup>, Grzegorz Hess<sup>c</sup> and Konrad Szaciłowski<sup>a</sup>

<sup>a</sup>AGH University of Science and Technology, Academic Centre for Materials and Nanotechnology, Kraków, Poland;

<sup>b</sup>AGH University of Science and Technology, Faculty of Physics and Applied Computer Science, Kraków, Poland;

<sup>c</sup>Department of Neurophysiology and Chronobiology, Jagiellonian University, Institute of Zoology and Biomedical Research, Kraków, Poland

## ABSTRACT

Nanodevices that show the potential for non-linear transformation of electrical signals and various forms of memory can be successfully used in new computational paradigms, such as neuromorphic or reservoir computing. In this work, we present single-node Echo State Machine (SNESM) RC system based on bridge synapse as a computational substrate (consisting of 4 memristors and a differential amplifier) used for epileptic seizure detection. The results show that the evolution of the signal in a feedback loop helps improve the classification accuracy of the system for that task. The transformation in SNESM changes the correlation and distribution of the complexity parameters of the input signal. In general, there are more differences in the correlation of complexity parameters between the transformed signal and the input signal, which may explain the improvement in the classification scores. SNESM could prove to be a useful time series signal processing system designed to improve accuracy in classification tasks.

## ARTICLE HISTORY

Received 8 June 2022




Accepted 8 June 2022


## KEYWORDS

Memristors; reservoir computing; bridge synapse; epileptic seizure

## 1. Introduction

Nowadays, one can observe a drastic technological development and a real ‘explosion’ of data created and accumulated through various activities. Scientists are beginning to pay attention to an effect that we are already slowly beginning to observe in the world, the so-called informational black hole. This concept is based on the fact that such a large amount of information is generated that we are physically unable to process it [1–4]. For this reason, vital information can get lost in a ‘black hole’ overwhelmed by the commonly generated data noise. This should not come as a surprise at a time when we can have, among many others, a smart refrigerator, smart light bulbs, TV, telephone, washing machine, vacuum cleaner, curtains, heating, and assistant (e.g. Apple Siri, Google Assistant, Samsung Bixby) in our homes. These complex information collection and processing systems are known as the ‘Internet of Things’ (IoT) [5–7]. Additionally, a huge portion of data is generated every second in cyberspace. We use social media, messengers, online stores, video players, etc. The data collected on each of these platforms is analyzed and profiled in order to be able to provide us with more personalised advertisements and to make a bigger profit for the service provider. Furthermore, it provides us with information published by our friends or groups to which we belong or subscribe, topics which attract our attention because of our aesthetic, intellectual, or political preferences [8]. The collection and analysis of those

**CONTACT** Dawid Przczyzna  dawidp@agh.edu.pl; Konrad Szaciłowski  szacilow@agh.edu.pl  AGH University of Science and Technology, Academic Centre for Materials and Nanotechnology, al. Mickiewicza 30, Kraków 30-059, Poland

 Supplemental data for this article can be accessed here. <https://doi.org/10.1080/17445760.2022.2088751>

data translates into real-world effects in the form of monetary gains/losses [9,10], our choices as customers, and finally as voters (the case of Cambridge Analytica affecting the US presidential election and Brexit) [11].

To address the computational problems of the modern age, scientists are working to improve existing hardware and software technologies, as well as develop unconventional and/or hybrid approaches known as heteroic computing [12]. The growth of the first approach is commonly known to be subjected to Moore's law, whereas the second approach attempts to overcome its limitations through embedded multifunctionality and interaction with the environment [13]. Moore's law states that computational capabilities of conventional transistor technologies will double every few years. However, there is a lower limit to miniaturisation due to (i) the granularity of matter and (ii) the effects of quantum tunnelling of electrons through the gate of the transistor and (iii) heat management problems, which are the main reasons for looking for other computational technologies [14–19]. Second major issue is the so-called Von Neuman Bottleneck. It is a problem that limits the computing abilities of classic computers resulting from the separation of memory functions and processing that require communication between these components, which in turn limits the speed of the computing process. One of the novel technologies that aims to resolve some of modern computing problems is the application of memristors (and other memristive elements) and memristive circuits [20–24].

In a classic configuration, capacitive material (e.g. dielectric or semiconductor) is placed between metal electrode contacts in a sandwich-type system. Basically, memristive materials have two resistance states, called HRS (high-resistive state) and LRS (low-resistive state). By applying electrical pulses (or scans) of proper voltage, materials can be SET or RESET to LRS or HRS depending on the memristor type and its initial state. Due to some preservation of states after the turning off of the power source, resistive switching effect is hoped to be used as building block for novel non-volatile memory. In this configuration, it would be a new genre of information storage elements, called ReRAM (resistive, random access memory) [25], which would compete with currently available flash memory and some other continuously developed technologies (magnetoresistive random access memory, etc.). Nevertheless, the high demands on the energy efficiency of the switching, its statistical repeatability, and speed of operation make the new materials are still being sought to meet them. The application of novel elements, such as memristors, allows delegatement of some of the computational steps of artificial neural networks to be realised *in materia* [26].

Many scientists conduct intensive research that draws inspiration from biological neural structures in order to achieve more efficient computational structures, potentially of a universal nature. The high popularity is evident by an increasing number of publications appearing each year, scientific journals, and numerous conference meetings related to this subject. Interested readers are referred to recent reviews on the subject [27–30]. As can be seen, neuromorphic computing appears to be moving towards 'conventional' computing, or at least towards special purpose computing modules [31]. Recurrent neural networks, which are especially good at representing dynamics of given input due to feedback loops present in the system, exhibit problems with costly learning process. To solve this problem, Jäger and Maas independently proposed the Echo State Network (ESN) [32] and the Liquid State Machine (LSM) approaches [33]. In their constructs, in contract with artificial neural networks, the information processing layer is not to be trained, only the readout layer is subjected to training procedures. Thus, they suggested the importance of the multidimensional, rich, and dynamic state space of the information processing layer [26,34]. Over time, both of these approaches to efficient training of recurrent neural networks were incorporated into a common conceptual framework named Reservoir Computing (RC) and the information processing layer was named the 'reservoir' [35,36]. The reservoir in the RC paradigm describes a computational substrate capable of representing various inputs in a multidimensional configuration space of states, where computation is represented as a trajectory between successive states of the system in this space. Hence, as a proof of concept, RC has been implemented in simple systems as a bucket of water, where the data set with human speech was encoded as

a series of water splashes [37]. Pictures of the perturbed water surface were used as basis for classification tasks. In our previous work we have shown that RC computing systems can be implemented even in such primitive setups as a doped cement and successfully used to classify simple signal according to its shape [38].

These unconventional computing systems must have several features in order to function properly, namely they must show appropriate internal dynamics, volatile memory, and the echo property of previous states. The RC circuits are based on: (i) a nonlinear element (e.g. a memristor) that also provides memory functions, (ii) an input layer that provides information/signal for processing, (iii) readout layer, and optionally (iv) a delayed feedback loop that provides internal system dynamics [39,40]. The readout layer is the only part of the system that needs to be 'trained' and that is capable of sampling and representing the internal state of the reservoir. In other words, only simple model training is performed on the given features of signal transformed by the reservoir. In this case, no sophisticated ANN network is needed as readout, simple models such as linear regression, decision tree, etc. suffice. There is an obvious trade-off between the complexity of reservoir layer and the complexity of the readout process needed for a given classification/prediction task [41].

Single-node echo-state machine (SNESM) are novel RC systems that has only one physical node operating in the delayed feedback loop [26,42–45]. Basically, both the signal and the physical node state change each time the signal passes through the device in each cycle. The evolution of the loop signal can potentially improve clustering and classification capabilities of the RC system. Wlaźlak et. al. showed implementation of SNESM system based on a single hardware memristor for the signal classification task based on its amplitude [43,46]. In our previous work we have shown clustering of musical consonant/dissonant intervals through signal evolution in the software RC system based on the bridge synapse operating in the feedback loop [47]. Bridge synapse consists of four memristors and a differential amplifier. It was shown that bridge synapse is good at supporting lots of analog states, which can be beneficial from the perspective of rich state space needed for a good reservoir computing substrate.

Epilepsy is a disease that affects approximately 50 million people worldwide [48]. Epilepsy is diagnosed based on the appearance of seizures, which are defined as transient signs and/or symptoms resulting from abnormal activity of a population of brain nerve cells [49]. Therefore, epilepsy is considered a chronic brain disease characterised by an enduring disposition towards recurrent unprovoked seizures and by the neurobiological, cognitive, psychological, and social consequences of this condition [50]. Causes of epilepsy are different and include structural, genetic, infectious, metabolic, immune, and finally unknown factors [49]. There are several types of epilepsy that are classified on the basis of the type of seizure and pattern of brain activity [51] recorded with the use of non-invasive electroencephalography (EEG) through electrodes affixed to the scalp [52]. Currently seizures can be controlled and it is estimated that 70% of patients could live without seizures with appropriate medication [48]. However, the occurrence of seizures is unpredictable and, therefore, the development of methods of seizure detection is of great importance for a significant improvement in the quality of the patient, especially with a risk of sudden unexpected death in epilepsy (SUDEP) [53]. It should be noted that while in many cases seizures are associated with muscle activity, usually stiffening and then jerking of an arm or leg (tonic-clonic seizures), there are also types that are not associated with motor manifestations, for example, symptoms like hot and cold feelings, abnormal visual, olfactory, auditory, gustatory and somatic sensations, or seizures characterised by interruption of activities that occur suddenly with impairment of consciousness (absence seizures) [50]. Currently, EEG combined with video recordings are the most reliable methods for detecting epileptic seizures; however, they are only available in ambulatory monitoring. Thus, portable seizure detection devices have been proposed as an alternative solution [54].

As of today, deep learning methods allow classification of epilepsy using EEG signals with a precision of 99%, but those models require large datasets for training and classification tasks, and are cost ineffective [55]. Artificial data augmentation methods often must be used as a large amount of epilepsy seizure data is generally hard to obtain. One of the advantages of RC systems is their capability

of operating with scarce, incomplete data employing only the simplest classifiers (at the read-out layer) like linear regression, gradient descent, or decision trees. There is no need for multilayer artificial neural networks to train the SNESM read-out layer, as the reservoir performs data transformation that aims at simplifying classification task. The SNESM system gives additional benefit in the form of dataset extension. Each consecutive signal epoch is slightly different version of the base signal due to non-linear transformation and damping in a delay-based RC system. Echo of the primary signal may be easier to classify due to changes in its complexity and correlations between the parameters that describe it.

In this work, we present characteristics (noise characteristics and total harmonic distortion) of KNOWM memristors and bridge synapse based on them. Furthermore, we present analysis of reservoir layer and results of evolution of classification accuracy score of analyzed signal in the SNESM system based on hardware bridge synapse. For the classification task, we used a dataset containing cases of epilepsy, walking, running and sawing (overall 408 instances) collected from three different patients using a triaxial accelerometer attached to the dominating hands, which is a common technique of a non-invasive and non-disturbing way of monitoring motor activity [56–58]. On the contrary, other techniques, such as electroencephalography, electrocardiography, and electromyography, are impractical in daily life. The data for each patient were then analyzed separately. A scarce dataset is used on purpose, as with the RC approach, and the system could be calibrated individually for each patient in a cost-effective manner. Evolution of the signal in the system, especially damping, noise, and distortion accumulation, as well as nonlinear filtering influences improvement of a f1-score of classification of used signals. F1 score is a statistical analysis used to test the classification accuracy of the system [59]. For this data set we have found that echo of the base signal presented a better classification accuracy of epilepsy in relation to unprocessed waveforms. Furthermore, when epochs were analyzed collectively, further improvements of classification accuracy were obtained. In addition, changes in distribution and correlation between complexity parameters are shown for the input signal and transformed signal, which could explain changes in classification scores. This work poses as proof-of-concept that evolution of the signal in SNESM systems can highlight features of given signal or transform it in such a way that the overall classification of it can be improved in the case of scarce dataset and simple classification model.

### 1.1. KNOWM memristors

KNOWM Inc. memristors are semi-commercial memristive devices designed for scientific research [60]. It is very convenient at prototyping various memristive circuits. Several scientific works use KNOWM memristors in their research [61,62]. The researchers presented the possibility of constructing a hardware chaotic Chua oscillator without the need to use equivalent circuits [63]. The other group showed the characteristics of the impulse response and the possibility of coupling the operation of KNOWM memristors with an ultrasonic transducer [64]. These memristors are good candidates for the construction of hardware neural networks based on thin-film nanomaterials because of their good and mostly repeatable performance and simplicity in the prototyping of networks with various structures. The schematic layer diagram of the device is shown in Figure 1.

The mechanism of operation of KNOWM memristors proposed by the manufacturers is as follows. After manufacture, the devices are in the HRS state ( $M\Omega - G\Omega$  range). When the device is put into operation for the first time, a so-called self-directed channel is formed when a positive potential to the upper electrode. In this case, the required potential is the same as that used during normal operation of the device. Applying a positive potential to the memristor generates Sn ions from the SnSe layer and forces them into the active  $Ge_2Se_3$  layer (here W-doped). The Sn ions are intended to facilitate the transport of Ag to the active layer at the Ge–Ge binding sites. This occurs due to the energetically beneficial process in which the electrons entering the active layer ( $Ge_2Se_3$ ) from the negatively polarised bottom electrode (with the simultaneous formation of Sn ions from the SnSe layer) are strongly localised around

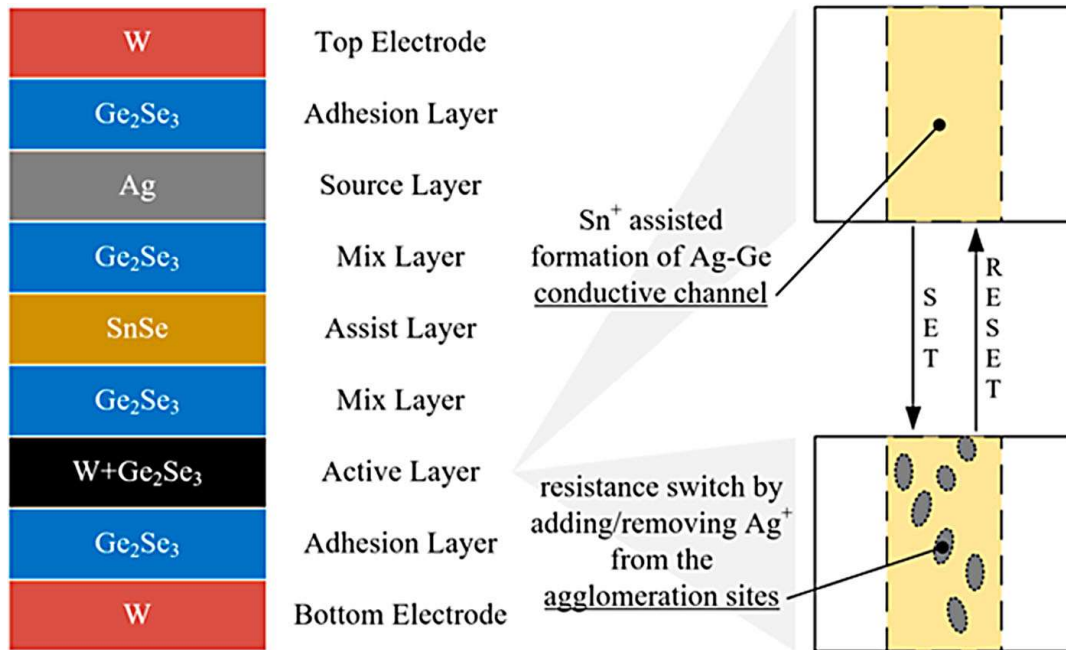


**Figure 1.** Layer diagram of the thin-film stack of nanomaterials in KNOWM memristive devices and depiction of the switching mechanism. Reprinted from Ref. [65].

Ge–Ge dimers. During this reaction, the glassy network of  $\text{Ge}_2\text{Se}_3$  is distorted, creating an ‘opening’ near the Ge–Ge sites. That opening allows the  $\text{Ag}^+$  ions to access possible Ag–Ge binding site more easily and become preferred conductive channels in the active layer for  $\text{Ag}^+$  movement during device operation. As a result, the Sn ions facilitate the energetically favourable Ag/Ge substitution reaction at the Ge–Ge bond. This self-directed conductive channel is a result of the natural structure of the glass and follows the position of the initial Ge–Ge dimers in the glass. Since Ag tends to agglomerate with other Ag atoms, the Ag–Ge substitution sites may favour Ag agglomeration in the glass. Accordingly, the resistance of the device is altered by adding or removing Ag from agglomeration sites within this *in situ* generated path. It is anticipated that conduction may occur between clusters of Ag agglomerations in the glass. Therefore, the path need not be composed of conductive metallic filaments that include two opposing electrodes, as in CBRAM devices. In the case of KNOWM memristors, the device resistance is dictated by the Ag concentration in a given place of the agglomeration and the distance between successive places of the Ag agglomeration. Resistance regulation is carried out by the movement of  $\text{Ag}^+$  ions between the device layers, forced by the application of a positive or negative electric potential [60].

## 2. Results

### 2.1. Large-amplitude sinusoidal voltammetry

LASV (large amplitude sinusoidal voltage) is a classic electrochemical measurement technique, used here to characterise memristive devices, to determine threshold of their switching potential, speed of operation, and its repeatability. The probing signal is a simple sinusoidal wave of given frequency and amplitude. The scans were performed in the potential window for which switching from ON/OFF (or Low Resistive State/High Resistive State) states is repeatable, in order to determine the optimal ‘SET’ and ‘RESET.’

To prevent memristors from being burnt, measurements were made with a series  $5\text{ k}\Omega$  resistor in the circuit to limit the current. Too high currents (above  $1\text{ mA}$ ) irreversibly damage KNOWM memristors, irreversibly switching them to LRS. On the other hand, too low currents prevent the system from

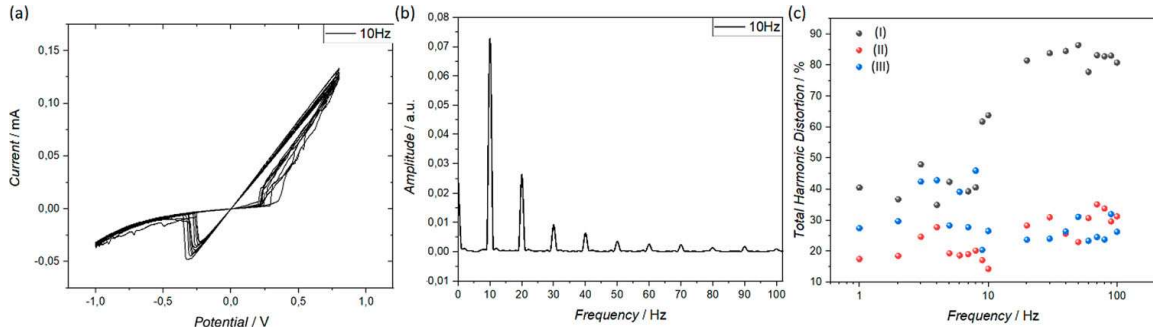


**Figure 2.** Exemplary LASV signal measured at 10 Hz (a) and Fourier spectra (with rectangular apodizing function window) based on it (b). Total harmonic distortion determined on the basis of Fourier transform, for frequencies ranging from 1 to 100 Hz (c). Results presented for single memristor (I), bridge synapse without differential amplifier (II), and with differential amplifier (III).

switching to the LRS state. This was observed during memristor tests in which a 20 k $\Omega$  resistor was used. For a single chip (16 memristors), for a 20 k $\Omega$  resistor, 4 out of 16 memristors did not switch to the LRS state. In the case of the 5 k $\Omega$  resistor, all memristors were switching and had good cycling repeatability.

In this study, LASV measurements were performed at 19 different scan speeds ranging from 1 to 100 Hz (example in Figure 2a). The results are shown in Figs. S1 and S2. In this frequency range, KNOWM memristors operate reliably, as producers show in the data sheet, that they can operate even at 1000 Hz. LASV measurements were performed for three scenarios: for a single memristor and for a bridge synapse without and with a differential amplifier.

## 2.2. Total harmonic distortion

On the basis of the results from LASV measurements, an analysis of the frequency distortion was performed. This was done by determining the total harmonic distortion (*THD*) parameter. It tells us about the contribution of higher harmonics of the total signal to the fundamental frequency of the signal and can thus be considered as a simple experimental index of device linearity [66]. It is especially useful in the characterisation of memristive devices, because it gives a clear distinction between unipolar and bipolar memristors [67]. To determine THD, Fourier spectra of the analyzed signals are needed (an example spectrum is shown in Figure 2b). Additionally, Fig. S3 shows a Fourier transform of an exemplary driving signal. Based on the calculated Fourier transform for all frequencies analyzed, the fundamental  $THD_F$  was determined on the basis of the following formula (1):

$$THD_F = \frac{\sqrt{V_2^2 + V_3^2 + V_4^2 + \dots}}{V_1}, \quad (1)$$

where  $V_n$  is the  $n$ th amplitude of the frequency of successive higher-harmonic peaks observed in the Fourier spectra. The THD parameter in its fundamental form can take values greater than 100%, hence the following correction can be applied as normalisation (2):

$$THD_R = \frac{THD_F}{\sqrt{1 + THD_F^2}}, \quad (2)$$

where  $R$  in  $THD_R$  stands for 'root mean square.'

Fourier spectra clearly indicate bipolar character of the studied memristors, as all even and odd harmonics are equally well represented in the spectra (Figure 2b) [67]. The results in Figure 2(c) show that higher  $THD_R$  occurs at frequencies above 10 Hz for a single KNOWM memristor, while for bridge synapse circuits,  $THD_R$  is generally constant (apart from several cases in lower frequency range shown

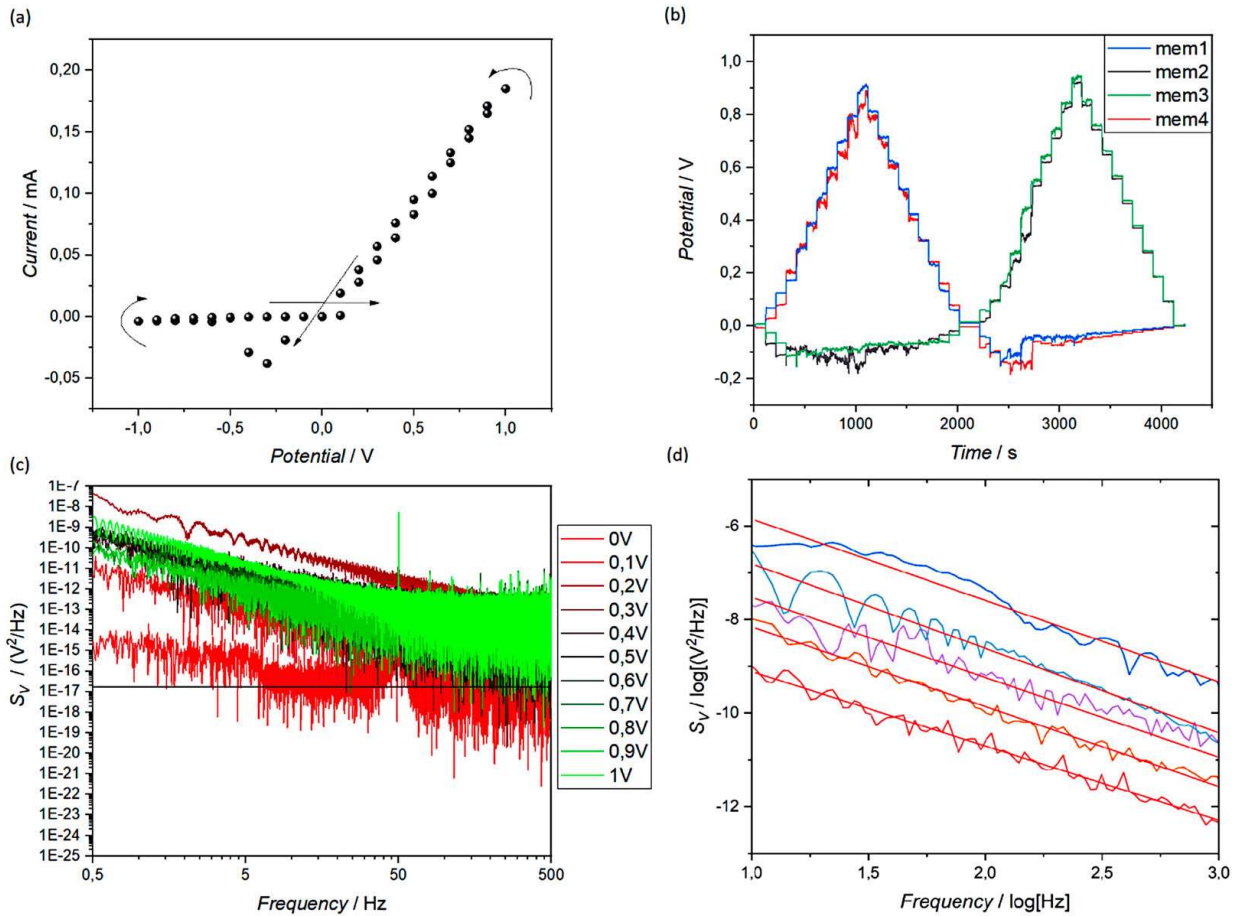


**Figure 3.** Average current values for the noise measured in the potential window  $\pm 1$  V for 100 s for each step of 100 mV. The arrows indicate the direction of the measurement. Measurement performed for a single memristor (a). Voltage difference recorded between individual elements of the bridge synapse during noise recording measurement (b). Noise measured for KNOWM memristors presented in frequency domain, for potentials from 0 V to 1 V. The black line indicates the thermal base floor measured at 0 V (c). An example of fitting a line to the several filtered noise spectra (d).

in Figure 2c). This is a marked difference between KNOWM memristors and reported theoretical models, where the introduction of a differential amplifier into the Wien-like bridge resulted in a much increased *THD* [47].

### 2.3. Noise analysis

Chronoamperometric methods were used to characterise the noise present in KNOWM devices in the  $\pm 1$  V range. A set of potentials was applied step manner (step size 100 mV) to the device, and the response was measured for 100 s. The average values of the measured current at each step during the measurement are shown in Figure 3(a). These values resemble the classic hysteresis loop observed during LASV measurements. Presented in the time domain, the alternating switching of the four memristors in the bridge synapse (without differential amplifier) can be observed in Figure 3(b). If plotted in I-V (or V-V) domain, the result from Figure 3(b) would resemble the one on the Figure 3(a). In the next step, a Fourier transform was performed to each voltage step to calculate the noise spectra (Figure 3c).

The slope of the noise spectra was determined in order to compare the noise character at different potentials (Figure 3d). Due to the fact that the results are presented on a logarithmic scale, in order to reliably fit the lines, it is necessary to interpolate recorded traces, and reduce point density to achieve uniform data point distribution in all frequency ranges.

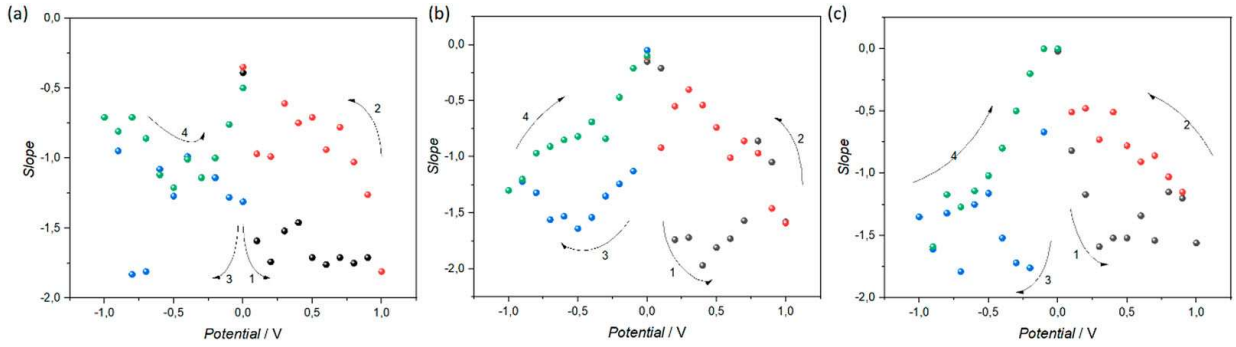


**Figure 4.** Collected slope values of noise spectra at different DC potentials. Arrows indicate direction of the experiment. Results for single KNOWM memristor (a), synaptic bridge (b), and a circuit comprising a bridge synapse and a differential amplifier (c).

Generally, the noise spectra observed in the case of KNOWM devices are of red/brown character [68], described by the power law of the form (3):

$$S_V(f) \propto \frac{1}{f^\gamma} \quad (3)$$

where  $S_V(f)$  is the spectral power density of the signal and  $\gamma$  is a parameter that reflects the noise type (0 for white noise,  $-1$  for pink one, and  $-2$  for the brown noise). In the studies cases, we can see that the thermal noise of the KNOWM memristor evolved from white through pink to brown noise, depending on the applied potential and its history, as the noise exponent for all studied circuits follows the hysteresis loop, however, the points are a bit more scattered. During the stepwise voltage scans, the  $\gamma$  parameter changed from close to zero at very low voltages down to  $-2$  for voltages higher than ca. 0.5 V. At ca. 1 V (the point of transition from HRS to LRS), the noise parameter gradually increased to zero with decreasing voltage (Figure 4a). This behaviour indicates that the charge carrier dynamics in multilayer KNOWM memristors is complex and voltage-dependent. Voltage dependence may suggest electron-hopping-type conductivity [69].

Santa et al. suggest internal fluctuations between metastable atomic positions as one of the possible mechanisms of observing  $1/f$  type noise in Ag filament-based memristive materials. Furthermore, redox exchange is another possible mechanism, which in our studies would originate from the binding of  $\text{Ag}^+$  ions to the Ge-Ge sites during the switching. Diffusion of  $\text{Ag}^+$  ions inside Ag clusters may also have an influence on registered noise [70,71]. This suggestion is consistent with the observed characteristics. In the HRS conductivity is dominated by the hopping impurity mechanism, and results in low  $\gamma$  values ( $\gamma \leq -1$ ), which depend on applied potential only weakly. In the LRS state, the  $\gamma$  values are significantly higher ( $\gamma \geq -1$ ), and increase with decreasing voltage across the device. It is associated with mixed conductivity type/; Ohmic via filaments (or silver agglomerates) and impurity hopping in the bulk of the material.

The observable noise signature demonstrates the presence of multiple conductivity channels that form a complex network within a single device. The source of the noise can thus be described as an internal switching dynamics of an atomic switch network with a small world architecture [36].

It is in accordance with the literature studying  $1/f$  noise present in memristive devices. For a bridge synapse (Figures 4b and c), white noise is observed at potential close to 0V. The most symmetric response is observed for the bridge synapse without a differential amplifier (Figure 4b), as this configuration is symmetrical in design. Symmetric switching of the KNOWM memristors in the bridge synapse is shown in Figure 3(b).

#### 2.4. Analysis of simple signal transformation in SNESM

As part of the initial characterisation of signal transformation in the SNESM system, simple signals of various shapes and frequencies were applied to the reservoir. Frequency ranged from 1 to 10 Hz in



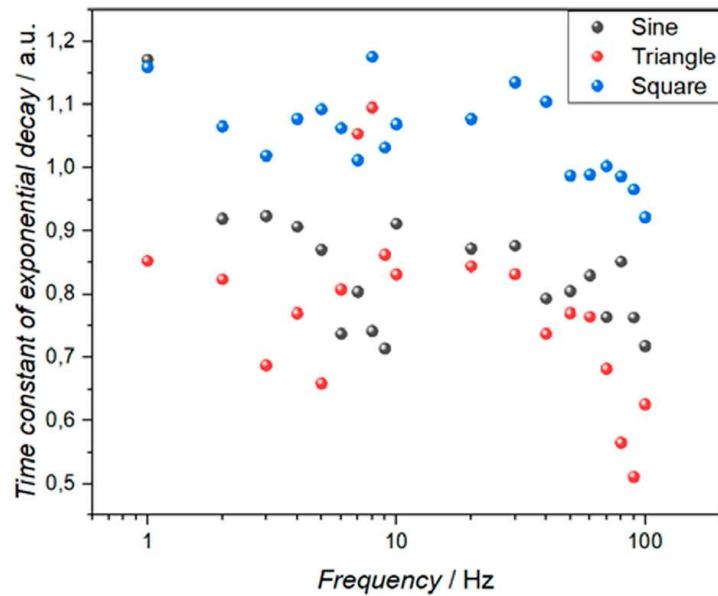


**Figure 5.** Collection of the values of exponential decay time constant for three signal shapes. Signal measured in SNESM with bridge synapse as computational substrate.

1 Hz steps and from 10 Hz to 100 Hz in 10 Hz steps were used. The delay time of the returned signal was determined as 20% of the signal packet duration, which provided an equal relative distance of repeated packets between different frequencies (an example shown in Fig. S4).

To analyze differences in signal damping, an exponential decay function was fitted to the maximal potential values of all signal packages. The time constant of the fitted exponent was collected for all of the studied frequencies and signal shapes (results shown in Figure 5).

Results show that for nearly all studied frequencies, clear separation of time constant can be noticed, however, a substantial overlap is also present in some frequency ranges (ca. 5–10 and 50–100 Hz). That result further suggests that signals of various shapes and frequencies can be represented in the SNESM system differently, possibly enabling their classification. Furthermore, signals of different shapes are filtered in a different way by a reservoir. Generally, triangular-shaped waves were damped the most, whereas square waves were passing with less attenuation. This result supports the presence of two fundamental reservoir requirements: separation and generalisation properties – signals of different shapes are separated by the system, and this separation is generalised across different frequencies (with slight deviations at 1, 5 and 6 Hz). Finally, the memory of KNOWM memristor (in addition to its resistive switching properties) can be represented as changes in the noise characteristics, which is sensitive to the system history, which is another important feature sought in the RC paradigm.

## 2.5. Epilepsy detection

The classification possibilities and the influence of the RC system on signal evolution were tested in the recognition of signals representing an epilepsy attack in patients. The dataset contains results for three patients, with 136 instances per patient. The classes included in the dataset are 'walking,' 'running,' 'sawing,' and 'epileptic seizure.' The data set contains time series of equal length.

Due to the nonlinear nature of the operation of memristors, which translates into non-linearity in the transformation of signals through the entire bridge synapse, strong filtering of negative part of signals can be observed (Figure 6b). Individual signal epochs exhibit stationary character which was confirmed with the augmented Dickey-Fuller as well as the Kwiatkowski-Phillips-Schmidt-Shin test. Subsequently, 11 parameters characterising the complexity of the signal were calculated, which served as features for the ML model training. An example of the correlation analysis (Pearson's correlation

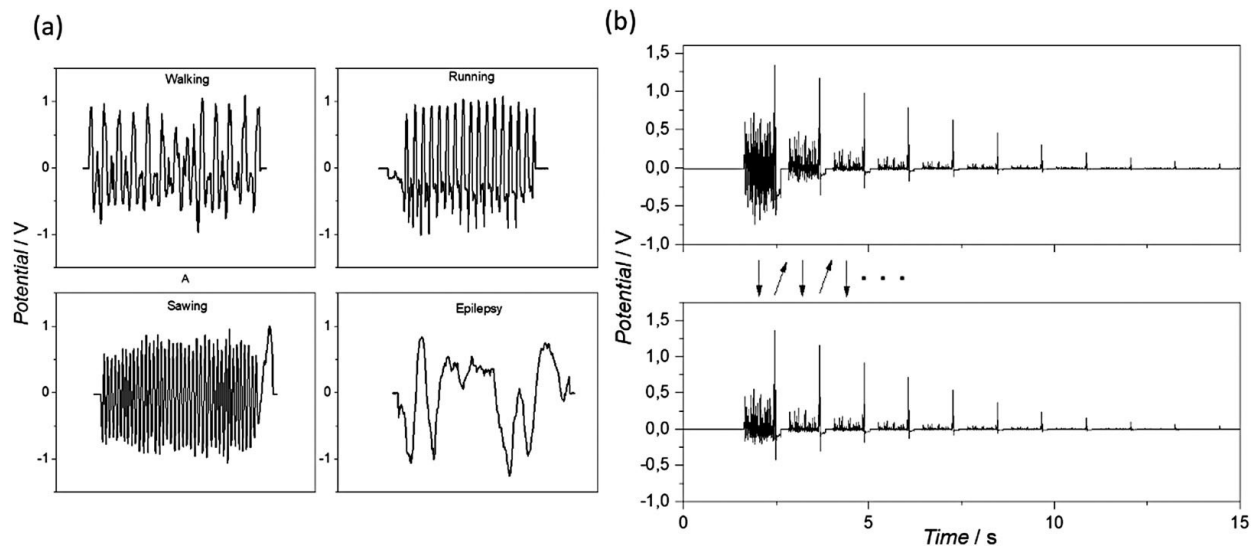


**Figure 6.** Examples of four classes of signals from the dataset (after standardisation) (a). Evolution of the signal in the SNESM system (b). First, the driving signal passes through the system, then is delayed and feed back again (arrows indicate direction of data flow).

parameter) of the calculated features can be seen on Figure 7. The presence of positive and negative correlations in the dataset is desirable, potentially contributing to a good classification accuracy. The calculated parameters were then used in training/testing a decision tree classification algorithm.

The analysis was performed for a maximum of 7 epochs of the signal (an increasing part of the signal was filtered in further epochs). Analysis was performed for each individual epoch (Figure 8a) as well as for several epochs at the same time (Figure 8b). The classic F1-score statistical parameter was used to determine the accuracy of the classification performed by the SNESM. It is the harmonic mean of the 'precision' (known as a positive predictive value) and 'recall' (also known as sensitivity) classification parameters. Precision is the fraction of relevant instances (target class, 'Epilepsy' in this study) among the other instances, whereas recall is the fraction of the relevant instances that have been classified correctly among other instances from the same class that have been omitted. F1 scores are biased to the lowest value of each precision and recall, so when the F1 score increases, both precision and recall parameters will be increased and balanced. In Figure 8 are presented results of the classification accuracy for increasing number of consecutive signal epochs.

The results obtained show that after several cycles, system exhibits an improvement of classification accuracy in comparison to unprocessed data. When the data were analyzed collectively, several epochs at once, further improvements in accuracy were obtained. To illustrate and compare the operation of the SNESM system for different patients, results were normalised in relation to the accuracy of unprocessed data, representing '1.' This method of data presentation allows for a simpler comparison of data sets from different patients for which the initial classification accuracy serving as a reference may differ. Apart from the case of patient no. 2, the first signal epoch actually worsens the classification accuracy. However, taking into account first and second signal epoch, accuracy is improved for all patients even though for individual epochs the accuracy was worse than reference. This effect may arise due to SNESM capabilities of data expansion and data transformation (Figure 9).

To inspect changes in complexity of the transformed signal histograms of two cases were compared – unprocessed signal and epoch no. 5 of this signal transformed by the SNESM for patient no. 1. Those signals were chosen as in this case, the highest improvement of classification accuracy was observed for a single signal epoch. Almost all of the calculated complexity parameters show distinct changes in their distribution, which can be one of the main reasons for improvement in the classification task in question. Not only those distributions changed, but also correlations between individual parameters have changed, where for transformed signal, more positive correlations are present for parameters which previously exhibited weak correlation (Figures 7a and b). At the same time, for the 2nd epoch

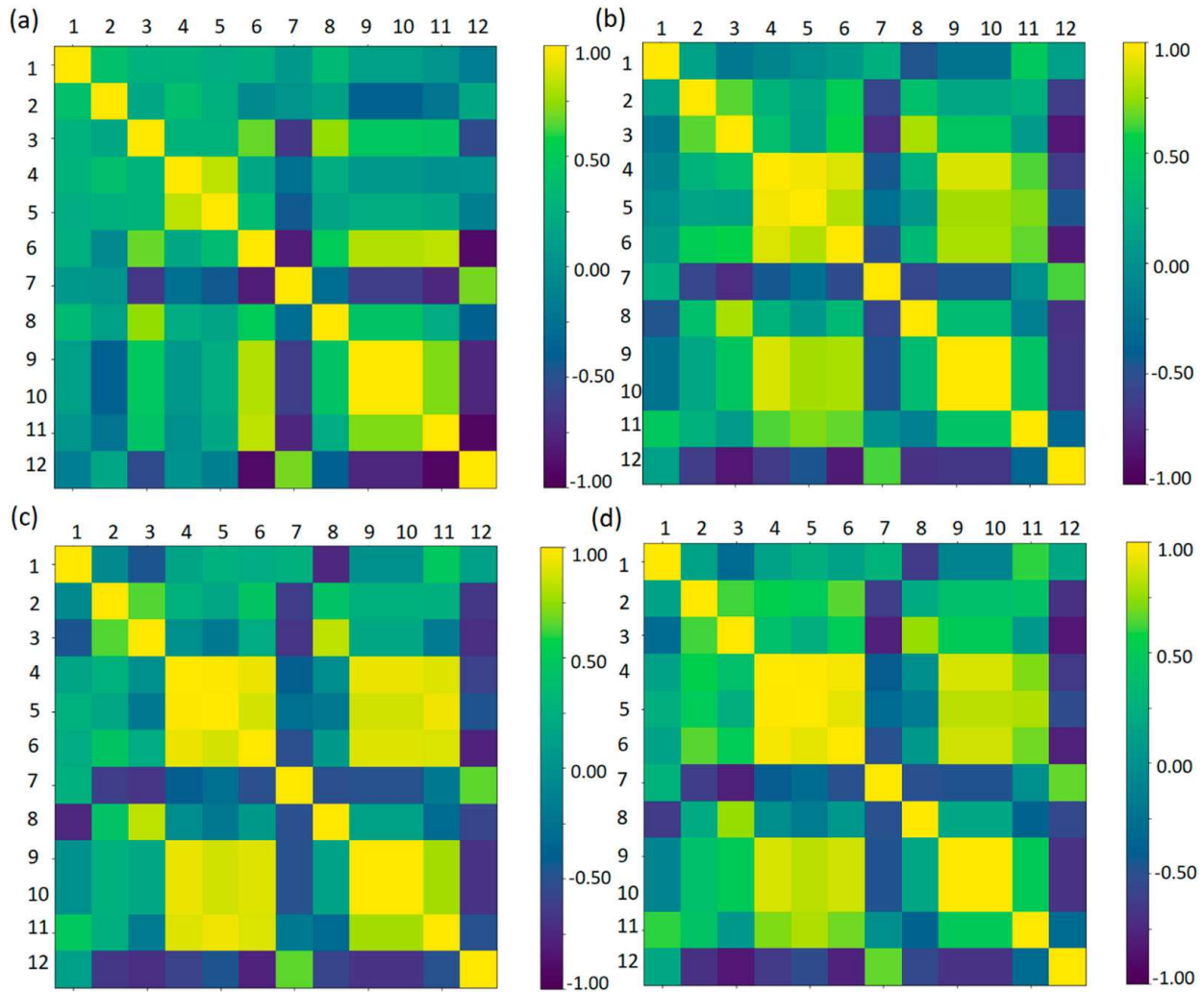


**Figure 7.** Exemplary result of Pearson's correlation for the "features" of the signal used by the reservoir system (a). The numbers correspond to the following parameters: 1 - 'Permutation entropy,' 2 - 'Spectral entropy,' 3 - 'Singular value decomposition entropy,' 4 - 'Approximate entropy,' 5 - 'Sample entropy,' 6 - 'Hjorth mobility,' 7 - 'Hjorth complexity,' 8 - 'Number of zero crossings,' 9 - 'Petrosian Fractal Dimension,' 10 - 'Katz Fractal Dimension,' 11 - 'Higuchi Fractal dimension,' 12 - 'Detrended Fluctuational Analysis.' Results for unprocessed input data (patient no. 1) (a) data transformed with SNESM: all 5 epochs (b), only second epoch (c), only 5th epoch (d).

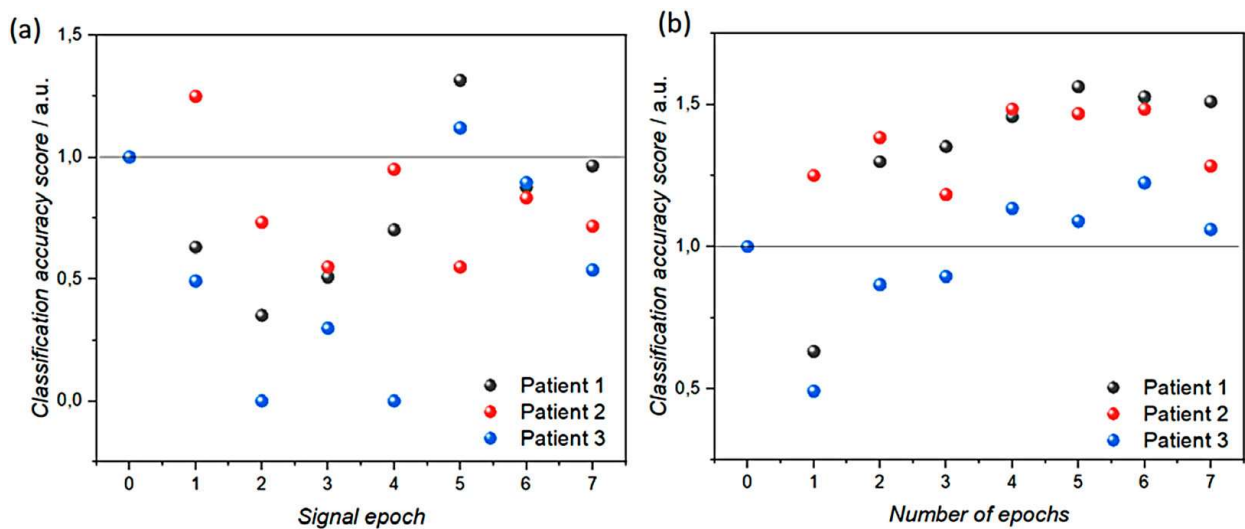


**Figure 8.** Result of classification precision scores for consecutive signal epochs (a) and for several epochs at once (b). The number '0' symbolises unprocessed input data that serve as a reference.

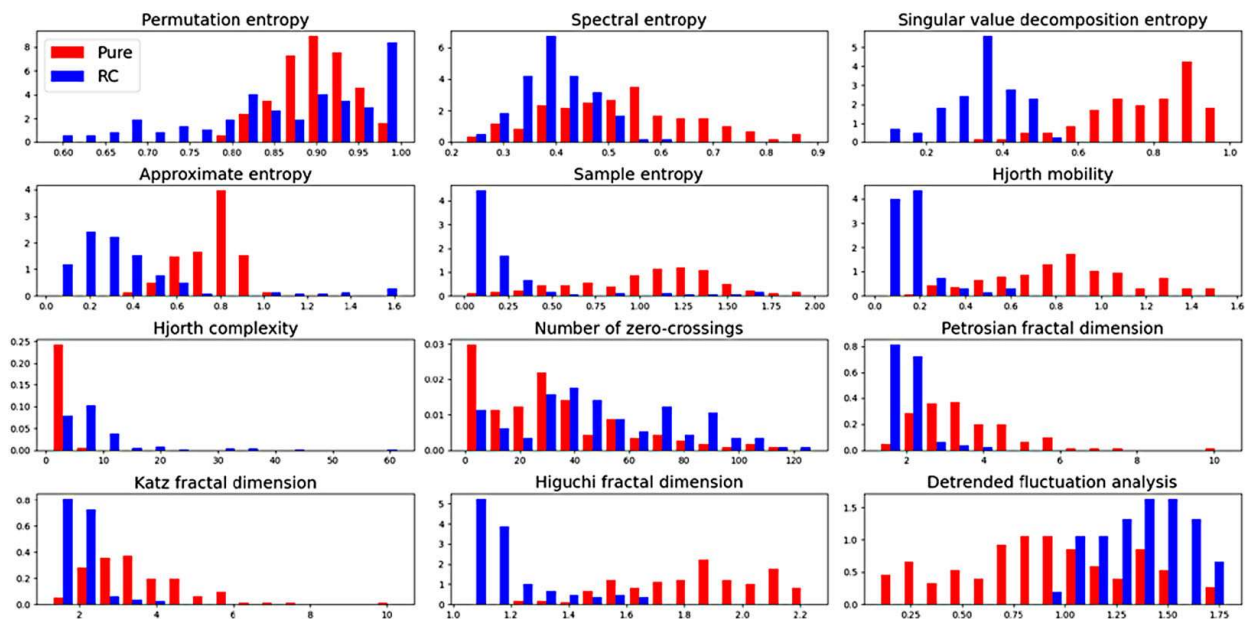


**Figure 9.** Comparison of histograms for the complexity parameters of the unprocessed signal ('Pure,' coloured red) and the transformed signal in the reservoir computing system ('RC,' coloured blue) for the patient no. 1 (Epoch no. 5 for RC).

case, the highest number of extreme correlation values can be observed, where for this case the classification accuracy result was the worst. The correlation results for the fifth epoch (Figure 7d) are more similar to the correlation results for the cumulative five epochs (Figure 7b), which may suggest that there are some optimal parameter correlation values that maximise the final ability of the system to accurately classify data.

### 3. Summary

In this work we have presented measurements and analysis of  $THD_R$  and noise in KNOWM memristors and bridge synapse based on them. Furthermore, the bridge synapse was incorporated into SNESM as a computational node. Analysis was performed on damping of signal of three standard different shapes (sin, square, and triangle) based on time constants of fitted exponential decay curves. After establishing rich internal dynamics, memory, separability, and generalisation properties, the SNESM system was tested as a tool to improve the classification of epilepsy. The system was tested under the constraints of scarce datasets (data from three patients classified in parallel) and using a simple classification model (decide tree). The results show an improvement in classification accuracy for several transformed signal epochs. Further improvements were achieved when signal epochs were analyzed collectively. This result shows that by transforming and filtering data in the SNESM system, certain properties of a given signal are amplified and others weakened, which is represented by different values of its non-linear dynamics parameters and changes of their correlation.

Nonlinear transformation, filtering of the signal, and its evolution in the feedback loop have a positive effect on the overall classification accuracy score. Results of similar nature were shown in one of our previous works, where signal filtering through an artificial neuron helped to improve overall data separability [72]. As was shown before, bridge synapse exhibits rich dynamics represented in several ways: in its noise characteristics,  $THD_R$  and time constant of exponential decay. As various RC systems aim to be more general in their computation capabilities, those facts may serve as an indication that this SNESM based RC can be a good computational system for other classification tasks. Results of characterisation of KNOWM memristors and bridge synapse-based SNESM system suggests the possibility of employing such systems for other computational and/or classification/prediction tasks, with scarce datasets and simple classification models.

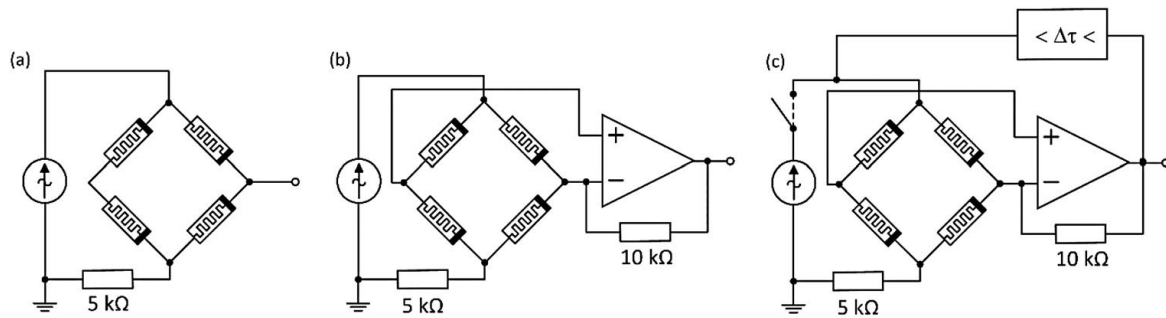


**Figure 10.** Schematics of the systems studied. Bridge synapse without (a), with differential amplifier (b), and incorporated into SNESM system (c).

## 4. Experimental

Three different circuits used in this study are shown in Figure 10. BioLogic Sp-150 was used to measure LASV and chronoamperometric noise measurements. ADA-24 PicoLog was used to probe individual KNOWN memristors in the bridge synapse. An analog channel of BioLogic was used to record signals of simple shapes (sin, triangle, and square). Fitting of exponential decay curves and collection of their time constants were performed using Python (Pandas and SciPy packages). OriginPro was used in calculations of the fast Fourier Transform for THD and noise analysis.

The dataset for the classification task was downloaded from the 'UEA & UCR Time Series Classification Repository' (<https://www.timeseriesclassification.com/description.php?Dataset=Epilepsy>). Firstly, the data set was standardised using Python. The arbitrary function generator TTI TG5012A was used to apply the signals to the RC system. Data were uploaded from a flash drive in bits of four (maximum TTI TG5012A memory). Each waveform required additional scaling to be in the  $1V_{pp}$  range due to the observed lack of consistency in the amplitudes of the signals generated by the TTI TG5012A. Before each measurement, an Agilent oscilloscope was used to fine-scale the signal. The Rigol DG4062 generator was used as the arbitrary trigger for the TTI TG5012A signal source. Furthermore, the TTI WA301 amplifier was used as a current buffer. The bridge synapse includes the TL082 operational amplifier (powered by a 9V battery) in differential mode – the negative input of the operational amplifier has an additional feedback from the amplifier output connected through a 10 kΩ resistor. The analog channel of the Biologic SP-150 potentiostat was used to record the data. Custom-made delay line (Chip, Poland) was used in the setup. The generator signal was first sent to delay, then to the Kacper-01 analog potentiostat (Instytut Fotonowy, Poland), which transmitted the signal to the synaptic bridge. The differential amplifier passed the signal back to the delay (via the TTI amplifier). The delay signal was recorded, delayed, attenuated ( $\sim 10\%$ ) and finally circulated back to the system until fully suppressed.

The recorded signal was then analyzed using Python. To analyze reservoir properties, an exponential decay function was fitted to maximal amplitudes of given repeated signal instances. Time constants of exponential decay were collected and presented in Figure 5. The extraction of signal complexity features was performed using the Antropy Python package. A short description of the calculated complexity parameters can be found in the SI. The parameters with appropriate labels were passed through a simple machine learning pipeline (using Python Scikit learn package). Initially, general descriptions of the data (histograms and correlation matrix) were generated. A 10-fold cross-validation was used to divide the data set into training and testing sets. It involves dividing the data set into 10 parts, using 9 parts as a training set and 1 part as a testing set. This procedure is then repeated 10 times so that each piece of data is used as both a training and a testing set. As a classification model, the Decision Tree Classifier implemented in scikit-learn Python package was used. The complexity parameters of the unprocessed signal were used as a reference. Model training was performed on an unprocessed signal and for each consecutive delay signal epoch. In the next step, an increasing number of signal epochs were collectively used in training/testing the model.

## Disclosure statement

No potential conflict of interest was reported by the author(s).

## Funding

The authors acknowledge the financial support from the Polish National Science Center within the OPUS (grant agreement No. UMO-2020/37/B/ST5/00663) and PRELUDIUM (grant agreement No. UMO-2018/31/N/ST5/03112) projects. DP has been partly supported by the EU Project POWR 03.02.00-00-I004/16.

## References

- [1] Schuster AJ. Understanding information. Cham: Springer; 2017.
- [2] Zgurovsky MZ, Zaychenko YP. Big data: conceptual analysis and applications. Cham: Springer; 2020, Vol. 58.
- [3] Schuster AJ. Understanding information: from the big bang to big data. Cham: Springer; 2017.
- [4] Sangaiah AK, Thangavelu A, Sundaram VM. Cognitive computing for big data systems over iot. Cham: Springer; 2018.
- [5] Reis R. Challenges in the design of integrated systems for iot. Cham: Springer International Publishing; 2020, p. 179–196.
- [6] Yassine A, Singh S, Hossain MS, et al. Iot big data analytics for smart homes with fog and cloud computing. *Future Gener Comput Syst*. 2019;91:563–573.
- [7] Reis R. Strategies for reducing power consumption and increasing reliability in iot. Cham: Springer International Publishing; 2019, p. 76–88.
- [8] Zafarani R, Abbasi MA, Liu H. Social media mining: an introduction. Cham: Cambridge University Press; 2014.
- [9] Lee TK, Cho JH, Kwon DS, et al. Global stock market investment strategies based on financial network indicators using machine learning techniques. *Expert Syst Appl*. 2019;117:228–242.
- [10] Tkáč M, Verner R. Artificial neural networks in business: two decades of research. *App. Soft Comput*. 2016;38:788–804.
- [11] Rathi R. Effect of Cambridge Analytica's Facebook ads on the 2016 US presidential election. [cited 2022 May 15]. Available from: <https://towardsdatascience.com/effect-of-cambridge-analyticas-facebook-ads-on-the-2016-us-presidential-election-dacb5462155d>.
- [12] Kendon V, Sebald A, Stepney S. Heterotic computing: past, present and future. *Philos Trans Royal Soc A: Math, Phys Eng Sci*. 2015;373; doi:10.1098/rsta.2014.0225.
- [13] Arden W, Brillouët M, Cogez P, et al. More-than-moore white paper. *Version* 2010, 2, 14.
- [14] Szaciłowski K. Infochemistry information processing at the nanoscale. Chichester: John Wiley & Sons; 2012.
- [15] Adamatzky A, Akl SG, Sirakoulis GC. From parallel to emergent computing. Boca Raton: CRC Press; 2019.
- [16] Stepney S, Adamatzky A. Inspired by nature. Cham: Springer International Publishing; 2018.
- [17] Adamatzky A. Advances in unconventional computing prototypes, models and algorithms. Cham: Springer International Publishing; 2017.
- [18] Adamatzky A. Advances in unconventional computing theory. Cham: Springer International Publishing; 2017.
- [19] Adamatzky A. Handbook of unconventional computing. Singapore: World Scientific; 2020, p. 1208.
- [20] Pilarczyk K, Właźlak E, Przyczyna D, et al. Molecules, semiconductors, light and information: towards future sensing and computing paradigms. *Coord Chem Rev* 2018;365:23–40.
- [21] Li Y, Wang Z, Midya R, et al. Review of memristor devices in neuromorphic computing: materials sciences and device challenges. *J Phys D: Appl Phys*. 2018;51:503002.
- [22] Liao K, Lei P, Tu M, et al. Memristor based on inorganic and organic two-dimensional materials: mechanisms, performance, and synaptic applications. *ACS Appl Mater Interfaces*. 2021;13:32606–32623.
- [23] Chua L, Sirakoulis GC, Adamatzky A. Handbook of memristor networks. Cham: Springer Nature; 2019.
- [24] Adamatzky A, Chua L. Memristor networks. New York: Springer; 2014.
- [25] Ito S, Hayakawa Y, Wei Z, et al. In *Reram technologies for embedded memory and further applications*, 2018 IEEE International Memory Workshop (IMW), 2018; IEEE: pp 1–4.
- [26] Przyczyna D, Zawal P, Mazur T, et al. In-materio neuromimetic devices: dynamics, information processing and pattern recognition. *Jpn J Appl Phys* 2020;59:050504.
- [27] Kumar S, Wang X, Strachan JP, et al. Dynamical memristors for higher-complexity neuromorphic computing. *Nature Reviews Materials*. 2022. <https://doi.org/10.1038/s41578-022-00434-z>
- [28] Park H-L, Lee T-W. Organic and perovskite memristors for neuromorphic computing. *Org Electron*. 2021;98; doi:10.1016/j.orgel.2021.106301.
- [29] Zhou G, Wang Z, Sun B, et al. Volatile and nonvolatile memristive devices for neuromorphic computing. *Advanced Electronic Materials*. 2022. doi:10.1002/aeml.2101127.
- [30] Właźlak E, Przyczyna D, Gutierrez R, et al. Towards synthetic neural networks: Can artificial electrochemical neurons be coupled with artificial memristive synapses? *Jpn J Appl Phys* 2020;59:SI0801.
- [31] Akopyan F, Sawada J, Cassidy A, et al. Truenorth: design and tool flow of a 65 mw 1 million neuron programmable neurosynaptic chip. *IEEE Trans. Comp.-Aided Des. Integr. Circ. Syst*. 2015;34:1537–1557.

- [32] Jaeger H. The “echo state” approach to analysing and training recurrent neural networks—with an erratum note. *Bonn, Germany: German National Research Center for Information Technology GMD Technical Report 2001*, 148, 13.
- [33] Maass W, Natschläger T, Markram H. Real-time computing without stable states: a new framework for neural computation based on perturbations. *Neural Comput* 2002;14:2531–2560.
- [34] Otto A, Just W, Radons G. Nonlinear dynamics of delay systems: an overview. *Philos Trans Royal Soc A: Math, Phys Eng Sci*. 2019;377; doi:10.1098/rsta.2018.0389.
- [35] Konkoli Z, Nichele S, Dale M, et al. Reservoir computing with computational matter. In: *Computational matter*. Cham: Springer; 2018. p. 269–293.
- [36] Nakajima K, Fischer I. Reservoir computing. Theory, physical implementations, and applications. Singapore: Springer Nature Singapore; 2021.
- [37] Fernando C, Sojakka S. In *Pattern recognition in a bucket*, European conference on artificial life, 2003; Springer: pp 588–597.
- [38] Przyczyna D, Suchecki M, Adamatzky A, et al. Towards embedded computation with building materials. *Materials (Basel)*. 2021;14:1724.
- [39] Hart JD, Larger L, Murphy TE, et al. Delayed dynamical systems: networks, chimeras and reservoir computing. *Phil Trans. A*. 2019;377; doi:10.1098/rsta.2018.0123.
- [40] Biswas D, Banerjee T. Time-delayed chaotic dynamical systems. Cham: Springer Nature; 2018.
- [41] Konkoli Z. On reservoir computing: from mathematical foundations to unconventional applications. In: Adamatzky A, editor. *Advances in unconventional computing*. Vol. 1: theory. Cham: Springer International Publishing; 2017.
- [42] Lis M, Omuna S, Przyczyna D, et al. From oscillatory reactions to robotics: a serendipitous journey through chemistry, physics and computation. In: *Handbook of unconventional computing*. Singapore: World Scientific; 2022. p. 1–80.
- [43] Właźlak E, Marzec M, Zawal P, et al. Memristor in a reservoir system—experimental evidence for high-level computing and neuromorphic behavior of pbi2. *ACS Appl Mater Interfaces*. 2019;11:17009–17018.
- [44] Właźlak E, Zawal P, Szaciłowski K. Neuromorphic applications of a multivalued [sni4{(c6h5)2so}2] memristor incorporated in the echo state machine. *ACS Applied Electronic Materials*. 2020;2:329–338.
- [45] Przyczyna D, Pecqueur S, Vuillaume D, et al. Reservoir computing for sensing—an experimental approach. *Int. J. Unconv. Comput*. 2019;14:267–284.
- [46] Właźlak E, Zawal P, Szaciłowski K. Neuromorphic applications of a multivalued [sni4{(c6h5)2so}2] memristor incorporated in the echo state machine. *ACS Appl. Electron. Mater*. 2020;2:329–338.
- [47] Przyczyna D, Szaciłowska M, Przybylski M, et al. Recognition of musical dissonance and consonance in a simple neuromorphic computing system. *Int. J. Unconv. Comput*. 2022;17:81–104.
- [48] Epilepsy. [cited 2022 June 3]. Available from: <https://www.who.int/news-room/fact-sheets/detail/epilepsy>.
- [49] Falco-Walter JJ, Scheffer IE, Fisher RS. The new definition and classification of seizures and epilepsy. *Epilepsy Res*. 2018;139:73–79.
- [50] Sarmast ST, Abdullahi AM, Jahan N. Current classification of seizures and epilepsies: scope, limitations and recommendations for future action. *Cureus*. 2020;12:e10549.
- [51] Scheffer IE, Berkovic S, Capovilla G, et al. Ilae classification of the epilepsies: position paper of the ilae commission for classification and terminology. *Epilepsia*. 2017;58:512–521.
- [52] Noachtar S, Rémi J. The role of eeg in epilepsy: a critical review. *Epilepsy Behav*. 2009;15:22–33.
- [53] Frei MG. Seizure detection. *Scholarpedia*. 2013;8:5780.
- [54] Regalia G, Onorati F, Lai M, et al. Multimodal wrist-worn devices for seizure detection and advancing research: focus on the empatica wristbands. *Epilepsy Res*. 2019;153:79–82.
- [55] Ullah I, Hussain M, Aboalsamh H. An automated system for epilepsy detection using eeg brain signals based on deep learning approach. *Expert Syst Appl*. 2018;107:61–71.
- [56] Velez M, Fisher RS, Bartlett V, et al. Tracking generalized tonic-clonic seizures with a wrist accelerometer linked to an online database. *Seizure*. 2016;39:13–18.
- [57] Onorati F, Regalia G, Caborni C, et al. Prospective study of a multimodal convulsive seizure detection wearable system on pediatric and adult patients in the epilepsy monitoring unit. *Front Neurol* 2021;12:724904–724904.
- [58] Van de Vel A, Cuppens K, Bonroy B, et al. Long-term home monitoring of hypermotor seizures by patient-worn accelerometers. *Epilepsy Behav* 2013;26:118–125.
- [59] Williams CKI. The effect of class imbalance on precision-recall curves. *Neural Comput* 2021;33:853–857.
- [60] Knowm sdc memristors. [cited 2022 May 15]. Available from: [https://knowm.org/downloads/Knowm\\_Memristors.pdf](https://knowm.org/downloads/Knowm_Memristors.pdf).
- [61] Gomez J, Vourkas I, Abusleme A. Exploring memristor multi-level tuning dependencies on the applied pulse properties via a low cost instrumentation setup. *IEEE Access*. 2019;7:59413–59421.
- [62] Marković I, Potrebić M, Tošić D. Memristors as candidates for replacing digital potentiometers in electric circuits. *Electronics (Basel)*. 2021;10:181.
- [63] Volos CK, Pham V-T, Nistazakis HE, et al. A dream that has come true: chaos from a nonlinear circuit with a real memristor. *Int J Bifurcation Chaos*. 2020;30; doi:10.1142/S0218127420300360.
- [64] Dos Santos S, Furui S. In *A memristor based ultrasonic transducer: the memosducer*, 2016 IEEE International Ultrasonics Symposium (IUS), 2016; IEEE: pp 1–4.

- [65] Ostrovskii V, Fedoseev P, Bobrova Y, et al. Structural and parametric identification of known memristors. *Nanomaterials*. 2021;12:63.
- [66] Giner-Sanz JJ, Ortega EM, Pérez-Herranz V. Total harmonic distortion based method for linearity assessment in electrochemical systems in the context of eis. *Electrochim Acta*. 2015;186:598–612.
- [67] Pershin YV, Chien C-C, Di Ventra M. The Fourier signatures of memristive hysteresis. *J Phys D: Appl Phys* 2021;54:245302.
- [68] Vasseur DA, Yodzis P. The color of environmental noise. *Ecology*. 2004;85:1146–1152.
- [69] Chen T, Bobbert PA, van der Wiel WG. 1/f noise and machine intelligence in a nonlinear dopant atom network. *Small Science*. 2021;1; doi:10.1002/sssc.2000014.
- [70] Santa B, Balogh Z, Gubicza A, et al. Universal 1/f type current noise of Ag filaments in redox-based memristive nanojunctions. *Nanoscale*. 2019;11:4719–4725.
- [71] Santa B, Balogh Z, Pósa L, et al. Noise tailoring in memristive filaments. *ACS Appl Mater Interfaces*. 2021;13:7453–7460.
- [72] Przycyna D, Lis M, Pilarczyk K, et al. Hardware realization of the pattern recognition with an artificial neuromorphic device exhibiting a short-term memory. *Molecules*. 2019;24:2738.



# KNOWM Memristors in a Bridge Synapse delay-based Reservoir Computing system for detection of epileptic seizures

Dawid Przyczyna,<sup>\*1,2</sup> Grzegorz Hess<sup>3</sup> and Konrad Szaciłowski<sup>\*1</sup>

1. *AGH University of Science and Technology, Academic Centre for Materials and Nanotechnology, al. Mickiewicza 30, 30-059 Kraków, Poland*
2. *AGH University of Science and Technology, Faculty of Physics and Applied Computer Science, al. Mickiewicza 30, 30-059 Kraków, Poland*
3. *Jagiellonian University, Department of Neurophysiology and Chronobiology, Institute of Zoology and Biomedical Research, ul. Gronostajowa 9, 30-387 Kraków, Poland*

## Electronic Supplementary Information

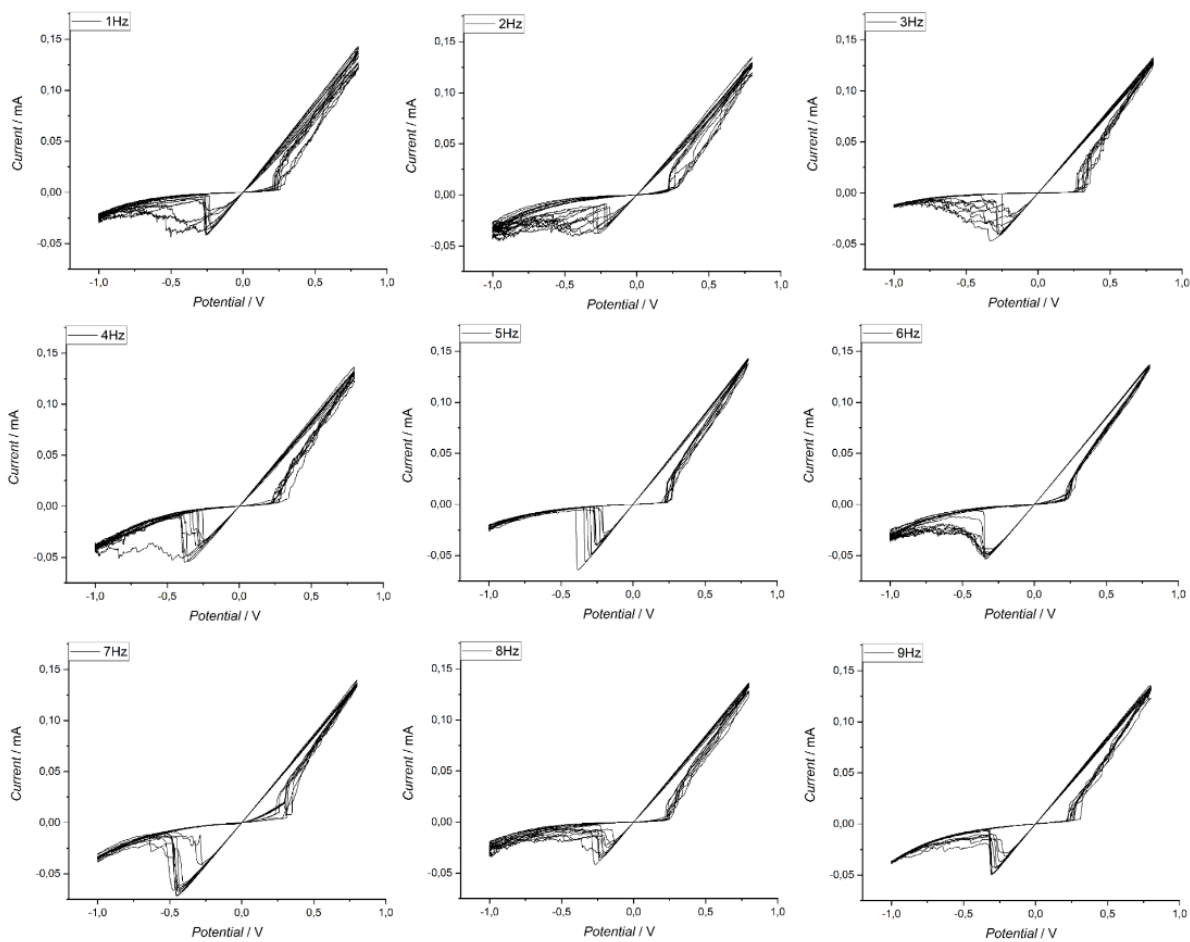


Figure S1. Cyclic voltammetry measurements for the KNOWM memristor at different scanning speeds (1-9Hz).

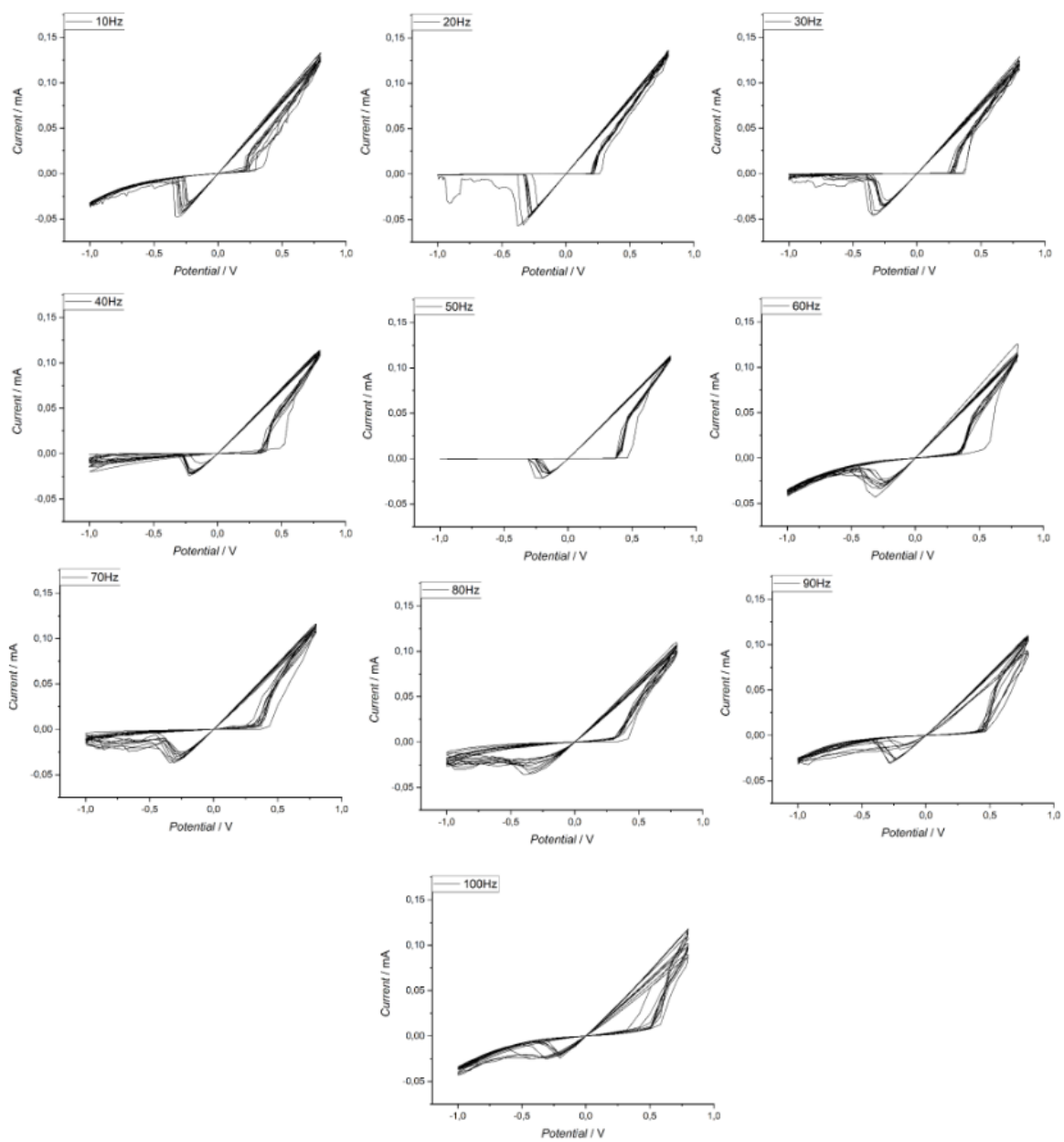


Figure S2. Cyclic voltammetry measurements for the KNOWM memristor at different scanning speeds (10-100Hz).

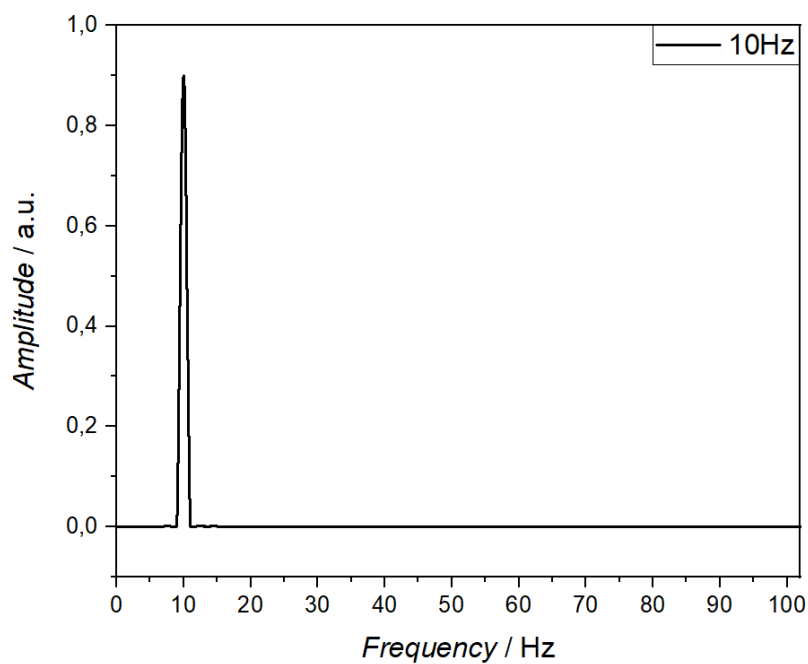


Figure S3. Exemplary Fourier Transform for the control signal used in this study (sinusoidal wave of 10Hz)

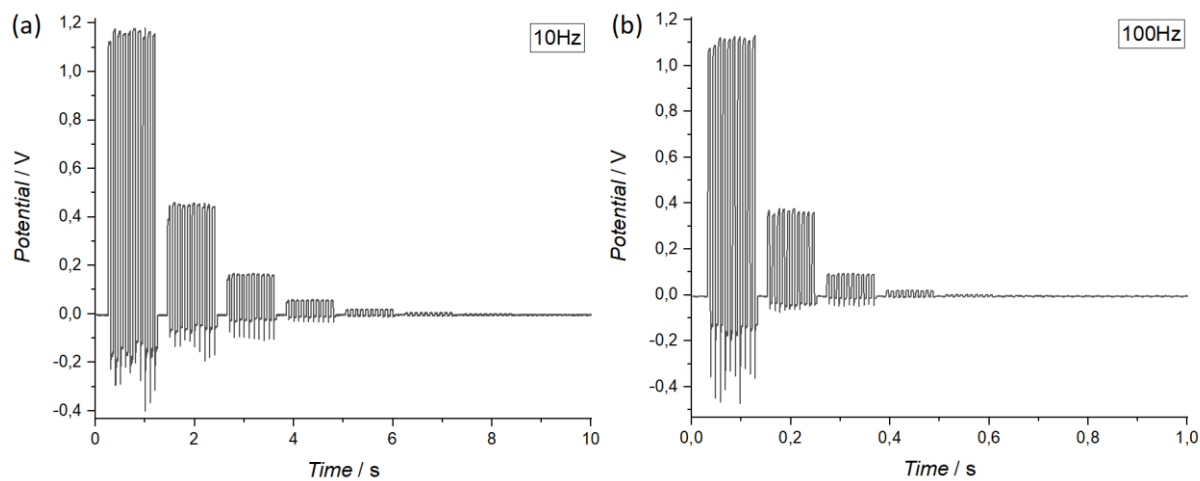


Figure S4. Illustration of setting equal relative delay time for different frequencies (on the example of 10Hz (a) and 100Hz (b)). The delay time was set to  $t = 1.2$  seconds and  $t = 0.12$  seconds, respectively.

## *Oświadczenia współautorów*



### Oświadczenie o udziale w publikacjach mgr inż. Dawida Przyczyna

Ja, niżej podpisany Konrad Szaciłowski oświadczam, że mój udział w wymienionych poniżej publikacjach mgr. inż. Dawida Przyczyna polegał na:

D1. Ewelina Właźlak, Dawid Przyczyna, Rafael Gutierrez, Gianarelio Cuniberti, Konrad Szaciłowski „Towards synthetic neural networks: can artificial electrochemical neurons be coupled with artificial memristive synapses?”, *Jpn. J. Appl. Phys.* 2020, 59, SI0801

zdefiniowaniu zakresu tematycznego oraz przygotowaniu części manuskryptu, w szczególności części dotyczącej oscylatorów elektrochemicznych;

D2. Dawid Pprzyczyna, Maria Lis, Kacper Pilarczyk, Konrad Szaciłowski „Hardware realization of the pattern recognition with an artificial neuromorphic device exhibiting a short-term memory”, *Molecules* 2019, 24, 2738

zaprojektowaniu układu pomiarowego oraz opracowaniu algorytmu do przetwarzania danych pomiarowych, a w szczególności do zdefiniowania wskaźników sepoarowalności;

D3. Dawid Przyczyna, Maciej Suchecki, Andrew Adamatzky, Konrad Szaciłowski „Towards Embedded Computation with Building Materials”, *Materials* 2021, 14, 1724

zaprojektowaniu części eksperymentów, interpretacji wyników otrzymanych w pomiarach elektrochemicznych oraz analizie części danych związanych z wieloparametrową klasyfikacją sygnałów (przedstawioną na Rys. 8 przedmiotowej publikacji);

D4. Dawid Przyczyna, Sebastien Pecqueur, Dominique Vuillaume, Konrad Szaciłowski „Reservoir computing for sensing: an experimental approach”, *Int. J. Unconv. Comput.*, 2019, 14, 267

zaprojektowaniu układów pomiarowych i części eksperymentów;

D5. Dawid Przyczyna, Maria Szaciłowska, Marek Przybylski, Marcin Strzelecki, Konrad Szaciłowski „Recognition of Musical Dissonance and Consonance in a Simple Neuromorphic Computing System”, *Int. J. Unconv. Comput.* 2022, 17, 81

zdefiniowaniu hipotezy badawczej oraz zaprojektowaniu i doborze parametrów synapsy oraz wstępnej obróbce numerycznej wyników;

D6. Dawid Przyczyna, Grzegorz Hess, Konrad Szaciłowski „KNOWM Memristors in a Bridge Synapse delay-based Reservoir Computing system for detection of epileptic seizures”, *Int. J. Parallel Dist. Syst.* 2022, 10.1080/17445760.2022.2088751

konsultacji konstrukcji obwodów pomiarowych i wykonaniu części analizy spektralnej szumu.

Prof. dr hab. Grzegorz Hess

Zakład Neurofizjologii i Chronobiologii

Instytut Zoologii i Badań Biomedycznych Uniwersytetu Jagiellońskiego

ul. Gronostajowa 9

30-387 Kraków

Kraków, 1.07.2022 r.

### **Oświadczenie o udziale w publikacji**

Oświadczam, że mój udział w publikacji:

D6. Dawid Przyczyna, Grzegorz Hess, Konrad Szaciłowski „KNOWM Memristors in a Bridge Synapse delay-based Reservoir Computing system for detection of epileptic seizures”, *Int. J. Parallel Dist. Syst.* 2022, 10.1080/17445760.2022.2088751.

polegał na dyskusji tytułowego zagadnienia epilepsji, przygotowaniu fragmentów wstępu oraz redakcji manuskryptu.





## Akademickie Centrum Materiałów i Nanotechnologii AGH

prof. dr hab. inż. Marek Przybylski  
DYREKTOR

ACMiN/2022

Kraków, 1.07.2022 r.

### O Ś W I A D C Z E N I E o udziale w publikacji

Ja, niżej podpisany Marek Przybylski oświadczam, że mój udział w publikacji:

D5. Dawid Przyczyna, Maria Szaciłowska, Marek Przybylski, Marcin Strzelecki, Konrad Szaciłowski, „Recognition of Musical Dissonance and Consonance in a Simple Neuromorphic Computing System”, Int. J. Unconv. Comput. 2022, 17, 81

polegał na dyskusji wyników oraz pomocy w redakcji manuskryptu.

Z poważaniem –



Otrzymują:

1. Adresat,
2. a/a

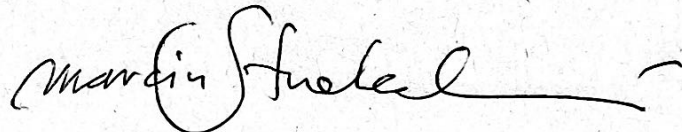
## OŚWIADCZENIE

o udziale w publikacji

Ja, niżej podpisany Marcin Strzelecki oświadczam, że mój udział w publikacji:

D5. Dawid Przyczyna, Maria Szaciłowska, Marek Przybylski, Marcin Strzelecki,  
Konrad Szaciłowski „Recognition of Musical Dissonance and Consonance in a Simple  
Neuromorphic Computing System”, *Int. J. Unconv. Comput.* 2022, 17, 81

polegał na dyskusji na temat wyników, przygotowaniu fragmentów wstępu tworzących  
kontekst muzyczny do prowadzonych badań oraz redakcji manuskryptu.

A handwritten signature in black ink, reading "Marcin Strzelecki". The signature is written in a cursive style with a long horizontal line extending to the right.

Kraków 02.07.2022

## OŚWIADCZENIE

o udziale w publikacji

Ja, niżej podpisana Maria Lis oświadczam, że mój udział w publikacji:

D2. Dawid Przychyna, Maria Lis, Kacper Pilarczyk, Konrad Szaciłowski „Hardware realization of the pattern recognition with an artificial neuromorphic device exhibiting a shortterm memory”, *Molecules* 2019, 24, 2738

polegał na przygotowaniu fotoelektrod na bazie siarczku kadmu, wykonywaniu neuromimetycznych pomiarów fotoelektrochemicznych, analizowaniu proszkowej dyfraktometrii promieniami X, analizie widm UV-Vis metodą Tauca, pisaniu fragmentów manuskryptu oraz jego redakcji.



Podpis